Investigating correlation among geometrical parameters of isotropic and anisotropic fibrous porous media

by
Esmari Maré

Thesis presented in partial fulfilment of the requirements for the degree of
Master of Science
in the Faculty of Science at Stellenbosch University

The financial assistance of the National Research Foundation (NRF) towards this research is hereby acknowledged. Opinions expressed and conclusions arrived at, are those of the author and are not necessarily to be attributed to the NRF.

Supervisor: Prof S Fidder-Woudberg December 2020

Declaration

By submitting this thesis electronically, I declare that the entirety of the work contained therein is my own, original work, that I am the sole author thereof (save to the extent explicitly otherwise stated), that reproduction and publication thereof by Stellenbosch University will not infringe any third party rights and that I have not previously in its entirety or in part submitted it for obtaining any qualification.

Date: December 1, 2020

Abstract

In this study four main geometrical models available in the literature that approximate the micro-structure of metal foams (i.e. the cubic unit cell model, the tetrakaidecahedron model, the dodecahedron model and the rectangular three-strut Representative Unit Cell (RUC) model), are outlined. Furthermore, an anisotropic two-strut RUC model is discussed in order to accommodate predictions of the morphological and transport properties of fibre-like materials due to its geometric model structure representing fibres more closely than metal foams. Equations for the prediction of the specific surface area in terms of the pore diameter and the porosity for each of the model geometries are presented and the predictions are compared to experimental data from the literature. Comparison of the model predictions show that the tetrakaidecahedron, dodecahedron and RUC models give similar results and correspond well with the experimental data. A kinetic approach is also considered where the transport properties, such as the experimental permeability obtained from the pressure drop, and porosity data of fibrous media are used to determine the specific surface area. Thereafter, a combined geometric and kinetic approach is investigated which combines the use of the transport properties of the fibrous media and the geometrical models that represent the fibrous media in order to determine the specific surface area. The two-strut and three-strut RUC models receive special attention in this study due to the advantage that the rectangular geometry allows for relatively simple geometric adaptations. Equations predicting the permeability and the specific surface area of the existing isotropic three-strut and anisotropic two-strut RUC models, as well as the compressed three-strut and two-strut RUC models, are proposed and compared to experimental data obtained involving foams and fibres. The isotropic and anisotropic RUC models are furthermore adapted to account for the Klinkenberg effect, an effect that accounts for the increase in gas permeability, compared to liquid permeability, and its influence on the specific surface area predictions are investigated. The model predictions are compared to a variety of available experimental data for fibrous media from the literature and the correspondence proves to be satisfactory. It is also shown that the permeability prediction of the two-strut model is more accurate for compressed layered fibrous media consisting of the stacking of fibres into parallel sheets than the compressed three-strut model, as expected. The analytical modelling approach presented adds value to this field of study in comparison with the empirical studies in the literature which mostly comprise of curve fitting procedures together with the introduction of empirical coefficients into the permeability equations to obtain correlation with experimental data.

Uittreksel

In hierdie studie word vier hoofgeometriese modelle wat beskikbaar is in die literatuur en wat die mikrostruktuur van metaalsponse benader (dit is, die kubiese eenheidsel model, die tetrakaidekahedron model, die dodekahedron model en die reghoekige driebeen verteenwoordigende eenheidsel (VES) model) uiteengesit. Daarbenewens word 'n anisotrope VES-model met twee bene bespreek om voorsiening te maak vir die voorspellings van die morfologiese en vloei eienskappe van veselagtige materiale as gevolg van die geometriese model-struktuur, wat vesels nader verteenwoordig as metaalsponse. Vergelykings vir die voorspelling van die spesifieke oppervlakarea in terme van die poriediameter en die porositeit word voorgestel vir elk van die modelgeometrieë en die voorspellings vergelyk met eksperimentele data vanuit die literatuur. Vergelyking van die modelvoorspellings toon dat die tetrakaidekahedron-, dodekahedron- en VES-modelle soortgelyke resultate lewer en goed ooreenstem met die eksperimentele data. 'n Kinematiese benadering word ook beskou waar die vervoer-eienskappe, soos die eksperimentele permeabiliteit verkry vanaf die drukval, en porositeit data van veselagtige poreuse media gebruik word om die spesifieke oppervlakarea te bepaal. Daarna word 'n gekombineerde geometriese en kinematiese benadering ondersoek wat die gebruik van die vervoer-eienskappe van die veselagtige poreuse media kombineer met die geometriese modelle wat die veselagtige media voorstel om die spesifieke oppervlakarea te bepaal. Daar word in hierdie studie veral aandag gegee aan die twee-been en drie-been VES-modelle as gevolg van die voordeel dat die reghoekige geometrie relatief eenvoudige geometriese aanpassings moontlik maak. Vergelykings wat die permeabiliteit en die spesifieke oppervlakarea van die bestaande isotrope drie-been en anisotrope twee-been VES-modelle voorspel, sowel as dié van die drie-been en twee-been VES-modelle wat aangepas is om rekenskap aan samepersing te gee, word voorgestel en vergelyk met eksperimentele data wat verkry is van sponse en vesels. Die isotrope en anisotrope VES-modelle word verder aangepas om rekening te hou met die Klinkenberg-effek, 'n effek wat verantwoordelik is vir die toename in die gaspermeabiliteit in vergelyking met die vloeistofpermeabiliteit, en die invloed daarvan op die spesifieke oppervlakarea voorspellings, word ondersoek. Die modelvoorspellings word vergelyk met 'n verskeidenheid beskikbare eksperimentele data vir veselagtige media vanuit die literatuur, en die ooreenkoms blyk bevredigend te wees. Daar word ook getoon dat die voorspelling van die permeabiliteit van die twee-been model akkurater is vir saamgeperste veselagtige media wat bestaan uit 'n stapel van vesels in parallelle velle as die drie-been model, soos te verwagte. Die analitiese modelleringsbenadering voeg waarde toe tot die empiriese studies in die literatuur, wat meestal bestaan uit krommepassing prosedures tesame met die bekendstelling van empiriese koëffisiënte in die permeabiliteitsvergelykings om korrelasie met eksperimentele data te verkry.

Acknowledgements

The author wishes to acknowledge the following people for their various contributions towards the completion of this work:

- Professor Sonia Fidder-Woudberg who went above and beyond to help me navigate the landscape of research, thesis writing and mathematical modelling and who invested so much in me and my future.
- My parents, Liesl and Siegfried Maré, who supported me on all fronts and carried me in prayer through this journey.
- My grandparents, Lisa and Salie de Swardt, who gave so freely of themselves to help me countless times.
- My siblings, Abigail, Siegfried and Stephanie, who prayed for me, encouraged me and reminded me of the important things in life.
- My friends and housemates who encouraged me throughout and inspired me to finish the race well.
- Jeandré, Sharon, Kyla, Louise, Vidius, Elizna, Hlubi, Karien, Jason, Tosca and Adriaan.
- CoE-MaSS for financial assistance.
- Most importantly, God whom without, this would not have been possible, who inspired me, gave me a love for maths, guided me, carried me when it was tough and ran with me all the way.

The support of the South African DST-NRF Centre of Excellence in Mathematical and Statistical Sciences (CoE-MaSS) towards this research is hereby acknowledged. Opinions expressed and conclusions arrived at, are those of the authors and are not necessarily to be attributed to the CoE.

Table of Contents

Nomenclature

Standard characters

A	[m^2]	base area of container enclosing porous medium
A_{add}	[m^2]	area added to "fat" dodecahedron model
A_o	[m^2]	RUC base area
$A_{p_\parallel}$	[m^2]	streamwise cross-sectional flow area
$A_{p_\perp}$	[m^2]	transverse cross-sectional flow area
A_s	[m^2]	total surface area
A_{strut}	[m^2]	surface area of strut
a_0	[N.s.m^{-4}]	Darcy coefficient in Darcy-Forchheimer equation
a_1	[kg.m^{-2}]	Forchheimer coefficient in Darcy-Forchheimer equation
a', b'	[-]	coefficients in kinetic specific surface area approach
a'', b''	[-]	coefficients in combined specific surface area approach
B	[m]	linear dimension
B_1, B_2	[-]	empirical coefficients
b	[Pa]	Klinkenberg factor
C	[-]	empirical coefficient
c	[m]	linear dimension
c_{Pan}	[-]	proportionality constant
c_d	[-]	interstitial form drag coefficient
c', d'	[-]	coefficients in kinetic specific surface area approach
c'', d''	[-]	coefficients in combined specific surface area approach
D_h	[m]	hydraulic diameter
D_p	[m]	face diameter
d	[m]	RUC cell size
d_p	[m]	RUC pore diameter
d_s	[m]	RUC strut diameter
$d_{s_\parallel}$	[m]	RUC strut diameter parallel to streamwise direction
$d_{s_{\parallel_o}}$	[m]	RUC uncompressed strut diameter parallel to streamwise direction
$d_{s_\perp}$	[m]	RUC strut diameter perpendicular to streamwise direction
$d_{s_{\perp_o}}$	[m]	RUC uncompressed strut diameter perpendicular to streamwise direction
$d_\parallel$	[m]	RUC streamwise cell dimension
$d_{\parallel_o}$	[m]	RUC uncompressed streamwise cell dimension
$d_\perp$	[m]	RUC transverse cell dimension
$d_{\perp_o}$	[m]	RUC uncompressed transverse cell dimension
E_1 , E_2	[-]	empirical coefficients

e	[-]	compression ratio
e', f'	[-]	coefficients in kinetic specific surface area approach
F	[m^2]	inertial coefficient
f, g_c	[m^2]	coefficient in combined specific surface area approach
g_k	[m^2]	coefficient in kinetic specific surface area approach
h	[m]	dodecahedron node parameter
h_f	[m]	compressed filter thickness
h_o	[m]	uncompressed filter thickness
h_s	[m]	perpendicular height of triangular strut of tetrakaidecahedron and dodecahedron models
K	[m^2]	permeability coefficient of Darcy regime
K_F	[m^{-1}]	permeability coefficient of Forchheimer regime
K_g	[m^2]	gas permeability
K_l	[m^2]	liquid permeability
Kn	[-]	Knudsen number
k	[-]	ratio of linear dimensions
L	[m]	linear dimension
l_s	[m]	strut length
M	[g.mol^{-1}]	molecular weight
n	[-]	Klinkenberg coefficient
$\underline{n}$	[-]	unit vector perpendicular to fluid-solid surface
$\underline{\hat{n}}$	[-]	macroscopic direction of flow
p	[Pa]	pressure
p_{avg}	[Pa]	average of inlet and outlet pressures
p_f	[Pa]	intrinsic pressure
q	[m.s^{-1}]	magnitude of superficial velocity
R	[J.mol^{-1}.K^{-1}]	universal gas constant
R_h	[m]	hydraulic radius
S	[m^2]	surface area
S_{add}	[m^2]	specific surface area added to "fat" dodecahedron model
S_{face}	[m^2]	RUC solid cross-sectional area facing upstream
S_{fs}	[m^2]	RUC fluid-solid surface area
S_v	[m^{-1}]	specific surface area
$S_{\parallel}$	[m^2]	RUC solid surface parallel to streamwise direction
$S_{\perp}$	[m^2]	RUC solid surface perpendicular to streamwise direction
s_{D_h}	[m]	standard deviation of hydraulic diameter measurements
T	[K]	absolute temperature
t	[s]	time
U	[m^3]	compressed RUC cell volume
U_f	[m^3]	RUC fluid volume
U_{f_o}	[m^3]	uncompressed RUC fluid volume
U_o	[m^3]	uncompressed RUC cell volume
U_s	[m^3]	RUC solid volume
U_t	[m^3]	RUC transfer volume
$U_{\parallel}$	[m^3]	RUC streamwise fluid volume
$U_{\perp}$	[m^3]	RUC transverse fluid volume
u	[m.s^{-1}]	magnitude of fluid velocity
u_b	[m.s^{-1}]	magnitude of velocity at pore boundaries
V_{add}	[m^3]	volume added to "fat" dodecahedron model
V_f	[m^3]	fluid volume

V_o	[m^3]	volume of fibrous porous medium
V_s	[m^3]	volume of struts
$\underline{v}$	[$m.s^{-1}$]	velocity
v_{avg}	[$m.s^{-1}$]	magnitude of average velocity
v_∞	[$m.s^{-1}$]	magnitude of approaching velocity
$w_\parallel$	[$m.s^{-1}$]	magnitude of streamwise average duct velocity
$w_\perp$	[$m.s^{-1}$]	magnitude of transverse average duct velocity
x,y	[m]	distance along Cartesian coordinate

Greek symbols

α	[-]	ratio of average streamwise and transverse duct velocities
β	[-]	slip coefficient
ϵ	[-]	porosity
ϵ_o	[-]	porosity of uncompressed state
λ	[m]	molecular mean free path
μ	[$N.s.m^{-2}$]	dynamic viscosity
ρ	[$kg.m^{-3}$]	fluid density
ρ_g	[$kg.m^{-3}$]	foam apparent density
ρ_s	[$kg.m^{-3}$]	strut density
σ	[-]	tangential momentum accommodation coefficient
$\underline{\underline{\tau}}$	[$N.m^{-2}$]	shear stress
τ_w	[$N.m^{-2}$]	magnitude of wall shear stress
$\tau_{w_\parallel}$	[$N.m^{-2}$]	magnitude of streamwise wall shear stress
$\tau_{w_\perp}$	[$N.m^{-2}$]	magnitude of transverse wall shear stress
ϕ	[-]	golden ratio
ψ	[-]	RUC geometric factor
ψ_o	[-]	RUC geometric factor of uncompressed state

Acronyms

CT	Computer Tomography
DVI	Digital Volumetric Imaging
MRI	Magnetic Resonance Imaging
PPI	Pores Per linear Inch
REV	Representative Elementary Volume
RUC	Representative Unit Cell
SEM	Scanning Electron Microscopy

Subscripts

$_b$	pore boundary
$\parallel$	parallel to streamwise direction
$\perp$	perpendicular to streamwise direction

Operators

Δ	change in streamwise property
∇	gradient
$\langle\,\rangle$	phase average
$\langle\,\rangle_f$	intrinsic phase average

List of Figures

List of Tables

CHAPTER 1

Introduction

Porous media can refer to unconnected solids such as granular porous media or fibres, or it can refer to connected solid matrices such as open-celled foams. Fibres and foamlike media are placed in the category of *fibrous media* by some authors in the literature, such as in Higdon and Ford [13], and the same will be done in this study. This study will focus on fibrous media. Data obtained using open-celled foams and arbitrarily orientated fibres in parallel planes will be used for analysis and validation of some of the models considered.

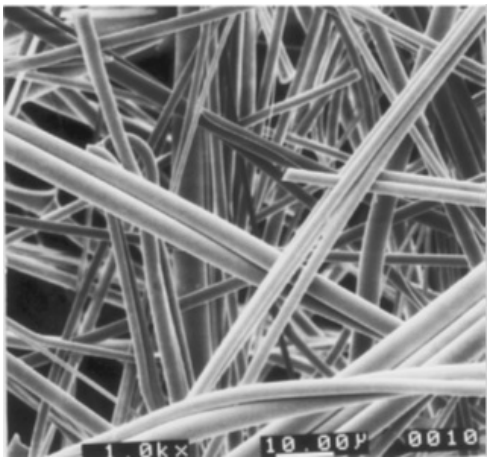

FIGURE 1.1: *Fibres with arbitrary orientations (Source: Woudberg and Du Plessis [1])*

Open-celled foams are networks of interconnected solid struts of cellular materials. The unit cells in a foam tend to take on the shape of a polyhedron with pentagonal or hexagonal faces and a spherical inner space, as described by Giani et al. [14], although the actual cells in the foam can differ significantly in shape throughout the foam. Figure 1.2(a) is an image of an actual metal foam. Another type of open-celled foam is ceramic-based foams (e.g., Al_2O_3, cordierite, SiC, etc. (Edouard et al. [15])), which are more common than metal-based foams (e.g., aluminum, copper, etc. (Edouard et al. [15])). Figure 1.2(b) is an image of an actual ceramic foam. The focus of this study is mostly on metal-based foams, but since the morphology of the foams is addressed as being similar (e.g. Edouard et al. [15]), literature referring to ceramic foams will also be used.

Metal foams have a vast range of industrial applications. To name a few, they are used in catalytic beds, compact heat sinks for power electronics, air cooled condensers, multi-functional heat exchangers (Mancin et al. [16]), in the design of aircraft wing structures in the aerospace industry (Bhattacharya et al. [17]), etc. The properties that make foams so attractive to processes

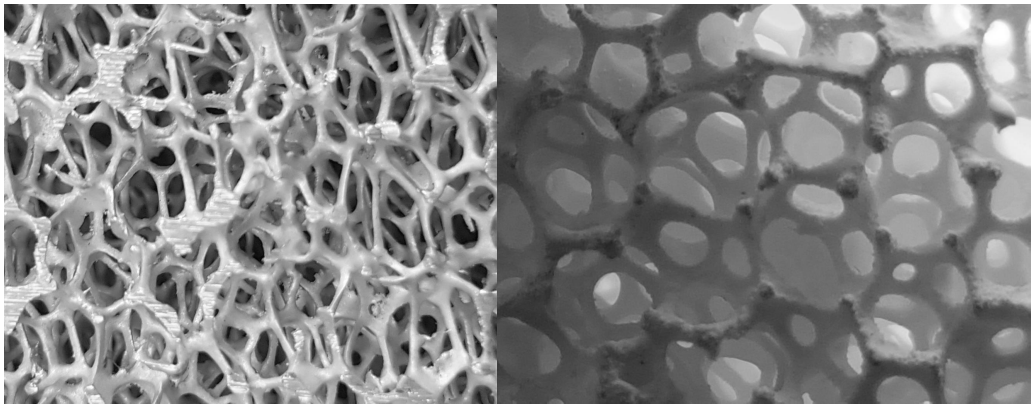

(a) *Metal foam* (b) *Ceramic foam*

FIGURE 1.2: *Open-celled foams*

requiring gas filters, heat exchangers and catalyst supports are that they exhibit a high mechanical strength, a large external surface area and a high porosity. Inayat et al. [18] stated that these physical properties in turn lead to metal foams having good chemical resistance, enhanced heat and mass transfer properties and low pressure drops. Fibres find application in filtration and the textile environment, which include various industrial and consumer products (Woudberg et al. [6], Jaganathan et al. [9]). Coalescing filters make use of fibres as a filter medium, such as glass fibres, and removes droplets of liquid from aerosols and other air streams which also have numerous applications in industry, e.g. filtration of cabin air, dehumidification etc. (Manzo et al. [19]). Consequently, for design and optimization, the parameters of fibrous porous media and knowledge thereof are of great importance.

In order to characterize open-celled metal foams, morphological parameters are needed, such as the pore diameter, the strut diameter and the specific surface area. These parameters and others, will be defined in this study. It will also be explained how they are measured and how they are calculated mathematically.

Due to the intricate nature of metal foams and their complex structures, it is difficult to find reliable correlations among the morphological parameters that affect transport phenomena. The micro structure of metal foams are approximated by mainly four different isotropic geometric models, as illustrated in Figure 1.3. These are the cubic unit cell model (Lu et al. [20]), the tetrakaidecahedron model (Richardson et al. [4]), the dodecahedron model (Huu et al. [21]) and the three-strut rectangular Representative Unit Cell (RUC) model (Du Plessis et al. [22]). Another model that will also be considered, introduced by Van Heyningen [7], is the anisotropic two-strut RUC model is illustrated in Figure 1.4. It provides a more realistic representation of a fibrous porous medium made up of a stacking of fibre layers. All the aforementioned models will be described by defining the relationship between the pore-scale linear dimensions of each of them.

In Chapter 2 the different correlations among the morphological parameters of each of the respective isotropic model geometries, as well as the anisotropic two-strut RUC model, will be investigated and equations for the prediction of the specific surface area will be given. Thereafter, a kinetic approach will be considered in which permeability data is used to determine the specific surface area. The word "kinetic" in this context refers to the fact that the permeability results from the pressure drop prediction involving the kinetic characteristics of the flow, although the permeability is a geometric parameter. A combined approach will be utilized as well, in which the method of deriving the specific surface area equations uses both kinetic and geometric

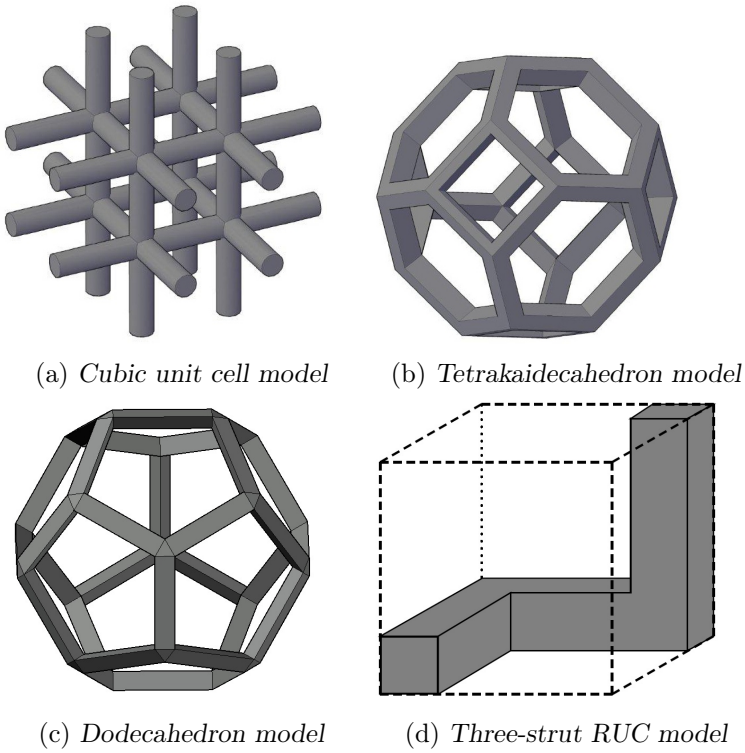

(a) *Cubic unit cell model* (b) *Tetrakaidecahedron model*

(c) *Dodecahedron model* (d) *Three-strut RUC model*

FIGURE 1.3: *Isotropic geometric models for metal foams*

properties. Experimental data available in the literature for the pore-scale linear dimensions and specific surface area will be used to compare the model predictions of the geometric approach and the values obtained from the kinetic and combined approaches. The aim is to determine whether the more complex geometries of the tetrakaidecahedron and dodecahedron models are necessary to provide more accurate predictions than the simpler cubic unit cell and RUC models, when compared to experimental data.

The approach where the geometrical parameters of the respective isotropic models and the anisotropic two-strut RUC model are used to determine the specific surface area, i.e. the geometric approach, will be based on the work done on these models by various authors in the literature. In some cases different methods of obtaining results for a specific model geometry will also be discussed. The kinetic approach and combined kinetic-geometric approach will be

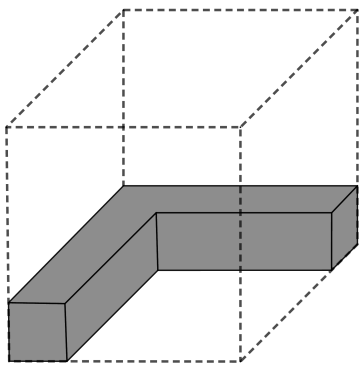

FIGURE 1.4: *Two-strut RUC model*

based on methods introduced elsewhere in the literature and also be applied to the two-strut and three-strut RUC models.

Different authors in the literature have utilized the four isotropic geometric models for various purposes. The cubic unit cell model was proposed by Lu et al. [20], who investigated the use of open-celled foams in heat transfer applications and developed the model in order to predict temperature distribution in terms of a variety of heat transfer parameters. Giani et al. [14] also used the cubic unit cell model to study the mass-transfer properties of open-celled foams and deduced expressions for the specific surface area in order to determine mass-transfer coefficients which make use of the specific surface area parameter. Lacroix et al. [23] conducted the study to obtain a pressure drop for SiC foams by also utilizing the cubic unit cell geometry. They investigated the pressure drop predictions using an Ergun-type equation and merely made use of the model geometry to determine the specific surface area in order to find correlations among other parameters necessary for the pressure drop predictions. Mass transfer and pressure drop properties of open-cell foams were also investigated by Garrido et al. [3]. They made use of specific surface area predictions in order to determine mass transfer coefficients and furthermore obtained experimental specific surface area values which they then compared to the predictions obtained from both the cubic unit cell and the tetrakaidecahedron models. They observed an overestimation of the specific surface area of both the morphological models and also mentioned that the overestimation could be due to an assumption of constant thickness of struts in the geometric models, whereas ceramic foams tend to have accumulation of solid material around the nodes in the foams. Gibson and Ashby [24] considered different polyhedra in which the structures of foams could be modelled and concluded that the tetrakaidecahedron gave the most consistent agreement with observed properties. Some geometric relationships were furthermore derived by Gibson and Ashby for the tetrakaidecahedron unit cell. These results from Gibson and Ashby were also used by Richardson et al. [4], who studied and measured the pressure drop of flow through ceramic foams, focused on the foam application as a catalyst support and derived a specific surface area equation from the tetrakaidecahedron model. They included the consideration of different specific surface area models from which the specific surface area could be determined in order to find pressure drop predictions. Buciuman and Kraushaar-Czarnetzki [25] also made use of the tetrakaidecahedron model. They focused on ceramic foams as catalyst carriers and created a geometrical model in order to describe the foam hydrodynamic properties, as well as to find correlations for the transfer of heat and mass in the catalyst carriers. Inayat et al. [18] investigated specific surface area predictions given by various model geometries and compared it to experimental data. The model geometries they considered were the cubic unit cell model, the dodecahedron model and the tetrakaidecahedron model. They determined that the tetrakaidecahedron geometry was the most suitable model for describing foam structures and also made adjustments to the strut geometry of the model in order to accommodate the changes in strut morphologies at different porosities. Huu et al. [21] modelled solid foams using a pentagonal dodecahedron geometric approach due to the dodecahedron structure having such a close resemblance to a foam cell. They made adjustments to the strut geometry as well to represent morphologies at different porosity ranges of the dodecahedron model and furthermore provided corresponding specific surface area expressions. The foam (or three-strut) RUC model was originally introduced by Du Plessis and Masliyah [26], but with application to lower porosities. In order to predict the pressure gradient of flow through metal foams, Du Plessis et al. [22] introduced a high porosity three-strut RUC model. Further developments of the three-strut RUC model was made by Woudberg and Du Plessis [1], who used this model to propose an Ergun-type equation for porous foams. Van Heyningen [7] introduced the two-strut RUC model in order to predict the effect of compression on the permeability of fibrous media.

Another geometric approach found in the literature that was used to determine the specific

surface area of open-cell foams, apart from the four geometric models discussed, was proposed by Grosse et al. [27] and was furthermore considered by Inayat et al. [18] in their study. Grosse et al. [27] used the Weaire-Phelan structure to model foams where the unit cell of the Weaire-Phelan structure consists of a combination of dodecahedra and tetrakaidecahedra. The pentagonal dodecahedra with 12 identical pentagonal faces equalled a total of 2 dodecahedra per unit cell and the tetrakaidecahedra with 2 hexagonal faces, 8 pentagonal faces of identical shape and 4 pentagonal faces similar to the dodecahedra faces, comprised of 6 tetrakaidecahedra per unit cell. The predictions of the specific surface area obtained using this model, however, did not correlate well with their experimental data and therefore the coefficients of the specific surface area equation was empirically adjusted in order to approximate the data more accurately.

The kinetic approach of determining the specific surface area of fibrous media entails the relation between the specific surface area and permeability measurements. In the literature this relation generally exists in order to determine the permeability of or pressure drop over the fibrous media and not the use of the permeability values to determine the specific surface area. The relations between the parameters can, however, still be utilized as proposed in this study. Huu et al. [21], for example, used an Ergun-type equation to determine the pressure drop of solid foams from the pore diameter. A pore diameter expression in terms of the specific surface area was utilized in order to obtain a correlation between the pressure drop and the specific surface area. Dietrich et al. [2] deduced an Ergun-type equation in terms of the hydraulic diameter in order to determine hydraulic diameter values from pressure drop measurements. The hydraulic diameter can easily be related to the specific surface area, which they did in order to obtain the Ergun-type equation, but not in order to provide a method of attaining the specific surface area from pressure drop measurements. The relationships provided can, however, still be implemented in this way. Edouard et al. [15] performed a comparison of available models in the literature, both empirical and theoretical, that relate the structural parameters (such as the strut diameter, pore size, porosity and specific surface area) with the permeability of foams. They concluded that the approaches proposed by Du Plessis et al. [22] and Lacroix et al. [23], in comparison to all the approaches they considered in their review, were more adaptable to approximate the pressure drop over a foam. Du Plessis et al. [22] derived an Ergun-type equation from the foam (i.e. three-strut) RUC model which was given in terms of tortuosity. Lacroix et al. [23] used the Ergun equation for flow, through a homogeneous and rigid porous medium, and a relation between the pore diameter and strut diameter in order to express the equation in terms of the strut diameter.

Moreira and Coury [28] also investigated the influence of the structural parameters of ceramic foams on the permeability of foams and similarly used Ergun-type equations and the expression for the specific surface area, as determined by Richardson et al. [4], in order to calculate the pressure drop from specific surface area measurements. The approach used by these authors are considered a combined approach due to the use of a geometric model, as given by the equation obtained from Richardson et al. [4], as well as the pressure drop given by the Ergun-type equation. The results were not satisfactory when compared to experimental data for the pressure drop and Moreira and Coury [28] consequently determined an Ergun-type empirical correlation by fitting data. The combined approach to be introduced in this study is, as opposed to this, aimed at obtaining analytical expressions for the specific surface area from permeability data.

In Chapter 3 the adaptation of the RUC models representing anisotropic compressed fibrous media will be outlined together with the specific surface area predictions of the adapted models using the geometric, kinetic and combined approaches. In the study of Woudberg et al. [6] an analytical anisotropic three-strut RUC model was proposed for fibrous porous media that accounts for the effect of compression on the permeability. The anisotropic three-strut model

will be included in this study and extended, along with the work of Van Heyningen [7] for the compression of the two-strut RUC model, to elaborate on the subject matter of the adaptation of the RUC models towards compression. This is an important adaptation due to the significant effects that compression has on the morphology and flow properties of foams and fibres and especially metal foams used in heat exchanger devices. It was, for example, specifically stated by Le Coq [8] based on their results that the deformation of porous media should be taken into account for the prediction and optimization of filtration processes. It improves the structural rigidity and increases the surface area density for optimal heat transfer of metal foams (Dukhan et al. [29], Antohe et al. [30]). The compression results in a decrease in porosity, pore diameter and permeability. For the same pumping power, Dukhan et al. [29] reported thermal resistances provided by compressed foam heat exchangers of two to three times lower than that of commercial heat exchangers.

Furthermore, very few researchers in the literature have studied compression of fibrous porous media (e.g. Antohe et al. [30], Dukhan et al. [29], Jaganathan et al. [9] and Le Coq [8]), compared to that of non-compressed isotropic media. As a result of the complex geometry of compressed fibrous media, authors have mainly relied on experimental measurements together with empirical models to describe the geometric properties of the media and kinematics of flow. Antohe et al. [30] empirically fitted the Forchheimer equation to their experimental pressure drop data (for airflow through compressed aluminium foams) and provided constant values for the empirical coefficients that were introduced. Boomsma and Poulikakos [31] also followed such a procedure, but instead of using air they used water as traversing fluid. Jaganathan et al. [9] made use of image analysis to study the effect of compression on the pore size distribution of non-woven fibrous materials. An empirical equation containing three empirical coefficients was proposed for the mean pore diameter as a function of pressure. Many authors make use of the empirical Ergun equation for granular media to correlate experimental pressure drop data of fibrous media by adjusting the empirical coefficients. Dukhan et al. [29], for example, introduced a set of empirical curve fitting coefficients into the Ergun equation to obtain correlation with experimental pressure drop data for compressed aluminium foams. They also mention the necessity of making use of empirical equations due to the lack of analytical equations that can take the effect of cell deformation into account. These authors used their experimental permeability data for airflow through compressed aluminium foams to fit an exponential function in terms of porosity containing two empirical coefficients that were stated to contain the geometrical foam characteristics.

In Chapter 4 the Klinkenberg effect will be incorporated into the predictions of the isotropic and anisotropic RUC models for the permeability and specific surface area, which takes into account the slip effect of the gas phase used to obtain the required data on the permeability. It has been shown in the literature that different permeability values are obtained in experiments depending on whether a gas or a liquid was used to obtain the data. One reason for this phenomenon is that in porous media with small enough pore diameters (where the pore diameter is comparable to the molecular mean free path of the gas molecules), slip flow occurs at pore walls and therefore a slip boundary condition needs to be incorporated into the Navier Stokes equation (Hooman et al. [32]). The importance of the Klinkenberg effect is its involvement in the prediction of the permeability constants which is used to derive the majority of parameters in fluid transport (Innocentini and Pandofelli [33]). Most studies involving the Klinkenberg slip factor concern granular tight media (e.g. Civan [34], Li et al. [35], Tanikawa and Shimamoto [36]) which is of importance in soil mechanics and the petroleum and gas recovery industries. Analytical and numerical studies involving slip flow are scarce due to the complexity of the actual porous structures involved, as opposed to empirical studies (Zheng et al.[37]). Other examples of where the effect could be of significance are in industrial applications such as electronic cooling and

micro-reactors, as stated by Hooman et al. [32] who, in order to predict the gas permeability through a porous medium, presented a theoretical model that involved slip flow in the pores. Marschall and Milos [38] specifically considered the gas permeability of fibrous materials due to the insulation properties of these media and their use in many spacecraft and hypersonic vehicles. Marschall and Milos [38] showed in their investigations that the Klinkenberg formulation represented the permeability-pressure relationship well. Another example is the case where Hosseini and Vahedi Tafreshi [39] investigated and modelled the permeability of gas flow through nanofibers, taking the effect of slip around the fibres into account. They also highlighted the importance of the permeability of fibrous media in numerous applications, the number of studies dedicated to this topic and the significance of the slip flow occurrence on the predictions of the permeability.

State of the art work in the field of the present study includes that of Aldakheel et al. [40] who measured the gas permeability of fibrous media subject to compression for use as gas diffusion layers in proton membrane exchange fuel cells. Turtoi et al. [41] measured the water permeability of non-woven textiles subject to compression and fitted the Carman-Kozeny equation to the data. The permeability of air and helium flow through fibrous blankets for use in space vehicles were measured by Ehrlich and Schwille [42] in both the non-slip and slip flow regimes. For the latter regime the Klinkenberg equation, which will be elaborated on in Chapter 4, was incorporated by adapting Darcy's law and correlations between the Klinkenberg slip factor and permeability presented for fibrous media. Awin and Dukhan [43] investigated experimentally the effect of the internal structure of open-cell metal foams on the performance of proton exchange membrane fuel cells. The foams were mechanically compressed but the permeability not provided since it did not form part of the study. Several advantages were given for the use of compressed metal foams in these devices. Tan et al. [44] studied numerically the use of aluminium foams as heat sinks for the thermal management of solar cells. The effect of porosity and pore density on the flow field was investigated. Experimental measurements, including the porosity, permeability and pore diameter, produced by Hernández [45] for compressed aluminium foams were used as input parameters in their numerical procedure, although it was assumed in the numerical simulations that the foams were isotropic. Hossain and Shabani [46] have measured experimentally the pressure drop of airflow through uncompressed and compressed aluminium foams. They have applied a previous version of the isotropic three-strut RUC model, presented by Fourie and Du Plessis [47], to the pressure drop data for only the uncompressed foams. According to them, the data for the compressed samples could not be compared to any model due to the anisotropy involved.

None of the aforementioned studies have considered the combined effects of gas slippage and compression of fibrous porous media in the permeability prediction and thus adds novelty to this study. Incorporating it is therefore worthwhile investigating and compliments the empirical, numerical and experimental studies mentioned above.

In Chapter 4 the Klinkenberg effect will thus be incorporated in the isotropic and uncompressed three- and two-strut RUC models by adapting the equations for the permeability predictions. Due to the dependence of the specific surface area predictions of the RUC models obtained using both kinetic and combined approaches on the permeability, the specific surface area equations can and will also be adapted to incorporate the Klinkenberg effect. The same adaptations will furthermore be incorporated into the permeability and specific surface area (obtained using a combined approach) predicted by the compressed RUC models.

The main objective of this study is therefore to further develop the three- and two-strut RUC models. The refined set of objectives are to study the morphological parameters, of fibrous porous media, and relationships among them using isotropic geometric models for foams found

in the literature and give expressions for the prediction of the specific surface area in terms of the porosity. A kinetic and a combined kinetic-geometric approach will furthermore be used to determine the specific surface area by utilizing permeability data. Expressions for the predictions of the specific surface area of the two-strut RUC model will be proposed and a comparison provided of the permeability predictions of the three- and two-strut RUC models. Another objective is to adapt the three- and two-strut RUC models to account for compressed fibrous media and to obtain specific surface area and permeability expressions for the adapted models. Finally, the Klinkenberg effect will be incorporated into the parameter predictions of the uncompressed and compressed RUC models.

1.1 Outputs

The results of Chapter 2 have been presented by the author of this thesis at the International Conference on Computational and Experimental Methods in Multiphase and Complex Flow with reference:

> **Maré, E.** and Woudberg, S. (2019), A geometric versus kinetic modelling approach for characterizing porous media foams, in *Multiphase Flow IX* (Editors: S Hernández and P. Vorobieff), *Proceedings of the 10th International Conference on Computational and Experimental Methods in Multiphase and Complex Flow*, Lisbon, Portugal, 21-23 May 2019, WIT Press, UK, pp. 191-202.

The results of Chapters 3 and 4 have been accepted for publication in the international Powder Technology journal in collaboration with the group of Laurence le Coq at IMT Atlantique in Nantes, France, with reference:

> Woudberg, S., **Maré, E.**, Van Heyningen, M.C., Theron, F. and Le Coq, L. (2021), Predicting the permeability and specific surface area of compressed and uncompressed fibrous media including the Klinkenberg effect, *Powder Technology*, vol. 377, pp. 488-505. Impact factor: 4.142.

In the next section the different pore-scale parameters that characterize the morphology of foams will be defined. The methods used to determine these parameters experimentally will also briefly be discussed.

1.2 Measurable Parameters

Important morphological fibrous media parameters to be defined include the porosity, specific surface area, hydraulic diameter, pores per linear inch number for metal foams, strut diameter, pore diameter and face diameter.

Definition 1.2.1. *Porosity:* The porosity ϵ is the ratio between the volume available for fluid flow through the porous structure and the total volume of the medium, thus it may be given by the relationship (Bird et al. [48]),

$$\epsilon = \frac{\text{volume of voids}}{\text{volume of porous medium}} = \frac{V_f}{V_o} \ , \tag{1.1}$$

and it can further be derived that

$$\begin{aligned}\epsilon &= 1 - \frac{\text{volume of struts}}{\text{volume of fibrous medium}} \\ &= 1 - \frac{\text{volume of struts}}{\text{mass of fibrous medium}} \cdot \frac{\text{mass of fibrous medium}}{\text{volume of fibrous medium}} \\ &= 1 - \frac{\text{apparent density}}{\text{strut density}} ,\end{aligned}$$

which can be written in the following form:

$$\epsilon = 1 - \frac{\rho_g}{\rho_s} , \tag{1.2}$$

where ρ_g is the apparent density and ρ_s is the strut density. Equation (1.2) is generally used in the literature for calculating the porosity, as stated by Edouard et al. [15], since the apparent density and strut density can easily be determined. The apparent density can be derived by using the weight and the volume of the fibrous medium, as in Buciuman and Kraushaar-Czarnetzki [25] and Richardson et al. [4]. The strut density can be measured as done by Richardson et al. [4] using a Helium (He) multipycnometer, an instrument that uses He displacement to measure the volume of solid materials.

Definition 1.2.2. *Specific surface area:* The specific surface area, denoted by S_v, is the measure of the total surface area of the fibrous medium per unit volume (m^{-1}) (Schaschke [49]). In other words, it is the fluid-dynamically relevant outer surface areas of the struts or fibres related to the volume of the fibrous medium, as stated in Grosse et al. [27], and can be presented as:

$$S_v = \frac{A_s}{V_o} , \tag{1.3}$$

where A_s is the total surface area of the fibrous medium presented to the flow and V_o is the total volume of the medium.

Definition 1.2.3. *Hydraulic diameter:* The hydraulic diameter, denoted by D_h, is equal to four times the hydraulic radius R_h where the hydraulic radius is the cross-section through which the fluid flows divided by the wetted perimeter (Bird et al. [48] and Dietrich et al. [2]), i.e.

$$\begin{aligned}D_h &= 4R_h \\ &= 4 \cdot \frac{\text{cross-section available for flow}}{\text{wetted perimeter}} .\end{aligned} \tag{1.4}$$

The wetted perimeter is the circumference of the area of the porous medium that is in contact with the fluid, as given by Schaschke [49]. The hydraulic diameter can therefore be obtained in terms of the specific surface area as follows (Bird et al. [48]):

$$\begin{aligned}R_h &= \frac{\text{cross-section available for flow}}{\text{wetted perimeter}} \\ &= \frac{\text{volume available for flow}}{\text{total wetted surface}} \\ &= \frac{\text{volume of bed}}{\text{volume of bed}} \cdot \frac{\text{volume of voids}}{\text{wetted surface}} \\ &= \epsilon \cdot \frac{V_o}{A_s} \\ &= \frac{\epsilon}{S_v} .\end{aligned} \tag{1.5}$$

Thus the hydraulic diameter can be expressed as:

$$D_h = 4 \cdot \frac{\epsilon}{S_v} \ . \tag{1.6}$$

Equation (1.6) is the general definition for the hydraulic diameter of a porous medium and the dimensionless specific surface area-porosity relationship derived from it, that is $S_v D_h$ as a function of ϵ, is shown in Figure 1.5.

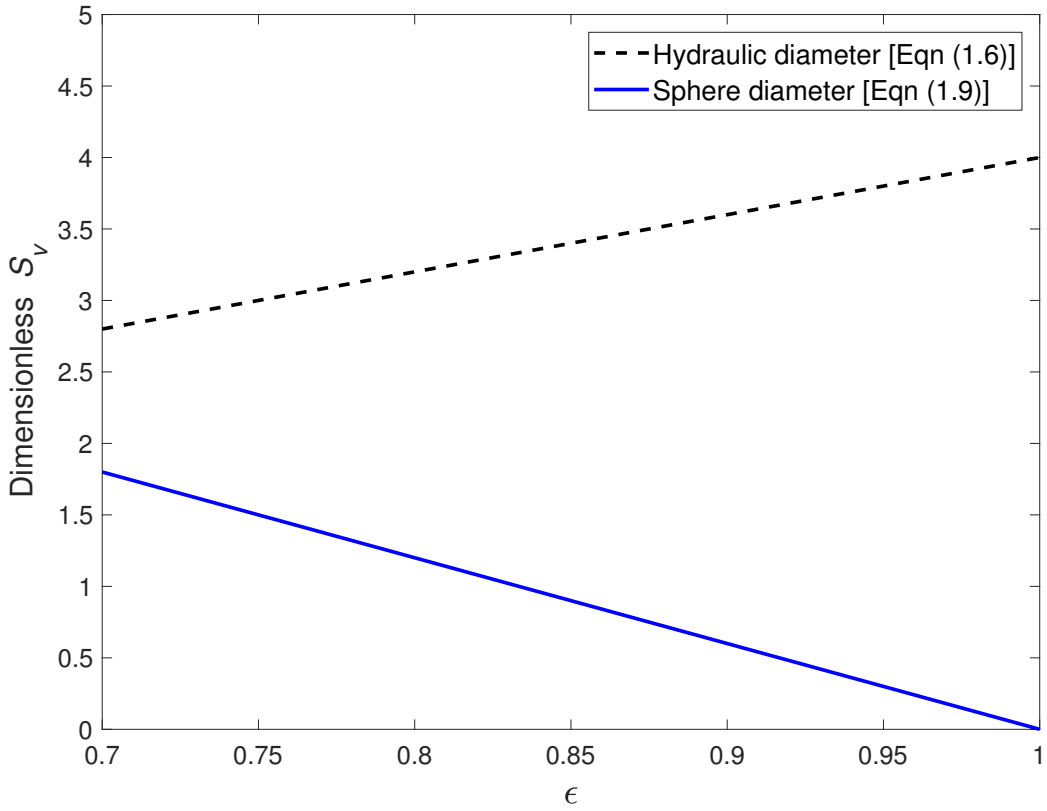

FIGURE 1.5: *Dimensionless specific surface area versus porosity according to equations (1.6) and (1.9)*

In Figure 1.5 it can be observed that the specific surface area resulting from equation (1.6) increases with increasing porosity according to the general definition of the hydraulic diameter. It would however be expected that the specific surface area would decrease with increasing porosity as shown by most other predictions in the literature for the specific surface area as a function of porosity (e.g. Giani et al. [14], Lu et al. [20] and Buciuman and Kraushaar-Czarnetzki [25]). Therefore equation (1.6) might not be applicable in determining the specific surface area for fibrous media. This point will be elaborated on further in Chapter 2.

Definition 1.2.4. *Pores Per linear Inch (PPI) number:* The average number of pores per linear inch, denoted as the PPI number, refers to the pore density of a foam. It is also correlated to the pore size, for example, a high PPI number is equivalent to a small pore size (Dietrich et al. [2]). The relationship between the PPI number and the hydraulic diameter can be determined experimentally. An example of such an empirical correlation for foams with a porosity of 0.8 is given by Dietrich et al. [2]:

$$D_h = 0.028 \cdot \mathrm{PPI}^{-0.721} \ . \tag{1.7}$$

Another example, given by Mancin et al. [16], is

$$D_h = 25.4 \cdot \mathrm{PPI}^{-1}\,, \tag{1.8}$$

which is applicable to aluminum foams with porosities higher than 0.9.

The PPI number is usually provided by the manufacturer. It depends on the material used to produce the foams since most of the metal foams are prepared from different foam templates and thus the PPI number only reflects the range of pore sizes. This results in a wide variation between the measured pore sizes and the pore sizes calculated from the PPI number. Therefore the PPI number is generally not used in analytical equations to determine other morphological parameters and will not be used during this study either.

Definition 1.2.5. *Strut diameter:* The strut diameter, denoted by d_s, (also known as the ligament diameter, as in Mancin et al. [16]) is defined as the thickness in the middle of the strut. This is usually the thinnest part between the knots of metal foams (Grosse et al. [27]). The strut diameter of a metal foam is indicated in Figure 1.6.

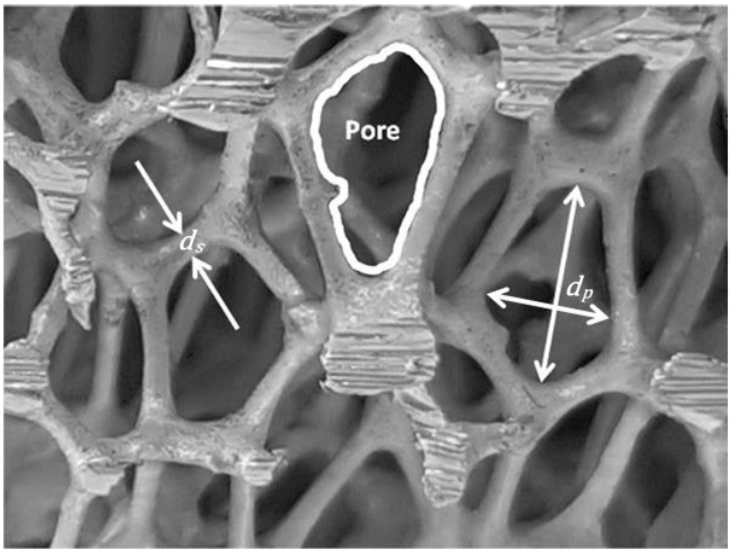

FIGURE 1.6: *Strut and pore diameters of a metal foam*

Definition 1.2.6. *Pore diameter:* The pore diameter, denoted by d_p (or window or inner diameter) is the distance between two struts (Grosse et al. [27]), as also shown in Figure 1.6 for a foam. The sizes of the pores vary significantly, therefore the pore diameter given is usually an average statistically determined from a Guassian normal distribution of experimentally determined values (Garrido et al. [3]).

The pore diameter can also be defined by the following equation, as done by Huu et al. [21]:

$$d_p = \frac{6(1-\epsilon)}{S_v}\,. \tag{1.9}$$

Equation (1.9) was obtained by setting d_p equal to the mean sphere diameter for granular porous media, as defined by Lacroix et al. [23]. The resulting dependency of the dimensionless specific surface area on the porosity determined using equation (1.9) is also shown in Figure 1.5. In this case the specific surface area decreases as the porosity increases, which is the expected specific surface area-porosity relationship. Therefore equation (1.9) will be used as a more representative specific surface area-porosity relationship.

Definition 1.2.7. *Face diameter:* The face diameter (or cell diameter), denoted by D_p, is defined as the sum of the average pore diameter and strut diameter, i.e. the average distance between opposite struts that form the boundaries of a pore, and can thus be represented by the following equation (Garrido et al. [3]):

$$D_p = d_p + d_s \ . \tag{1.10}$$

The aforementioned parameters can be measured experimentally.

Experimental measurements of the pore and strut diameters discussed in the literature are mostly performed by image analyses, also known as *X-ray Computer Tomography (CT)*. This is where thin slices of each foam type are cut and analysed under magnification, and the lengths of, for example, over a 100 of the windows and struts are then statistically evaluated. In Figure 1.7 it is shown how a foam can be analysed by placing it under a microscope that is connected to a computer, for which the measurements can be performed with the aid of software. For the pore diameters, two orthogonal lengths are usually measured for each pore (as shown on the right hand side in Figure 1.6) of which the average is calculated. The diameter of a strut is measured where the strut is the thinnest, as specified by Garrido et al. [3].

FIGURE 1.7: *Foam analysis under magnification*

Computer tomography is also used to acquire measurements for porosity (Grosse et al. [27]), but another way is through *mercury porosimetry* in which a non-wetting fluid such as mercury is used to fill the porous medium and the porosity is determined from the measured mercury intrusion into the pores (Garrido et al. [3]).

In order to obtain measurements of the specific surface area CT and *Magnetic Resonance Imaging (MRI)* are used (Grosse et al. [27]). Another technique used to acquire images to measure the dimensions of porous media is *serial sectioning-imaging*, where images of two dimensional cross-sections of the medium are combined to form a three dimensional image. In Jaganathan et al. [9] a Digital Volumetric Imaging (DVI) instrument was used to measure dimensions by serial sectioning-imaging.

As already mentioned, permeability data will be used together with fibrous media transport properties and kinetic models to determine a means of calculating the specific surface area of a foam or fibre sample of a certain porosity. Equations to determine the permeability will also

be determined for the three- and two-strut RUC models due to the significant role that the permeability of fibrous media play in many applications, one being the use of this parameter to determine the specific surface area. Permeability of fibrous media will, however, first be defined.

Definition 1.2.8. *Permeability:* The permeability, denoted by K, is the measure of ease with which a fluid flows through a porous medium (Speight [50]). It can be determined by making use of Darcy's law and is therefore often measured in a unit called the Darcy which is equal to $9.8697 \times 10^{-13}\,\mathrm{m}^2$ (Dukhan [29]). In this study the units of permeability will however be given in m^2.

Experimental measurement of the permeability of porous media is done by measuring the pressure drop of a fluid pumped through the specific porous medium and consequently using the following equation, known as the Darcy-Forchheimer equation, to determine the permeability values:

$$\frac{\Delta p}{L} = \frac{\mu}{K}\, q + \frac{\rho}{K_F}\, q^2\,, \tag{1.11}$$

where $\Delta p/L$ is the pressure gradient, μ is the dynamic viscosity of the fluid, ρ is the density of the fluid, K and K_F are the permeability coefficients of the Darcy and Forchheimer regimes, respectively, and q is the magnitude of the superficial velocity.

In order to determine K and K_F, some authors (e.g. Hunt and Tien [51]) divide both sides of equation (1.11) by q and then perform a least squares fit on the resulting linear function of the velocity with the given pressure drop data. The coefficients of the function is then determined using the y-intercept and the slope of the function which, in turn, is then used to determine K and K_F, respectively. Other authors in the literature perform a least squares fit directly on equation (1.11), from which the coefficients of q and q^2 are then determined (e.g. Bhattacharya et al. [17] and Dietrich et al. [2]). This method of using a parabolic fit relies on extrapolation and therefore results in a higher error in the final results, as argued by Antohe et al. [30]. Bhattacharya et al. [17] stated that they found the difference in the results between the linear and quadratic fits to be negligible and preferred the parabolic method because of its convenience. For either method, the permeability coefficients can then be obtained accordingly by setting the coefficient terms given in equation (1.11) equal to the corresponding terms of the linear or quadratic equations.

In Chapter 4 the incorporation of the Klinkenberg effect will require two parameters which will also be defined: the molecular mean free path and the tangential momentum accommodation coefficient.

Definition 1.2.9. *Molecular mean free path:* The molecular mean free path, denoted by λ, is defined as the mean distance that the gas molecule travels before it collides with another molecule and is given by (Chastanet et al. [52])

$$\lambda = \frac{\mu\sqrt{\pi RT/2M}}{p}\,, \tag{1.12}$$

where R is the universal gas constant, T is the absolute temperature and M is the molecular weight.

An example of where the molecular mean free path parameter was acquired in the literature is in the study of Miguel and Serrenho [53], who measured the permeability of fibrous media using an experimental gas flow method and investigated why it could be affected when obtained using different gases with different humidity and ambient temperatures. In order to perform the required experiments for their study, they determined the Knudsen numbers for air and helium

used as gases in their experiments which requires the molecular mean free path values. They determined the mean free path of an air molecule to be $\lambda_{\text{air}} = 70$ nm and of a helium molecule to be $\lambda_{\text{helium}} = 200$ nm. Another example is in the study of Marmoret et al. [12] who, however, gave the mean free path of an air molecule as $\lambda_{\text{air}} = 63.4$ nm, which seems to be a closer representation to the actual value, based on the number of significant figures.

Definition 1.2.10. *Tangential momentum accommodation coefficient:* The tangential momentum accommodation coefficient, denoted by σ, is the fraction of molecules experiencing a scattering at the walls of the pore and accounts for the loss in momentum, as defined by Barber and Emerson [54]. It furthermore depends on the wall properties and ranges mostly between the values of 0.2 and 1. For a smooth surface σ tends towards 0 and for a rough surface it tends towards 1.

The tangential momentum accommodation coefficient can be determined experimentally as illustrated, for example, by Acharya and Martin [55]. They investigated the gas surface interaction between a variety of gases and materials by using a disk spin down experiment. This experiment requires the spinning of a disk in the gas at various gas pressures, with the surface consisting of the fibrous material under consideration. The torque of the spinning disk is then used, along with the gas pressures, to determine σ. Acharya and Martin [55] determined, amongst others, the σ value to be 0.72 for air flow over aluminum and 0.90 for air flow over carbon fibre.

In the following chapter the four isotropic geometric models for foams and the anisotropic two-strut RUC model for fibres will be discussed. A geometric approach will be presented which makes use of the geometric properties of the models to determine the specific surface area of fibrous media. Specific surface area equations will also be determined by making use of transport properties of fibrous media in a kinetic approach and furthermore in a combined kinetic-geometric approach where the transport properties as well as geometric models will be utilized for this purpose.

1.3 Chapter summary

The industrial importance of metal foams and other fibrous media, of contribute to the beneficial physical properties of high porosities and large external surface areas, and hence the need for geometric models describing the geometric properties of these media were presented in the introduction of this study. A brief literature study on the geometric models and model approaches used to obtain correlations among the parameters of foams and fibrous media were presented, as well as a summary of studies in the literature concerning model adaptations to incorporate effects such as compression and the Klinkenberg effect in the parameter predictions. The outputs by the author of this thesis that resulted from this study were also given. The measurable parameters used to describe the properties of the foams and fibres in the models available in the literature were defined and a brief explanation was given of some of the methods used to obtain these parameters experimentally from media samples.

CHAPTER 2

Isotropic fibrous media

In this chapter the specific surface area of isotropic fibrous media will be determined, by making use of the pore-scale parameters and transport properties of the media. Models used in the literature to approximate the geometry of foams and fibres will be investigated and utilized for this purpose. Different approaches in obtaining expressions for the specific surface area, as well as other pore-scale parameters, have been identified and will be discussed. The different approaches are the geometric, kinetic and combined kinetic-geometric approaches. The permeability equations derived from the three- and two-strut RUC models will furthermore be analysed with regards to their applicability to porous media with foam and fibre morphologies.

2.1 Specific surface area: Geometric approach

As mentioned in Chapter 1, the geometric models currently used in the literature to approximate the micro-structure of fibrous media are the cubic unit cell model (Lu et al. [20]), the tetrakaidecahedron model (Richardson et al. [4]), the dodecahedron model (Huu et al. [21]), the three-strut RUC model (Woudberg and Du Plessis [1]) and the two-strut RUC model (Van Heyningen [7]). In this section these geometric models will be used to determine correlations among the morphological parameters and finally to determine expressions for the specific surface area in terms of the porosity. Experimental data for metal foams will then be used to analyse the results obtained from these model predictions.

Before moving on to the discussion of the models, it should first be noted that the cubic unit cell, tetrakaidecahedron and dodecahedron models were introduced to represent a unit cell of all the cells that could be packed to form the greater porous foam sample. The cells of the dodecahedron model do not pack perfectly, but the assumption that all the cells take on the dodecahedron shape will be retained and will be discussed further in a subsequent section. Due to the unit cell approximation for these geometric models, one unit cell in scale represents the entire foam. Therefore, some of the parameters defined in Chapter 1 will be adjusted accordingly. These parameters include the total volume of the foam, V_o, which will represent the volume of a unit cell for these models, the total volume of voids, V_f, which will represent the inter-connected volume of voids within a unit cell and the total surface area, A_s, which will represent the total surface area of a unit cell. Furthermore the volume of struts, denoted by V_s, would per definition, be the volume of all the struts in a foam sample but will in the context of these models represent the total volume of struts within a unit cell.

The RUC models are based on a different assumption, however, and the concept of this model was introduced by Du Plessis and Masliyah [26]. The latter authors used a Representative Elementary

Volume (REV) of the porous medium, from which the average geometric characteristics of a porous medium are determined and incorporated into a rectangular Representative Unit Cell (RUC). That is, the rectangular solid struts or fibres represent the average solid geometry of the fibrous porous medium under consideration. Another notation for the volume parameters will accordingly be introduced for this model in a subsequent section.

The cubic unit cell model will be investigated first.

2.1.1 Cubic unit cell model

The structure of the cubic unit cell model resembles a cube with cylindrical fibres on the edges, as shown in Figure 2.1. The model was first introduced by Lu et al. [20], as mentioned in the introduction in Chapter 1.

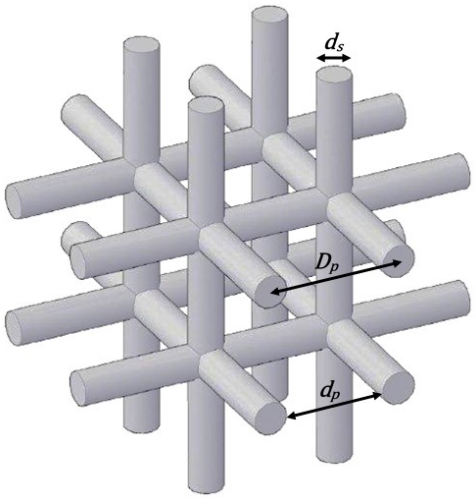

FIGURE 2.1: *Cubic unit cell model*

One approach in finding expressions for the parameters of the cubic unit cell model was presented by Giani et al. [14]. The cell volume was computed by using the volume of a cube and the pore diameter as indicated in Figure 2.1, yielding:

$$V_o = d_p^3 \,. \tag{2.1}$$

It can be noted that the computed volume does not include the solid struts. This method therefore does not distinguish between the respective pore and face diameters. Continuing with the pore diameter as defined in Chapter 1 we can, however, find an expression for the strut volume.

For any foam or fibre sample, the total volume consists of the void and strut volumes, therefore

$$V_o = V_f + V_s \,, \tag{2.2}$$

and equation (1.1) can furthermore be rewritten by making V_f the subject of the equation to obtain

$$V_f = \epsilon V_o \,. \tag{2.3}$$

The expression for the strut volume can be deduced from equations (2.2) and (2.3) and utilizing equation (2.1), the strut volume for the cubic unit cell model of Giani et al. [14] can be obtained,

i.e.

$$V_s = (1-\epsilon)V_o = (1-\epsilon)d_p^3\,. \tag{2.4}$$

The strut volume can also be determined by using the volume of a cylinder as follows:

$$\begin{aligned} V_s &= \text{cross sectional area of strut} \cdot \text{length of strut} \cdot \frac{\text{number of struts}}{\text{number of cells sharing a strut}} \\ &= \pi\Big(\frac{d_s}{2}\Big)^2 \cdot d_p \cdot \frac{12}{4} = \frac{3\pi d_s^2 d_p}{4}\,. \end{aligned} \tag{2.5}$$

Equations (2.4) and (2.5) are therefore equal since both define V_s. An expression for d_s in terms of d_p can hence be deduced, i.e.

$$(1-\epsilon)d_p^3 = \frac{3\pi d_s^2 d_p}{4}\,,$$

yielding

$$d_s = 2d_p\sqrt{\frac{1-\epsilon}{3\pi}}\,. \tag{2.6}$$

The specific surface area, given by equation (1.3), can then be determined in terms of d_p by incorporating equation (2.1), since

$$\begin{aligned} S_v &= \frac{\text{circumference of strut} \cdot \text{length of strut} \cdot \frac{\text{number of struts}}{\text{number of cells sharing a strut}}}{\text{cubic cell volume}} \\ &= \frac{\pi d_s d_p}{4} \cdot \frac{12}{V_o} \\ &= \frac{3\pi d_s}{d_p^2}\,. \end{aligned} \tag{2.7}$$

Substituting equation (2.6) into equation (2.7) leads to (Giani et al. [14])

$$S_v = \frac{2}{d_p}\sqrt{3\pi(1-\epsilon)}\,, \tag{2.8}$$

which is an expression for the specific surface area in terms of the porosity and the pore diameter.

The specific surface area in terms of the porosity and the strut diameter can furthermore be determined by rearranging equation (2.6) to define d_p in terms of d_s and substituting this expression into equation (2.8), yielding

$$S_v = \frac{4}{d_s}(1-\epsilon)\,. \tag{2.9}$$

Equations (2.1), (2.4), (2.5), (2.6), (2.8) and (2.9) are equivalent to those given by Giani et al. [14]. Equation (2.9) was additionally used in other instances in the literature, e.g. by Lacroix et al. [23] and Garrido et al. [3]. The influence of the porosity on the specific surface area of equation (2.8), expressed in dimensionless form, i.e. $S_v d_p$, is shown in Figure 2.2 which shows that the specific surface area decreases as the porosity increases, which makes physical sense.

Another approach in finding expressions for the parameters of the cubic unit cell model was given by Lacroix et al. [23]. In this method the volume of the cube was computed using the face diameter, defined by equation (1.10), i.e.

$$V_o = D_p^3\,. \tag{2.10}$$

The strut volume V_s can therefore be expressed as

$$V_s = (1-\epsilon)D_p^3\,, \tag{2.11}$$

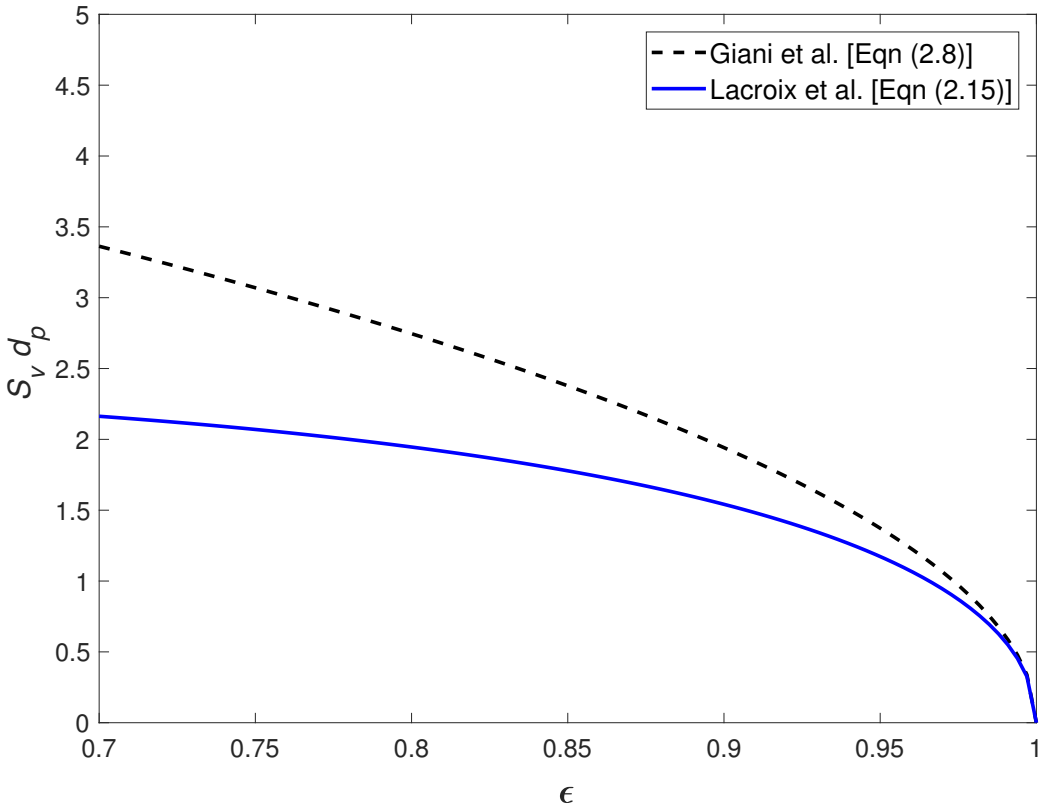

FIGURE 2.2: *Dimensionless specific surface area versus porosity for the cubic unit cell model*

and similar to obtaining equation (2.5), V_s can also be given by

$$V_s = \frac{3\pi d_s^2 D_p}{4}\,. \tag{2.12}$$

Using equations (2.11) and (2.12) and the definition of D_p, given by equation (1.10), the following expression for d_s (in terms of d_p) can be obtained:

$$d_s = \frac{2d_p\sqrt{\frac{1-\epsilon}{3\pi}}}{1-2\sqrt{\frac{1-\epsilon}{3\pi}}}\,. \tag{2.13}$$

The specific surface area in terms of the strut diameter remains the same as in equation (2.9), due to cancellation of the face diameter when d_p is replaced with D_p. In this case, however,

$$S_v = \frac{2}{D_p}\sqrt{3\pi(1-\epsilon)}\,. \tag{2.14}$$

After substituting equation (2.13) into equation (1.10), equation (2.14) can be used to determine the specific surface area in terms of the pore diameter for the cubic unit cell model of Lacroix et al. [23], yielding:

$$S_v = \frac{2}{d_p}\cdot\left[\sqrt{3\pi(1-\epsilon)} - 2(1-\epsilon)\right]. \tag{2.15}$$

Equations (2.9), (2.10), (2.12) and (2.13) are equivalent to those given by Lacroix et al. [23]. The prediction of equation (2.15), non-dimensionalized with d_p, is also shown in Figure 2.2. Equation

(2.15) has a similar trend as equation (2.8) in which the dimensionless specific surface area decreases with increasing porosity. At the porosities applicable to metal foams, which is around the value of 0.9, the relative percentage difference between the dimensionless predictions of equations (2.8) and (2.15) is approximately 21%. The latter percentage value increases considerably with a decrease in porosity.

In summary, there are two different geometric approaches found in the literature to determine the specific surface area for the cubic unit cell model that yield the same expression for the strut diameter but different expressions for the pore diameter. The two different approaches also yield different expressions for the porosity based on this model.

The tetrakaidecahedron model will be discussed next.

2.1.2 Tetrakaidecahedron model

The tetrakaidecahedron model resembles a truncated octahedron, having six square faces and eight hexagonal faces as defined by Buciuman and Kraushaar-Czarnetzki [25]. Figure 2.3(a) shows the general shape of a tetrakaidecahedron unit cell and indicates the side length l_s. For this model, triangular strut geometry is used with an edge width d_s, as shown in Figure 2.3(b). Similarly to the cubic unit cell model, there are also two approaches for finding expressions for the specific surface area of the tetrakaidecahedron model, as obtained from the literature. The one approach makes use of the face diameter D_p and the other the pore diameter d_p.

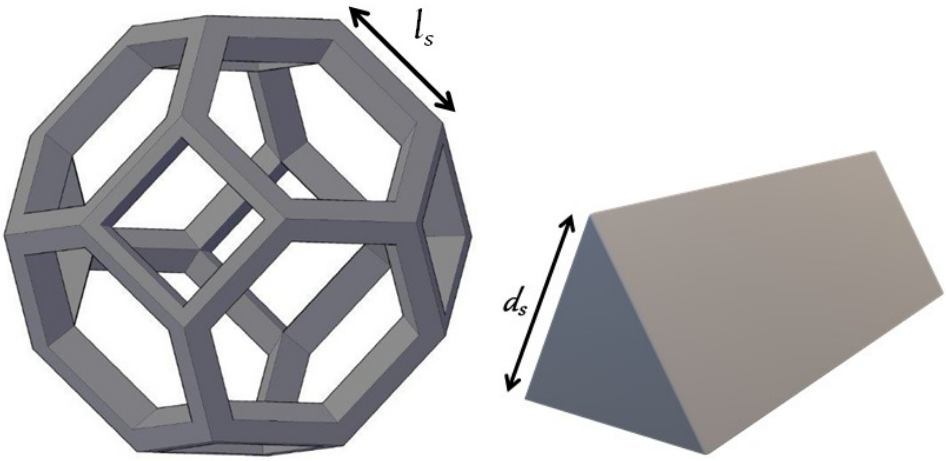

(a) *Shape of tetrakaidecahedron* (b) *Triangular strut geometry*

FIGURE 2.3: *Geometrical features of tetrakaidecahedron model*

The approach in which D_p is used is based on the work of Gibson and Ashby [24] as used by Buciuman and Kraushaar-Czarnetzki [25]. This method starts with the formula derived by Gibson and Ashby [24] for the relative density ratio of a package of tetrakaidecahedra in terms of d_s and l_s, given by

$$\frac{\rho_g}{\rho_s} = 1.06 \left(\frac{d_s}{l_s} \right)^2 . \tag{2.16}$$

The relative density ratio was obtained by dividing the strut volume by the cell volume and then empirically adjusting the coefficient to 1.06.

The side length, l_s, can be determined in terms of the face diameter, D_p, by taking D_p to be the diameter of a circle and setting the area of this circle equal to that of the average area of the

faces of a tetrakaidecahedron. The average is calculated since the faces of a tetrakaidecahedron are not all the same. As mentioned earlier, it consists of 6 square faces and 8 hexagonal faces. The area of a hexagon is determined by dividing the hexagon into 6 equilateral triangles with edges the length of l_s, i.e. 6 times an area equal to $\sqrt{3}/4\, l_s^2$. The area of a circle can be expressed as

$$\text{Area of circle} = \pi \left(\frac{D_p}{2}\right)^2 , \tag{2.17}$$

and the average interfacial area is given by

$$\begin{aligned} \text{Average area of faces} &= \frac{6(\text{Area of square}) + 8(\text{Area of hexagon})}{14} \\ &= \frac{6(l_s^2) + 8(\frac{3\sqrt{3}}{2} l_s^2)}{14} = \frac{3 + 6\sqrt{3}}{7}\, l_s^2 . \end{aligned} \tag{2.18}$$

Setting equations (2.17) and (2.18) equal, yields

$$l_s = 0.64 D_p . \tag{2.19}$$

Equation (2.19) was determined since it is practically easier to find a value for D_p than for l_s. With the substitution of equation (2.19) into equation (2.16), the relative density ratio can be expressed in terms of d_s and D_p, as follows:

$$\frac{\rho_g}{\rho_s} = 1.06 \left(\frac{d_s}{0.64 D_p}\right)^2 = 2.59 \left(\frac{d_s}{D_p}\right)^2 . \tag{2.20}$$

Using equation (2.20), d_s can be expressed in terms of the relative density ratio, which in turn leads to d_s as a function of porosity by using equation (1.2), thus

$$d_s = \frac{D_p}{\sqrt{2.59}} \sqrt{\frac{\rho_g}{\rho_s}} = 0.62 D_p \sqrt{1 - \epsilon} . \tag{2.21}$$

The total surface area, A_s, and the total volume, V_o, must first be determined to obtain an expression for the specific surface area, S_v, of the cell. In order to determine A_s the surface area of a triangular prism, excluding the areas of the triangles, is used due to the assumption of triangular strut geometry. Due to there being 36 struts in a tetrakaidecahedron cell where each strut is shared by 3 cells, it follows that

$$A_s = \text{number of struts per cell} \cdot \text{area of a prism} = \left(\frac{36}{3}\right) \cdot (3 d_s l_s) = 36 d_s l_s . \tag{2.22}$$

The calculation of V_o for a tetrakaidecahedron is explained in Appendix A, and is found to be equal to $8\sqrt{2}\, l_s^3$. Substituting equation (2.22) and the expression for V_o, given by equation (A.1), into equation (1.3) for the specific surface area, leads to

$$S_v = \frac{A_s}{V_o} = \frac{36 d_s l_s}{8\sqrt{2}\, l_s^3} = 3.18 \frac{d_s}{l_s^2} . \tag{2.23}$$

Substituting equations (2.19) and (2.21) into equation (2.23), yields the specific surface area in terms of the face diameter and porosity, i.e.

$$S_v = \frac{4.82}{D_p} \sqrt{1 - \epsilon} . \tag{2.24}$$

In order to determine the specific surface area in terms of d_p for this approach, equation (1.10) can first be substituted into equation (2.21) to obtain d_s in terms of d_p, that is

$$d_s = \frac{0.62\, d_p \sqrt{1-\epsilon}}{1 - 0.62\sqrt{1-\epsilon}}\,. \tag{2.25}$$

Equation (2.25) can then be substituted back into equation (1.10) to find an expression for D_p in terms of d_p, which can in turn be substituted into equation (2.24), yielding

$$S_v = \frac{4.82\sqrt{1-\epsilon} - 2.99\,(1-\epsilon)}{d_p}\,. \tag{2.26}$$

Equations (2.16), (2.18) to (2.20) and (2.23) are equivalent to those given by Buciuman and Kraushaar-Czarnetzki [25].

For the second approach, the specific surface area is determined in terms of the pore diameter, d_p, as done by Richardson et al. [4]. The formula of relative density as derived by Gibson and Ashby [24] and given by equation (2.16), is used to determine the edge width and the side length in terms of the pore diameter and the porosity. This is done by first substituting the relative density given by equation (2.16), into equation (1.2), yielding

$$\epsilon = 1 - 1.06\left(\frac{d_s}{l_s}\right)^2\,. \tag{2.27}$$

Equation (2.27) can be rearranged to give l_s in terms of d_s and ϵ, i.e.

$$l_s = \frac{1.030\, d_s}{\sqrt{1-\epsilon}}\,. \tag{2.28}$$

Furthermore, l_s can be determined in terms of d_s and d_p. This is done by setting d_p equal to the diameter of a circle with an area that is equivalent to the area of a hexagon, divided into equilateral triangles with edges the length of $(l_s - d_s)$, thus yielding

$$\pi\left(\frac{d_p}{2}\right)^2 = \frac{3\sqrt{3}}{2}\,(l_s - d_s)^2\,. \tag{2.29}$$

Solving for l_s yields

$$l_s = d_s + \sqrt{\frac{\pi}{6\sqrt{3}}}\,d_p\,. \tag{2.30}$$

In order to find d_s in terms of d_p and ϵ, equation (2.28) can be substituted into equation (2.30), that is

$$\frac{1.030\, d_s}{\sqrt{1-\epsilon}} = d_s + \sqrt{\frac{\pi}{6\sqrt{3}}}\,d_p\,, \tag{2.31}$$

and d_s can thereupon be solved to obtain (Richardson et al. [4])

$$d_s = \frac{0.5338\, d_p \sqrt{1-\epsilon}}{1 - 0.971\sqrt{1-\epsilon}}\,. \tag{2.32}$$

Finding l_s in terms of d_p is done by substituting equation (2.32) into equation (2.28), yielding (Richardson et al. [4])

$$l_s = \frac{1.030}{\sqrt{1-\epsilon}} \cdot \frac{0.5338\, d_p \sqrt{1-\epsilon}}{1 - 0.971\sqrt{1-\epsilon}} = \frac{0.5498\, d_p}{1 - 0.971\sqrt{1-\epsilon}}\,. \tag{2.33}$$

The specific surface area can be determined in terms of d_p by using equation (2.23), since this expression stays the same for this approach in determining S_v, and substituting equations (2.32) and (2.33) obtained for d_s and l_s, respectively. This produces the following equation for S_v:

$$S_v = \frac{5.621\left(1 - 0.971\sqrt{1-\epsilon}\right)\sqrt{1-\epsilon}}{d_p}\,. \tag{2.34}$$

The expression obtained for S_v by Richardson et al. [4] is, however,

$$S_v = \frac{12.979\left(1 - 0.971\sqrt{1-\epsilon}\right)\sqrt{1-\epsilon}}{d_p}\,. \tag{2.35}$$

Due to the discrepancies between equations (2.34) and (2.35) it is thus possible that there was a mistake made in the calculation of the coefficient in the equation of Richardson et al. [4] for the specific surface area.

Another approach to determine the specific surface area of the tetrakaidecahedron is to follow an approach similar to that which Huu et al. [21] used to determine the specific surface area of the dodecahedron. This is a new approach not published elsewhere in the literature. It starts with determining the porosity. The relative density ratio in this formula is determined by dividing the strut volume by the cell volume. The cell volume is the expression determined in Appendix A, given by equation (A.1). The strut volume V_s is determined as shown in Appendix B.1, equation (B.3). The porosity can be determined by using equation (1.2) in which the relative density ratio is equal to the strut volume ,V_s, divided by the cell volume ,V_o, i.e.

$$\epsilon = 1 - \frac{V_s}{V_o}\,. \tag{2.36}$$

The porosity can hence be expressed as

$$\epsilon = 1 - \frac{3\sqrt{3}\,d_s^2\,l_s + \frac{1}{\sqrt{2}}\,d_s^3}{8\sqrt{2}\,l_s^3}\,, \tag{2.37}$$

where l_s is defined as the length of the strut excluding the node. Equation (2.37) can also be rewritten as follows:

$$\frac{\frac{1}{\sqrt{2}}}{8\sqrt{2}}\left(\frac{d_s}{l_s}\right)^3 + \frac{3\sqrt{3}}{8\sqrt{2}}\left(\frac{d_s}{l_s}\right)^2 - (1-\epsilon) = 0\,, \tag{2.38}$$

and defining k as d_s/l_s, equation (2.38) becomes

$$\frac{\frac{1}{\sqrt{2}}}{8\sqrt{2}}\,k^3 + \frac{3\sqrt{3}}{8\sqrt{2}}\,k^2 - (1-\epsilon) = 0\,. \tag{2.39}$$

In order to determine the specific surface area, equation (2.23) can first be written in terms of k and l_s, i.e.

$$S_v = 3.18\,\frac{k}{l_s}\,. \tag{2.40}$$

Defining l_s as in equation (2.19), equation (2.40) becomes

$$S_v = 3.18\,\frac{k}{0.64\,D_p} = \frac{5\,k}{D_p}\,, \tag{2.41}$$

and using equations (1.10) for D_p and (2.25) for d_s, the specific surface area in terms of d_p results in

$$S_v = \frac{5\,k\,\left(1 - 0.62\sqrt{1-\epsilon}\right)}{d_p}\,. \tag{2.42}$$

Similarly, defining l_s as in equation (2.33), equation (2.40) becomes

$$S_v = 3.18\,k\frac{1 - 0.971\sqrt{1-\epsilon}}{0.5498\,d_p} = 5.784\,\left(1 - 0.971\sqrt{1-\epsilon}\right)\,\frac{k}{d_p}\,, \tag{2.43}$$

where k needs to be solved from equation (2.39).

The influence of the porosity on the specific surface area of equations (2.26), (2.34), (2.35), (2.42) and (2.43) are illustrated in Figure 2.4.

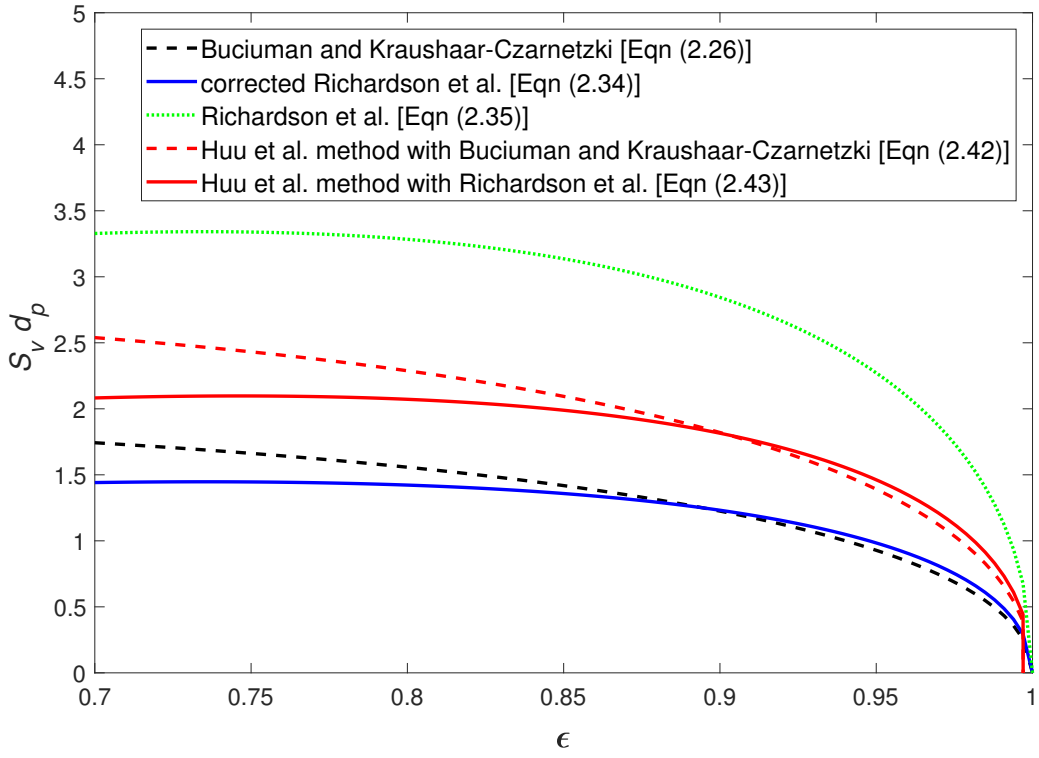

FIGURE 2.4: *Dimensionless specific surface area versus foam porosity for the tetrakaidecahedron model*

All the equations show a similar trend in which the specific surface area decreases with increasing porosity. It can be observed that equation (2.35), which is the expression for S_v given by Richardson et al. [4], provide much higher values as opposed to the other S_v-equations and therefore reinforces the assumption of a mistake made in the calculation of the coefficient of equation (2.35). It can furthermore be observed that the Buciuman and Kraushaar-Czarnetzki method represented by equation (2.26) and the Richardson et al. method equation (2.34) represented by give similar results.

The dodecahedron model will be investigated next.

2.1.3 Dodecahedron model

The dodecahedron shape is formed by 12 pentagonal faces, as illustrated in Figures 2.5(a) and (b). As mentioned previously, the dodecahedra do not pack perfectly. This observation was shown by Gibson and Ashby [24]. It will, however, be assumed that all open cells of the solid foam can be represented by packed pentagonal dodecahedra, similarly as Huu et al. [21] assumed in their calculations. Furthermore, Bhattacharya et al. [17] observed that the strut shape depends on the porosity of the foam, that is, the struts tend towards triangular prisms in the case of high porosities ($\epsilon > 0.9$) and towards cylindrical shape in the case of lower porosities ($\epsilon < 0.9$). Both cases of the dodecahedron model using the approaches followed by Huu et al. [21] will be considered in this study to determine the specific surface areas of the dodecahedron model for $\epsilon > 0.9$ (with triangular strut geometry), and $\epsilon < 0.9$ (with cylindrical strut geometry).

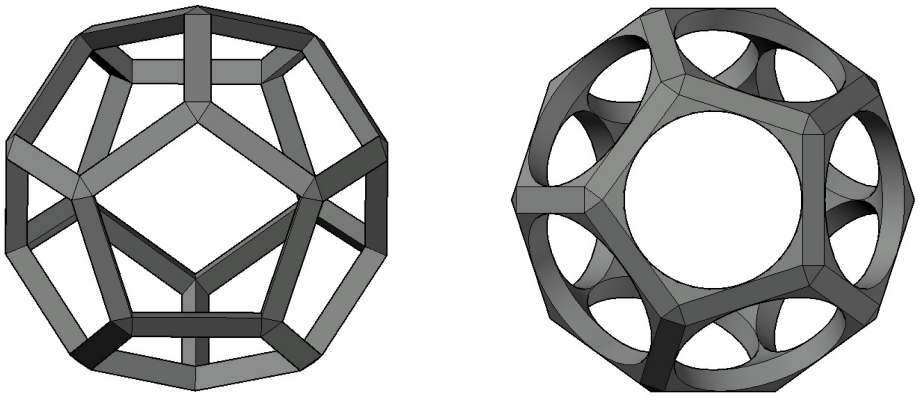

(a) *"Slim" model* (b) *"Fat" model*

FIGURE 2.5: *Dodecahedron model*

Huu et al. [21] also made a distinction between "slim" and "fat" struts, where "slim" struts have triangular nodes that resemble foams of very high porosities ($\epsilon > 0.9$), and "fat" struts are more rounded at the edges and resemble foams of lower porosities ($\epsilon < 0.9$). This distinction will also be taken into consideration. In Figure 2.5(a) the "slim" dodecahedron is portrayed and in Figure 2.5(b) the "fat" dodecahedron is shown.

Four expressions for the specific surface area will therefore be determined using the dodecahedron model geometry. First the "slim" dodecahedron will be presented with triangular and cylindrical struts, respectively. Thereafter the "fat" dodecahedron with triangular and cylindrical struts will be considered.

Triangular "slim" strut geometry

An expression for the specific surface area for this version of the dodecahedron model with parameters as indicated in Figures 2.6(a) and (b) can be determined by first finding an expression for the porosity in terms of these parameters. The porosity can be deduced by utilizing equation (2.36) once more. The cell volume V_o, i.e. the volume of a dodecahedron, in terms of the golden ratio, denoted by ϕ, is

$$V_o = \frac{\sqrt{5}\,\phi^4}{2}\,c^3\,, \tag{2.44}$$

and the strut volume V_s is determined as shown in Appendix B.2, equation (B.4).

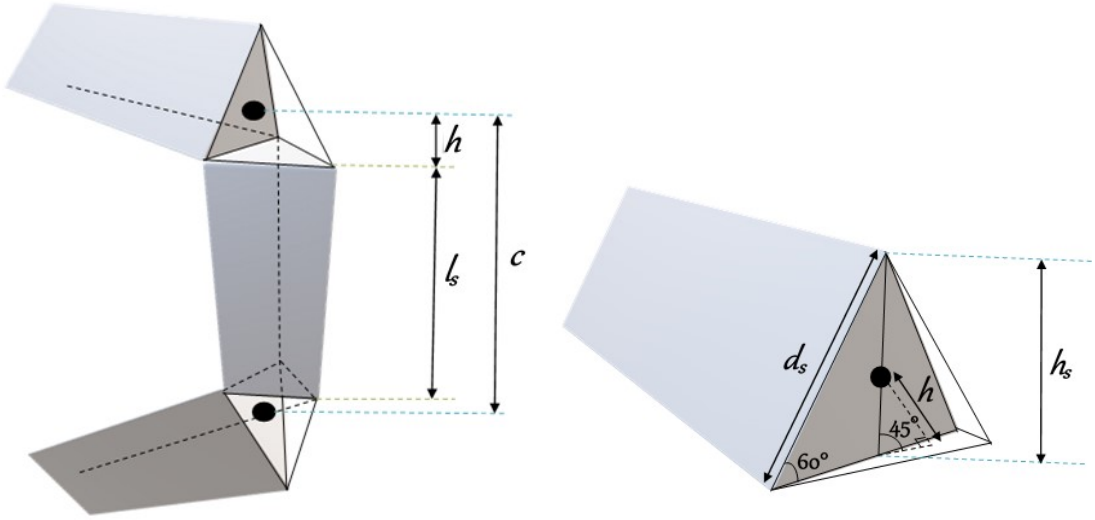

(a) *Strut parameters* (b) *Geometry for determining h*

FIGURE 2.6: *Dodecahedron with triangular strut parameters*

The golden ratio is given by

$$\phi = \frac{1+\sqrt{5}}{2}\,. \tag{2.45}$$

Using the geometry as shown in Figure 2.6(b), h can be determined in terms of d_s and hence equals $\frac{1}{4}\sqrt{\frac{2}{3}}\,d_s$. The side length, l_s, in terms of c and d_s can first be obtained by setting $c = l_s + 2h$, as deduced from Figure 2.6(a), and results in

$$l_s = c - \frac{1}{2}\sqrt{\frac{2}{3}}\,d_s\,. \tag{2.46}$$

Substituting equation (2.46) into equation (B.4), given in Appendix B, leads to

$$V_s = \frac{5\sqrt{3}}{2}\,d_s^2\,c - \frac{5\sqrt{2}}{6}\,d_s^3\,. \tag{2.47}$$

By substituting equations (2.44) and (2.47) into equation (2.36), the porosity can be expressed as

$$\epsilon = 1 - \frac{\frac{5\sqrt{3}}{2}\,d_s^2\,c - \frac{5\sqrt{2}}{6}\,d_s^3}{\frac{\sqrt{5}\,\phi^4}{2}\,c^3}\,. \tag{2.48}$$

Equation (2.48) can also be rewritten as follows:

$$-\frac{\sqrt{10}}{3\phi^4}\left(\frac{d_s}{c}\right)^3 + \frac{\sqrt{15}}{\phi^4}\left(\frac{d_s}{c}\right)^2 - (1-\epsilon) = 0\,, \tag{2.49}$$

and defining k as d_s/c, equation (2.49) then becomes (Huu et al. [21])

$$-\frac{\sqrt{10}}{3\phi^4}k^3 + \frac{\sqrt{15}}{\phi^4}k^2 - (1-\epsilon) = 0\,. \tag{2.50}$$

The specific surface area can be determined by using equation (1.3), where V_o is given by equation (2.44) and $A_s = 30/3 \times$ (area of a strut), since there are 30 struts and each strut is shared

amongst 3 cells. The area of a strut, A_{strut}, can be expressed as:

$$A_{\text{strut}} = 3 \times d_s \times l_s = 3\, d_s\, c \left(1 - \frac{1}{2}\sqrt{\frac{2}{3}}\, k\right) . \tag{2.51}$$

It therefore follows that:

$$S_v = \frac{\frac{30}{3}\, 3\, d_s\, c \left(1 - \frac{1}{2}\sqrt{\frac{2}{3}}\, k\right)}{\frac{\sqrt{5}\,\phi^4}{2}\, c^3} = \frac{60\, d_s \left(1 - \frac{1}{2}\sqrt{\frac{2}{3}}\, k\right)}{\sqrt{5}\,\phi^4\, c^2} . \tag{2.52}$$

In order to determine an equation for S_v in terms of d_p, an expression for d_p must first be obtained. Using the geometry of a pentagon, it can be determined that

$$d_p = \frac{l_s}{\tan\frac{\pi}{5}} , \tag{2.53}$$

and since $(\tan\frac{\pi}{5})^{-1} = \phi/\sqrt{3-\phi}$, it follows that

$$d_p = l_s \frac{\phi}{\sqrt{3-\phi}} . \tag{2.54}$$

Substituting equation (2.46) into equation (2.54) and using the relation $d_s = kc$ leads to

$$d_p = c \left(1 - \frac{1}{2}\sqrt{\frac{2}{3}}\, k\right) \frac{\phi}{\sqrt{3-\phi}} , \tag{2.55}$$

which can be rewritten as

$$\frac{1}{c} = \frac{\phi}{\sqrt{3-\phi}} \frac{\left(1 - \frac{1}{2}\sqrt{\frac{2}{3}}\, k\right)}{d_p} . \tag{2.56}$$

Substituting equation (2.56) into equation (2.52) and again using the relation $d_s = kc$, results in the following expression for the specific surface area in terms of d_p (Huu et al. [21]):

$$S_v = \frac{60\, k}{\sqrt{5}\,\phi^3\sqrt{3-\phi}\, d_p} \left(1 - \frac{1}{2}\sqrt{\frac{2}{3}}\, k\right)^2 , \tag{2.57}$$

where k can be solved from equation (2.50).

Similar equations to equations (2.44), (2.46) to (2.50) and (2.52) are given by Huu et al. [21]. The predictions made by equation (2.57) is shown in Figure 2.7 for porosity values in the range of 0.9 to 1.

Cylindrical "slim" strut geometry

The specific surface area and parameter relationships of this version of the dodecahedron model is more theoretical than physical since it makes use of some of the equations and relationships determined for the triangular strut geometry version of the dodecahedron model. The steps followed in determining the specific surface area of the cylindrical strut geometry version of the dodecahedron model are furthermore similar to the steps used to determine the triangular strut geometry version of the model. Equation (2.36) is used to determine the porosity where V_o is also given by equation (2.44), and V_s is determined as shown in Appendix B.3, equation (B.5), by making use of triangular nodes since the model is "slim" together with cylindrical

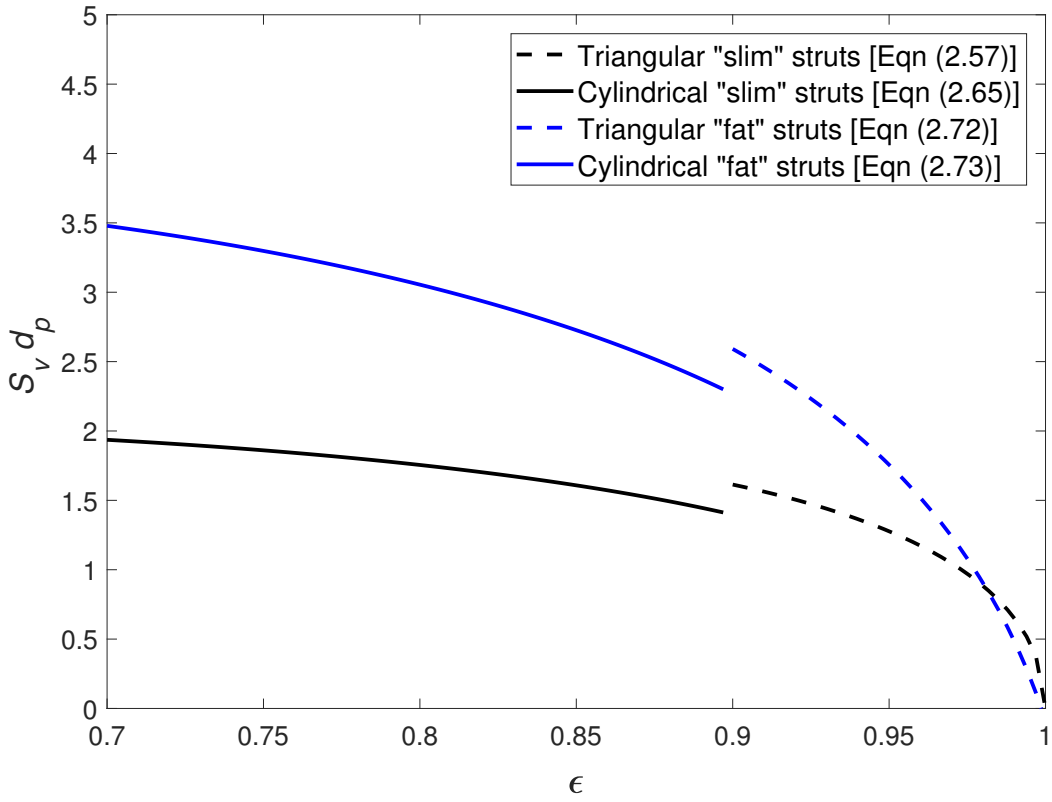

FIGURE 2.7: *Dimensionless specific surface area versus foam porosity for the dodecahedron model*

struts. Substituting equation (2.46) into the determined strut volume given by equation (B.5), in Appendix B, results in

$$V_s = \frac{5\,\pi}{2}\, d_s^2\, c + \left[\frac{5\sqrt{2}}{12} - \frac{5\,\pi}{4}\sqrt{\frac{2}{3}}\right] d_s^3\,. \tag{2.58}$$

This leads to

$$\epsilon = 1 - \frac{\frac{5\,\pi}{2}\, d_s^2\, c + \left[\frac{5\sqrt{2}}{12} - \frac{5\,\pi}{4}\sqrt{\frac{2}{3}}\right] d_s^3}{\frac{\sqrt{5}\,\phi^4}{2}\, c^3}\,, \tag{2.59}$$

which can be rewritten as

$$\frac{\sqrt{5}\,\pi}{\phi^4}\left(\frac{d_s}{c}\right)^2 + \left[\frac{\sqrt{10}}{6\phi^4} - \frac{\sqrt{5}\,\pi}{2\sigma^4}\sqrt{\frac{2}{3}}\right]\left(\frac{d_s}{c}\right)^3 - (1-\epsilon) = 0\,. \tag{2.60}$$

Defining k again as d_s/c, equation (2.60) becomes (Huu et al. [21])

$$\left(\frac{\sqrt{10}}{6\phi^4} - \frac{\sqrt{5}\pi}{2\phi^4}\sqrt{\frac{2}{3}}\right) k^3 + \frac{\sqrt{5}\pi}{\phi^4} k^2 - (1-\epsilon) = 0\,. \tag{2.61}$$

The specific surface area for the cylindrical strut geometry is determined in a similar manner as in the case of the triangular strut geometry, that is

$$S_v = \frac{\frac{30}{3}\, A_{\text{strut}}}{V_o}\,. \tag{2.62}$$

Using cylindrical geometry with a constant strut diameter as shown in Figure 2.8, A_{strut} can be expressed as

$$A_{\text{strut}} = 2\,\pi \left(\frac{d_s}{2}\right) \times l_s = \pi\, d_s\, c \left(1 - \frac{1}{2}\sqrt{\frac{2}{3}}\, k\right) . \tag{2.63}$$

Substituting equations (2.44) and (2.63) into equation (2.62) results in

$$S_v = \frac{\frac{30}{3}\,\pi\, d_s\, c \left(1 - \frac{1}{2}\sqrt{\frac{2}{3}}\, k\right)}{\frac{\sqrt{5}\,\phi^4}{2}\, c^3} = \frac{20\,\pi\, d_s}{\sqrt{5}\,\phi^4\, c^2} \left(1 - \frac{1}{2}\sqrt{\frac{2}{3}}\, k\right) . \tag{2.64}$$

In order to determine an expression for S_v in terms of d_p, equation (2.56) can be used, as well as $d_s = k\, c$, which, when substituted into equation (2.64), leads to (Huu et al. [21])

$$S_v = \frac{20\,\pi\, k}{\sqrt{5}\,\phi^3 \sqrt{3-\phi}\, d_p} \left(1 - \frac{1}{2}\sqrt{\frac{2}{3}}\, k\right)^2 , \tag{2.65}$$

where k can be solved from equation (2.61).

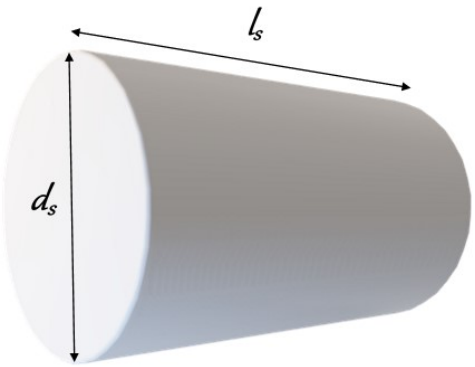

FIGURE 2.8: *Dodecahedron cylindrical strut parameters*

The predictions made by equation (2.65) is also shown in Figure 2.7 for porosity values in the range of 0.7 to 0.9.

Triangular and cylindrical "fat" strut geometry

In the case of "fat" strut geometry the edges are more rounded and therefore the strut volume is increased by adding the volume accumulated around the edges. The calculation of the volume added, denoted by V_{add}, is explained in Appendix C. The total strut volume for the triangular and cylindrical strut geometries can consequently be determined by adding V_{add} to the respective strut volumes of the "slim" model. For the case of the triangular strut geometry, equation (C.6) given in Appendix C will be added to equation (2.47), yielding

$$\begin{aligned} V_s = {} & \frac{5\sqrt{3}}{2}\, d_s^2\, c - \frac{5\sqrt{2}}{6}\, d_s^3 + 6\, d_s \left[\frac{5\,\phi}{4\sqrt{3-\phi}} - \frac{\pi\,\phi^2}{4\,(3-\phi)}\right] \left(c - \frac{1}{2}\sqrt{\frac{2}{3}}\, d_s\right)^2 \\ & + \frac{5\,\sin^2\left(\frac{\pi}{5}\right)\,\phi^2 \left(c - \frac{1}{2}\sqrt{\frac{2}{3}}\, d_s\right)^3}{8\sqrt{3}\,(3-\phi)} \sqrt{\frac{1}{4} - \frac{\sin^2\left(\frac{\pi}{5}\right)\,\phi^2}{9 - 3\,\phi}} . \end{aligned} \tag{2.66}$$

With the substitution of equations (2.66) and (2.44) into equation (2.36) and introducing k as d_s/c once more, the following equation is obtained:

$$-\frac{\sqrt{10}}{3\,\phi^4}k^3+\frac{\sqrt{15}}{\phi^4}k^2+\frac{12\,k}{\sqrt{5}\,\phi^4}\left[\frac{5\,\phi}{4\sqrt{3-\phi}}-\frac{\pi\,\phi^2}{4\,(3-\phi)}\right]\left(1-\frac{1}{2}\sqrt{\frac{2}{3}}\,k\right)^2$$
$$+\frac{5\,\sin^2\left(\frac{\pi}{5}\right)}{4\sqrt{15}\,(3-\phi)\,\phi^2}\sqrt{\frac{1}{4}-\frac{\sin^2\left(\frac{\pi}{5}\right)\,\phi^2}{9-3\,\phi}}\left(1-\frac{1}{2}\sqrt{\frac{2}{3}}\,k\right)^3-(1-\epsilon)=0\,. \tag{2.67}$$

Similarly the strut volume for cylindrical strut geometry can be determined by adding equation (C.6) given in Appendix C to equation (2.58), i.e.

$$V_s=\frac{5\,\pi}{2}\,d_s^2\,c+\left[\frac{5\,\sqrt{2}}{12}-\frac{5\,\pi}{4}\sqrt{\frac{2}{3}}\right]d_s^3+6\,d_s\left[\frac{5\,\phi}{4\sqrt{3-\phi}}-\frac{\pi\,\phi^2}{4\,(3-\phi)}\right]\left(c-\frac{1}{2}\sqrt{\frac{2}{3}}\,d_s\right)^2$$
$$+\frac{5\,\sin^2\left(\frac{\pi}{5}\right)\,\phi^2\left(c-\frac{1}{2}\sqrt{\frac{2}{3}}\,d_s\right)^3}{8\sqrt{3}\,(3-\phi)}\sqrt{\frac{1}{4}-\frac{\sin^2\left(\frac{\pi}{5}\right)\,\phi^2}{9-3\,\phi}}\,, \tag{2.68}$$

and the implicit equation of k in terms of ϵ can be expressed as follows:

$$\left[\frac{2\sqrt{10}}{12\phi^4}-\frac{\sqrt{5}\pi}{2\phi^4}\sqrt{\frac{2}{3}}\right]k^3+\frac{\sqrt{5}\pi}{\phi^4}k^2+\frac{12\,k}{\sqrt{5}\,\phi^4}\left[\frac{5\,\phi}{4\sqrt{3-\phi}}-\frac{\pi\,\phi^2}{4\,(3-\phi)}\right]\left(1-\frac{1}{2}\sqrt{\frac{2}{3}}\,k\right)^2$$
$$+\frac{5\,\sin^2\left(\frac{\pi}{5}\right)}{4\sqrt{15}\,(3-\phi)\,\phi^2}\sqrt{\frac{1}{4}-\frac{\sin^2\left(\frac{\pi}{5}\right)\,\phi^2}{9-3\,\phi}}\left(1-\frac{1}{2}\sqrt{\frac{2}{3}}\,k\right)^3-(1-\epsilon)=0\,. \tag{2.69}$$

The added surface area of the "fat" model is the same for both triangular and cylindrical struts, as approximated by Huu et al. [21]. The calculation for the total added surface area A_{add} is given by equation (C.9) in Appendix C and combined with equation (2.44), the added specific surface area can be obtained using equation (1.3), i.e.

$$S_{\text{add}}=\frac{\frac{12}{2}\,\pi\,d_p\,d_s+\frac{20}{16}\,\sqrt{3}\,d_p^2\,\sin^2\left(\frac{\pi}{5}\right)}{\frac{\sqrt{5}\,\phi^4}{2}\,c^3}\,. \tag{2.70}$$

In order to determine S_{add} in terms of d_p and ϵ, equation (2.55) and the relation $d_s=kc$ can be utilized along with equation (2.70). After simplification, it follows that

$$S_{\text{add}}=\frac{\left(1-\frac{1}{2}\sqrt{\frac{2}{3}}\,k\right)}{\phi\,\sqrt{3-\phi}}\left[\frac{12\,\pi\,k\,\left(1-\frac{1}{2}\sqrt{\frac{2}{3}}\,k\right)}{\sqrt{5}\,\phi\,\sqrt{3-\phi}\,d_p}+\frac{\sqrt{15}\,\sin^2\left(\frac{\pi}{5}\right)\,\left(1-\frac{1}{2}\sqrt{\frac{2}{3}}\,k\right)^2}{2\,(3-\phi)\,d_p}\right]\,. \tag{2.71}$$

The specific surface area for the triangular "fat" model can therefore be obtained by adding equations (2.57) and (2.71), yielding (Huu et al. [21])

$$S_v=\frac{60\,k}{\sqrt{5}\,\phi^3\sqrt{3-\phi}\,d_p}\left(1-\frac{1}{2}\sqrt{\frac{2}{3}}\,k\right)^2+\frac{\left(1-\frac{1}{2}\sqrt{\frac{2}{3}}\,k\right)}{\phi\,\sqrt{3-\phi}}\left[\frac{12\,\pi\,k\,\left(1-\frac{1}{2}\sqrt{\frac{2}{3}}\,k\right)}{\sqrt{5}\,\phi\,\sqrt{3-\phi}\,d_p}\right.$$
$$\left.+\frac{\sqrt{15}\,\sin^2\left(\frac{\pi}{5}\right)\,\left(1-\frac{1}{2}\sqrt{\frac{2}{3}}\,k\right)^2}{2\,(3-\phi)\,d_p}\right]\,, \tag{2.72}$$

where k can be solved from equation (2.67). Similarly, S_v for the cylindrical "fat" model is obtained by adding equations (2.65) and (2.71), yielding (Huu et al. [21])

$$S_v = \frac{20\,\pi\,k}{\sqrt{5}\,\phi^3\sqrt{3-\phi}\,d_p}\left(1-\frac{1}{2}\sqrt{\frac{2}{3}}\,k\right)^2 + \frac{\left(1-\frac{1}{2}\sqrt{\frac{2}{3}}\,k\right)}{\phi\,\sqrt{3-\phi}}\left[\frac{12\,\pi\,k\,\left(1-\frac{1}{2}\sqrt{\frac{2}{3}}\,k\right)}{\sqrt{5}\,\phi\,\sqrt{3-\phi}\,d_p} + \frac{\sqrt{15}\,\sin^2\left(\frac{\pi}{5}\right)\left(1-\frac{1}{2}\sqrt{\frac{2}{3}}\,k\right)^2}{2\,(3-\phi)\,d_p}\right], \tag{2.73}$$

where k is solved using equation (2.69).

The predictions for the specific surface area provided by equations (2.72) and (2.73) for the triangular and cylindrical "fat" dodecahedron models, respectively, are shown in Figure 2.7. The "fat" model predictions are displayed similarly to the "slim" model predictions in that the triangular strut equation, i.e. equation (2.72), was plotted for the porosity range of 0.9 to 1 and the cylindrical strut equation, i.e. equation (2.73), was plotted for the porosity range of 0.7 to 0.9.

Although the trends of all the equations (i.e. equations (2.57), (2.65), (2.72) and (2.73)) are as expected, that is, the specific surface area decreases with increasing porosity, the expectation that the two curves for both sets of the "slim" and "fat" model equations would be similar at 0.9 is not met. The "slim" model equations furthermore predict lower values than the "fat" model equations, as expected.

Finally, the RUC models will be discussed.

2.1.4 RUC models

Two RUC models will be considered, i.e. the three-strut RUC model and the two-strut RUC model as shown in Figures 2.9(a) and (b), respectively. The three-strut RUC model represents the network of struts of actual foamlike media as three perpendicular square struts indicated by the shaded volumes in Figure 2.9(a), whereas the two-strut RUC model represents the network of struts by two perpendicular square struts indicated by the shaded volumes in Figure 2.9(b). The latter model is introduced to represent the stacking of actual fibre layers more accurately than the three-strut model and is discussed in this chapter, even though it is not isotropic. The next chapter deals with anisotropy introduced into the two models as a result of compression.

The three-strut RUC model will be investigated first.

Three-strut RUC model

The three-strut RUC model that gives a representation of metal foams was proposed by Du Plessis et al. [22], as mentioned in Chapter 1, and will be considered in this study. In the RUC model d represents the cell size, d_s the linear dimension of the square strut, U_o the cell volume, U_s the strut volume and U_f the fluid volume (Woudberg and Du Plessis [1]). This notation, as previously mentioned in the beginning of this section, will be used to further analyse the RUC models.

An approach followed by Woudberg and Du Plessis [1] to determine the specific surface area of the three-strut RUC model is used. They aimed at using geometrical parameters to attain

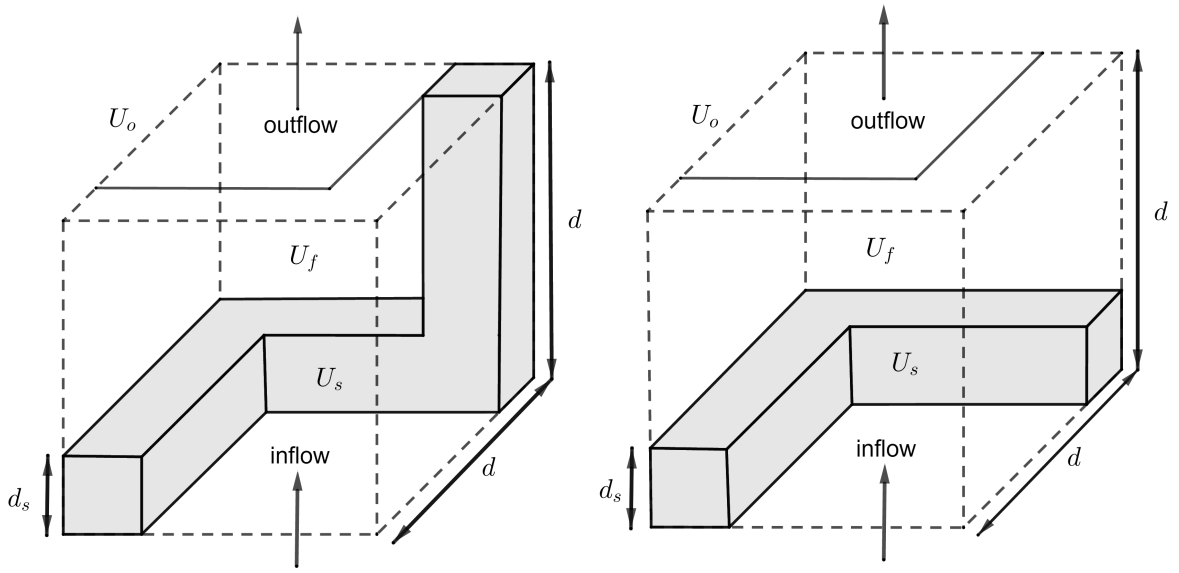

(a) *Three-strut model* (b) *Two-strut model*

FIGURE 2.9: *RUC models*

an Ergun-type equation and their approach therefore resulted in the means to attain a specific surface area equation for this study. The starting point is to find the relationship between the porosity and geometric factor, which is denoted by ψ and is defined as

$$\psi = \frac{U_f}{U_{||} + U_t}\,, \tag{2.74}$$

where $U_{||}$ is defined as the total streamwise fluid volume, i.e. the fluid volume that is parallel to the direction of the superficial velocity, and U_t is known as the transfer volume and is defined as fluid volumes that are not bordered by solid surfaces (Woudberg and Du Plessis [1]).

Equation (1.1) for ϵ can be rewritten in RUC notation as

$$\epsilon = \frac{U_f}{U_o}\,, \tag{2.75}$$

and using the parameters indicated in Figure 2.9(a) it can be deduced that

$$U_o = d^3\,, \tag{2.76}$$

and hence

$$U_s = 3d_s^2(d - d_s) + d_s^3\,. \tag{2.77}$$

Since $U_f = U_o - U_s$, it follows that

$$U_f = d^3 - 3d_s^2(d - d_s) - d_s^3\,, \tag{2.78}$$

and substituting equations (2.76) and (2.78) into equation (2.75) leads to

$$\epsilon = \frac{d^3 - 3dd_s^2 + 2d_s^3}{d^3} = 1 - 3\left(\frac{d_s}{d}\right)^2 + 2\left(\frac{d_s}{d}\right)^3\,. \tag{2.79}$$

It can further be deduced from Figure 2.9(a) that (Woudberg and Du Plessis [1])

$$U_{||} = (d - d_s)^2\, d_s\,, \tag{2.80}$$

and that

$$U_\perp = 2(d - d_s)^2 \, d_s \,, \tag{2.81}$$

where $U_\perp$ is defined as the total transverse fluid volume, that is the fluid volume that is perpendicular to the direction of the superficial velocity.

An easier way of visualizing the quantified results of these fluid volumes is by inverting the fluid and solid volumes in Figure 2.9(a), i.e. exchanging the parameters d_s and $d - d_s$. Since $U_\parallel$, U_t and $U_\perp$ encompass the entire fluid volume, it follows that

$$U_f = U_\parallel + U_t + U_\perp \,, \tag{2.82}$$

and substituting equations (2.78), (2.80) and (2.81) into equation (2.82) leads to the following expression for U_t:

$$U_t = (d - d_s)^3 \,. \tag{2.83}$$

In order to determine a relationship for ψ in terms of ϵ, the following equation is obtained by substituting equations (2.78), (2.80) and (2.83) into equation (2.74):

$$\psi = 1 + 2\frac{d_s}{d} \,. \tag{2.84}$$

Rearranging equation (2.84) leads to

$$\frac{d_s}{d} = \frac{\psi - 1}{2} \,. \tag{2.85}$$

and another rearrangement, that will prove to be useful, results in

$$\frac{d - d_s}{d} = \frac{3 - \psi}{2} \,. \tag{2.86}$$

Substituting equation (2.85) into equation (2.79) then leads to the following third degree polynomial

$$\psi^3 - 6\psi^2 + 9\psi - 4\epsilon = 0 \,, \tag{2.87}$$

which can be solved using the cardanic method of solving a cubic polynomial, as described in Appendix D. This method then yields

$$\psi = 2 + 2\cos\left[\frac{4\pi}{3} + \frac{1}{3}\cos^{-1}(2\epsilon - 1)\right] \,, \tag{2.88}$$

as given by equation (D.3) in Appendix D.

In order to determine the specific surface area, the parameters specified in Figure 2.9(a) are used to express the total surface area as

$$A_s = 12(d - d_s)\, d_s \,, \tag{2.89}$$

which, when substituting equations (2.76) and (2.89) into equation (1.3) where U_o is used instead of V_o, leads to

$$S_v = \frac{12(d - d_s)\, d_s}{d^3} = \frac{12}{d} \cdot \frac{d - d_s}{d} \cdot \frac{d_s}{d} \,. \tag{2.90}$$

Substituting equations (2.85) and (2.86) into equation (2.90) then yields

$$S_v = \frac{3}{d}(3 - \psi)(\psi - 1) \,. \tag{2.91}$$

Since d is equivalent to D_p, equation (2.91) is thus also an expression for the specific surface area in terms of D_p, i.e.

$$S_v = \frac{3}{D_p}(3-\psi)(\psi-1)\,. \tag{2.92}$$

This also implies that an expression for D_p in terms of d_s can be obtained through rearranging equation (2.85), resulting in

$$d = D_p = \frac{2\,d_s}{\psi-1}\,. \tag{2.93}$$

Substituting equation (2.93) into equation (2.92) leads to the expression for the specific surface area in terms of d_s:

$$S_v = \frac{3}{2\,d_s}(3-\psi)(\psi-1)^2\,. \tag{2.94}$$

Similarly, using equation (1.10) and equation (2.93), an expression for D_p in terms of d_p can be obtained, i.e.,

$$D_p = \frac{2\,d_p}{3-\psi}\,, \tag{2.95}$$

which can be substituted into equation (2.92), leading to the expression for the specific surface area in terms of d_p:

$$S_v = \frac{3}{2\,d_p}(3-\psi)^2(\psi-1)\,, \tag{2.96}$$

where ψ is given by equation (2.88).

Two-strut RUC model

The same parameters as defined for the three-strut model is also applicable to the two-strut model, as illustrated in Figure 2.9(b) for the two-strut model. The approach to determine the specific surface area is similar to the approach followed for the three-strut model. Due to the fact that U_o still represents the cell volume, equation (2.76) is also applicable to the two-strut model. It can however be deduced from Figure 2.9(b) that

$$U_s = 2d_s^2 d - d_s^3\,, \tag{2.97}$$

and since $U_f = U_o - U_s$, the fluid volume is given by

$$U_f = d^3 - 2d_s^2 d + d_s^3\,. \tag{2.98}$$

Substituting equations (2.76) and (2.98) into equation (2.75) for the porosity leads to

$$\epsilon = \frac{d^3 - 2d_s^2 d + d_s^3}{d^3} = 1 - 2\left(\frac{d_s}{d}\right)^2 + \left(\frac{d_s}{d}\right)^3\,. \tag{2.99}$$

The total streamwise and transverse fluid volumes can be deduced from Figure 2.9(b), resulting in

$$U_{\parallel} = (d-d_s)^2 d_s\,, \tag{2.100}$$

and

$$U_{\perp} = (d-d_s)^2 d_s\,. \tag{2.101}$$

Substituting equations (2.100) and (2.101) into equation (2.82), which also applies to the two-strut RUC model, the total transfer volume is deduced, i.e.

$$U_t = (d-d_s)^3\,. \tag{2.102}$$

Adding equations (2.100) and (2.102) yields

$$U_{\parallel} + U_t = d^2(d - d_s)\,. \tag{2.103}$$

A useful expression for the relationship between ψ and ϵ can be determined by equating the ratio of the porosity and the geometric factor by making use of equations (2.74) and (2.75), leading to

$$\frac{\epsilon}{\psi} = \frac{U_f/U_o}{U_f/(U_{\parallel} + U_t)} = \frac{U_{\parallel} + U_t}{U_o}\,. \tag{2.104}$$

Substituting equations (2.76) and (2.103) into equation (2.104) then yields

$$\frac{\epsilon}{\psi} = \frac{d - d_s}{d}\,. \tag{2.105}$$

Rearrangement of equation (2.105) gives

$$\frac{d_s}{d} = 1 - \frac{\epsilon}{\psi}\,. \tag{2.106}$$

Equation (2.106) can then in turn be substituted into equation (2.99), rearranged and simplified to obtain the third degree polynomial for the geometric factor, i.e.

$$\psi^3 - \psi^2 - \epsilon\psi + \epsilon^2 = 0\,. \tag{2.107}$$

Equation (2.107) can then be solved using the cardanic method (described in Appendix D). The solution for the geometric factor in terms of the porosity is hence given by equation (D.5) in Appendix D, i.e.

$$\psi = \frac{2}{3}\sqrt{3\epsilon + 1}\cos\left[\frac{1}{3}\cos^{-1}\left(\frac{9\epsilon - 27\epsilon^2 + 2}{2\sqrt{27\epsilon^3 + 27\epsilon^2 + 9\epsilon + 1}}\right)\right] + \frac{1}{3}\,. \tag{2.108}$$

Having acquired the equation for ψ in terms of ϵ, the specific surface area can then be determined in terms of ϵ and ψ. The total surface area can be deduced from Figure 2.9(b), resulting in

$$A_s = 8(d - d_s)d_s + 2d_s^2\,. \tag{2.109}$$

The specific surface area can thus be determined by substituting equations (2.76) and (2.109) into equation (1.3), i.e.

$$S_v = \frac{8(d - d_s)d_s + 2d_s^2}{d^3} = \frac{8}{d}\cdot\frac{d - d_s}{d}\cdot\frac{d_s}{d} + \frac{2}{d}\left(\frac{d_s}{d}\right)^2\,. \tag{2.110}$$

Substituting equations (2.105) and (2.106) into equation (2.110) then finally yields

$$S_v = \frac{2}{d}\left(1 - \frac{\epsilon}{\psi}\right)\left(1 + \frac{3\epsilon}{\psi}\right)\,. \tag{2.111}$$

Once again d can be set equal to D_p, which therefore leads to the specific surface area in terms of D_p by expressing equation (2.111) as

$$S_v = \frac{2}{D_p}\left(1 - \frac{\epsilon}{\psi}\right)\left(1 + \frac{3\epsilon}{\psi}\right)\,. \tag{2.112}$$

Accordingly, equation (2.105) can also be rearranged to give

$$d = D_p = \frac{d_s}{1 - \frac{\epsilon}{\psi}}\,. \tag{2.113}$$

Substituting equation (2.113) into equation (2.112) thus leads to

$$S_v = \frac{2}{d_s}\left(1-\frac{\epsilon}{\psi}\right)^2\left(1+\frac{3\epsilon}{\psi}\right), \tag{2.114}$$

which is the specific surface area in terms of d_s. Equations (1.10) and (2.113) can furthermore be used to find an expression for D_p in terms of d_p, given by

$$D_p = \frac{\psi}{\epsilon} d_p, \tag{2.115}$$

which, when substituted into equation (2.112), leads to an expression for the specific surface area in terms of d_p, i.e.

$$S_v = \frac{2\epsilon}{\psi\, d_p}\left(1-\frac{\epsilon}{\psi}\right)\left(1+\frac{3\epsilon}{\psi}\right), \tag{2.116}$$

where ψ can be obtained from equation (2.108).

In Figure 2.10 the predictions provided by equations (2.96) and (2.116), for the three-strut and two-strut RUC models, respectively, are shown. A decrease in specific surface area with increasing porosity is obtained in both cases. The two-strut model predictions are furthermore lower than the three-strut model predictions.

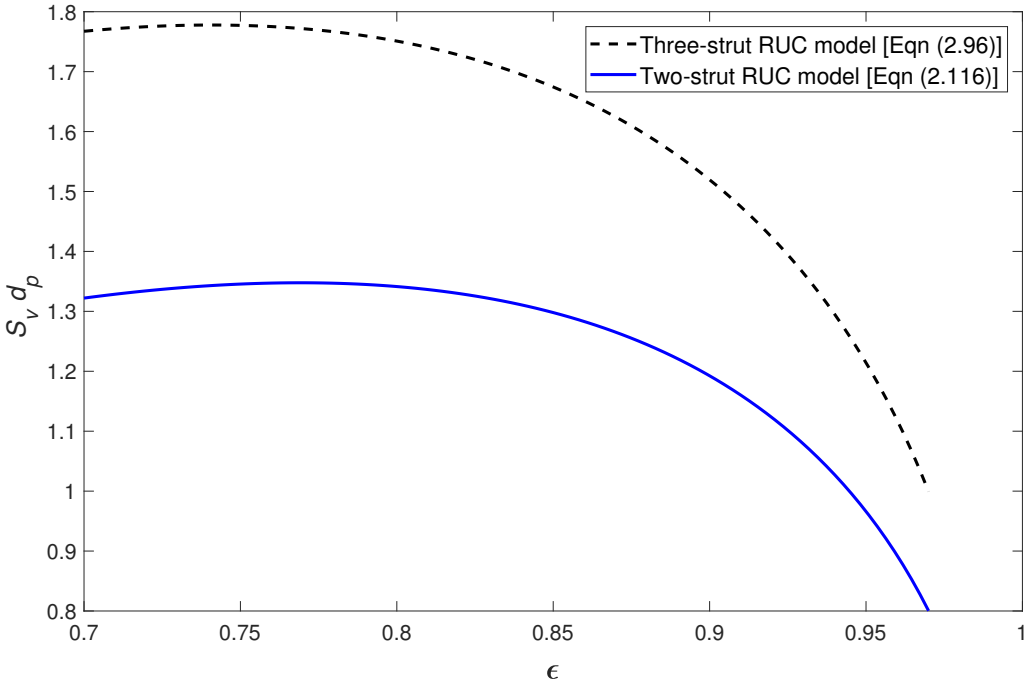

FIGURE 2.10: *Dimensionless specific surface area versus porosity for the RUC model*

2.1.5 Comparison of geometric approaches

A summary of all the specific surface area equations obtained from the different geometric models considered is given in Table 2.4, in the Chapter summary, Section 2.6, at the end of the chapter, and will now be evaluated by comparing the models to each other and with experimental data

found in the literature. The specific surface area in terms of the pore diameter will be used to compare the models.

All the relevant specific surface area predictions were non-dimensionalised by multiplying with d_p. The predictions based on the geometric approach are shown in Figure 2.11, containing the two cubic unit cell model predictions, the four tetrakaidecahedron model predictions (where only the corrected Richardson model is shown), the four dodecahedron model predictions and the single three- and two-strut RUC model predictions.

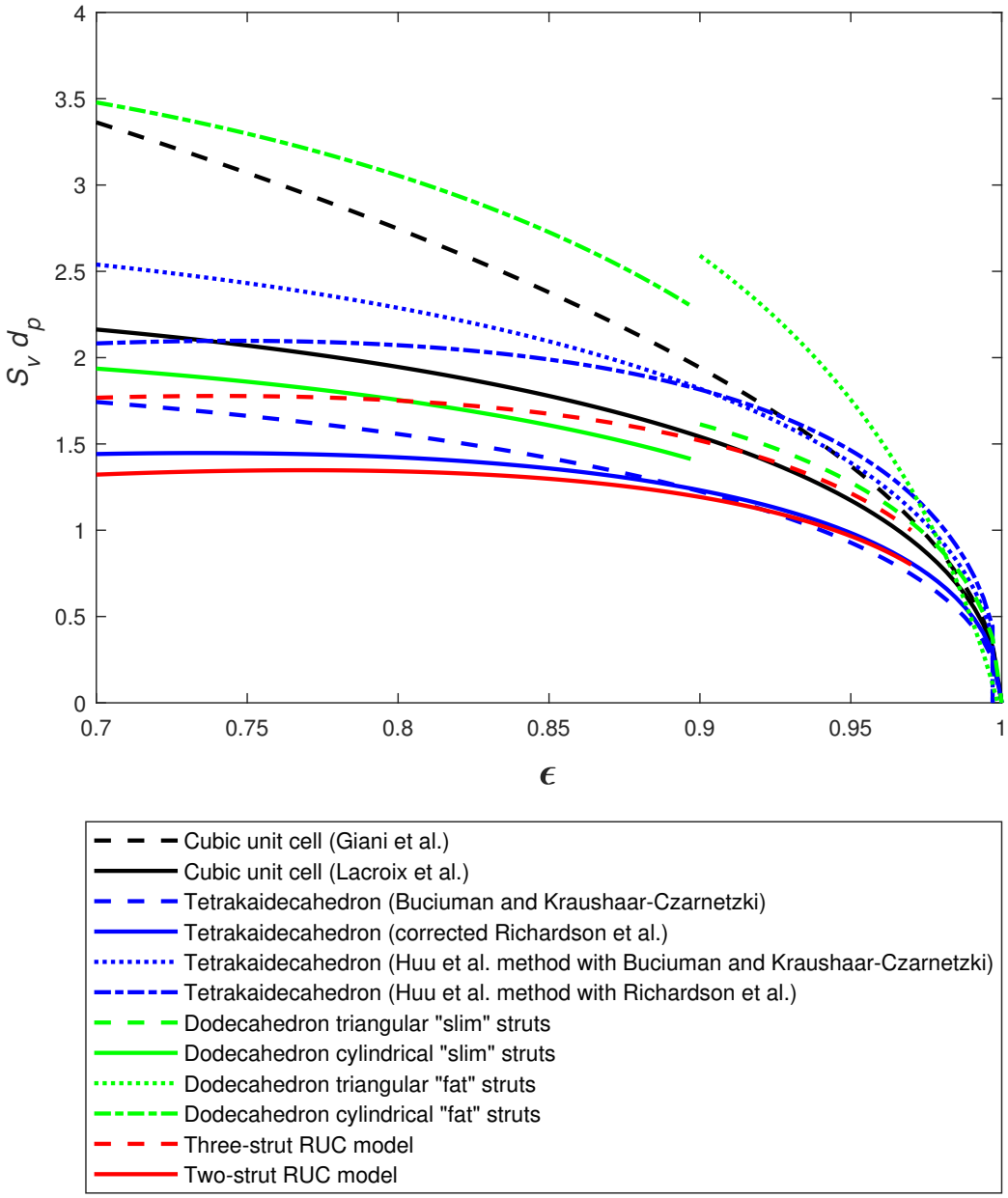

FIGURE 2.11: *Dimensionless specific surface area versus porosity based on all the geometric approaches*

As can be seen in Figure 2.11, all the models show a decreasing specific surface area with increasing porosity, with the exceptions of the the tetrakaidecahedron models obtained using the corrected Richardson et al. [4] expression and the Huu method with the Richardson expression, the three-strut RUC model and the two-strut RUC model, which increases slightly for $\epsilon < \pm 0.8$ before decreasing with an increase in porosity. For $\epsilon < 0.97$, the "fat" dodecahedron model predicts the highest specific surface area values, followed by the tetrakaidecahedron model obtained using the Huu method with the Richardson expression for $\epsilon > 0.97$. For $\epsilon < 0.93$ the two-strut RUC model predicts the lowest values. The two-strut RUC model will, however, not be considered in the comparison with experimental data due to the data being acquired from foams and the model being specifically introduced for layers of fibres. Apart from the two-strut model, the corrected Richardson version of the tetrakaidecahedron model predicts the lowest values for $\epsilon < 0.9$.

Besides the two-strut RUC model, the three-strut model will also be used to conduct a more in depth study of compressed fibrous media. This is to illustrate through direct comparison that the compressed two-strut model is a physically more realistic representation of a stacking of fibre layers than the compressed three-strut model that was applied by Woudberg and Du Plessis [1] to non-woven fibrous media. The geometric model predictions closest to dimensionless specific surface area predictions of the three-strut RUC model, including the three-strut RUC model predictions, are shown in Figure 2.12. The models revealing the closest correspondence to the specific surface area predictions of the three-strut RUC model are the cubic unit cell model, the tetrakaidecahedron model as given by Buciuman and Kraushaar-Czarnetzki and the "slim" dodedcahedron models.

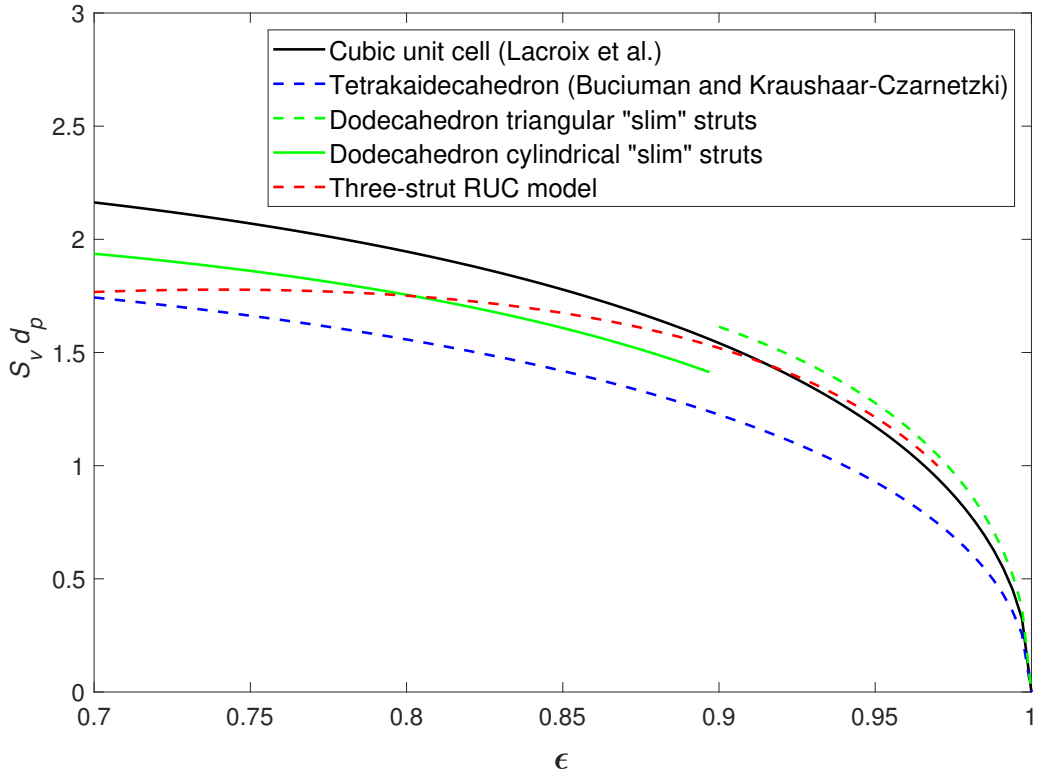

FIGURE 2.12: *Dimensionless specific surface area versus porosity based on the geometric approach of the models that correspond best with the predictions of the three-strut RUC model*

The comparison of the geometric models with experimental data will be addressed in the next section.

Comparison to experimental data

The experimental data for the evaluation of the dimensionless specific surface area equations obtained in the geometric approach were obtained from two sources, i.e. Dietrich et al. [2] and Garrido et al. [3]. Dietrich et al. [2] gathered their experimental data from ceramic-based foams in order to determine the hydraulic diameter of the foams by using an Ergun-type equation. Garrido et al. [3] used their data to investigate the mass transfer properties of the foams, as well as the correlations among the morphology of the foams and the pressure drop of flow through the foams. They also used ceramic-based foams in their experiments and study. The data from these sources is given in Table 2.1.

TABLE 2.1: *Experimental data from the literature used to validate the predictions for $S_v d_p$ obtained from the geometric, kinetic (Section 2.2) and combined (Section 2.3) approaches*

Dietrich et al. [2] (ceramic-based foams)				
ϵ	d_p[mm]	S_v[m^{-1}]	$K \times 10^9$[m^2]	$K_F \times 10^5$[m]
0.754	1.529	1090	130	88
0.808	2.253	664	77	187
0.802	1.091	1204	54	114
0.806	0.884	1402	32	98
0.809	0.625	1884	20	76
0.854	1.464	1109	144	180
Garrido et al. [3] (ceramic-based foams)				
ϵ	d_p[mm]	S_v[m^{-1}]	$K \times 10^9$[m^2]	$K_F \times 10^5$[m]
0.818	1.933	675.4	28.58	3.13
0.804	1.192	1187.0	9.17	1.67
0.816	0.871	1437.8	7.23	1.45
0.813	0.666	1884.3	6.23	1.49
0.852	2.252	629.3	39.5	5.94
0.858	1.131	1109.1	14.66	1.98
0.852	0.861	1422.4	11.07	1.89
0.848	0.687	1816.3	9.95	1.83
0.777	1.069	1290.3	6.74	1.36

Dietrich et al. [2] used the weight of the foams and the measuring of its geometry to determine the porosities, light microscopy to determine the pore diameters and MRI measurements to determine the specific surface area values. In the case of the data obtained from Garrido et al. [3], the porosities were determined using mercury porosimetry, the pore diameters were determined by making use of image analyses, and the specific surface area values were obtained from MRI measurements. Pressure drop measurements were used to obtain the permeability coefficients K and K_F, which will be used and discussed later in this chapter in the Kinetic approach section, (Section 2.2), and the Combined approach section, (Section 2.3).

In order to compare the geometric models with the experimental data obtained from Dietrich et al. [2], the dimensionless specific surface area was plotted for each of the porosity values as given in Table 2.1, as well as the corresponding Dietrich specific surface area data points multiplied by

the pore diameter data points. Only the dodecahedron models with cylindrical struts are plotted for this set of data since the porosity values are less than 0.9. The results are shown in Figure 2.13.

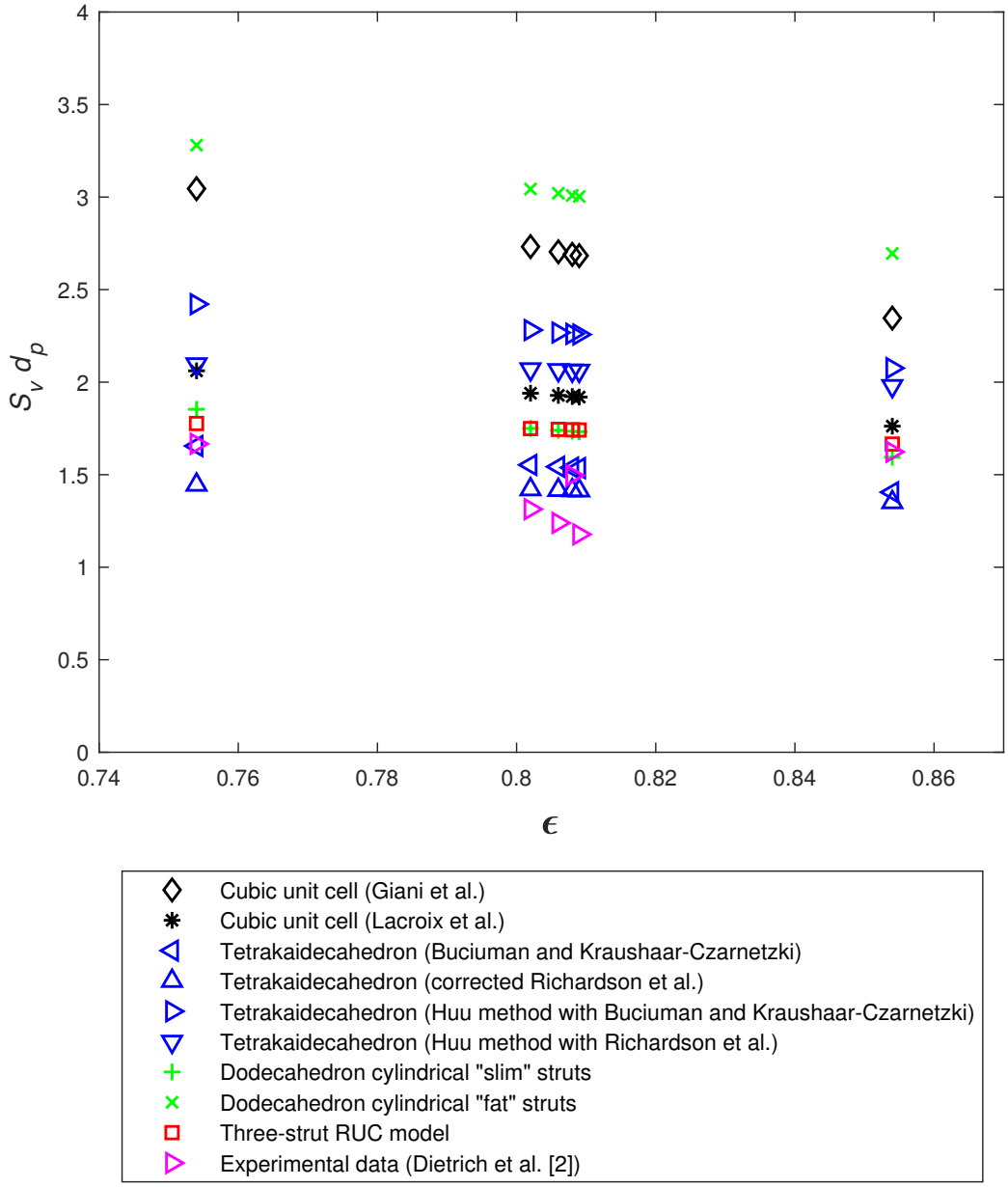

FIGURE 2.13: *Dimensionless specific surface area based on the geometric approach compared to experimental data obtained from Dietrich et al. [2]*

It can be observed in Figure 2.13 that all the geometric approaches slightly over-predict the dimensionless specific surface area, when compared to the experimental data obtained from Dietrich et al. [2]. It is furthermore evident from Figure 2.13 that the model that corresponds the best with the experimental data is the tetrakaidecahedron model resulting from the corrected

Richardson et al. method, i.e. equation (2.34). This model yields an average percentage difference of 13% when compared to the data. The tetrakaidecahedron model obtained using the Buciuman and Kraushaar-Czarnetzki method, given by equation (2.26), performed second best with an average percentage difference of 15%, followed by the three-strut RUC model, given by equation (2.96) and the "slim" dodecahedron model with cylindrical struts (equation (2.65)). The model that provides the least accurate correspondence with the Dietrich et al. data is the "fat" dodecahedron with cylindrical struts.

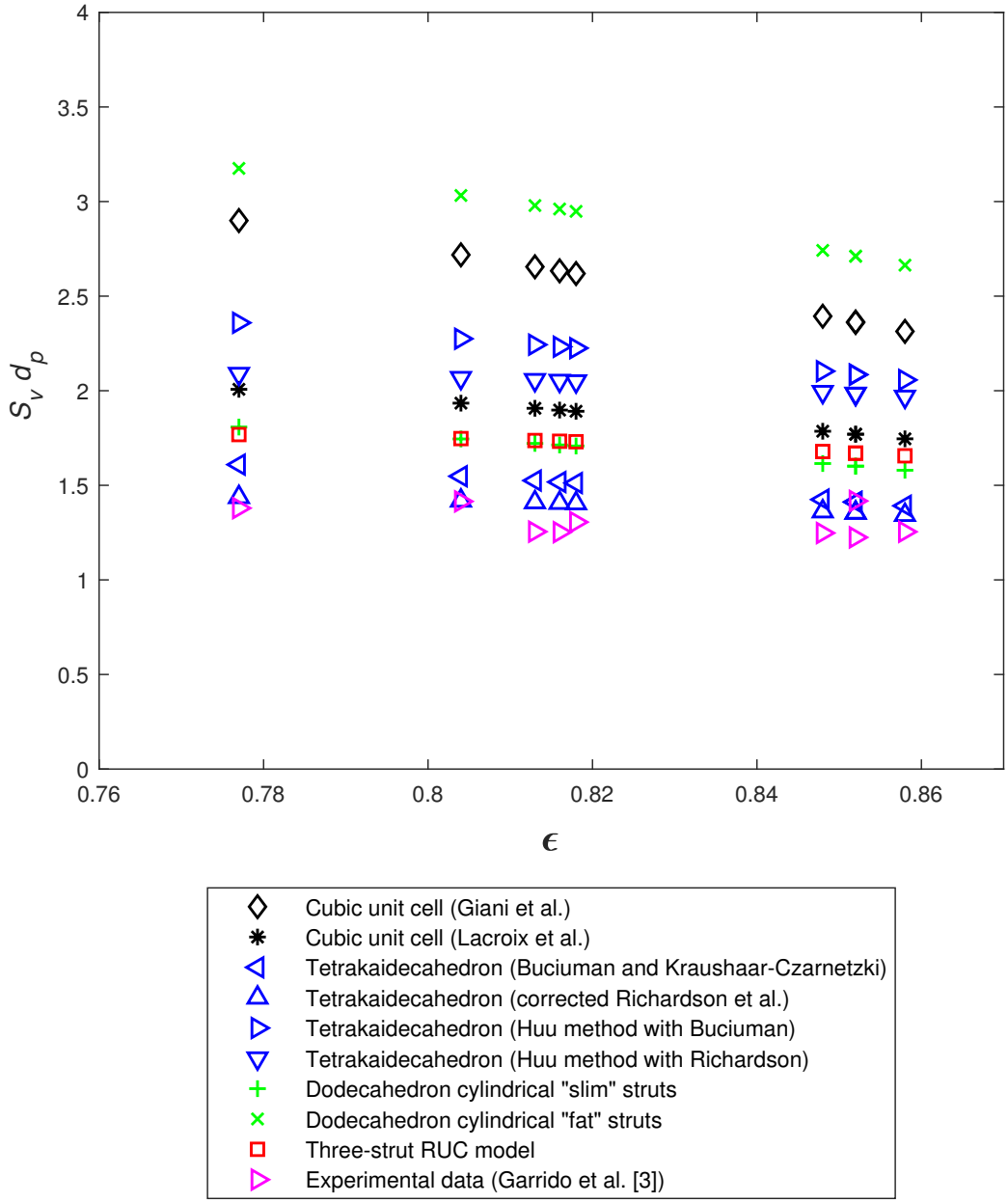

FIGURE 2.14: *Dimensionless specific surface area based on the geometric approach compared to experimental data obtained from Garrido et al. [3]*

Comparison of the geometric models with the Garrido et al. [3] experimental data are done similarly to the comparison with the Dietrich et al. [2] data, and is illustrated in Figure 2.14. Due to the porosity values being less than 0.9, only the dodecahedron models with cylindrical struts are taken into consideration.

In Figure 2.14 similar results are obtained with respect to the general over-prediction of the geometric models, as well as to the accuracy of the model predictions compared to the experimental data. In this case the tetrakaidecahedron corrected Richardson and Buciuman and Kraushaar-Czarnetzki models differ with an average percentage difference of 8% and 14% when compared to the experimental data, respectively.

In both Figures 2.13 and 2.14 the two newly proposed versions of the tetrakaidecahedron model for predicting the specific surface area based on the geometric approach that separately incorporates the strut lengths of Buciuman and Kraushaar-Czarnetzki [25] and Richardson et al. [4] provide more accurate predictions for the dimensionless specific surface area in comparison to the experimental data considered than the model predictions provided by the cubic unit cell model of Giani et al. [14] and dodecahedron model of Huu et al. [21] with cylindrical "fat" struts.

If the complexity of the geometric models based on geometry and modelling procedures in decreasing order are the tetrakaidecahedron, dodecahedron, RUC and cubic unit cell model then the models with the more complex geometry, i.e. the tetrakaidecahedron and dodecahedron models, (when considered together) provided the closest correspondence to the experimental data in comparison to the predictions of the simpler geometric models, i.e. the RUC and cubic unit cell models. This is because the tetrakaidecahedron model provide the most accurate predictions. The more complex models do not necessarily provide more accurate predictions if the models are considered individually since the three-strut RUC model provided slightly more accurate predictions than the dodecahedron model when compared with the one data set.

In the following section the specific surface area equations for foams using a kinetic approach will be derived and evaluated.

2.2 Specific surface area: Kinetic approach

The onset of determining the specific surface area using a kinetic approach, is the Darcy-Forchheimer equation, i.e. equation (1.11). As mentioned in Chapter 1, equation (1.11) is used to determine K and K_F from experimental data for the pressure drop. These permeability coefficients will be used to find an expression for the specific surface area. In order to determine K and K_F, three approaches will be considered. The one approach will be based on the study of Dietrich et al. [2], another approach will be based on the study of Huu et al. [21], and the final approach will be based on the RUC modelling approach of Woudberg and Du Plessis [1].

The approach based on the work done by Dietrich et al. [2] will be discussed first and will be referred to as the Dietrich formulation.

2.2.1 Dietrich formulation

Dietrich et al. [2] compared an Ergun-type equation for solid foams with equation (1.11). The Ergun-type equation is given by

$$\frac{\Delta p}{L} = B_1 \frac{\mu}{\epsilon D_h^2} q + B_2 \frac{\rho}{\epsilon^2 D_h} q^2 \,, \tag{2.117}$$

where B_1 and B_2 are empirical constants. Comparing equations (1.11) and (2.117), expressions for B_1 and B_2 can thus be obtained, i.e.

$$B_1 = \frac{\epsilon D_h^2}{K} \tag{2.118}$$

and

$$B_2 = \frac{\epsilon^2 D_h}{K_F}\,, \tag{2.119}$$

where D_h is as defined in equation (1.6). The values of K and K_F are determined first by fitting various experimental data from different foams and using the correlation between the data and equation (1.11). From the values of K and K_F, corresponding values can be obtained for B_1 and B_2 if the measured values for ϵ and D_h are known. The results found by Dietrich et al. [2] are $B_1 = 110$ and $B_2 = 1.45$. Using the value of B_1, equation (2.118) can therefore be written in terms of D_h as follows:

$$D_h = \sqrt{\frac{110\,K}{\epsilon}}\,. \tag{2.120}$$

Substituting equation (1.6) into equation (2.120) leads to

$$\frac{4\epsilon}{S_v} = \sqrt{\frac{110\,K}{\epsilon}}\,,$$

and consequently

$$S_v = \sqrt{\frac{8\epsilon^3}{55\,K}}\,, \tag{2.121}$$

which is an expression for the specific surface area in terms of the permeability coefficient K.

Similarly S_v can be determined in terms of K_F using the value of B_2 and equations (2.119) and (1.6). This results in

$$S_v = \frac{4\epsilon^3}{1.45\,K_F}\,. \tag{2.122}$$

In the next section the approach followed by Huu et al. [21], referred to as the Huu formulation, will be outlined.

2.2.2 Huu formulation

The approach followed by Huu et al. [21] is similar to that of Dietrich et al. [2], but instead of using the Ergun equation as defined in terms of D_h, they used the Ergun equation defined in terms of d_p, that is

$$\frac{\Delta p}{L} = E_1\,\frac{\mu(1-\epsilon)^2}{\epsilon^3 d_p^2}\,q + E_2\,\frac{\rho(1-\epsilon)}{\epsilon^3 d_p}\,q^2\,, \tag{2.123}$$

where $E_1 = 150$ and $E_2 = 1.75$.

Huu et al. [21] defined the pore diameter d_p to be as in equation (1.9) which, like the hydraulic diameter, is a common parameter used when describing flow through porous media, although usually specifically applied to porous media consisting of spherical particles.

Comparing equations (1.11) and (2.123), the following expressions for K and K_F can respectively be deduced:

$$K = \frac{\epsilon^3 d_p^2}{E_1(1-\epsilon)^2}\,, \tag{2.124}$$

and

$$K_F = \frac{\epsilon^3 d_p}{E_2(1-\epsilon)}\,. \tag{2.125}$$

With the substitution of equation (1.9) and the value for E_1 into equation (2.124), S_v can be determined in terms of K as follows:

$$K = \frac{\epsilon^3}{150(1-\epsilon)^2}\left[\frac{6(1-\epsilon)}{S_v}\right]^2\,,$$

thus yielding

$$S_v = \sqrt{\frac{6\epsilon^3}{25\,K}}\,. \tag{2.126}$$

Similarly S_v can be determined in terms of K_F by substituting equation (1.9) and the value for E_2 into equation (2.125), leading to

$$S_v = \frac{6\epsilon^3}{1.75\,K_F}\,. \tag{2.127}$$

The approach using the RUC models, referred to as the RUC formulation, will be considered next.

2.2.3 RUC formulation

In the RUC formulation an Ergun-type equation is deduced by making use of the three- and two-strut RUC models. The method of attaining the specific surface area equations using these models and their transport properties will be presented first for the three-strut RUC model and then for the two-strut RUC model.

Three-strut RUC model

In the three-strut RUC approach, expressions for K and K_F are determined as shown in the study of Woudberg and Du Plessis [1]. An Ergun-type equation for porous foams was derived for the three-strut RUC model by Woudberg [56]. The onset of determining the Ergun-type equation for foams is the streamwise pressure gradient obtained by doing closure modelling of the volume averaged Navier-Stokes equation, yielding

$$-\nabla\langle p\rangle = \frac{1}{U_o}\iint_{S_{\text{fs}}}(\underline{n}p - \underline{n}\cdot\underline{\underline{\tau}})\mathrm{d}S\,, \tag{2.128}$$

where $\langle p\rangle$ is the phase averaged pressure, S_{fs} is the total fluid-solid surface areas in the RUC, $\underline{n}$ is the unit vector that is directed inwardly and perpendicular to the fluid-solid surfaces and $\underline{\underline{\tau}}$ is the shear stress tensor. Assuming a low Reynolds number limit, as well as a uniform porosity, equation (2.128) becomes (Woudberg [56])

$$-\nabla\langle p\rangle_f = \frac{S_\parallel + S_\perp}{\epsilon U_o}\tau_{w_\parallel}\psi\underline{\hat{n}}\,, \tag{2.129}$$

where $\langle p\rangle_f$ denotes the intrinsic phase averaged pressure, $S_\parallel$ and $S_\perp$ are the solid surfaces parallel and perpendicular to the streamwise direction, respectively, $\tau_{w_\parallel}$ is the magnitude of the

streamwise average wall shear stress and $\underline{\hat{n}}$ is the macroscopic direction of flow. Equation (2.129) can also be written in the following form (Woudberg [56]):

$$\Delta p = \frac{S_{\parallel}\tau_{w_{\parallel}} + S_{\perp}\tau_{w_{\perp}}}{A_{p_{\parallel}}}\,, \tag{2.130}$$

where $A_{p_{\parallel}}$ represents the cross-sectional flow area in the streamwise direction and $\tau_{w_{\perp}}$ the magnitude of the transverse average wall shear stress.

Equation (2.130) can be used to show how the low Reynolds number term in the Ergun-type equation for foams, proposed by Woudberg [56], is obtained. Plane Poiseuille flow is assumed, since it corresponds to the rectangular geometry. Accordingly, the wall shear stress can be determined by using the formula for the wall shear stress for flow between parallel plates, i.e.

$$\tau_w = \frac{6\mu v_{\text{avg}}}{B}\,, \tag{2.131}$$

where v_{avg} is the average velocity and B is the distance between the plates. The average duct velocity in the streamwise direction is given by

$$w_{\parallel} = \frac{qd^2}{d_p^2}\,, \tag{2.132}$$

where the parameters correspond to those shown in Figure 2.9(a). The wall shear stresses for the RUC are therefore given by

$$\tau_{w_{\parallel}} = \tau_{w_{\perp_1}} = \tau_{w_{\perp_2}} = \frac{6\mu w_{\parallel}}{d_p}\,, \tag{2.133}$$

where $\tau_{w_{\perp_1}}$ and $\tau_{w_{\perp_2}}$ represent the wall shear stress for the two transverse ducts and are equal to $\tau_{w_{\parallel}}$ because isotropy is under consideration in the present chapter.

Substituting equation (2.132) into equation (2.133) therefore leads to

$$\tau_{w_{\parallel}} = \tau_{w_{\perp_1}} = \tau_{w_{\perp_2}} = \frac{6\mu q d^2}{d_p^3}\,. \tag{2.134}$$

The solid surfaces parallel and perpendicular to the streamwise direction are furthermore given by

$$S_{\parallel} = S_{\perp_1} = S_{\perp_2} = 4 d_s d_p\,, \tag{2.135}$$

and the cross-sectional area in the streamwise direction is

$$A_{p_{\parallel}} = d_p^2\,. \tag{2.136}$$

The pressure drop can therefore be obtained by substituting equations (2.134), (2.135) and (2.136) into equation (2.130), which leads to

$$\Delta p = \frac{72 d_s d^2}{d_p^4}\mu q\,, \tag{2.137}$$

where three ducts were taken into account, corresponding to the three duct sections of the three-strut RUC model. The pressure gradient is then given by

$$\frac{\Delta p}{L} = \frac{\Delta p}{d} = \frac{72 d_s d}{d_p^4}\mu q\,. \tag{2.138}$$

Using the definitions for the geometric factor and the porosity given by equations (2.74) and (2.75), respectively, and substituting into it the expressions for the parameters U_o, $U_\parallel$ and U_t given by equations (2.76), (2.80) and (2.83), leads to the following equation for the porosity-geometric factor ratio:

$$\frac{\epsilon}{\psi} = \frac{d_p^2}{d^2}\,. \tag{2.139}$$

Equations (2.139), (2.85) and (2.86) can furthermore be expressed as

$$d_p^2 = \frac{\epsilon}{\psi} d^2\,, \tag{2.140}$$

$$d_s = \frac{d(\psi - 1)}{2}\,, \tag{2.141}$$

and

$$d = \frac{2 d_p}{3 - \psi}\,, \tag{2.142}$$

respectively.

Substituting equations (2.140), (2.141) and (2.142) into equation (2.138) then leads to the low Reynolds number term in the Ergun-type equation for foams, i.e.

$$\frac{\Delta p}{L} = \frac{9\psi^2(\psi - 1)(3 - \psi)^2}{\epsilon^2 d_p^2} \mu q\,. \tag{2.143}$$

In the higher Reynolds number limit, that is for the steady laminar limit of the inertial flow regime, form drag predominates over viscous drag, so the shear stress term is negligible. Thus equation (2.128) simplifies to (Woudberg [56])

$$-\nabla \langle p \rangle = \frac{1}{U_o} \iint_{S_{\text{fs}}} \underline{n} p \, \mathrm{d}S\,, \tag{2.144}$$

which can be expressed as

$$-\nabla \langle p \rangle = \frac{S_{\text{face}}}{U_o} \Delta p \, \underline{\hat{n}}\,, \tag{2.145}$$

where S_{face} is the cross-sectional solid area that faces upstream.

The pressure drop Δp can be obtained by dividing the total drag force on a single submerged body by the projected cross-sectional area of the body, i.e. (Woudberg [56])

$$\Delta p = c_d \frac{\rho \, v_\infty^2}{2} \tag{2.146}$$

where v_∞ is the approaching velocity, and c_d is the interstitial form drag coefficient with a value of $c_d = 2$ (Woudberg and Du Plessis [1]). The interstitial form drag coefficient is an empirical value determined for flow past a single square rod and is used for the foam RUC model. Substitution of equation (2.146) into equation (2.145), along with the assumption that the approaching velocity is equal to the streamwise average duct velocity (Woudberg [56]), leads to

$$-\nabla \langle p \rangle = \frac{S_{\text{face}}}{U_o} \rho \, w_\parallel^2 \, \underline{\hat{n}}\,, \tag{2.147}$$

and the streamwise pressure gradient is accordingly given by

$$-\nabla \langle p \rangle_f = \frac{S_{\text{face}}}{\epsilon U_o} \rho \, w_\parallel^2 \, \underline{\hat{n}}\,. \tag{2.148}$$

Substituting equation (2.139) into equation (2.132) and consequently substituting equation (2.132) into equation (2.148) leads to

$$-\nabla\langle p\rangle_f = \frac{S_{\text{face}}\psi^2}{\epsilon^3 U_o}\,\rho\, q^2\,\underline{\hat{n}}\,. \tag{2.149}$$

The cell volume can be deduced as

$$U_o = \frac{8d_p^3}{(3-\psi)^3}\,, \tag{2.150}$$

by substituting equation (2.142) into (2.76) for the cell volume and the cross-sectional area of solid that faces upstream is furthermore given by

$$S_{\text{face}} = 2d_p d_s\,. \tag{2.151}$$

Substituting equations (2.141) and (2.142) into equation (2.151) leads to

$$S_{\text{face}} = \frac{2d_p^2(\psi-1)}{(3-\psi)}\,, \tag{2.152}$$

which is S_{face} in terms of the pore diameter. Substituting equations (2.150) and (2.152) into equation (2.149) then yields

$$-\nabla\langle p\rangle_f = \frac{\psi^2(\psi-1)(3-\psi)^2}{4\epsilon^3 d_p}\rho q^2\underline{\hat{n}}\,, \tag{2.153}$$

which is the higher Reynolds number term in the Ergun-type equation for foams.

Therefore the total expression for the pressure gradient is:

$$\frac{\Delta p}{L} = \frac{9\psi^2(\psi-1)(3-\psi)^2}{\epsilon^2 d_p^2}\,\mu q + \frac{\psi^2(\psi-1)(3-\psi)^2}{4\epsilon^3 d_p}\,\rho q^2\,, \tag{2.154}$$

where ψ is given by equation (2.88).

Comparing equation (1.11) with equation (2.154), the following expressions for K and K_F can thus be obtained:

$$K = \frac{\epsilon^2 d_p^2}{9\psi^2(\psi-1)(3-\psi)^2}\,, \tag{2.155}$$

and

$$K_F = \frac{4\epsilon^3 d_p}{\psi^2(\psi-1)(3-\psi)^2}\,. \tag{2.156}$$

The pore diameter can furthermore be defined in two ways. The first option utilizes the hydraulic diameter in equation (1.6), as in the Dietrich formulation, and approximates the flow through the RUC as flow through a square duct. It can therefore easily be determined, by making use of equation (1.4), that $D_h = d_p$, and that $d_p = 4\epsilon/S_v$ accordingly, which, when substituted into equation (2.155), leads to S_v in terms of K, i.e.

$$S_v = \frac{4\epsilon^2}{3\psi(3-\psi)\sqrt{K(\psi-1)}}\,. \tag{2.157}$$

Similarly, S_v in terms of K_F can be determined by substituting $d_p = 4\epsilon/S_v$ into equation (2.156), leading to

$$S_v = \frac{16\epsilon^4}{\psi^2(\psi-1)(3-\psi)^2 K_F}\,. \tag{2.158}$$

In the second option d_p is used, given by equation (1.9), as in the Huu formulation, and substituting it into equation (2.155) yields

$$S_v = \frac{2\epsilon(1-\epsilon)}{\psi(3-\psi)\sqrt{K(\psi-1)}}\,, \tag{2.159}$$

which is S_v in terms of K. Substituting equation (1.9) into equation (2.156) furthermore leads to

$$S_v = \frac{24\epsilon^3(1-\epsilon)}{\psi^2(\psi-1)(3-\psi)^2 K_F}\,, \tag{2.160}$$

which is S_v in terms of K_F.

Two-strut RUC model

Similarly as in the case of the three-strut RUC model formulation, the derivation of the two-strut RUC model formulation starts with equation (2.130) for the low Reynolds number limit. Plane Poiseuille flow is still applicable and the formula for the wall shear stress given by equation (2.131) is again applicable. The average duct velocity for the two-strut RUC model in the streamwise direction is also given by equation (2.132), but the average duct velocity in the transverse direction of the two-strut RUC model is given by

$$w_\perp = \frac{qd}{d_p}\,. \tag{2.161}$$

The wall shear stresses are therefore given by

$$\tau_{w_\parallel} = \frac{6\mu w_\parallel}{d_p} = \frac{6\mu q d^2}{d_p^3}\,, \tag{2.162}$$

and

$$\tau_{w_\perp} = \frac{6\mu w_\perp}{d_p} = \frac{6\mu q d}{d_p^2}\,, \tag{2.163}$$

which differs from that of the three-strut RUC model for which all the wall shear stresses were equal, because the two-strut RUC model is anisotropic (although it is noted that this chapter is devoted to isotropic models).

The solid surfaces parallel to the streamwise direction are given by

$$S_\parallel = 4 d_s d_p\,, \tag{2.164}$$

as in the case of the three-strut model, but the solid surfaces perpendicular to the streamwise direction are given by

$$S_\perp = 4 d_s d_p + 2 d_s^2\,. \tag{2.165}$$

The cross-sectional area in the streamwise direction is the same as in equation (2.136). The pressure drop can therefore be obtained by substituting equations (2.136), (2.162) to (2.164) and (2.165) into equation (2.130), leading to

$$\Delta p = \frac{12 d_s d(4d - d_s)}{d_p^4}\mu q\,, \tag{2.166}$$

and consequently the pressure gradient is given by

$$\frac{\Delta p}{L} = \frac{\Delta p}{d} = \frac{12 d_s (4d - d_s)}{d_p^4}\mu q\,. \tag{2.167}$$

Equations (2.105) and (2.106) can be used to express d and d_s in terms of d_p as follows:

$$d = \frac{\psi d_p}{\epsilon}\,, \tag{2.168}$$

and

$$d_s = d_p\left(\frac{\psi}{\epsilon} - 1\right)\,. \tag{2.169}$$

By substituting equations (2.168) and (2.169) into equation (2.167), the low Reynolds number term in the Ergun-type equation can be determined, given by

$$\frac{\Delta p}{d} = \frac{12(\psi-\epsilon)(3\psi+\epsilon)}{\epsilon^2 d_p^2}\mu q\,. \tag{2.170}$$

In the case of the high Reynolds number limit, equation (2.148) will be used. Substituting equation (2.168) into equation (2.162) leads to the average duct velocity parallel to the streamwise flow, i.e.

$$w_{\parallel} = \frac{\psi^2}{\epsilon^2} q\,. \tag{2.171}$$

The solid cross-sectional area that faces upstream is also given by equation (2.151) and substituting equation (2.169) for d_s into equation (2.151) leads to S_{face} in terms of d_p, i.e.

$$S_{\text{face}} = 2d_p^2\left(\frac{\psi}{\epsilon} - 1\right)\,. \tag{2.172}$$

An expression for the cell volume can furthermore be obtained by substituting equation (2.168) into equation (2.76) and results in

$$U_o = \frac{\psi^3 d_p^3}{\epsilon^3}\,. \tag{2.173}$$

Substituting equations (2.171), (2.172) and (2.173) into equation (2.148) then finally leads to

$$-\nabla\langle p\rangle_f = \frac{2\psi(\psi-\epsilon)}{\epsilon^3 d_p}\rho q^2\,\underline{\hat{n}}\,, \tag{2.174}$$

which is the higher Reynolds number term in the Ergun-type equation. The total equation for the pressure gradient is therefore:

$$\frac{\Delta p}{L} = \frac{12(\psi-\epsilon)(3\psi+\epsilon)}{\epsilon^2 d_p^2}\mu q + \frac{2\psi(\psi-\epsilon)}{\epsilon^3 d_p}\rho q^2\,, \tag{2.175}$$

where ψ is given by equation (2.108).

Comparing equation (1.11) with equation (2.175), the following expressions for the permeability coefficients K and K_F are therefore obtained:

$$K = \frac{\epsilon^2 d_p^2}{12(\psi-\epsilon)(3\psi+\epsilon)}\,, \tag{2.176}$$

and

$$K_F = \frac{\epsilon^3 d_p}{2\psi(\psi-\epsilon)}\,. \tag{2.177}$$

The pore diameter can once again be defined in two different ways, either by using equation (1.6) or equation (1.9). The former equation leads to the specific surface area in terms of K and K_F, given by

$$S_v = \frac{2\epsilon^2}{\sqrt{3(\psi-\epsilon)(3\psi+\epsilon)K}}\,, \tag{2.178}$$

and

$$S_v = \frac{2\epsilon^4}{\psi(\psi-\epsilon)K_F}\,, \tag{2.179}$$

respectively.

Using equation (1.9), leads to the following specific surface area in terms of K

$$S_v = \frac{3\epsilon(1-\epsilon)}{\sqrt{3(\psi-\epsilon)(3\psi+\epsilon)K}}\,, \tag{2.180}$$

and in terms of K_F

$$S_v = \frac{3\epsilon^3(1-\epsilon)}{\psi(\psi-\epsilon)K_F}\,. \tag{2.181}$$

The kinetic approach formulations will now be evaluated by using data obtained from the literature.

2.2.4 Comparison of kinetic approaches

In order to evaluate the equations for S_v obtained from the Dietrich, Huu and RUC formulations, four sets of experimental data for K and K_F are considered. The two-strut RUC formulation was not considered for evaluation because the four experimental data sets are for foams only. The first two sets of experimental data, i.e. from Richardson et al. [4] and from Liu et al. [5], do not include experimental data for the specific surface area for comparison.

The method of Richardson et al. [4] was previously used to determine one of the approaches for determining the specific surface area using a geometric tetrakaidecahedron model. They also used image analysis to find the pore diameters of ceramic foams and calculated the porosities from the strut density and the foam apparent density. The strut density was measured using a He multipycnometer and the foam apparent density was measured using the volume of the foam, as mentioned in Chapter 1. They measured the pressure drop at different superficial air velocities and used the data from this experiment to obtain values for the two permeability coefficients.

Liu et al. [5] performed experiments on several samples of aluminium foams and obtained pressure drop measurements from which they determined frictional characteristics of the metal foams. Porosity measurements provided by the manufacturers of the foams were used. They furthermore used image analyses to determine the pore diameters and pressure drop measurements at different superficial velocities to determine the two permeability coefficients. The data sets of Richardson et al. [4] and Liu et al. [5] are presented in Table 2.2.

In the study of Richardson et al. [4], a_0 and a_1 are defined as shown in the following version of the Darcy-Forchheimer equation:

$$\frac{\Delta p}{L} = a_0 q + a_1 q^2\,. \tag{2.182}$$

Comparing equation (2.182) to equation (1.11), it can be deduced that

$$K = \frac{\mu}{a_0} \tag{2.183}$$

and

$$K_F = \frac{\rho}{a_1}\,, \tag{2.184}$$

where the physical properties of air as the working fluid is given by $\mu = 1.826 \times 10^{-4}\,\mathrm{kg.m^{-1}.s^{-1}}$ and $\rho = 1.161\,\mathrm{kg.m^{-3}}$.

TABLE 2.2: *Experimental data from the literature to determine K and K_F in the kinetic and combined approaches*

Richardson et al. [4] (ceramic-based foams)			
ϵ	d_p[mm]	a_0[Pa.s.m^{-2}]	a_1[Pa.s^{2}m^{-3}]
0.878	1.68	949	128
0.874	0.826	3790	651
0.802	0.619	4610	1070
0.857	0.359	7630	2050
Liu et al. [5] (aluminium foams)			
ϵ	d_p[mm]	$K \times 10^7$[m^2]	$F \times 10^2$[$-$]
0.914	1.208	3.7	9.98
0.918	1.190	6.23	18.2
0.870	0.827	1.25	9.93
0.909	0.805	1.02	7.38
0.935	0.814	2.42	13.0
0.958	0.800	14.2	34.0
0.935	0.685	1.33	10.3

In the data of Liu et al. [5], K represents the permeability and F is an inertia coefficient. Similarly, K and F are defined by the following version of the Darcy-Forchheimer equation,

$$\frac{\Delta p}{L} = \frac{\mu}{K}\, q + \frac{F}{\sqrt{K}}\, \rho q^2 \,, \tag{2.185}$$

which, when compared to equation (1.11), yields the following expressions for K and K_F:

$$K = K \tag{2.186}$$

and

$$K_F = \frac{\sqrt{K}}{F} \,. \tag{2.187}$$

The experimental values obtained for K and K_F using the data of Richardson et al. [4] and Liu et al. [5] can therefore be used to calculate the specific surface area at the measured porosities.

In Table 2.2 the experimental values for d_p at each porosity are also listed. These values of d_p are used to multiply with the calculated specific surface area so that a dimensionless specific surface area can be plotted against the porosity values. In Figure 2.15 the data of Richardson et al. [4] for K and K_F are used to determine the specific surface areas as specified by equations (2.121), (2.122), (2.126), (2.127), (2.157), (2.158), (2.159) and (2.160), and in Figure 2.16 the corresponding data of Liu et al. [5] was used. Figure 2.15 shows the equation numbers corresponding to the approach used but, due to these equation numbers remaining the same over the series of utilized data sets, the equation numbers are omitted in Figures 2.16, 2.17 and 2.18.

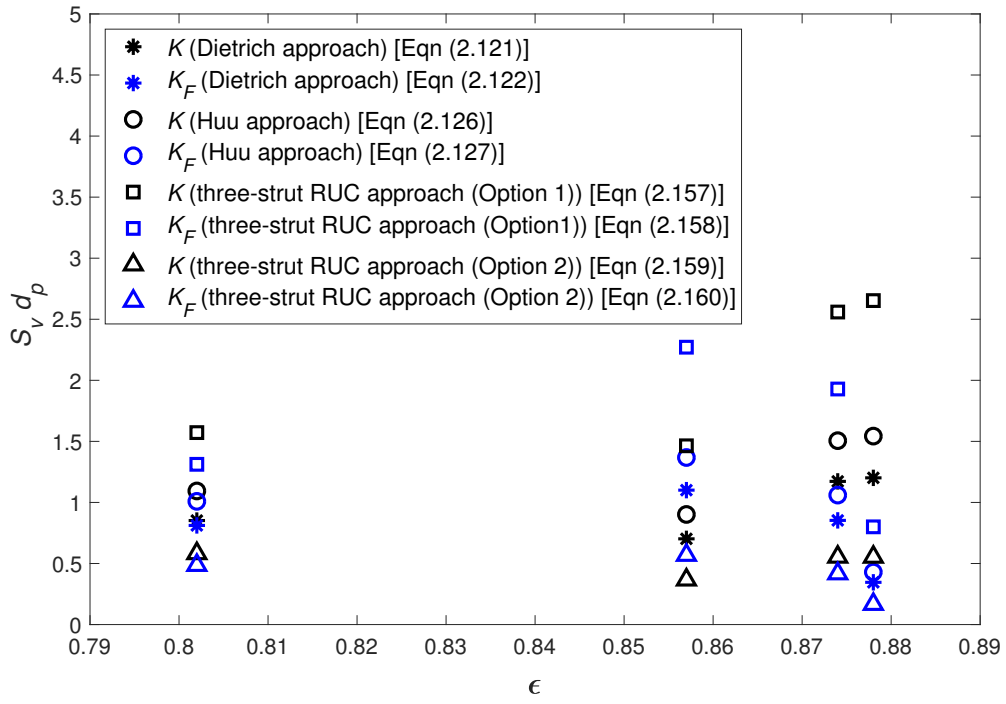

FIGURE 2.15: *Dimensionless specific surface area calculated from the Richardson et al. [4] data using the Dietrich, Huu and three-strut RUC formulations*

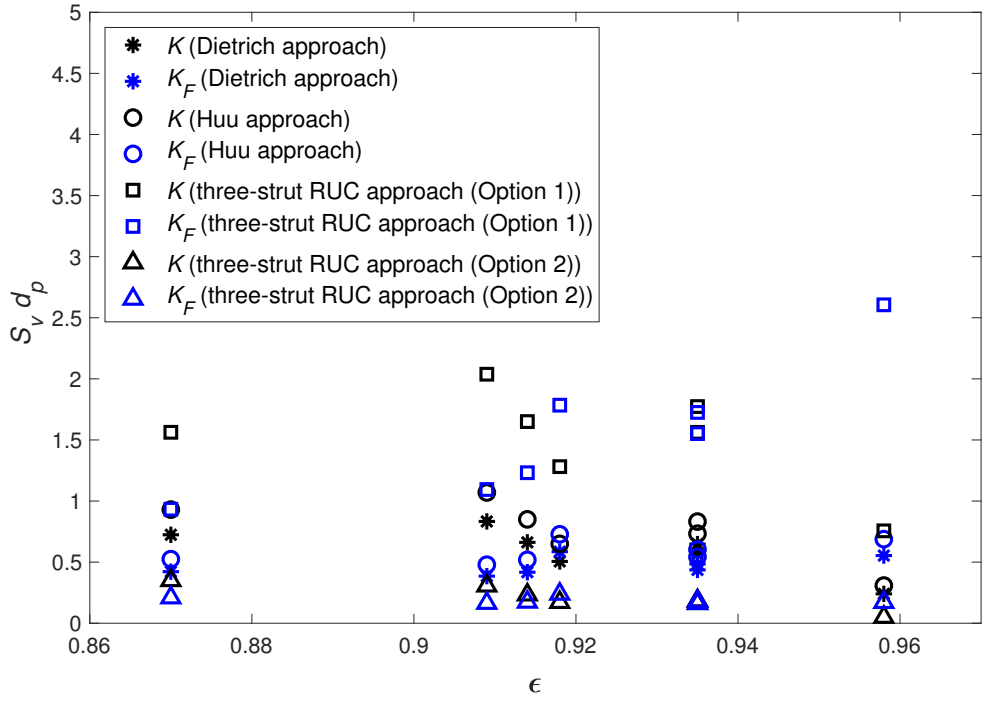

FIGURE 2.16: *Dimensionless specific surface area calculated from the Liu et al. [5] data using the Dietrich, Huu and three-strut RUC formulations*

When evaluating the specific surface area results obtained from the three approaches in Figures 2.15 and 2.16, it is evident that the majority of the predicted values range between 0 and 2.5, as expected considering the results obtained from the geometric approach as shown in Figure 2.11. In both Figures 2.15 and 2.16 it can be observed that the formulation that gives the lowest predicted specific surface area values is the RUC approach using the second option for defining d_p and the formulation that gives the highest values is the RUC approach using the first option for defining d_p. The two RUC model predictions can thus be regarded as upper and lower bounds between which the model predictions from the other formulations are enclosed.

Two data sets that include experimental data for the specific surface area for comparison with the kinetic approaches will be considered next.

Comparison to experimental data

The two data sets that include experimental data for the specific surface area are the data sets given by Dietrich et al. [2] and Garrido et al. [3]. In order to compare the kinetic approaches with experimental data, the data for the permeability values from Dietrich et al. [2] and Garrido et al. [3] were used as given in Table 2.1, as well as the experimental values for the specific surface area for the given measured porosities. The results obtained are shown in Figures 2.17 and 2.18, using the Dietrich et al. [2] and Garrido et al. [3] data, respectively, where the $S_v d_p$ values for the different formulations are plotted similarly to when the Richardson et al. [4] and Liu et al. [5] data were used.

The most accurate formulation in comparison to the experimental data in Figure 2.17 for the specific surface area in terms of K was the Dietrich formulation with an average percentage difference of 22%, followed by the RUC Option 2 formulation with a 33% average difference. For the specific surface area in terms of K_F, the Dietrich formulation once again provided the most accurate prediction (11% average difference) followed by the Huu formulation (32% average difference).

In Figure 2.18 the formulation with the smallest average percentage difference when compared to the experimental data for the specific surface area in terms of K was the RUC Option 2 formulation (38% average difference) followed by the Dietrich formulation (120% average difference). In the case where the specific surface area is in terms of K_F, the Huu and RUC Option 1 formulations provided the most accurate predictions with an average percentage difference of 20%.

From these results it can be deduced that the specific surface area values determined using K_F performed better than those obtained using K when compared to the Dietrich et al. [2] and Garrido et al. [3] data sets. Comparison of each of the formulation performances, for the specific surface areas determined using K as well as K_F, was then done by taking the average of all the average percentage differences of each formulation. This percentage difference obtained for the Dietrich formulation was 47%, for the Huu formulation it was 68%, for the RUC Option 1 formulation it was 127% and for the RUC Option 2 formulation it was 43%. In conclusion, the formulation that was therefore overall the most accurate, compared to these sets of experimental data, was the RUC Option 2 formulation and the formulation that was the least accurate was the RUC Option 1 formulation. The RUC Option 1 formulation makes use of the hydraulic diameter-specific surface area relationship as given by equation (1.6) and furthermore does not give the expected specific surface area versus porosity trend, as mentioned in Chapter 1 and illustrated in Figure 1.5. The use of equation (1.6) in the RUC Option 1 formulation may therefore be the reason for it giving the least accurate results.

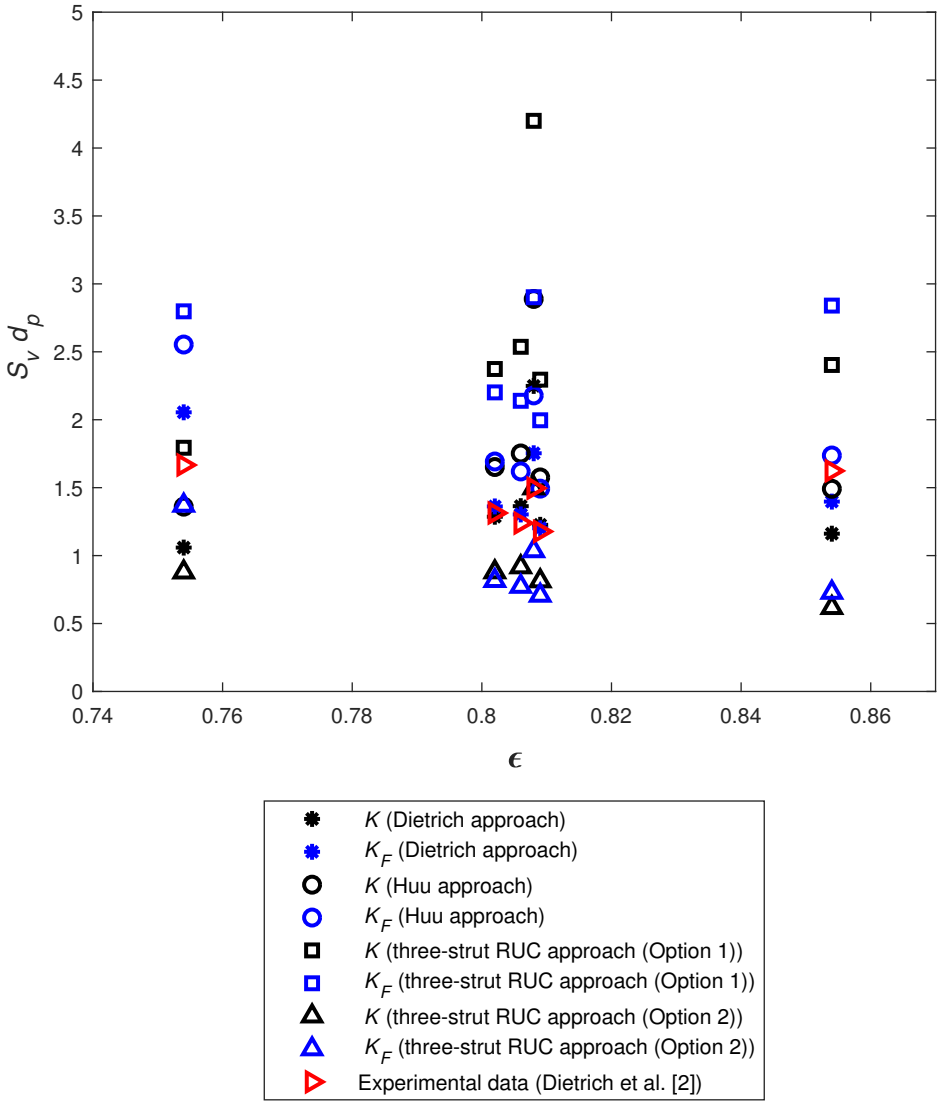

FIGURE 2.17: *Dimensionless specific surface area calculated from the Dietrich et al. [2] data using the Dietrich, Huu and three-strut RUC formulations*

In the next section an approach that combines the geometric and kinetic approaches will be investigated in order to determine the specific surface area.

2.3 Specific surface area: Combined approach

The Dietrich and RUC option 1 formulations of the kinetic approach both utilized the hydraulic diameter-specific surface area equation, equation (1.6). This relationship does not, however, predict the expected trend, as previously mentioned. In the Huu and RUC option 2 formulations of the kinetic approach equation (1.9) was utilized, but equation (1.9) was based on porous media consisting of spherical particles and not fibrous media. A combined approach is therefore

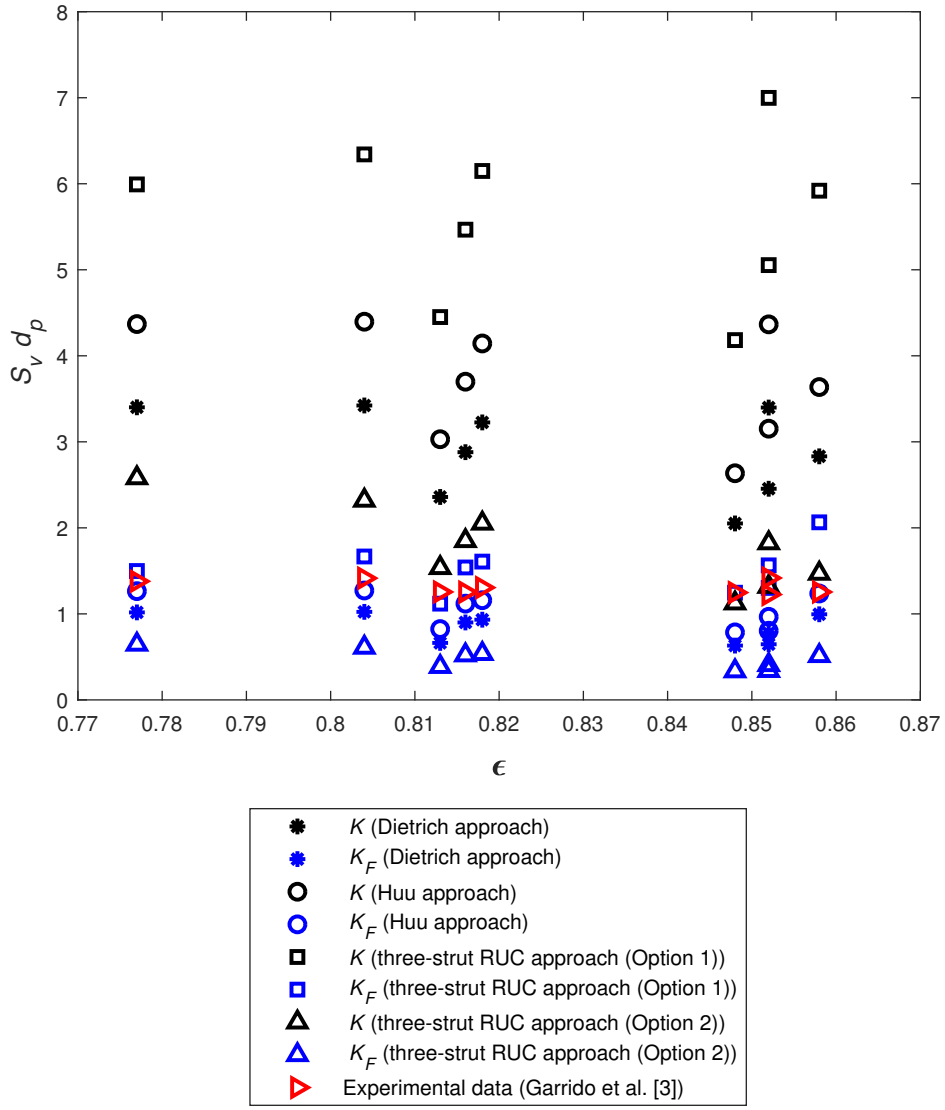

FIGURE 2.18: *Dimensionless specific surface area calculated from the Garrido et al. [3] data using the Dietrich, Huu and three-strut RUC formulations*

considered in which the pore diameter-specific surface area relationships based on the morphology of the specific fibrous porous medium is utilized. Consequently, in order to determine the specific surface area values using a combined approach, both the geometric and kinetic approaches are employed. In the kinetic approach equations (1.6) and (1.9), for D_h and d_p respectively, were used to obtain specific surface area equations in terms of the permeability coefficients. The combined approach makes use of the specific surface area equations in terms of only d_p obtained using the geometric approach. The two combined approaches considered in this study are the combined Huu formulation and the combined RUC formulation. The combined Huu formulation combines the kinetic Huu formulation outlined in Section 2.2.2 and the dodecahedron model presented in Section 2.1.3. The combined RUC formulation combines the kinetic RUC formulation outlined in Section 2.2.3 and the RUC models presented in Section 2.1.4.

The combined Huu formulation will be discussed first.

2.3.1 Combined Huu formulation

The results obtained from the combined Huu formulation are acquired by making use of the Ergun equation defined in terms of d_p, i.e. equation (2.123), or more specifically, the permeability coefficient equations (2.124) and (2.125) obtained from the Ergun equation. Next, d_p needs to be determined in terms of S_v. In this formulation, the dodecahedron model is used for this purpose. The pore diameter d_p can be determined by using any one of the four specific surface area equations presented for the dodecahedron model, i.e. equations (2.57), (2.65), (2.72) or (2.73), depending on the porosity range under consideration. The specific surface area equations (2.57) and (2.72) involving triangular strut geometry are used for high porosities (where $\epsilon > 0.9$) and the specific surface area equations involving cylindrical strut geometry are used for lower porosities (where $\epsilon < 0.9$). The resulting expressions for the specific surface area in terms of the permeability coefficients and porosity can therefore be categorized under the four dodecahedron model types as follows:

Triangular "slim" strut geometry

The specific surface area for the triangular "slim" strut geometry given by equation (2.57) can be used to obtain the following equation for d_p in terms of S_v:

$$d_p = \frac{60k}{\sqrt{5}\,\phi^3\sqrt{3-\phi}\,S_v}\left(1-\frac{1}{2}\sqrt{\frac{2}{3}}\,k\right)^2, \tag{2.188}$$

where k can be solved from equation (2.50).

Substituting equation (2.188) into equations (2.124) and (2.125) for K and K_F, respectively, where $E_1 = 150$ and $E_2 = 1.75$, leads to

$$S_v = \sqrt{\frac{\epsilon^3}{150(1-\epsilon)^2K}}\,\frac{60k}{\sqrt{5}\,\phi^3\sqrt{3-\phi}}\left(1-\frac{1}{2}\sqrt{\frac{2}{3}}\,k\right)^2, \tag{2.189}$$

and

$$S_v = \frac{\epsilon^3}{1.75(1-\epsilon)K_F}\,\frac{60k}{\sqrt{5}\,\phi^3\sqrt{3-\phi}}\left(1-\frac{1}{2}\sqrt{\frac{2}{3}}\,k\right)^2. \tag{2.190}$$

Equations (2.189) and (2.190) represent the specific surface area in terms of K and K_F, respectively.

Cylindrical "slim" strut geometry

The pore diameter for the cylindrical "slim" strut geometry is obtained from equation (2.65) and results in

$$d_p = \frac{20\,\pi\,k}{\sqrt{5}\,\phi^3\sqrt{3-\phi}\,S_v}\left(1-\frac{1}{2}\sqrt{\frac{2}{3}}\,k\right)^2. \tag{2.191}$$

Equation (2.191) can then in turn be substituted into equations (2.124) and (2.125) and consequently the specific surface area equations in terms of K and K_F, given by

$$S_v = \sqrt{\frac{\epsilon^3}{150(1-\epsilon)^2 K}}\,\frac{20\,\pi\,k}{\sqrt{5}\,\phi^3\sqrt{3-\phi}}\left(1-\frac{1}{2}\sqrt{\frac{2}{3}}\,k\right)^2, \tag{2.192}$$

and

$$S_v = \frac{\epsilon^3}{1.75(1-\epsilon)K_F}\,\frac{20\,\pi\,k}{\sqrt{5}\,\phi^3\sqrt{3-\phi}}\left(1-\frac{1}{2}\sqrt{\frac{2}{3}}\,k\right)^2, \tag{2.193}$$

respectively, can be obtained where k can be solved from equation (2.61).

Triangular "fat" strut geometry

In order to obtain d_p using the triangular "fat" dodecahedron model, equation (2.72) is used and leads to

$$d_p = \frac{60\,k}{\sqrt{5}\,\phi^3\sqrt{3-\phi}\,Sv}\left(1-\frac{1}{2}\sqrt{\frac{2}{3}}\,k\right)^2 + \frac{\left(1-\frac{1}{2}\sqrt{\frac{2}{3}}\,k\right)}{\phi\sqrt{3-\phi}}\left[\frac{12\,\pi\,k\,\left(1-\frac{1}{2}\sqrt{\frac{2}{3}}\,k\right)}{\sqrt{5}\,\phi\sqrt{3-\phi}\,S_v} + \frac{\sqrt{15}\,\sin^2\left(\frac{\pi}{5}\right)\left(1-\frac{1}{2}\sqrt{\frac{2}{3}}\,k\right)^2}{2\,(3-\phi)\,S_v}\right]. \tag{2.194}$$

Substituting equation (2.194) into equation (2.124) results in

$$S_v = \sqrt{\frac{\epsilon^3}{150(1-\epsilon)^2 K}}\left[\frac{60\,k}{\sqrt{5}\,\phi^3\sqrt{3-\phi}}\left(1-\frac{1}{2}\sqrt{\frac{2}{3}}\,k\right)^2 + \frac{\left(1-\frac{1}{2}\sqrt{\frac{2}{3}}\,k\right)}{\phi\sqrt{3-\phi}}\left[\frac{12\,\pi\,k\,\left(1-\frac{1}{2}\sqrt{\frac{2}{3}}\,k\right)}{\sqrt{5}\,\phi\sqrt{3-\phi}} + \frac{\sqrt{15}\,\sin^2\left(\frac{\pi}{5}\right)\left(1-\frac{1}{2}\sqrt{\frac{2}{3}}\,k\right)^2}{2\,(3-\phi)}\right]\right], \tag{2.195}$$

which is the specific surface area in terms of K and the porosity.

Similarly, substituting equation (2.194) into equation (2.125) leads to the specific surface area equation in terms of K_F and the porosity, i.e.

$$S_v = \frac{\epsilon^3}{1.75(1-\epsilon)K_F}\left[\frac{60\,k}{\sqrt{5}\,\phi^3\sqrt{3-\phi}}\left(1-\frac{1}{2}\sqrt{\frac{2}{3}}\,k\right)^2 + \frac{\left(1-\frac{1}{2}\sqrt{\frac{2}{3}}\,k\right)}{\phi\sqrt{3-\phi}}\left[\frac{12\,\pi\,k\,\left(1-\frac{1}{2}\sqrt{\frac{2}{3}}\,k\right)}{\sqrt{5}\,\phi\sqrt{3-\phi}} + \frac{\sqrt{15}\,\sin^2\left(\frac{\pi}{5}\right)\left(1-\frac{1}{2}\sqrt{\frac{2}{3}}\,k\right)^2}{2\,(3-\phi)}\right]\right]. \tag{2.196}$$

In both equations (2.195) and (2.196), k can be solved from equation (2.67).

Cylindrical "fat" strut geometry

Finally, d_p in terms of S_v for the cylindrical "fat" dodecahedron model can be determined from equation (2.73), resulting in

$$d_p = \frac{20\,\pi\,k}{\sqrt{5}\,\phi^3\sqrt{3-\phi}\,S_v}\left(1-\frac{1}{2}\sqrt{\frac{2}{3}}\,k\right)^2+\frac{\left(1-\frac{1}{2}\sqrt{\frac{2}{3}}\,k\right)}{\phi\,\sqrt{3-\phi}}\left[\frac{12\,\pi\,k\,\left(1-\frac{1}{2}\sqrt{\frac{2}{3}}\,k\right)}{\sqrt{5}\,\phi\,\sqrt{3-\phi}\,S_v}+\frac{\sqrt{15}\,\sin^2\left(\frac{\pi}{5}\right)\,\left(1-\frac{1}{2}\sqrt{\frac{2}{3}}\,k\right)^2}{2\,(3-\phi)\,S_v}\right]. \tag{2.197}$$

The specific surface area equations in terms of K and K_F can then be determined by substituting equation (2.197) into equations (2.124) and (2.125), respectively, leading to

$$S_v = \sqrt{\frac{\epsilon^3}{150(1-\epsilon)^2K}}\left[\frac{20\,\pi\,k}{\sqrt{5}\,\phi^3\sqrt{3-\phi}}\left(1-\frac{1}{2}\sqrt{\frac{2}{3}}\,k\right)^2+\frac{\left(1-\frac{1}{2}\sqrt{\frac{2}{3}}\,k\right)}{\phi\,\sqrt{3-\phi}}\left[\frac{12\,\pi\,k\,\left(1-\frac{1}{2}\sqrt{\frac{2}{3}}\,k\right)}{\sqrt{5}\,\phi\,\sqrt{3-\phi}}+\frac{\sqrt{15}\,\sin^2\left(\frac{\pi}{5}\right)\,\left(1-\frac{1}{2}\sqrt{\frac{2}{3}}\,k\right)^2}{2\,(3-\phi)}\right]\right], \tag{2.198}$$

and

$$S_v = \frac{\epsilon^3}{1.75(1-\epsilon)K_F}\left[\frac{20\,\pi\,k}{\sqrt{5}\,\phi^3\sqrt{3-\phi}}\left(1-\frac{1}{2}\sqrt{\frac{2}{3}}\,k\right)^2+\frac{\left(1-\frac{1}{2}\sqrt{\frac{2}{3}}\,k\right)}{\phi\,\sqrt{3-\phi}}\left[\frac{12\,\pi\,k\,\left(1-\frac{1}{2}\sqrt{\frac{2}{3}}\,k\right)}{\sqrt{5}\,\phi\,\sqrt{3-\phi}}+\frac{\sqrt{15}\,\sin^2\left(\frac{\pi}{5}\right)\,\left(1-\frac{1}{2}\sqrt{\frac{2}{3}}\,k\right)^2}{2\,(3-\phi)}\right]\right], \tag{2.199}$$

where k can be solved from equation (2.69).

The combined RUC formulation will be discussed next.

2.3.2 Combined RUC formulation

A combined kinetic-geometric formulation determined using both the three-strut RUC model and the two-strut RUC model will be determined as follows:

Three-strut RUC model

In order to determine the specific surface area using the combined three-strut RUC formulation, the pore diameter equation in terms of the specific surface area is obtained from the geometric three-strut RUC model and the permeability coefficient equations used are determined from the kinetic RUC formulation derived from the three-strut RUC model. Equation (2.96) from the three-strut RUC model is therefore used to obtain the equation for d_p in terms of S_v, i.e.

$$d_p = \frac{3}{2\,S_v}(3-\psi)^2(\psi-1)\,. \tag{2.200}$$

Substituting equation (2.200) into equations (2.155) and (2.156) for K and K_F respectively, leads to

$$S_v = \frac{\epsilon(3-\psi)}{2\psi}\sqrt{\frac{\psi-1}{K}}\,, \tag{2.201}$$

and

$$S_v = \frac{6\epsilon^3}{\psi^2 K_F}\,. \tag{2.202}$$

Equations (2.201) and (2.202) are therefore expressions for the specific surface area in terms of K and K_F, respectively, where ψ is given by equation (2.88).

Two-strut RUC model

Similarly to the derivation of the combined RUC formulation using the three-strut RUC model, the derivation using the two-strut RUC model uses the pore diameter obtained from the geometric two-strut RUC model and the permeability coefficient equations presented in the two-strut kinetic RUC formulation. In this case equation (2.116) is used to obtain the equation for d_p in terms of S_v, i.e.

$$d_p = \frac{2\epsilon}{\psi^3 S_v}(\psi-\epsilon)(3\epsilon+\psi)\,. \tag{2.203}$$

Substituting equation (2.203) into equations (2.176) and (2.177) for K and K_F, respectively, leads to the specific surface area equations:

$$S_v = \frac{\epsilon^2(\psi-\epsilon)(3\epsilon+\psi)}{\psi^3\sqrt{3(\psi-\epsilon)(3\psi+\epsilon)K}}\,, \tag{2.204}$$

and

$$S_v = \frac{\epsilon^4(3\epsilon+\psi)}{\psi^4 K_F}\,, \tag{2.205}$$

where ψ is given by equation (2.108).

2.3.3 Comparison of combined approaches

The combined approach is evaluated similarly to the kinetic approach. The same four sets of experimental data will be used to evaluate the different combined approach formulations. The two-strut RUC model formulation is not included in the evaluation, once again, because all the data sets considered are for foams only. The two sets of experimental data for K and K_F, i.e. the Richardson et al. [4] and Liu et al. [5] data given in Table 2.2, are used to evaluate the different combined approach formulations without experimental data for the specific surface area for comparison. The results obtained from using the Richardson et al. [4] data are shown in Figure 2.19, where the cylindrical "slim" and "fat" dodecahedron models were used in the combined Huu formulation due to the porosity values being lower than 0.9. The results obtained using the Liu et al. [5] data are shown in Figure 2.20. For this set of experimental data, however, the triangular "slim" and "fat" dodecahedron models were used in the combined Huu formulation since the porosity values are greater than 0.9.

In both Figures 2.19 and 2.20 it can be observed that the values for the dimensionless specific surface area obtained using K_F generally predicts lower values than those obtained using K. It can also be seen that the approach that predicts the lowest values for both data sets is the three-strut RUC approach, and the highest predictions result from the Huu "fat" approach.

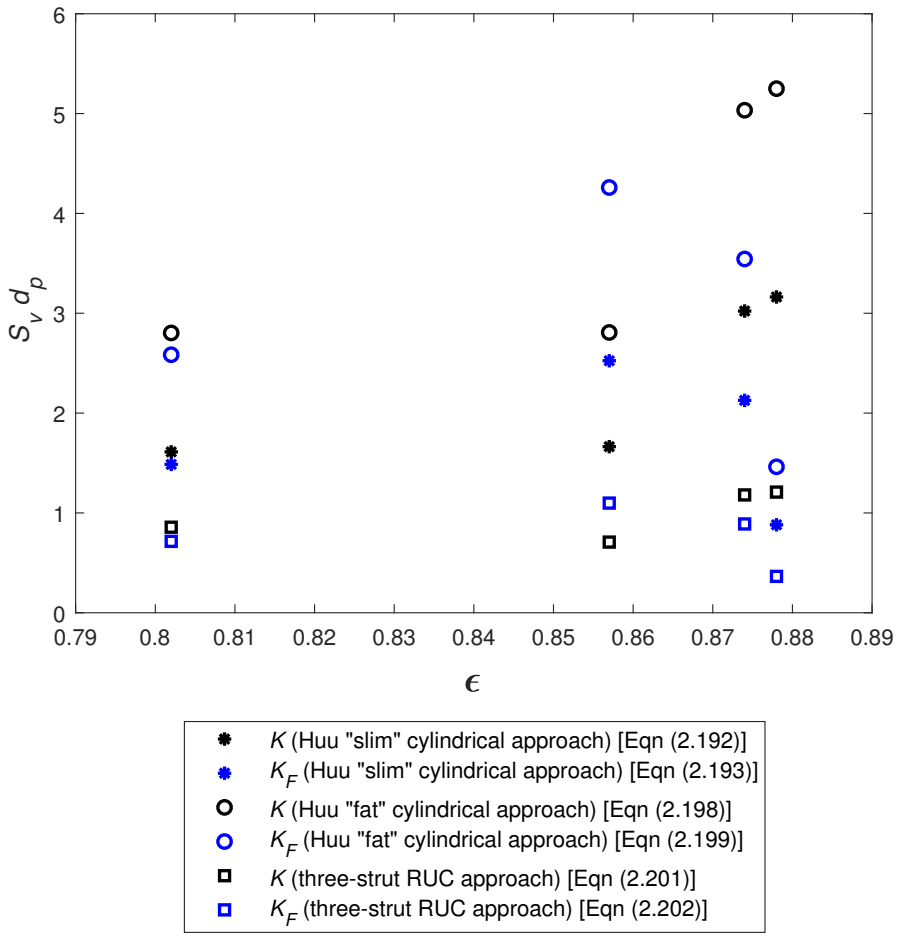

FIGURE 2.19: *Dimensionless specific surface area calculated from the Richardson et al. [4] data using the combined Huu and three-strut RUC formulations*

Comparison to experimental data

In order to compare the results obtained for the specific surface area using the combined approach with experimental data, the Dietrich et al. [2] and Garrido et al. [3] data, given in Table 2.1, is once again used. The $S_v d_p$-values obtained using the different combined approach formulations and the Dietrich et al. [2] data are shown in Figure 2.21, along with the experimental data for the dimensionless specific surface area. Similarly, the resulting values for $S_v d_p$ obtained using the Garrido et al. [3] data for K and K_F are shown in Figure 2.22. In both Figures 2.21 and 2.22, the cylindrical "slim" and "fat" dodecahedron models were used in the combined Huu formulation since the porosity values in these data sets are lower than 0.9.

The formulation that provides the most satisfactory correspondence with the Dietrich et al. [2] experimental data in Figure 2.21, is the three-strut RUC formulation, which gives an average percentage difference of 22% for the K approach and 7% for the K_F approach. The average percentage differences of the results obtained using the Huu formulation range between $90-100\%$ for the "slim" model approach and between $230-250\%$ for the "fat" model approach.

In Figure 2.22 the three-strut RUC formulation, on average considering both the K and K_F

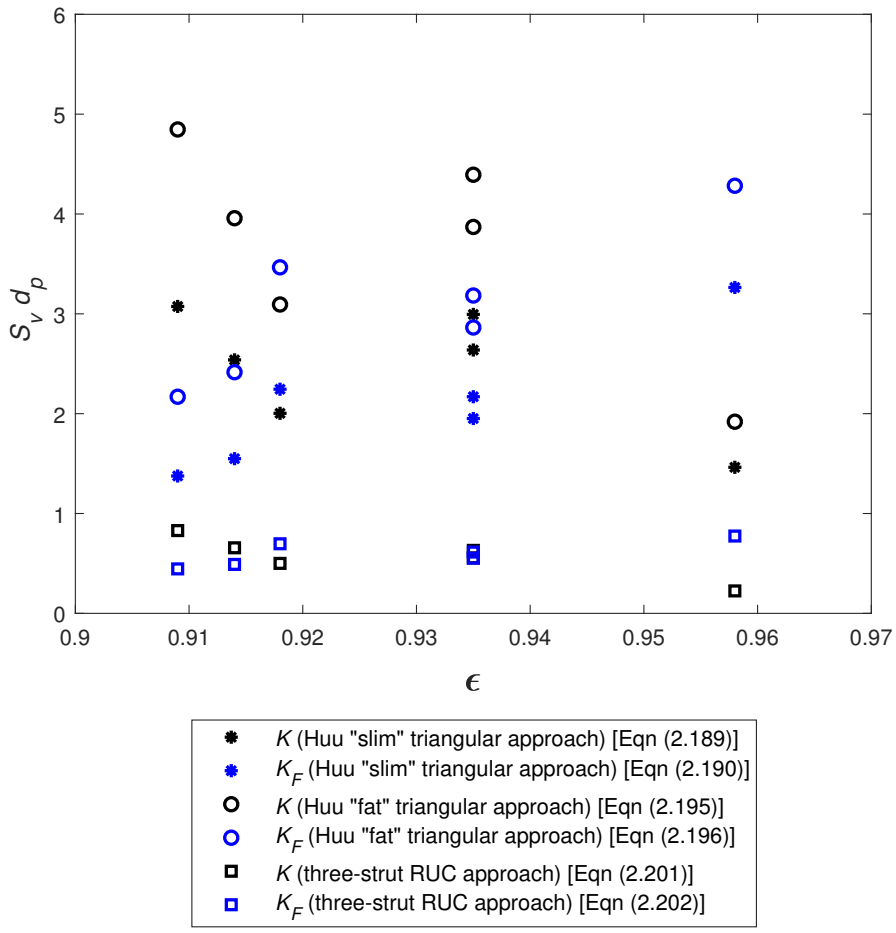

FIGURE 2.20: *Dimensionless specific surface area calculated from the Liu et al. [5] data using the combined Huu and three-strut RUC formulations*

approaches, provides the most accurate predictions when compared to the Garrido et al. [3] experimental data, with an average percentage difference of 81%.

2.4 Permeability: Predictions of RUC models

As already mentioned, the two-strut RUC model was included due to its geometry being a physically more realistic representation of the fibre morphology than the three-strut RUC model for fibre media that are formed by the stacking of different fibre layers into parallel planes. In this section the permeability predictions of both the RUC models will be evaluated and compared to an experimental data set involving glass fibres. Due to its more common occurrence in the literature, only the permeability coefficient of the Darcy regime, K, will be considered. The aim is to investigate whether the two-strut model provides more accurate permeability predictions than the three-strut model when concerning porous media with a fibre morphology.

The permeability equation for the three-strut RUC model is given by equation (2.155). This permeability equation is given in terms of the pore diameter d_p. Several data sets for fibres,

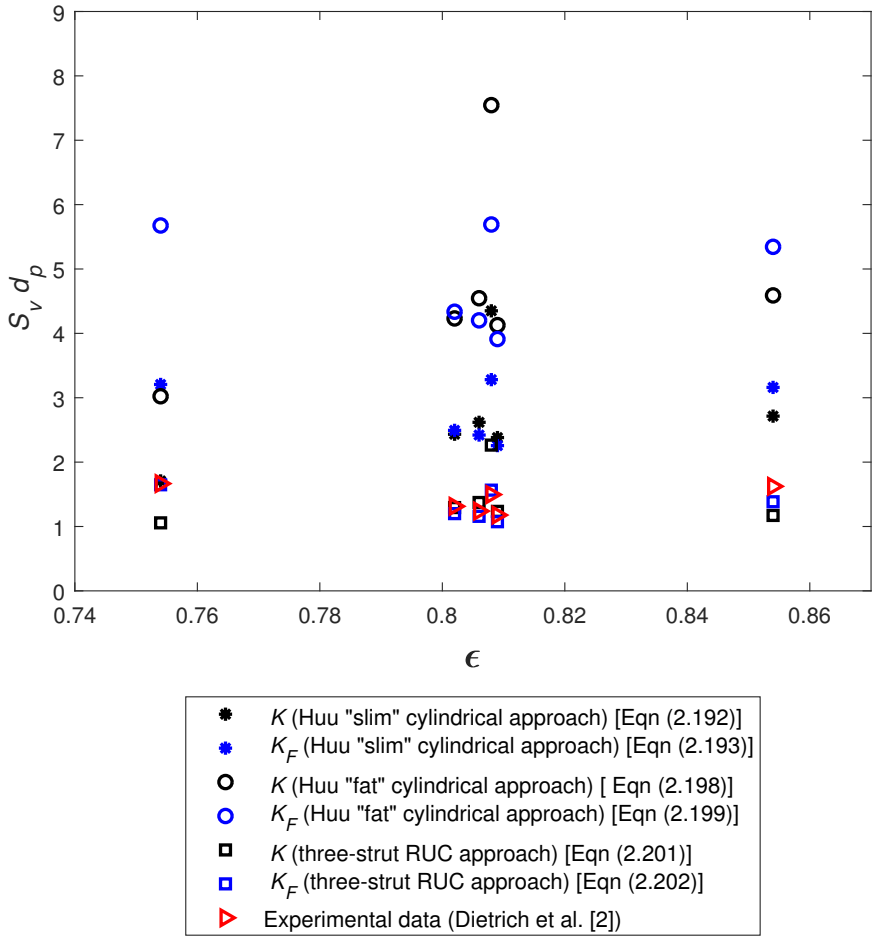

FIGURE 2.21: *Dimensionless specific surface area calculated from the Dietrich et al. [2] data using the combined Huu and three-strut RUC formulations compared to the Dietrich data*

including the one in this section, only provide data values for the strut diameter d_s and not for d_p. Therefore the permeability in terms of d_s will first be determined.

In order to determine d_p in terms of d_s for the three-strut RUC model, equations (2.93) and (2.95) can be used and leads to

$$d_p = \frac{d_s(3-\psi)}{(\psi-1)}\,. \tag{2.206}$$

Substituting equation (2.206) into equation (2.155), gives the permeability in terms of d_s:

$$K = \frac{\epsilon^2 d_s^2}{9\psi^2(\psi-1)^3}\,, \tag{2.207}$$

where ψ is given by equation (2.88).

The two-strut RUC model permeability equation is given by equation (2.176). Similarly to the three-strut RUC model, equation (2.169) can be rearranged to determine d_p in terms of d_s for the two-strut RUC model, which is then given by

$$d_p = \frac{d_s\epsilon}{(\psi-\epsilon)}\,. \tag{2.208}$$

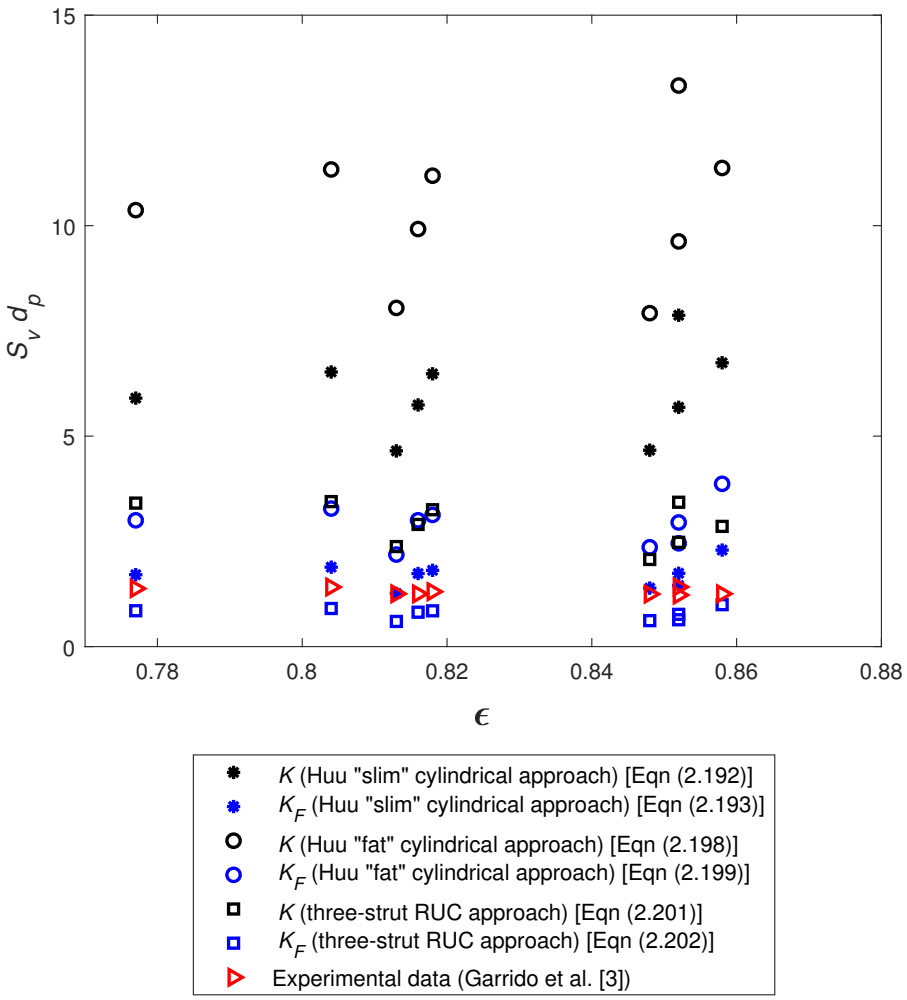

FIGURE 2.22: *Dimensionless specific surface area calculated from the Garrido et al. [3] data using the combined Huu and three-strut RUC formulations compared to the Garrido data*

Substituting equation (2.208) into equation (2.176) gives the permeability in terms of d_s:

$$K = \frac{\epsilon^4 d_s^2}{12(\psi - \epsilon)^3(3\psi + \epsilon)}, \tag{2.209}$$

where ψ is given by equation (2.108).

The data set that will be utilized to validate the models is obtained from Marmoret et al. [12]. The latter authors studied the permeability of fibrous porous media by conducting air permeability measurements involving two glass wool types (L1 and L2) of high porosities (i.e. $\epsilon > 0.9$). The fibre mats comprised of the stacking of fibres into different layers. In order to establish the fibre arrangements, binders were added to the glass fibres. The L1 samples contained more binders than the L2 samples, and since the presence of binders generate clusters and droplets, as demonstrated by Achchaq et al. [57], the three-strut and two-strut RUC models will only be analysed using the L2 fibre mat.

The porosity was calculated by Marmoret et al. [12] using the apparent bulk density of the

glass wool sample in a dry state and the strut density. The average diameter of the fibers was determined using a statistical analysis applied to scanning electron microscopy (SEM). The porosity value obtained for the glass wool L2 sample was 0.9542.

The permeability was determined using an air permeability tester and was still in the no-slip flow regime. The glass wool material was anisotropic not only in the plane perpendicular to the fibre layers but also in the plane of the fibres. Therefore three different permeability measurements were performed. The three different measurements corresponded with the three dimensions of the cube shaped glass wool samples given by 547, 473 and 336 μm^2, of which the latter value is the one measured perpendicular to the plane of the fibres. The data shown in Table 2.3 for the permeability is the average of the three permeability measurements in order to reduce the effect of anisotropy for the sake of comparison with the isotropic three-strut model.

Marmoret et al. [12] provided the strut diameter for the glass wool samples, which was equal to 14 μm for the L2 sample. Substituting this value, along with the porosity value, into equations (2.207) and (2.209) for the three- and two-strut RUC models, respectively, leads to the RUC model predictions for the permeability. The average experimental permeability value is shown in Table 2.3, along with the permeability values obtained by the three- and two-strut RUC models.

TABLE 2.3: *Model comparison to experimental permeability data of Marmoret et al. [12]*

Experimental K $[\mu\text{m}^2]$	Calculated K $[\mu\text{m}^2]$	
	Three-strut RUC model	Two-strut RUC model
452	725	546

Table 2.3 shows that the anisotropic two-strut model provides a more accurate permeability prediction than the isotropic three-strut model, as expected. Other than the two-strut model resembling the solid fibre structure more realistically, the anisotropy of the model in the streamwise direction may also have contributed to its more accurate performance. The remaining discrepancies may be due to non-random fibre orientations in the plane of the fibre bed, as opposed to the transverse isotropy assumed by the two-strut model, which contributes to the heterogeneity of the material. The two-strut RUC model prediction is at least of the same order of magnitude as the experimental data with a relative percentage error of 20% with respect to the average value.

2.5 Chapter summary

The geometry of isotropic fibrous media, and specifically metal foams, has been described by mainly four geometric models in the literature. Equations predicting the specific surface area of foams based on each one of the available models were derived and furthermore analysed and compared to each other and experimental data. More specifically, equations for the specific surface area in terms of the porosity and the pore diameter were provided for each of the models and the dimensionless specific surface area at different high porosity values were plotted for comparison. The geometric models that were investigated constituted of the cubic unit cell model, the tetrakaidecahedron model, the dodecahedron model and the rectangular three-strut Representative Unit Cell (RUC) model. Two specific surface area equations obtained using the cubic unit cell model were based on two approaches found in the literature. The one approach was based on the work done by Giani et al. [14] and the other was based on work done by Lacroix et al. [23]. In the case of the tetrakaidecahedron model, the equations predicting the specific surface area were obtained using three approaches found in the literature. The two direct app-

TABLE 2.4: *Summary of the specific surface area equations from geometric models*

Model	S_v i.t.o.	Eqn no.	$S_v[\mathrm{m}^{-1}]$
Cubic unit cell			
Giani et al. [14]	d_p	(2.8)	$\frac{2}{d_p}\sqrt{3\pi(1-\epsilon)}$
	d_s	(2.9)	$\frac{4}{d_s}(1-\epsilon)$
Lacroix et al. [23]	D_p	(2.14)	$\frac{2}{D_p}\sqrt{3\pi(1-\epsilon)}$
	d_p	(2.15)	$\frac{2}{d_p}\left[\sqrt{3\pi(1-\epsilon)}-2(1-\epsilon)\right]$
Tetrakaidecahedron			
Buciuman and Kraushaar-Czarnetzki [25]	D_p	(2.24)	$\frac{4.82}{D_p}\sqrt{1-\epsilon}$
	d_p	(2.26)	$\frac{4.82\sqrt{1-\epsilon}-2.99(1-\epsilon)}{d_p}$
	d_s		$\frac{2.99(1-\epsilon)}{d_s}$
Richardson et al. [4]	d_p	(2.35)	$\frac{12.979\left[1-0.971\sqrt{1-\epsilon}\right]\sqrt{1-\epsilon}}{d_p}$
Corrected Richardson	d_p	(2.34)	$\frac{5.621\left[1-0.971\sqrt{1-\epsilon}\right]\sqrt{1-\epsilon}}{d_p}$
Huu method			
Buciuman and Kraushaar-Czarnetzki version	D_p	(2.41)	$\frac{5k_1}{D_p}$
	d_p	(2.42)	$\frac{5k_1\left(1-0.62\sqrt{1-\epsilon}\right)}{d_p}$
Richardson version	d_p	(2.43)	$5.784\left[1-0.971\sqrt{1-\epsilon}\right]\frac{k_1}{d_p}$
Dodecahedron			
Huu et al. [21]			
Triangular "slim" strut geometry	d_p	(2.57)	$\frac{60\,k_2}{\sqrt{5}\,\phi^3\sqrt{3-\phi}\,d_p}\left(1-\frac{1}{2}\sqrt{\frac{2}{3}}\,k_2\right)^2$
Cylindrical "slim" strut geometry	d_p	(2.65)	$\frac{20\pi\,k_3}{\sqrt{5}\,\phi^3\sqrt{3-\phi}\,d_p}\left(1-\frac{1}{2}\sqrt{\frac{2}{3}}\,k_3\right)^2$
Triangular "fat" strut geometry	d_p	(2.72)	$\frac{60\,k_4}{\sqrt{5}\,\phi^3\sqrt{3-\phi}\,d_p}\left(1-\frac{1}{2}\sqrt{\frac{2}{3}}\,k_4\right)^2+S_{\mathrm{add}}(k_4)$
Cylindrical "fat" strut geometry	d_p	(2.73)	$\frac{20\pi\,k_5}{\sqrt{5}\,\phi^3\sqrt{3-\phi}\,d_p}\left(1-\frac{1}{2}\sqrt{\frac{2}{3}}\,k_5\right)^2+S_{\mathrm{add}}(k_5)$

RUC			
Du Plessis et al. [22] Three-strut model	D_p	(2.92)	$\frac{3}{D_p}(3-\psi_1)(\psi_1-1)$
	d_s	(2.94)	$\frac{3}{2d_s}(3-\psi_1)(\psi_1-1)^2$
	d_p	(2.96)	$\frac{3}{2d_p}(3-\psi_1)^2(\psi_1-1)$
Two-strut model	D_p	(2.112)	$\frac{2}{D_p}\left(1-\frac{\epsilon}{\psi_2}\right)\left(1+\frac{3\epsilon}{\psi_2}\right)$
	d_s	(2.114)	$\frac{2}{d_s}\left(1-\frac{\epsilon}{\psi_2}\right)^2\left(1+\frac{3\epsilon}{\psi_2}\right)$
	d_p	(2.116)	$\frac{2\epsilon}{\psi_2 d_p}\left(1-\frac{\epsilon}{\psi_2}\right)\left(1+\frac{3\epsilon}{\psi_2}\right)$
Coefficients /Parameters			
Equation (2.39)	$k=k_1$		$\frac{\frac{1}{\sqrt{2}}}{8\sqrt{2}}k^3+\frac{3\sqrt{3}}{8\sqrt{2}}k^2-(1-\epsilon)=0$
Equation (2.50)	$k=k_2$		$-\frac{\sqrt{10}}{3\phi^4}k^3+\frac{\sqrt{15}}{\phi^4}k^2-(1-\epsilon)=0$
Equation (2.61)	$k=k_3$		$\left(\frac{\sqrt{10}}{6\phi^4}-\frac{\sqrt{5}\,\pi}{2\phi^4}\sqrt{\frac{2}{3}}\right)k^3+\frac{\sqrt{5}\,\pi}{\phi^4}k^2-(1-\epsilon)=0$
	k_{add}		$\frac{12\,k}{\sqrt{5}\,\phi^4}\left[\frac{5\,\phi}{4\sqrt{3-\phi}}-\frac{\pi\,\phi^2}{4\,(3-\phi)}\right]\left(1-\frac{1}{2}\sqrt{\frac{2}{3}}\,k\right)^2$ $+\frac{5\,\sin^2\left(\frac{\pi}{5}\right)}{4\sqrt{15}\,(3-\phi)\,\phi^2}\sqrt{\frac{1}{4}-\frac{\sin^2\left(\frac{\pi}{5}\right)\phi^2}{9-3\,\phi}}\left(1-\frac{1}{2}\sqrt{\frac{2}{3}}\,k\right)^3=0$
Equation (2.67)	$k=k_4$		k_2+k_{add}
Equation (2.69)	$k=k_5$		k_3+k_{add}
Equation (2.71)	$S_{\text{add}}(k)$		$\frac{\left(1-\frac{1}{2}\sqrt{\frac{2}{3}}\,k\right)}{\phi\sqrt{3-\phi}}\left[\frac{12\,\pi\,k\,\left(1-\frac{1}{2}\sqrt{\frac{2}{3}}\,k\right)}{\sqrt{5}\,\phi\sqrt{3-\phi}\,d_p}+\frac{\sqrt{15}\,\left(1-\frac{1}{2}\sqrt{\frac{2}{3}}\,k\right)^2\sin^2\left(\frac{\pi}{5}\right)}{2\,(3-\phi)\,d_p}\right]$
Equation (2.88)	$\psi=\psi_1$		$\psi=2+2\cos\left[\frac{4\pi}{3}+\frac{1}{3}\cos^{-1}(2\epsilon-1)\right]$
Equation (2.108)	$\psi=\psi_2$		$\frac{2}{3}\sqrt{3\,\epsilon+1}\,\cos\left[\frac{1}{3}\cos^{-1}\left(\frac{9\epsilon-27\epsilon^2+2}{2\sqrt{27\epsilon^3+27\epsilon^2+9\epsilon+1}}\right)\right]+\frac{1}{3}$

roaches were obtained from Buciuman and Kraushaar-Czarnetzki [25] and Richardson et al. [4] and the other approach was based on the dodecahedron model obtained from the work of Huu

et al. [21]. The equations for the specific surface area of the dodecahedron model were all obtained from Huu et al. [21]. Two versions of the dodecahedron model were investigated, one with a "slim" strut geometry and one with a "fat" strut geometry. Each of these models were furthermore divided into two categories, one with triangular strut geometry representing higher porosity values, i.e. where $\epsilon > 0.9$, and one with cylindrical strut geometry representing lower porosity values, i.e. where $\epsilon < 0.9$. Four predicting equations for the specific surface area of the dodecahedron model were thus provided. Finally, the predicting equation for the specific surface area obtained using the three-strut RUC model was based on an approach followed by Woudberg and Du Plessis [1].

Another approach that was used to determine the specific surface area at different porosity values made use of the transport properties of foams, or more specifically, experimental permeability values obtained from the pressure drop. Three different formulations were given, i.e. the Dietrich, Huu and RUC formulations, which were based on the work of Dietrich et al. [2], Huu et al. [21] and Woudberg and Du Plessis [1], respectively. These formulations were obtained by comparing Ergun-type equations with the Darcy-Forchheimer equation in order to obtain the specific surface area in terms of the porosity and the permeability coefficient of the Darcy regime and the specific surface area in terms of the porosity and the permeability coefficient of the Forchheimer regime. The Ergun-type equation of the RUC formulation was deduced using the RUC models.

A final approach for determining the specific surface area was considered in which both geometric and transport properties were utilized to obtain the required predictions. Two formulations were presented, one based on the work of Huu et al. [21] and the other obtained using the RUC models. The Huu combined formulation comprised of combining the comparison of the Ergun-type equation, as given by Huu et al. [21], with the Darcy-Forchheimer equation and the specific surface area predicted by the dodecahedron model based on the geometric approach to obtain equations for the specific surface area in terms of the porosity and the respective permeability coefficients. The RUC combined formulation similarly consisted of combining the RUC-based Ergun-type equation with the specific surface area predicted by the three-strut RUC model based on the geometric approach to obtain the specific surface area in terms of the porosity and the permeability coefficients of the Darcy and Forchheimer regimes, respectively.

A two-strut RUC model was also presented, but was not compared with the experimental data for foams along with the other geometric, kinetic and combined approaches due to its structure resembling layered fibres media rather than foams. A geometrically obtained specific surface area equation in terms of the porosity and pore diameter and specific surface area equations in terms of the porosity and the respective permeability coefficients determined using the kinetic and combined kinetic-geometric approaches were, however, also provided. For both the two- and three-strut RUC models the Ergun-type equations based on their model structures were derived and in the process, equations predicting the permeability in terms of the porosity were determined. The two- and three-strut RUC models were lastly compared to the permeability data obtained from glass fibres.

In this chapter three approaches were therefore considered to determine specific surface area equations as a function of porosity: the geometric, kinetic and combined kinetic-geometric approaches. A summary of all the specific surface area equations obtained from the different geometric models that have been discussed is given in Table 2.4.

In the following chapter the RUC models will be adapted to account for anistropy, as a result of compression.

CHAPTER 3

Compressed RUC models

It has been investigated and proven in the literature that compression of fibrous porous media has noteworthy effects on the permeability (e.g. Dukhan et al. [29], Boomsma and Poulikakos [31], Antohe et al. [30] and Zhu et al. [58]). Due to the geometrical changes that the fibrous media undergo during compression, the pore-scale parameters of the media change as well. This results in the change of the relationships amongst the parameters. In Chapter 1 the importance of investigating changes caused by compression on fibrous media, and the models describing it were discussed.

In this chapter compression of the three-strut RUC model of Woudberg et al. [6] and the two-strut RUC model of Van Heyningen [7] will be investigated. In each case, the permeability will be determined in terms of porosity. In this study the specific surface area will additionally be determined using the geometric approach, the kinetic approach and the combined kinetic-geometric approach.

For both the RUC models one-dimensional compression is assumed in the streamwise direction and transverse isotropy is assumed in the plane perpendicular to the streamwise direction, therefore the parameters in the two transverse directions are the same. Furthermore, it is assumed

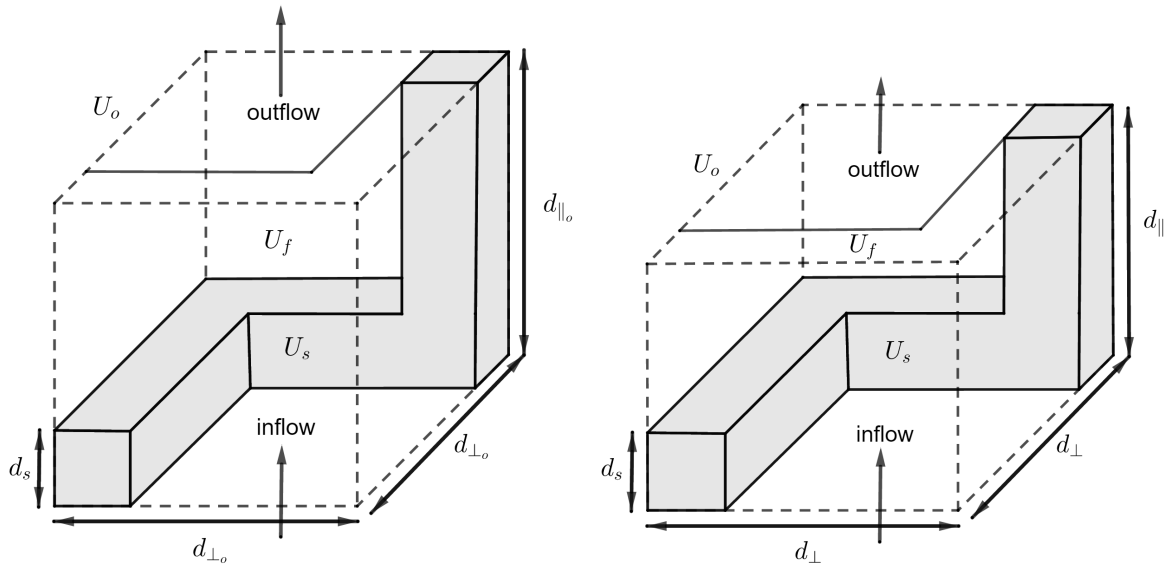

(a) *Uncompressed (isotropic) model* (b) *Compressed (anisotropic) model*

FIGURE 3.1: *Uncompressed and compressed three-strut RUC model (Woudberg et al. [6])*

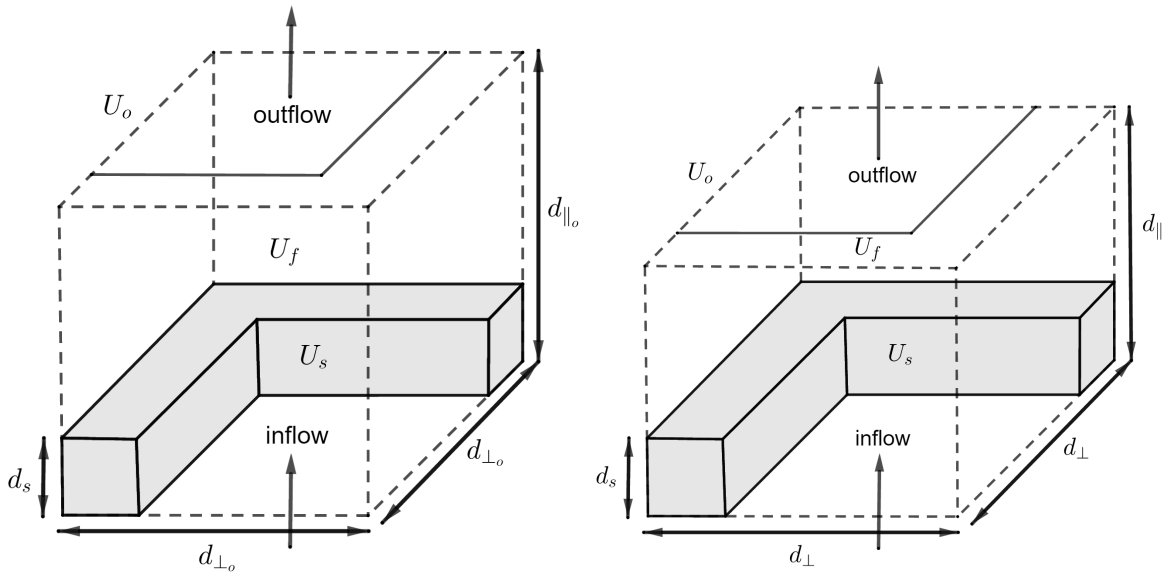

(a) *Uncompressed (anisotropic) model* (b) *Compressed (anisotropic) model*

FIGURE 3.2: *Uncompressed and compressed two-strut RUC model (Van Heyningen [7])*

that no lateral displacement occurs during compression. The change in micro-structure as a result of the compression will also be assumed to be only due to the compression of the material itself and not because of the fluid flow through the medium. Although the deformation may not in general be uniform, the average geometry on which the RUC model is based resembles the compression as being uniform. This represents a first order approach that allows for the physical process to be modelled mathematically in a relatively simplistic manner.

Two cases of compression will be considered. The first case is where the strut diameter in the streamwise direction remains constant, as illustrated in Figures 3.1 and 3.2 and referred to as the rigid compressed three- and two-strut RUC models, and the second case is where the strut diameter in the streamwise direction changes with compression, as illustrated in Figures 3.3 and 3.4. The second case in which d_s changes with compression will be referred to as the soft compressed three- and two-strut RUC models and is applicable in cases where materials such as soft polyester fibrous media are examined under compression.

The manner in which the experimental compression data will be incorporated into the modelling procedure will, however, be discussed first.

3.1 Application of experimental compression data

The streamwise cell dimension $d_{\parallel}$ changes at different stages of compression, due to the assumption that compression takes place in the streamwise direction. The following relationship has been introduced by Woudberg et al. [6]:

$$d_{\parallel} = d_{\parallel_o} e \,, \tag{3.1}$$

where $d_{\parallel_o}$ is the uncompressed (or initial) streamwise RUC dimension, as indicated in Figures 3.1(a), 3.2(a), 3.3(a) and 3.4(a), and e is the compression ratio, which can be determined experimentally by using the

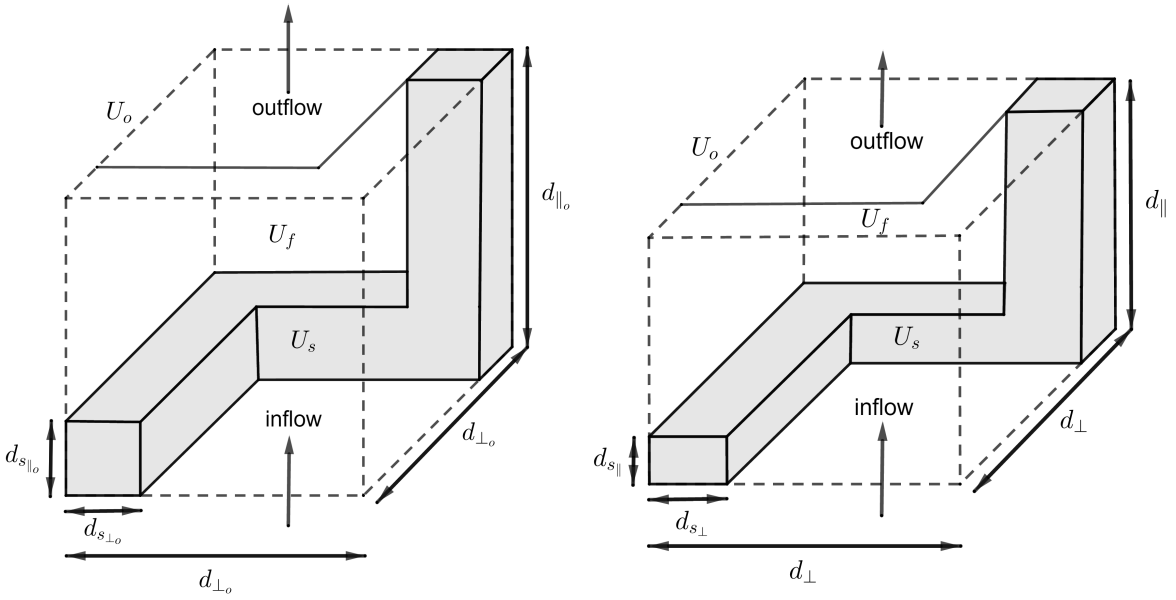

(a) *Uncompressed (isotropic) model* (b) *Compressed (anisotropic) model*

FIGURE 3.3: *Soft uncompressed and compressed three-strut RUC model*

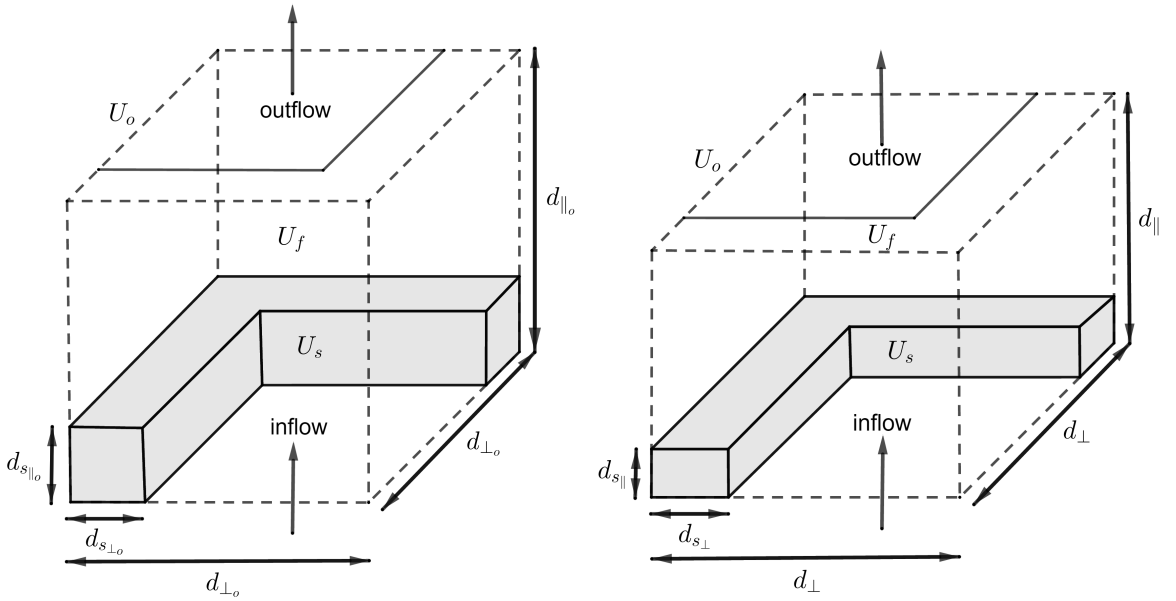

(a) *Uncompressed (anisotropic) model* (b) *Compressed (anisotropic) model*

FIGURE 3.4: *Soft uncompressed and compressed two-strut RUC model*

equation (Van Heyningen [7])

$$e = \frac{h_f}{h_o}\,. \tag{3.2}$$

In equation (3.2) h_o and h_f are the uncompressed and post-compressed filter thickness, respectively. Equations (3.1)and (3.2) are applicable to all the compressed models considered, i.e. the models shown in Figures 3.1(b), 3.2(b), 3.3(b) and 3.4(b).

Three ways in which the compression ratio can be determined in terms of the porosity will be considered, i.e. the regression relationship, the general non-linear relationship and the specific

non-linear relationship, as introduced by Van Heyningen [7]. Two sets of experimental data will be used to compare these expressions with each other, i.e. the data from Le Coq [8] and that from Jaganathan et al. [9], as presented in Table 3.1.

TABLE 3.1: *Compression ratio and corresponding porosity data sets obtained from Le Coq [8] and Jaganathan et al. [9].*

Le Coq [8]		**Jaganathan et al.** [9]	
ϵ	e	ϵ	e
0.94	1	0.9388	1
0.92	0.85	0.8805	0.5398
0.89	0.75	0.8240	0.3704
0.86	0.55	0.6558	0.205

The data from Le Coq [8] was obtained by performing mercury porosimetry on glass fibres and the average fibre diameter was measured to be $2.7\,\mu$m. Therefore, for the Le Coq data, $d_s = 2.7\,\mu$m. Jaganathan et al. [9] studied the change in pore sizes of fibrous media due to compression. The Jaganathan et al. [9] data was obtained by performing Digital Volumetric Imaging (DVI) on polyester fibers. The average fibre diameter was $d_s = 15\,\mu$m.

In the next subsections the three methods used to determine the compression ratio-porosity relationship are discussed and evaluated similarly as was done by Van Heyningen [7].

Regression relationship

The regression relationship is obtained by fitting a function through a set of experimental data points. In this case the set of data points is the corresponding compression ratio and porosity data points. For the Le Coq [8] data, a linear regression relationship is obtained and given by

$$e = 5.34\epsilon - 4.03\,. \tag{3.3}$$

For the Jaganathan et al. [9] data, a non-linear regression relationship is obtained, i.e.

$$e = 17.2\epsilon^2 - 24.8\epsilon + 9.04\,. \tag{3.4}$$

Equations (3.3) and (3.4) are plotted in Figures 3.5 and 3.6, respectively.

The results given by the regression relationships are, however, not viable at the lower porosities in both Figures 3.5 and 3.6. For the Le Coq data, the straight line fit in Figure 3.5 leads to a negative compression ratio for porosities lower than 0.75. The parabolic fit in Figure 3.6 for the Jaganathan et al. [9] data is also not feasible due to an increase in the compression ratio with a decrease in porosity for porosities lower than 0.72.

General non-linear relationship

The general non-linear relationship is obtained by using the definition of porosity. In order to find the relationship between the compression ratio and the porosity, the parameter A is defined as the base area of the container enclosing the porous medium. Accordingly, $U_o = Ah_o$ and

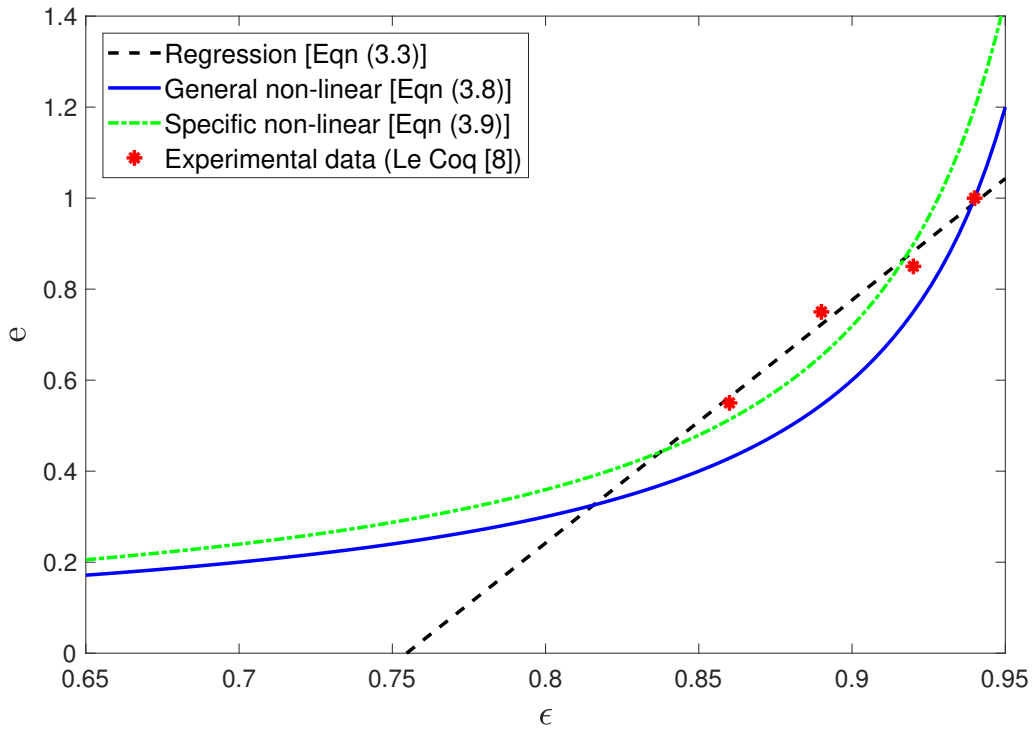

FIGURE 3.5: *Compression ratio-porosity relationships compared to Le Coq [8] data*

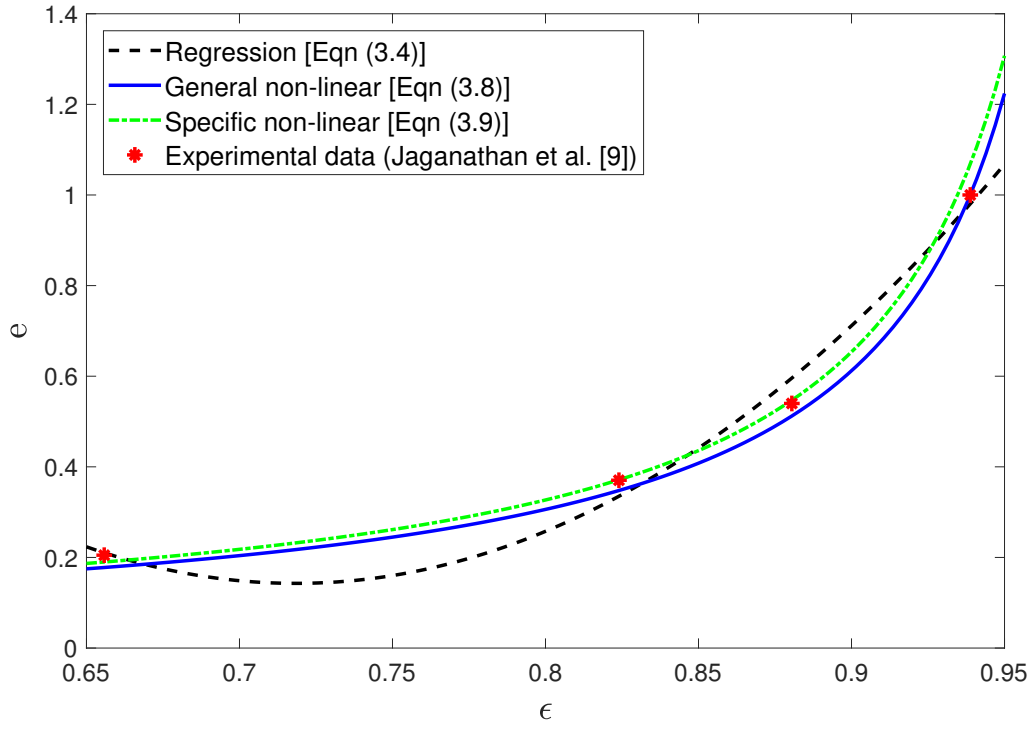

FIGURE 3.6: *Compression ratio-porosity relationships compared to Jaganathan et al. [9] data*

$U = Ah_f$, which represent the uncompressed volume of the porous medium and the volume after compression, respectively. The solid volume is assumed to remain constant under compression as in Woudberg et al. [6]. Let U_{f_o} denote the uncompressed fluid volume and U_f denote the fluid volume after compression. Furthermore, let ϵ_o represent the porosity of the uncompressed state. Therefore it can be deduced that

$$U_s = U_o - U_{f_o} = U_o(1 - \epsilon_o) = Ah_o(1 - \epsilon_o)\,. \tag{3.5}$$

Similarly it follows that

$$U_f = U - U_s = Ah_f - Ah_o(1 - \epsilon_o)\,. \tag{3.6}$$

Furthermore, with the substitution of $U = Ah$ as well as equation (3.6) into equation (2.75), it can thus be obtained that

$$\epsilon = \frac{U_f}{U} = 1 - \frac{(1 - \epsilon_o)}{e}\,, \tag{3.7}$$

which, when re-arranged, leads to the following relationship for the compression ratio in terms of the porosity (Woudberg et al. [6]):

$$e = \frac{1 - \epsilon_o}{1 - \epsilon}\,. \tag{3.8}$$

The values used for ϵ_o in the data sets of both Le Coq [8] and Jaganathan et al. [9] were the first data points given for the porosity in their respective data sets in Table 3.1. That is, for the general non-linear relationship in Figure 3.5 ϵ_o was set equal to 0.94 and in Figure 3.6, ϵ_o was set equal to 0.9388.

Specific non-linear relationship

The equation used to acquire the specific non-linear relationship takes on the form (Woudberg et al. [6])

$$e = \frac{C}{1 - \epsilon}\,, \tag{3.9}$$

where C is determined by substituting known experimental values for ϵ at corresponding e-values into equation (3.9) and taking the average.

The value for C obtained by substituting the data of Le Coq [8], is 0.0719 and the value for C obtained from the data of Jaganathan et al. [9], is 0.0654. Equation (3.9) with its respective C-values are also indicated in Figures 3.5 and 3.6.

A more gradual trend is observed for the general and specific non-linear relationships and comparison of the latter two non-linear relationships applied to the data of Le Coq [8] in Figure 3.5, as well as to the data of Jaganathan et al. [9] in Figure 3.6, leads to the conclusion that the specific non-linear relationship is the most accurate and representative one of the three considered, since it provides the most accurate correspondence with the data when both data sets are considered simultaneously. The specific non-linear relationship method will henceforth be used to determine the compression ratio, which in turn can be used, where possible, to compute $d_{\|}$ (given by equation (3.1)).

The first compressed model that will be discussed is the three-strut RUC model (Woudberg et al. [6]).

3.2 Compressed three-strut RUC model

The uncompressed (or isotropic) and compressed (or anisotropic) model representations are shown in Figure 3.1(a) and (b), respectively. The parameters are the same as those defined in Chapter 2, Section 2.1.4, except that the cell size d is no longer applicable to the model. Parameters $d_{\parallel}$ and $d_{\perp}$ are used instead, which represents the cell dimension in the streamwise direction and the cell dimension in the transverse directions, respectively.

In order to start the process of determining the specific surface area in terms of porosity, the porosity is deduced by using the parameters indicated in Figure 3.1. The total volume of the anisotropic RUC can be expressed as

$$U_o = d_{\perp}^2 d_{\parallel}\,, \tag{3.10}$$

and the total solid volume as

$$U_s = 2d_s^2(d_{\perp} - d_s) + d_s^2 d_{\parallel} = 2d_s^2 d_{\perp} - 2d_s^3 + d_s^2 d_{\parallel}\,. \tag{3.11}$$

Since $U_f = U_o - U_s$, the total fluid volume can therefore be expressed as

$$U_f = d_{\perp}^2 d_{\parallel} - 2d_s^2 d_{\perp} + 2d_s^3 - d_s^2 d_{\parallel}\,. \tag{3.12}$$

Substituting equations (3.10) and (3.12) into the porosity equation (2.75) therefore leads to the porosity in terms of d_s, $d_{\parallel}$ and $d_{\perp}$, i.e.

$$\epsilon = \frac{d_{\perp}^2 d_{\parallel} - 2d_s^2 d_{\perp} + 2d_s^3 - d_s^2 d_{\parallel}}{d_{\perp}^2 d_{\parallel}}\,. \tag{3.13}$$

The RUC dimension in the transverse direction, $d_{\perp}$, can be determined in terms of ϵ by first rearranging equation (3.13) to obtain the following second order polynomial in $d_{\perp}$:

$$d_{\parallel}(\epsilon - 1)d_{\perp}^2 + 2d_s^2 d_{\perp} + d_s^2 d_{\parallel} - 2d_s^3 = 0\,. \tag{3.14}$$

Using the quadratic formula $d_{\perp}$ can therefore be determined, leading to

$$d_{\perp} = \frac{d_s\left(d_s + \sqrt{d_s^2 + (1-\epsilon)d_{\parallel}(d_{\parallel} - 2d_s)}\right)}{d_{\parallel}(1-\epsilon)}\,. \tag{3.15}$$

Equation (3.1) for $d_{\parallel}$ and consequently equation (3.9) for e obtained from the specific non-linear relationship, allows for $d_{\perp}$ to be obtained in terms of porosity.

In order to determine the permeability coefficient K, the pressure drop equation for the anisotropic three-strut RUC model is determined first by using equation (2.130), i.e. the total pressure drop over the RUC in the Darcy regime (Woudberg [59]). Similarly, using equation (2.131) the wall shear stresses for the anisotropic three-strut RUC are therefore given by

$$\tau_{w_{\parallel}} = \frac{6\mu w_{\parallel}}{(d_{\perp} - d_s)}\,, \tag{3.16}$$

$$\tau_{w_{\perp_1}} = \frac{6\mu w_{\perp}}{(d_{\parallel} - d_s)} \tag{3.17}$$

and

$$\tau_{w_{\perp_2}} = \frac{6\mu w_{\perp}}{(d_{\perp} - d_s)}\,, \tag{3.18}$$

where $\tau_{w_\parallel}$ once again represents the wall shear stress in the streamwise duct and $\tau_{w_{\perp_1}}$ and $\tau_{w_{\perp_2}}$ represent the wall shear stresses for the two transverse ducts. In the denominators of equations (3.16), (3.17) and (3.18), $(d_\perp - d_s)$, $(d_\parallel - d_s)$ and $(d_\perp - d_s)$ are the respective corresponding distances between the parallel plates for each of the wall shear stresses. Furthermore, the magnitude of the average duct velocity in the streamwise direction can be deduced, since

$$w_\parallel = \frac{qA_o}{A_{p_\parallel}}\,, \tag{3.19}$$

where A_o is the total RUC base area perpendicular to the streamwise direction. From Figure 3.1(b) it can be deduced that

$$A_o = d_\perp^2\,, \tag{3.20}$$

and

$$A_{p_\parallel} = (d_\perp - d_s)^2\,. \tag{3.21}$$

Substituting equations (3.20) and (3.21) into equation (3.19) leads to

$$w_\parallel = \frac{qd_\perp^2}{(d_\perp - d_s)^2}\,. \tag{3.22}$$

Due to conservation of mass,

$$A_{p_\parallel} w_\parallel = A_{p_\perp} w_\perp\,, \tag{3.23}$$

where $A_{p_\perp}$ is the transverse cross-sectional flow area and $w_\perp$ is the magnitude of the average duct velocity in the transverse directions. From Figure 3.1(b) it can also be determined that

$$A_{p_\perp} = (d_\perp - d_s)(d_\parallel - d_s)\,. \tag{3.24}$$

The magnitude of the average duct velocity in the transverse directions can consequently be deduced from equations (3.21) to (3.24), yielding

$$w_\perp = \frac{d_\perp - d_s}{d_\parallel - d_s} \cdot \frac{qd_\perp^2}{(d_\perp - d_s)^2} = \frac{qd_\perp^2}{(d_\parallel - d_s)(d_\perp - d_s)}\,, \tag{3.25}$$

which is the same for both transverse directions.

Considering Figure 3.1(b) once again, it is evident that the total solid surfaces parallel to the streamwise direction is given by

$$S_\parallel = 4d_s(d_\perp - d_s)\,, \tag{3.26}$$

and the total solid surfaces in the two directions perpendicular to the streamwise direction are given by

$$S_{\perp_1} = 4d_s(d_\perp - d_s)\,, \tag{3.27}$$

and

$$S_{\perp_2} = 4d_s(d_\parallel - d_s)\,, \tag{3.28}$$

respectively. Substituting equations (3.22) and (3.25) for the average duct velocities into the corresponding equations (3.16), (3.17) and (3.18) for the wall shear stresses, and in turn substituting equations (3.16) to (3.18), along with equations (3.26) to (3.28) for the solid surfaces and

equation (3.21) for the streamwise cross-sectional flow area into equation (2.130) for the total pressure drop, leads to

$$\Delta p = \frac{24 d_s d_\perp^2 \mu q}{(d_\perp - d_s)^2} \left[\frac{2}{(d_\perp - d_s)^2} + \frac{1}{(d_\parallel - d_s)^2} \right] . \tag{3.29}$$

Equation (3.29) is therefore the pressure drop Δp in terms of d_s, $d_\parallel$ and $d_\perp$. The pressure gradient can then finally be obtained by dividing both sides of equation (3.29) by $d_\parallel$, i.e.

$$\frac{\Delta p}{d_\parallel} = \frac{24 d_s d_\perp^2 \mu q}{d_\parallel (d_\perp - d_s)^2} \left[\frac{2}{(d_\perp - d_s)^2} + \frac{1}{(d_\parallel - d_s)^2} \right] . \tag{3.30}$$

In order to determine the permeability, Darcy's law is applied, that is

$$\frac{\Delta p}{L} = \frac{\mu}{K} q \, . \tag{3.31}$$

Rearranging equation (3.31) and setting $L = d_\parallel$ produces

$$K = \frac{\mu q d_\parallel}{\Delta p} \, . \tag{3.32}$$

Comparison of equations (3.30) and (3.32) therefore leads to the permeability in terms of d_s, $d_\parallel$ and $d_\perp$, i.e.

$$K = \frac{d_\parallel (d_\perp - d_s)^2}{24 d_s d_\perp^2} \left[\frac{2}{(d_\perp - d_s)^2} + \frac{1}{(d_\parallel - d_s)^2} \right]^{-1} , \tag{3.33}$$

which is the permeability expressed implicitly in terms of porosity (due to the equations obtained for $d_\parallel$ and $d_\perp$) for the different levels of compression.

In Tables 3.2 and 3.3 two sets of data are given with which to evaluate the permeability with respect to porosity. The first data set given in Table 3.2 is data obtained from Le Coq [8].

TABLE 3.2: *Experimental data of Le Coq [8] for non-woven fibrous media with* $d_s = 2.7\,\mu m$

Experimental procedure	ϵ	e	D_h [μm]	K [μm^2]
mercury porosimetry	0.94	1	28	8.2
	0.92	0.85	17	2.0
	0.89	0.75	16.5	1.4
	0.86	0.55	16.0	0.17
permeametry	0.94	1	28	10
	0.92	0.85	17	2.1

As illustrated in Section 3.1, the compression ratio-porosity relationship is determined using the ϵ and e data, given in both Tables 3.1 and 3.2, to find a specific non-linear relationship given by equation (3.9), for which $C = 0.0719$. In the Le Coq data set only D_h is provided and not the pore diameter necessary to determine a value for $d_{\parallel_o}$. Therefore, to find a value for $d_{\parallel_o}$ the hydraulic diameter is defined as

$$D_h = d_\perp - d_s \, , \tag{3.34}$$

for the compressed RUC models.

The reason for this choice of definition for the hydraulic diameter, given by equation (3.34), is that for the isotropic three-strut model the solid and fluid volumes are interchangeable yielding both

low and high porosity models. The low porosity model furthermore resembles flow in a square duct and equation (3.34) corresponds to the hydraulic diameter of a square duct of dimension $d_\perp - d_s$. For the sake of uniformity and direct comparison, the same hydraulic diameter will be used for the two-strut model.

Equations (3.13) and (3.34) are then used to determine the following expression for $d_\parallel$:

$$d_\parallel = \frac{2d_s^2 D_h}{(1-\epsilon)(D_h + d_s)^2 - d_s^2}\,. \tag{3.35}$$

Equation (3.35) is then substituted into equation (3.1) to determine an expression for $d_{\parallel_o}$ which, along with the ϵ and D_h data provided in Table 3.2, is then used to calculate an average $d_{\parallel_o}$-value. Consequently, $d_{\parallel_o} = 10.1\,\mu$m. Using this value for $d_{\parallel_o}$ and equation (3.9) for e, $d_\parallel$ can be obtained using equation (3.1) and $d_\perp$ can furthermore be obtained using equation (3.15). The resulting plot for the permeability given by equation (3.33) as a function of porosity is presented in Figure 3.7.

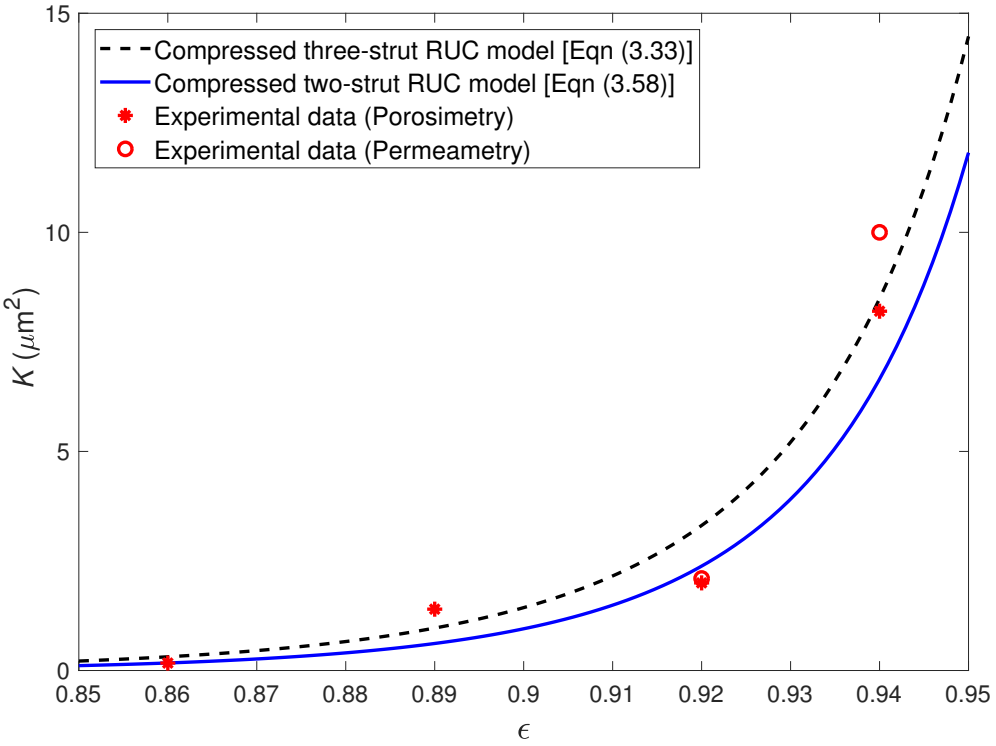

FIGURE 3.7: *Permeability versus porosity for the compressed RUC models compared to the experimental data of Le Coq [8]*

From Figure 3.7 it can be seen that the permeability predicted by the compressed three-strut RUC model compares well with the experimental permeability data.

The second data set, given in Table 3.3, is data obtained from Jackson and James [10] who investigated the permeability of fibrous media and gathered experimental permeability data for a variety of fibrous media. Two of the media will be considered, namely nylon and glass fibres.

TABLE 3.3: *Experimental data of Jackson and James [10] for nylon ($d_s = 0.193$ mm) and glass ($d_s = 0.164$ mm) fibrous media*

Fibrous media	ϵ	K [mm^2]
Nylon fibres $d_s = 0.193\,\text{mm}$	0.742	0.0028
	0.768	0.0036
	0.79	0.0047
	0.80	0.0051
	0.83	0.0074
	0.85	0.009
	0.86	0.0103
	0.87	0.0124
	0.9	0.0179
Glass fibres $d_s = 0.164\,\text{mm}$	0.68	0.001
	0.71	0.0015
	0.81	0.0042
	0.80	0.0037
	0.83	0.0053
	0.85	0.0067
	0.87	0.0101
	0.9	0.0128
	0.91	0.0168
	0.92	0.0202
	0.93	0.0256
	0.94	0.035
	0.955	0.0538

In the Jackson and James data set $1-\epsilon$ was provided, which was used to determine ϵ as given in Table 3.3. Furthermore, no e and D_h data was provided, so the general non-linear relationship is used to determine e, as given by equation (3.8), where $\epsilon_o = 0.9$ for nylon fibres and $\epsilon_o = 0.955$ for glass fibres. Another method therefore has to be employed to determine $d_{\parallel_o}$ according to which isotropy is assumed in the first state of compression.

Utilizing equations (2.85) and (2.88) and setting $d = d_{\parallel_o}$ and $\psi = \psi_o$, where ψ_o is the geometric factor of the uncompressed state, leads to

$$d_{\parallel_o} = \frac{2d_s}{\psi_o - 1}\,, \tag{3.36}$$

where

$$\psi_o = 2 + 2\cos\left[\frac{4\pi}{3} + \frac{1}{3}\cos^{-1}(2\epsilon_o - 1)\right]\,. \tag{3.37}$$

Therefore

$$d_{\parallel} = \frac{d_{\parallel_o}(1-\epsilon_o)}{1-\epsilon}\,, \tag{3.38}$$

where $d_{\parallel_o}$ is given by equation (3.36).

For the glass fibres, the value determined for $d_{\parallel_o}$ for the three-strut model is equal to 1.281 mm and for the nylon fibres it is equal to 0.986 mm.

Consequently, $d_\perp$ can be obtained by using equation (3.15) and K can then finally be obtained by using equation (3.33). The resulting plot for the permeability using the Jackson and James [10] data is shown in Figure 3.8.

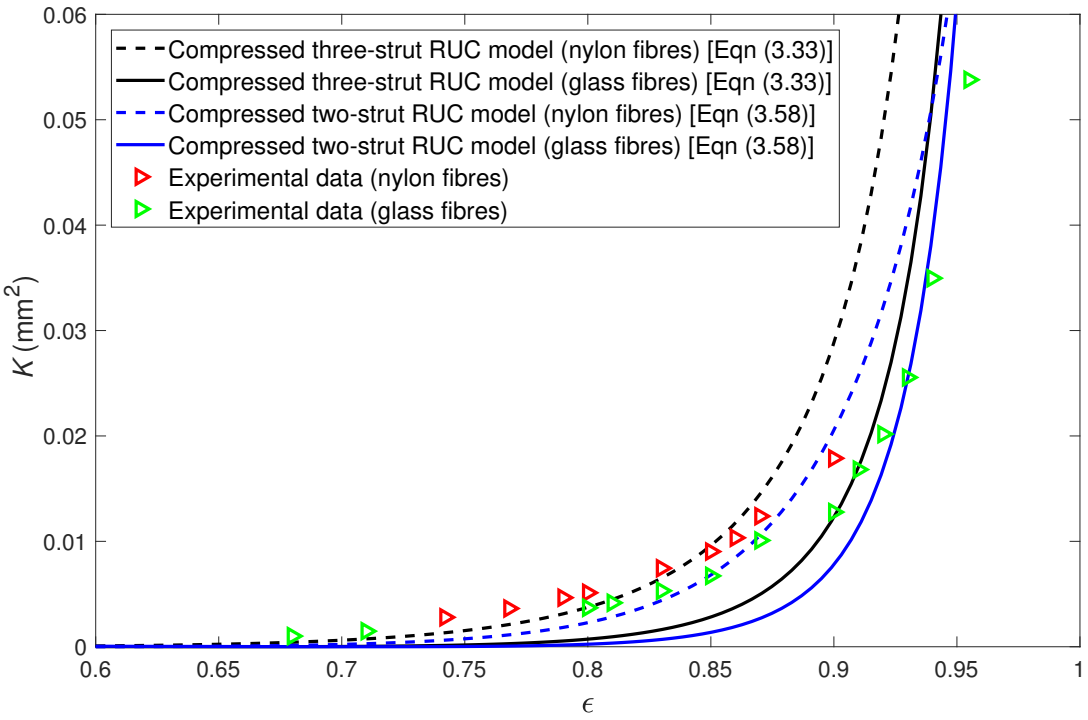

FIGURE 3.8: *Permeability versus porosity for the compressed RUC models compared to the experimental data of Jackson and James [10]*

The three-strut RUC model compares favourably to the experimental data in Figure 3.8 for the nylon fibres for porosity values less than 0.9. The predictions for the glass fibres are only accurate for the porosity values in the vicinity of 0.9.

Having had determined the permeability equation for the anisotropic three-strut RUC model, the specific surface area equations can also be deduced by utilizing equation (3.33). The first specific surface area equation considered is obtained from the geometric approach, the second approach considered is the kinetic approach and lastly the combined kinetic-geometric approach will be applied.

Geometric approach

In the geometric approach the total surface area can first be obtained by merely adding $S_\parallel$, $S_{\perp_1}$ and $S_{\perp_2}$, as given by equations (3.26), (3.27) and (3.28), respectively, i.e. yielding

$$A_s = 8d_s(d_\perp - d_s) + 4d_s(d_\parallel - d_s)\,, \tag{3.39}$$

and the cell volume is given by equation (3.10). The specific surface area equation is therefore given by

$$S_v = \frac{A_s}{U_o} = \frac{8d_s(d_\perp - d_s) + 4d_s(d_\parallel - d_s)}{d_\perp^2 d_\parallel}\,. \tag{3.40}$$

The predictions provided by equation (3.40) using the Le Coq [8] data are shown in Figure 3.9 and the predictions based on the Jackson and James [10] data are shown in Figure 3.10.

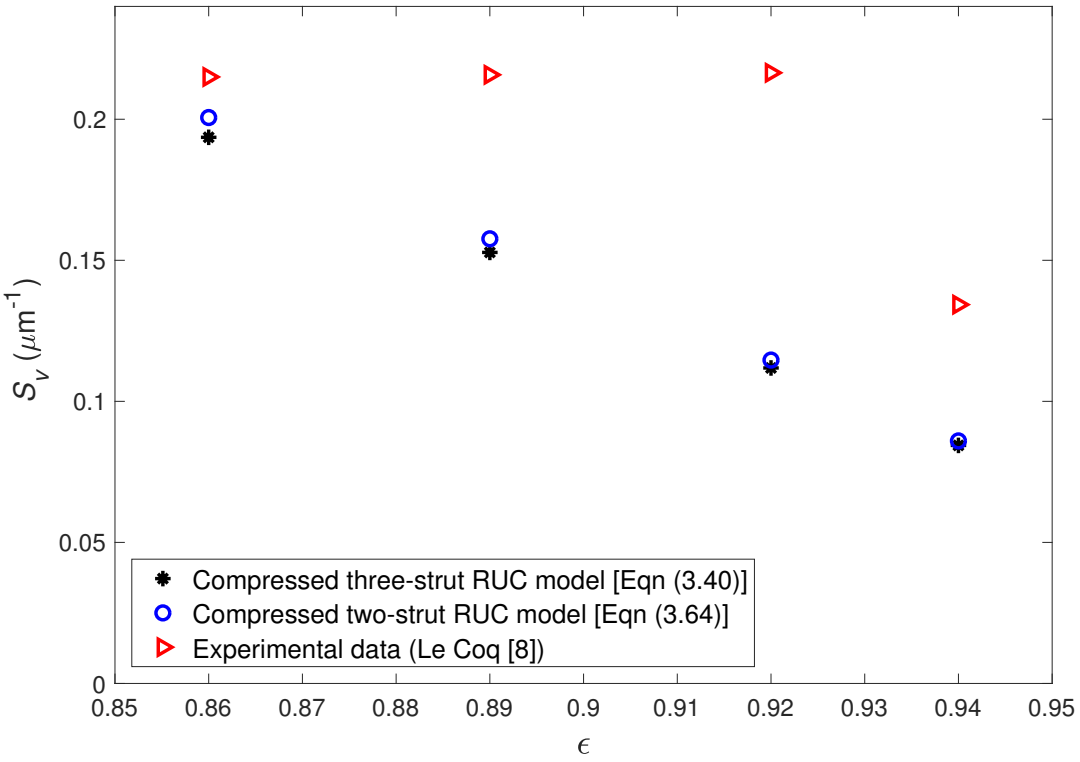

FIGURE 3.9: *Specific surface area versus porosity based on the geometric approach for the compressed three- and two-strut RUC models using the experimental data of Le Coq [8]*

The experimental data in Figure 3.9 for the specific surface area was determined using the hydraulic diameter data, as given in Table 3.2, and equation (1.6). The specific surface area values obtained by the compressed three-strut model under-predicts the experimental values of Le Coq [8], but since equation (1.6) was used for the hydraulic diameter the discrepancies are somewhat expected. The predicted values are at least of the same order of magnitude as the experimental values.

The trend of the predicted specific surface area in Figure 3.10 is as expected, i.e. it decreases with increasing porosity. Since neither measured specific surface area values nor hydraulic diameter values are included in the Jackson and James [10] data only the model predictions are shown in Figure 3.10.

Kinetic approach

In the kinetic approach, the permeability in terms of the hydraulic diameter is used to determine the specific surface area. The permeability is obtained in terms of D_h by substituting the expression

$$d_\perp = D_h + d_s \,, \tag{3.41}$$

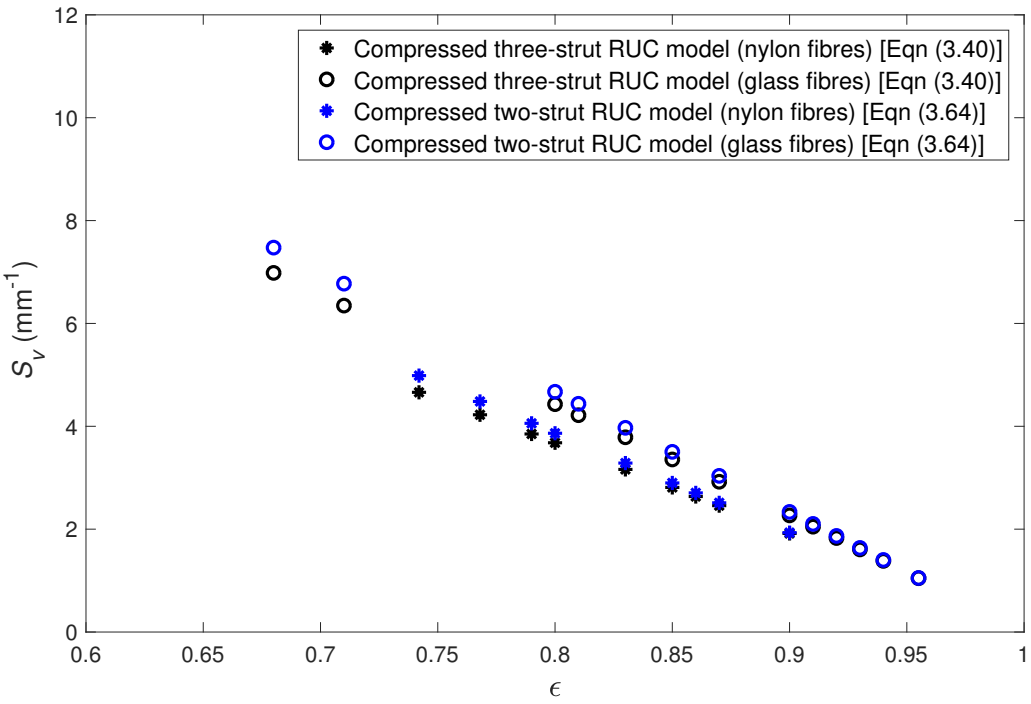

FIGURE 3.10: *Specific surface area versus porosity based on the geometric approach for the compressed three- and two-strut RUC models using the experimental data of Jackson and James [10]*

which is obtained from equation (3.34), into equation (3.33) for the permeability, yielding

$$K = \frac{d_{\parallel} D_h^2}{24 d_s (D_h + d_s)^2} \left[\frac{2}{D_h^2} + \frac{1}{(d_{\parallel} - d_s)^2} \right]^{-1} . \tag{3.42}$$

Equation (3.42) can then be rewritten as a fourth order polynomial in D_h, i.e.

$$\begin{aligned} &\left[24 K d_s - d_{\parallel}(d_{\parallel} - d_s)^2\right] D_h^4 + 48 K d_s^2 D_h^3 + 24 K d_s \left[2(d_{\parallel} - d_s)^2 + d_s^2\right] D_h^2 \\ &+ 96 K d_s^2 (d_{\parallel} - d_s)^2 D_h + 48 K d_s^3 (d_{\parallel} - d_s)^2 = 0 . \end{aligned} \tag{3.43}$$

Setting $g_k = (d_{\parallel} - d_s)^2$, the coefficients for the polynomial

$$a' D_h^4 + b' D_h^3 + c' D_h^2 + d' D_h + e' = 0 ,$$

are given by

$$a' = 24 K d_s - d_{\parallel} g_k , \quad b' = 48 K d_s^2 , \quad c' = 24 K d_s \left[2 g_k + d_s^2\right] , \quad d' = 96 K d_s^2 g_k \quad \text{and} \quad e' = 48 K d_s^3 g_k .$$

The roots of the fourth order polynomial equation are then used as the values for D_h, of which only the positive and real roots are retained. Equation (1.6), defining D_h in terms of S_v, is then in turn used to obtain values for the specific surface area. Some of the resulting predictive values for the specific surface area for both the Le Coq [8] and the Jackson and James [10] data are negative since some of the roots obtained from the polynomial are negative. The kinetic approach is therefore not an applicable method to use to predict values for the specific surface area.

Figure 3.11 shows, as an example, a few negative specific surface area values obtained for the glass fibre data of Jackson and James [10]. The kinetic approach is therefore not a preferred method of calculating the specific surface area values for the compressed three-strut model.

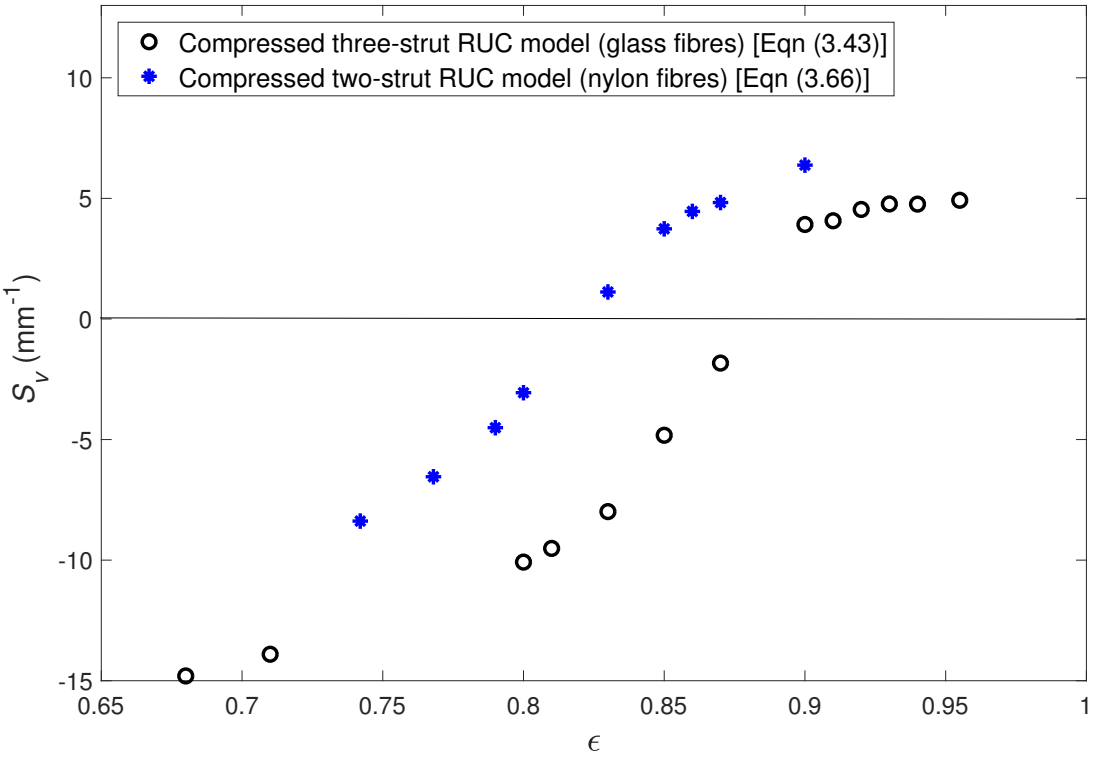

FIGURE 3.11: *Specific surface area versus porosity based on the kinetic approach for the compressed three- and two-strut RUC models using the experimental data of Jackson and James [10]*

The final approach considered for predicting the specific surface area is the combined kinetic-geometric approach.

Combined approach

In this approach $d_{\parallel}$ is used by rearranging equation (3.40) from the geometric approach, to obtain the following expression for $d_{\parallel}$ in terms of S_v:

$$d_{\parallel} = \frac{8d_s d_{\perp} - 12d_s^2}{S_v d_{\perp}^2 - 4d_s}\,. \tag{3.44}$$

Equation (3.44) is then substituted into equation (3.33) to obtain the permeability in terms of the specific surface area. After some algebraic rearrangement and simplification a third order

polynomial is obtained for the specific surface area, i.e.

$$\begin{aligned}
&\left[48Kd_s^3d_\perp^8 + 24Kd_sd_\perp^8g_c\right]S_v^3 \\
&+ \left[-768Kd_s^3d_\perp^7 + 576Kd_s^4d_\perp^6 - 8d_s^3d_\perp^5g_c^2 + 12d_s^4d_\perp^4g_c^2 - 288Kd_s^2d_\perp^6g_c\right]S_v^2 \\
&+ \left[3072Kd_s^3d_\perp^6 - 3072Kd_s^4d_\perp^5 + 128d_s^3d_\perp^4g_c^2 - 320d_s^4d_\perp^3g_c^2 + 192d_s^5d_\perp^2g_c^2 + 1152Kd_s^3d_\perp^4g_c\right]S_v \\
&- 512d_s^3d_\perp^3g_c^2 + 1792d_s^4d_\perp^2g_c^2 - 2048d_s^5d_\perp g_c^2 + 768d_s^6g_c^2 - 12288Kd_s^4d_\perp^4 + 24576Kd_s^5d_\perp^3 \\
&- 12288Kd_s^6d_\perp^2 - 1536Kd_s^4d_\perp^2g_c = 0\,,
\end{aligned} \tag{3.45}$$

where $g_c = (d_\perp - d_s)^2$. The coefficients of the polynomial in specific surface area resulting from the combined kinetic-geometric approach, i.e.

$$a''S_v^3 + b''S_v^2 + c''S_v + d'' = 0\,,$$

are therefore given by

$$\begin{aligned}
a'' &= 48Kd_s^3d_\perp^8 + 24Kd_sd_\perp^8g_c\,, \\
b'' &= -768Kd_s^3d_\perp^7 + 576Kd_s^4d_\perp^6 - 8d_s^3d_\perp^5g_c^2 + 12d_s^4d_\perp^4g_c^2 - 288Kd_s^2d_\perp^6g_c\,, \\
c'' &= 3072Kd_s^3d_\perp^6 - 3072Kd_s^4d_\perp^5 + 128d_s^3d_\perp^4g_c^2 - 320d_s^4d_\perp^3g_c^2 + 192d_s^5d_\perp^2g_c^2 + 1152Kd_s^3d_\perp^4g_c\,,
\end{aligned}$$

and

$$\begin{aligned}
d'' = &-512d_s^3d_\perp^3g_c^2 + 1792d_s^4d_\perp^2g_c^2 - 2048d_s^5d_\perp g_c^2 + 768d_s^6g_c^2 - 12288Kd_s^4d_\perp^4 + 24576Kd_s^5d_\perp^3 \\
&- 12288Kd_s^6d_\perp^2 - 1536Kd_s^4d_\perp^2g_c\,.
\end{aligned}$$

The roots obtained from the third order polynomial equation were then evaluated and the real and positive roots chosen for each porosity value.

The predictions provided by the anisotropic three-strut RUC model using the combined kinetic-geometric approach together with the Le Coq [8] data along with equation (1.6), are shown in Figure 3.12. The correspondence of the predicted values with the experimental data is slightly less (based on the average percentage difference) than that obtained with the geometric approach shown in Figure 3.9. Only the permeability data obtained from mercury porosimetry was used because the permeametry data yields results for the specific surface area that are almost indistinguishable.

The values predicted by the compressed three-strut RUC model using the combined approach and utilizing the Jackson and James [10] data are generally lower than that of the geometric approach. The specific surface area values obtained using the geometric approach are higher in magnitude for $\epsilon < 0.9$ than that obtained using the combined approach, as is noted in Figures 3.10 and 3.13, whereas the values obtained using the combined approach are higher in magnitude for $\epsilon > 0.9$.

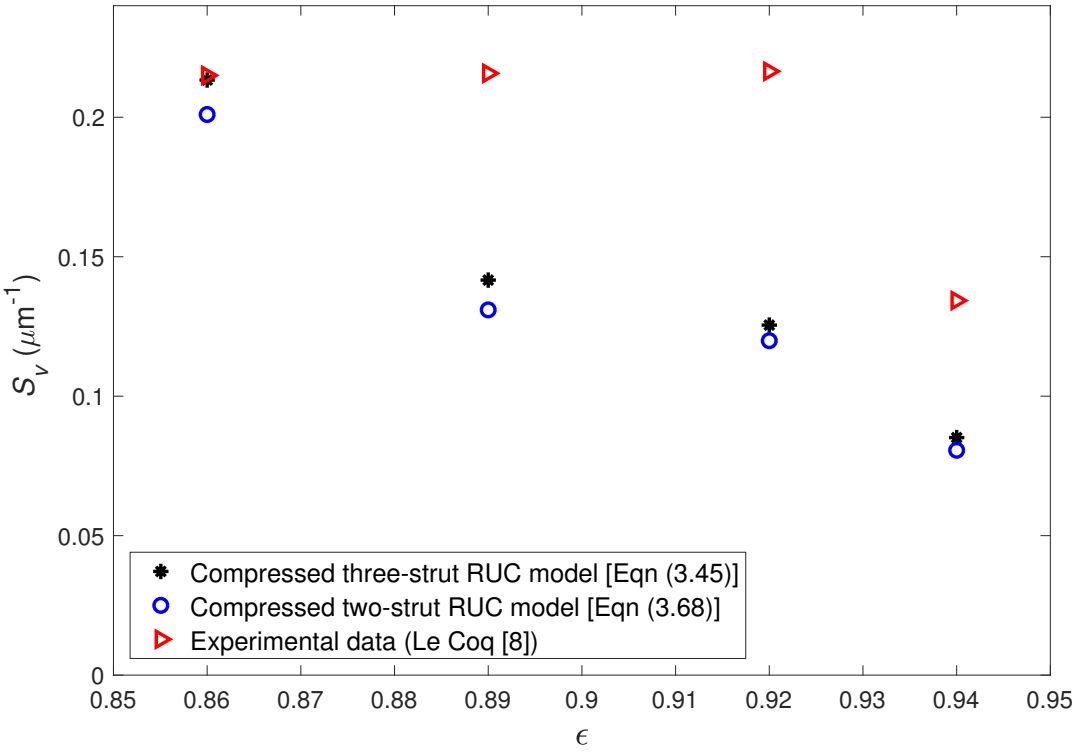

FIGURE 3.12: *Specific surface area versus porosity based on the combined kinetic-geometric approach for the compressed three- and two-strut RUC models using the experimental data of Le Coq [8]*

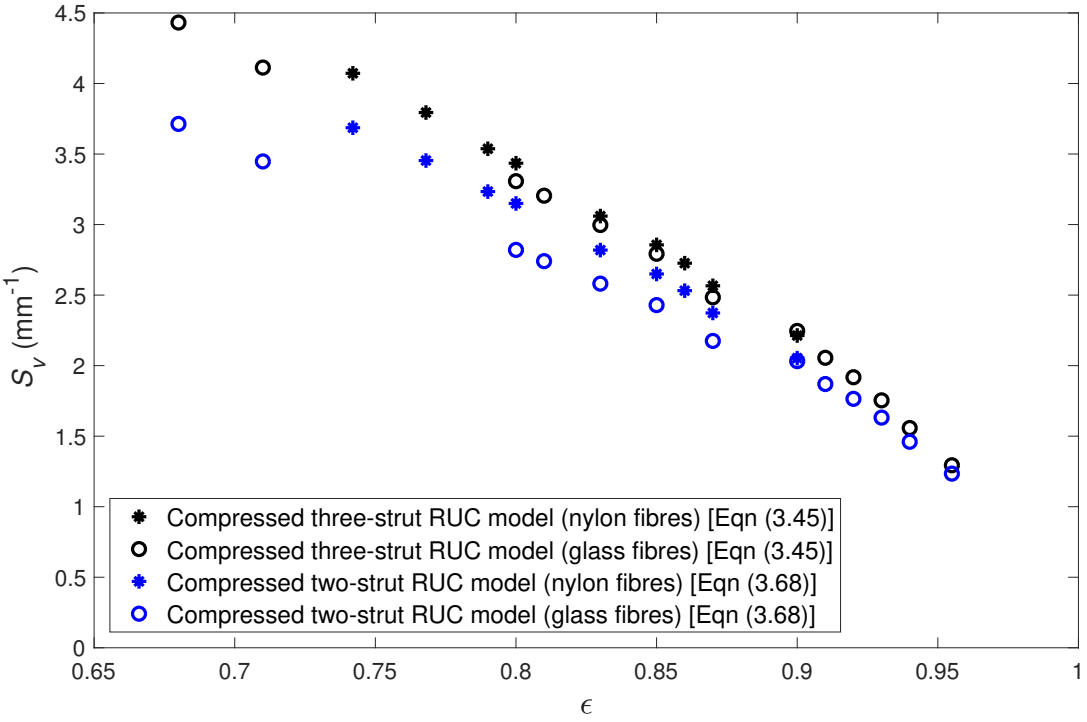

FIGURE 3.13: *Specific surface area versus porosity based on the combined kinetic-geometric approach for the compressed three- and two-strut RUC models using the experimental data of Jackson and James [10]*

3.3 Compressed two-strut RUC model

The second compressed RUC model is the two-strut RUC model. Figure 3.2(a) and (b) shows the cubic two-strut RUC model and the compressed version, respectively. The parameters used are similarly defined as for the compressed three-strut RUC model.

The porosity, defined by equation (2.75), can be deduced from Figure 3.2(b). The solid volume is given by

$$U_s = d_s^2 d_\perp + d_s^2(d_\perp - d_s) = 2d_s^2 d_\perp - d_s^3 \,. \tag{3.46}$$

Since equation (3.10) for U_o is also valid for the two-strut model and U_f is the difference between U_o and U_s, the porosity in terms of d_s, $d_\parallel$ and $d_\perp$ is given by

$$\epsilon = \frac{d_\perp^2 d_\parallel - 2d_s^2 d_\perp + d_s^3}{d_\perp^2 d_\parallel} \,. \tag{3.47}$$

The RUC dimension in the streamwise direction, $d_\parallel$, can also be represented by equation (3.1), where e is determined using the specific non-linear relationship, i.e. equation (3.9), where possible. Similarly to the compressed three-strut model, $d_\perp$ of the compressed two-strut model can be determined from equation (3.47), yielding

$$d_\perp = \frac{d_s\left(d_s + \sqrt{d_s^2 + d_\parallel d_s(\epsilon - 1)}\right)}{d_\parallel(1-\epsilon)} \,. \tag{3.48}$$

The next step is to determine the permeability coefficient by following the same modelling procedure as for the compressed three-strut model. The wall shear stresses determined for the compressed two-strut RUC model are

$$\tau_{w_\parallel} = \frac{6\mu w_\parallel}{(d_\perp - d_s)} \tag{3.49}$$

and

$$\tau_{w_\perp} = \frac{6\mu w_\perp}{(d_\parallel - d_s)} \,, \tag{3.50}$$

and the magnitude of the average duct velocity in the streamwise direction $w_\parallel$ is

$$w_\parallel = \frac{qA_o}{A_{p_\parallel}} = \frac{qd_\perp^2}{(d_\perp - d_s)^2} \,. \tag{3.51}$$

For the two-strut RUC model $A_{p_\parallel}$ is the same as in equation (3.21), but

$$A_{p_\perp} = d_\perp(d_\parallel - d_s) \,, \tag{3.52}$$

as determined from Figure 3.2(b).

Equation (3.23) is also applicable to the compressed two-strut RUC model since conservation of mass is still applicable and consequently the magnitude of the average duct velocity in the transverse direction can similarly be determined as in the case of the compressed three-strut RUC model, i.e.

$$w_\perp = \frac{(d_\perp - d_s)^2}{d_\perp(d_\parallel - d_s)} \cdot \frac{qd_\perp^2}{(d_\perp - d_s)^2} = \frac{qd_\perp}{(d_\parallel - d_s)} \,. \tag{3.53}$$

The solid surfaces parallel and perpendicular to the streamwise directions can be deduced by making use of Figure 3.2(b), resulting in

$$S_{\parallel} = 4d_s(d_{\perp} - d_s) \tag{3.54}$$

and

$$S_{\perp} = 4d_s(d_{\perp} - d_s) + 2d_s^2\,, \tag{3.55}$$

respectively.

Substituting equations (3.51) and (3.53) for the average duct velocities into equations (3.49) and (3.50) for the wall shear stresses, and then consequently substituting equations (3.49) and (3.50) and equations (3.54) and (3.55) for the solid surfaces into equation (2.130) for the total pressure drop, leads to

$$\Delta p = \frac{24 d_s d_{\perp} \mu q}{(d_{\perp} - d_s)^2} \left[\frac{d_{\perp}}{A_{p_{\parallel}}} + \frac{(d_{\perp} - d_s)^3}{(d_{\parallel} - d_s)^2 A_{p_{\parallel}}} + \frac{d_s (d_{\perp} - d_s)^2}{2(d_{\parallel} - d_s)^2 A_{p_{\parallel}}} \right]. \tag{3.56}$$

Substituting equation (3.21) into equation (3.56) and dividing by $d_{\parallel}$ then leads to the pressure gradient equation in terms of d_s, $d_{\parallel}$ and $d_{\perp}$, i.e.

$$\frac{\Delta p}{d_{\parallel}} = \frac{24 d_s d_{\perp}^2 \mu q}{d_{\parallel}(d_{\perp} - d_s)^2} \left[\frac{1}{(d_{\perp} - d_s)^2} + \frac{2d_{\perp} - d_s}{2d_{\perp}(d_{\parallel} - d_s)^2} \right]. \tag{3.57}$$

Comparing Darcy's law, i.e. equation (3.32), with equation (3.57) leads to the following permeability equation:

$$K = \frac{d_{\parallel}(d_{\perp} - d_s)^2}{24 d_s d_{\perp}^2} \left[\frac{1}{(d_{\perp} - d_s)^2} + \frac{2d_{\perp} - d_s}{2d_{\perp}(d_{\parallel} - d_s)^2} \right]^{-1}. \tag{3.58}$$

In order to utilize the Le Coq [8] data, an expression for $d_{\parallel_o}$ should be determined for the two-strut compressed RUC model, similarly as in the case of the three-strut model, due to no data being provided for the pore diameter. Equation (3.34) can once more be used, along with equation (3.47), to determine an expression for $d_{\parallel}$, yielding

$$d_{\parallel} = \frac{2d_s^2(D_h + d_s) - d_s^3}{(1 - \epsilon)(D_h + d_s)^2}\,. \tag{3.59}$$

Equation (3.59) can then be substituted into equation (3.1) and an average value for $d_{\parallel_o}$ can be determined by utilizing the data for ϵ, e and D_h. The $d_{\parallel_o}$-value determined equals 8.91 μm and using this value and the specific non-linear relationship, given by equation (3.9), to determine e, $d_{\parallel}$ can consequently be determined from equation (3.1).

In Figure 3.7 the predictions of equation (3.58) are compared to the experimental data of Le Coq [8]. It can be seen that the two-strut RUC model gives lower predicted values than the three-strut RUC model.

For the Jackson and James [10] data set the lack of e and D_h data once more leads to the use of equation (3.8), i.e. the general non-linear relationship, to determine e. An expression for $d_{\parallel_o}$ can also, similarly as in the case of the three-strut model, be determined using equations (2.106) and (2.108), which leads to

$$d_{\parallel_o} = \frac{d_s}{1 - \frac{\epsilon_o}{\psi_o}}\,, \tag{3.60}$$

where

$$\psi_o = \frac{2}{3}\sqrt{3\epsilon_o + 1}\,\cos\left[\frac{1}{3}\cos^{-1}\left(\frac{9\epsilon_o - 27\epsilon_o^2 + 2}{2\sqrt{27\epsilon_o^3 + 27\epsilon_o^2 + 9\epsilon_o + 1}}\right)\right] + \frac{1}{3}\,. \tag{3.61}$$

The streamwise pore diameter can once again be obtained from equation (3.1), i.e.

$$d_{\parallel} = \frac{d_{\parallel_o}(1-\epsilon_o)}{1-\epsilon}\,, \tag{3.62}$$

where $d_{\parallel_o}$ is given by equation (3.60). The value determined for $d_{\parallel_o}$ by the two-strut model for the glass fibres is 1.050 mm and for the nylon fibres it is equal to 0.810 mm.

The transverse pore diameter can then be solved using equation (3.48) and therefore the permeability can be determined using equation (3.58).

In Figure 3.8 the predictions of equation (3.58) are compared to the experimental data of Jackson and James [10]. The two-strut model under-predicts the experimental permeability data for the nylon fibres for the porosities below 0.9. As opposed to the three-strut model, the two-strut model yields fairly accurate predictions for the glass fibre for the porosities above 0.9.

The different approaches used to express the specific surface area as a function of porosity are once again the geometric, kinetic and combined approaches.

Geometric approach

The geometric approach for determining the specific surface area is performed by following the same procedure as for the three-strut model, thus yielding

$$A_s = 8(d_{\perp} - d_s)d_s + 2d_s^2\,, \tag{3.63}$$

and hence

$$S_v = \frac{8(d_{\perp} - d_s)d_s + 2d_s^2}{d_{\perp}^2 d_{\parallel}} = \frac{8d_s d_{\perp} - 6d_s^2}{d_{\perp}^2 d_{\parallel}}\,. \tag{3.64}$$

Equation (3.64) is also shown in Figure 3.9 as a function of porosity, using the Le Coq [8] data. It can be observed in Figure 3.9 that the predictions of the compressed two-strut RUC model based on the geometric approach, gives slightly higher predictions than those of the three-strut model.

In Figure 3.10 equation (3.64) is plotted using the Jackson and James [10] data. The same observations are made as in Figure 3.9 with regards to the predictions provided by the compressed two-strut model in comparison to that of the compressed three-strut model.

Kinetic approach

The specific surface area determined using a kinetic approach for the two-strut RUC model can be deduced by substituting equation (3.41) for the RUC dimension in the transverse direction in terms of the hydraulic diameter into equation (3.58) for the permeability. This substitution leads to the expression for the permeability in terms of the hydraulic diameter, i.e.

$$K = \frac{d_{\parallel} D_h^2}{24 d_s (D_h + d_s)^2}\left[\frac{1}{D_h^2} + \frac{2D_h + d_s}{2(D_h + d_s)(d_{\parallel} - d_s)^2}\right]^{-1}\,. \tag{3.65}$$

Subsequently a fifth order polynomial for D_h is obtained by expanding and rearranging equation (3.65) and leads to

$$\begin{aligned}&\left[24Kd_s - d_{\parallel}(d_{\parallel}-d_s)^2\right]D_h^5 + \left[60Kd_s^2 - d_sd_{\parallel}(d_{\parallel}-d_s)^2\right]D_h^4 + \left[24Kd_s(d_{\parallel}-d_s)^2 + 48Kd_s^3\right]D_h^3\\ &+ \left[72Kd_s^2(d_{\parallel}-d_s)^2 + 12Kd_s^4\right]D_h^2 + 72Kd_s^3(d_{\parallel}-d_s)^2D_h + 24Kd_s^4(d_{\parallel}-d_s)^2 = 0\,. \end{aligned} \tag{3.66}$$

Setting $g_k = (d_{\parallel}-d_s)^2$, the coefficients of the polynomial in D_h,

$$a'D_h^5 + b'D_h^4 + c'D_h^3 + d'D_h^2 + e'D_h + f' = 0\,,$$

are therefore given by

$$\begin{aligned}&a' = 24Kd_s - d_{\parallel}g_k\,,\quad b' = 60Kd_s^2 - d_sd_{\parallel}g_k\,,\quad c' = 24Kd_s\left(g_k + 2d_s^2\right)\,,\\ &d' = 12Kd_s^2\left(6g_k + d_s^2\right)\,,\quad e' = 72Kd_s^3g_k \text{ and } f' = 24Kd_s^4g_k\,.\end{aligned}$$

Using the hydraulic diameter equation, equation (1.6), S_v can then be determined from the polynomial roots. Similarly, as in the case of the compressed three-strut model, some of the roots were not positive and real. The specific surface area obtained therefore also contained negative values for both the data sets of Le Coq [8] and Jackson and James [10]. This approach was consequently also not preferred for predicting the specific surface area by using the compressed two-strut model. Figure 3.11 illustrates this with an example using the nylon fibre data given by Jackson and James [10] applied to the compressed two-strut model.

Combined approach

The combined kinetic-geometric approach for determining the specific surface area commences with determining $d_{\parallel}$ in terms of S_v by rearranging equation (3.64) as follows:

$$d_{\parallel} = \frac{8d_sd_{\perp} - 6d_s^2}{d_{\perp}^2S_v}\,. \tag{3.67}$$

Substituting equation (3.67) into equation (3.58) for the permeability leads to the specific surface area polynomial

$$\begin{aligned}&\left[24Kd_s^3d_{\perp}^8 + 12Kd_sd_{\perp}^7(2d_{\perp}-d_s)(d_{\perp}-d_s)^2\right]S_v^3\\ &+ \left[-48Kd_s^2d_{\perp}^6(8d_{\perp}d_s - 6d_s^2) - d_s^2d_{\perp}^4(d_{\perp}-d_s)^4(8d_{\perp}d_s - 6d_s^2)\right]S_v^2\\ &+ \left[24Kd_sd_{\perp}^4(8d_{\perp}d_s - 6d_s^2)^2 + 2d_sd_{\perp}^2(d_{\perp}-d_s)^4(8d_{\perp}d_s - 6d_s^2)^2\right]S_v\\ &- (d_{\perp}-d_s)^4(8d_{\perp}d_s - 6d_s^2)^3 = 0\,.\end{aligned} \tag{3.68}$$

Setting $g_c = (d_{\perp}-d_s)^2$ and $f = 8d_{\perp}d_s - 6d_s^2$, the coefficients of the polynomial

$$a''S_v^3 + b''S_v^2 + c''S_v + d'' = 0\,,$$

are therefore given by

$$\begin{aligned}&a'' = 24Kd_s^3d_{\perp}^8 + 12Kd_sd_{\perp}^7(2d_{\perp}-d_s)g_c\,,\quad b'' = -48Kd_s^2d_{\perp}^6f - d_s^2d_{\perp}^4g_c^2f\,,\\ &c'' = 24Kd_sd_{\perp}^4f^2 + 2d_sd_{\perp}^2g_c^2f^2 \text{ and } d'' = -g_c^2f^3\,.\end{aligned}$$

The specific surface area is then determined from the roots of the polynomial equation (3.68), where the real and positive root was chosen for each porosity value.

The results using the Le Coq [8] data is shown in Figure 3.12 and it can be observed that the two-strut model gives slightly lower predictions than the three-strut model, as opposed to the results in Figures 3.9 and 3.10 for the geometric approach where the two-strut model gives slightly higher predictions than the three-strut model predictions. Once again, only the mercury porosimetry data was utilized. Furthermore, the results obtained using the Jackson and James [10] data are shown in Figure 3.13. Similarly to Figures 3.9 and 3.10, it can be observed in Figure 3.13 that the two-strut model gives higher predictions than the three-strut model.

In the next section the RUC models will be adapted geometrically to account for the application of the models to soft polyester fibrous media.

3.4 Soft polyester fibrous media application

The three-strut and two-strut RUC models are adapted to account for the compression of soft polyester fibrous media by multiplying the streamwise strut diameters with the compression ratio. Van Heyningen [7] also adapted the two-strut RUC model in order to predict the permeability through compressed fibrous media but used specific compression ratios for the streamwise strut diameters. The adaptation to the two-strut model will therefore be more general in this study. The three-strut model will similarly be adapted in this study which was not done by Van Heyningen [7]. Specific surface area equations using the geometric, kinetic and combined approaches will also be derived based on the soft compressed three- and two-strut RUC models. In order to apply and evaluate these adapted RUC models, data obtained from Akaydin et al. [11] was used. The latter authors measured and investigated the permeability of soft fibrous material at different levels of compression. They obtained their data using regular polyester pillow material. In the Akaydin et al. [11] data set $1 - e$ was provided, which in turn was used to determine e. All the relevant data points are given in Table 3.4.

Due to the given e-values the specific non-linear relationship can be used, given by equation (3.9), to obtain an expression for e in terms of ϵ, resulting in a value of $C = 0.003$.

TABLE 3.4: *Experimental data of Akaydin et al. [11] for soft polyester fibre media with* $d_s = 10\,\mu m$

e	ϵ	K [μm^2]
0.15	0.9780	620
0.27	0.9883	1340
0.37	0.9914	2110
0.45	0.9930	2820
0.55	0.9941	3720
0.78	0.9959	6170
1	0.9968	9220

First the adaptation of the three-strut RUC model will be considered.

3.4.1 Three-strut RUC model

In the case of the adapted three-strut RUC model, geometrical adjustments were made as illustrated in Figure 3.3(b) in which d_s is divided into the two components $d_{s_\parallel}$, which denotes the streamwise solid dimension, and $d_{s_\perp}$, which denotes the transverse streamwise solid dimension.

In order to incorporate these parameters into the model procedure, $d_{s_\parallel}$ is set equal to ed_s and $d_{s_\perp}$ equal to d_s since the compression is only in the streamwise direction.

The permeability of the adapted three-strut RUC model can be attained by first determining an expression for $d_{\parallel_o}$. As in the case of the Jackson and James [10] data given in Section 3.2, no data for D_h is provided by Akaydin et al. [11]. Similarly $d_{\parallel_o}$ will be determined using equations (3.36) and (3.37) by assuming isotropy in the uncompressed state. The expression for $d_\parallel$ can be determined next using the obtained $d_{\parallel_o}$-value together with equation (3.1).

The porosity can furthermore be determined similarly as in the case of the rigid compressed models, but instead the solid and fluid volumes are deduced by using the parameters as indicated in Figure 3.3, yielding

$$\epsilon = \frac{d_\perp^2 d_\parallel - 2ed_s^2 d_\perp + 2ed_s^3 - d_s^2 d_\parallel}{d_\perp^2 d_\parallel} \,. \tag{3.69}$$

Equation (3.69) can also similarly as in the case of the rigid compressed models be utilized to determine $d_\perp$, yielding

$$d_\perp = \frac{d_s \left(ed_s + \sqrt{e^2 d_s^2 + (1-\epsilon) d_\parallel (d_\parallel - 2ed_s)} \right)}{d_\parallel (1-\epsilon)} \,. \tag{3.70}$$

Equation (2.130) for the pressure drop is utilized once more to determine the permeability. Consequently equation (2.131) is used again to obtain the wall shear stresses $\tau_{w_\parallel}$, $\tau_{w_{\perp_1}}$ and $\tau_{w_{\perp_2}}$. The wall shear stresses $\tau_{w_\parallel}$ and $\tau_{w_{\perp_2}}$ are the same as given by equations (3.16) and (3.18), respectively, whereas for the soft compressed three-strut RUC model $\tau_{w_{\perp_1}}$ becomes

$$\tau_{w_{\perp_1}} = \frac{6\mu w_\perp}{(d_\parallel - ed_s)} \,. \tag{3.71}$$

The magnitude of the average duct velocity in the streamwise direction, $w_\parallel$, is also the same as in equation (3.22). From Figure 3.3(b) the streamwise and transverse cross-sectional flow areas can be determined. The former is the same as in equation (3.21), but the latter is given by

$$A_{p_\perp} = (d_\perp - d_s)(d_\parallel - ed_s) \,, \tag{3.72}$$

for the soft compressed model. Utilizing equations (3.21) to (3.23) and (3.72) the magnitude of the average duct velocity in the transverse direction can be determined, i.e.

$$w_\perp = \frac{d_\perp - d_s}{d_\parallel - ed_s} \cdot \frac{qd_\perp^2}{(d_\perp - d_s)^2} = \frac{qd_\perp^2}{(d_\parallel - ed_s)(d_\perp - d_s)} \,, \tag{3.73}$$

due to equation (3.23) still being applicable.

The solid surfaces parallel and perpendicular to the streamwise direction can be determined by again considering Figure 3.3. The total solid surface parallel to the streamwise direction is determined to be

$$S_\parallel = 4ed_s(d_\perp - d_s) \,. \tag{3.74}$$

For the solid surfaces perpendicular to the streamwise direction, $S_{\perp_1}$ is the same as in equation (3.27) where-as

$$S_{\perp_2} = 4d_s(d_\parallel - ed_s) \,. \tag{3.75}$$

Substituting all the relevant equations into equation (2.130), leads to

$$\Delta p = \frac{24 d_s d_\perp^2 \mu q}{(d_\perp - d_s)^2} \left[\frac{(e+1)}{(d_\perp - d_s)^2} + \frac{1}{(d_\parallel - ed_s)^2} \right] \,. \tag{3.76}$$

Comparison of equation (3.76) to equation (3.32) finally yields the permeability equation, given by

$$K = \frac{d_{\parallel}(d_{\perp} - d_s)^2}{24 d_s d_{\perp}^2} \left[\frac{(e+1)}{(d_{\perp} - d_s)^2} + \frac{1}{(d_{\parallel} - e d_s)^2} \right]^{-1}, \tag{3.77}$$

which is graphically illustrated in Figure 3.14. The resulting model predictions are also shown for the cases where $d_{\parallel_o}$ are taken to be equal to 75% and 50% of the value of $d_{\parallel_o}$ where isotropy is assumed, representing relative percentage differences of 25% and 50%, respectively. This is due the original value being based on the assumption of isotropy which may represent an over-simplifying assumption due to the absence of D_h-values.

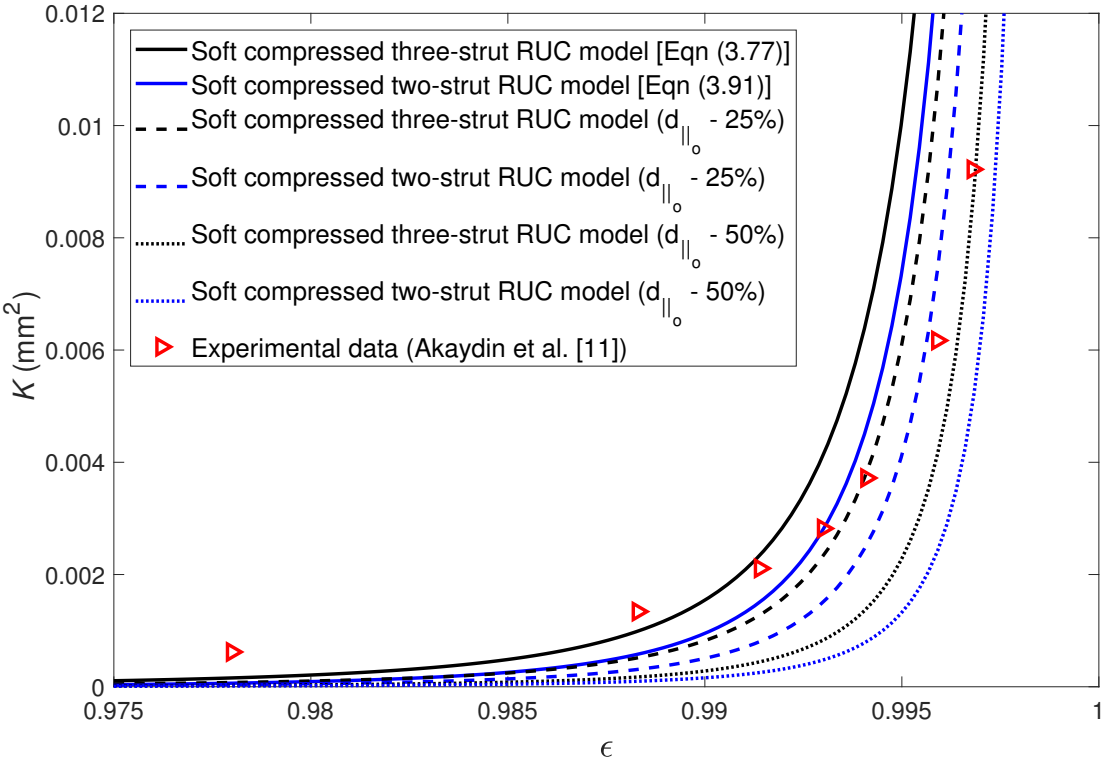

FIGURE 3.14: *Permeability versus porosity for the soft compressed RUC models compared to the experimental data of Akaydin et al. [11]*

In Figure 3.14 it is evident that the majority of data points are enclosed between the model predictions provided by the soft compressed three-strut RUC model based on the isotropic $d_{\parallel_o}$ and $d_{\parallel_o} - 50\%$ values. The prediction based on the $d_{\parallel_o} - 25\%$ seems to correspond the best with the permeability data although a slight difference in trend is observed.

The specific surface area for the soft compressed three-strut RUC model will be determined using the geometric, kinetic and combined kinetic-geometric approaches in the following section.

Geometric approach

In order to determine the specific surface area in terms of the porosity using a geometric approach, the total surface area can first be obtained by adding all the respective surface areas in equations

(3.74), (3.27) and (3.75), i.e.

$$A_s = S_{\parallel} + S_{\perp_1} + S_{\perp_2} = 4d_s(d_{\perp} - d_s)(e+1) + 4d_s(d_{\parallel} - ed_s)\,. \tag{3.78}$$

Substituting equations (3.78) and (3.10) into equation (1.3), where $V_o = U_o$, then leads to the specific surface area equation

$$S_v = \frac{4d_s(d_{\perp} - d_s)(e+1) + 4d_s(d_{\parallel} - ed_s)}{d_{\perp}^2 d_{\parallel}}\,. \tag{3.79}$$

The predictions provided by equation (3.79), using the data of Akaydin et al. [11], are shown in Figure 3.15. The predictions for the different approximations for $d_{\parallel_o}$ are once again shown.

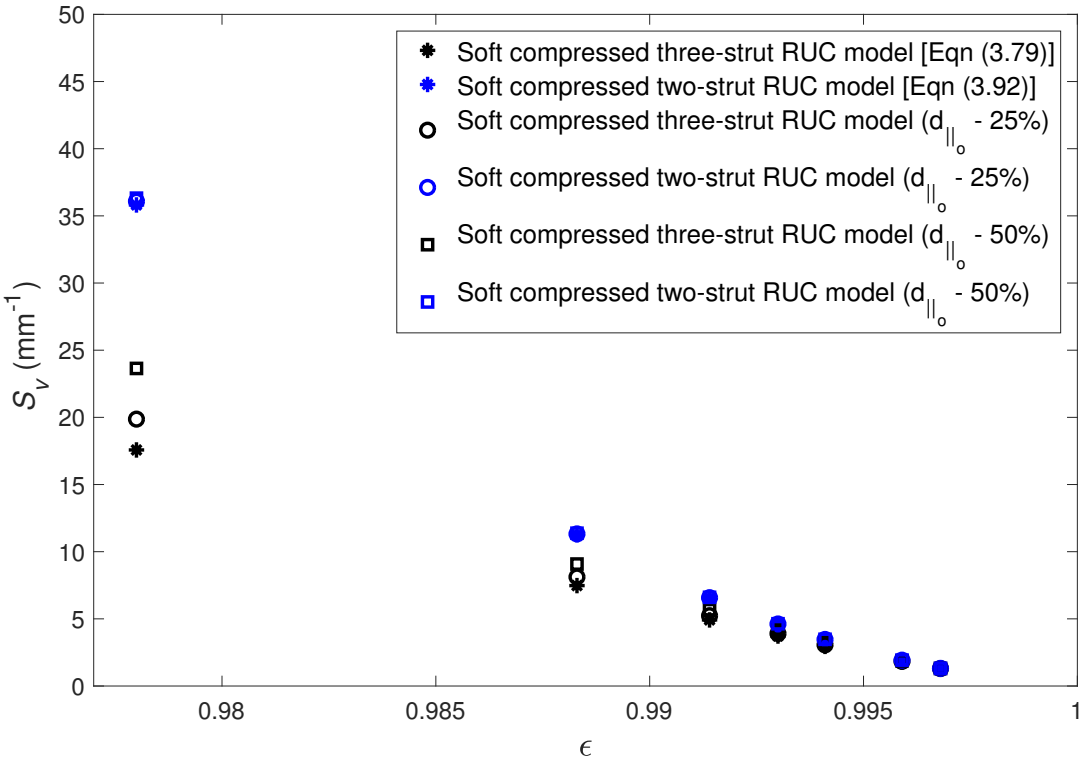

FIGURE 3.15: *Specific surface area versus porosity based on the geometric approach for the soft compressed three- and two-strut RUC models using the experimental data of Akaydin et al. [11]*

In Figure 3.15 it can be observed that as the $d_{\parallel_o}$-value decreases, the specific surface area predictions increase. The difference between the three-strut model predictions for the different $d_{\parallel_o}$-values becomes more enhanced as the porosity decreases.

Kinetic approach

The kinetic approach of determining the specific surface area starts with the substitution of equation (3.41) into the permeability, given by equation (3.77), and results in

$$K = \frac{d_{\parallel} D_h^2}{24d_s(D_h + d_s)^2}\left[\frac{(e+1)}{D_h^2} + \frac{1}{(d_{\parallel} - ed_s)^2}\right]^{-1}\,. \tag{3.80}$$

Rearranging equation (3.80) leads to the following fourth order polynomial in D_h:

$$\begin{aligned}&\left[24Kd_s - d_{\|}(d_{\|} - ed_s)^2\right] D_h^4 + 48Kd_s^2 D_h^3 + 24Kd_s\left[(e+1)(d_{\|} - ed_s)^2 + d_s^2\right] D_h^2 \\ &+ 48Kd_s^2(e+1)(d_{\|} - ed_s)^2 D_h + 24Kd_s^3(e+1)(d_{\|} - ed_s)^2 = 0\,. \end{aligned} \tag{3.81}$$

Setting $g_k = (d_{\|} - ed_s)^2$, the coefficients of the polynomial in D_h,

$$a' D_h^4 + b' D_h^3 + c' D_h^2 + d' D_h + e' = 0\,,$$

therefore becomes

$$\begin{aligned}&a' = 24Kd_s - d_{\|}g_k\,,\quad b' = 48Kd_s^2\,,\quad c' = 24Kd_s\left[(e+1)g_k + d_s^2\right]\,, \\ &d' = 48Kd_s^2(e+1)g_k \;\text{ and }\; e' = 24Kd_s^3(e+1)g_k\,.\end{aligned}$$

The specific surface area can then be determined by using the hydraulic diameter, defined by equation (1.6), and setting it equal to the polynomial roots. The positive and real polynomial root was chosen in each case, where possible. For the lowest porosity value, the roots were however all negative resulting in a negative value for the specific surface area. The predictions for the specific surface area are shown in Figure 3.16 as a function of porosity.

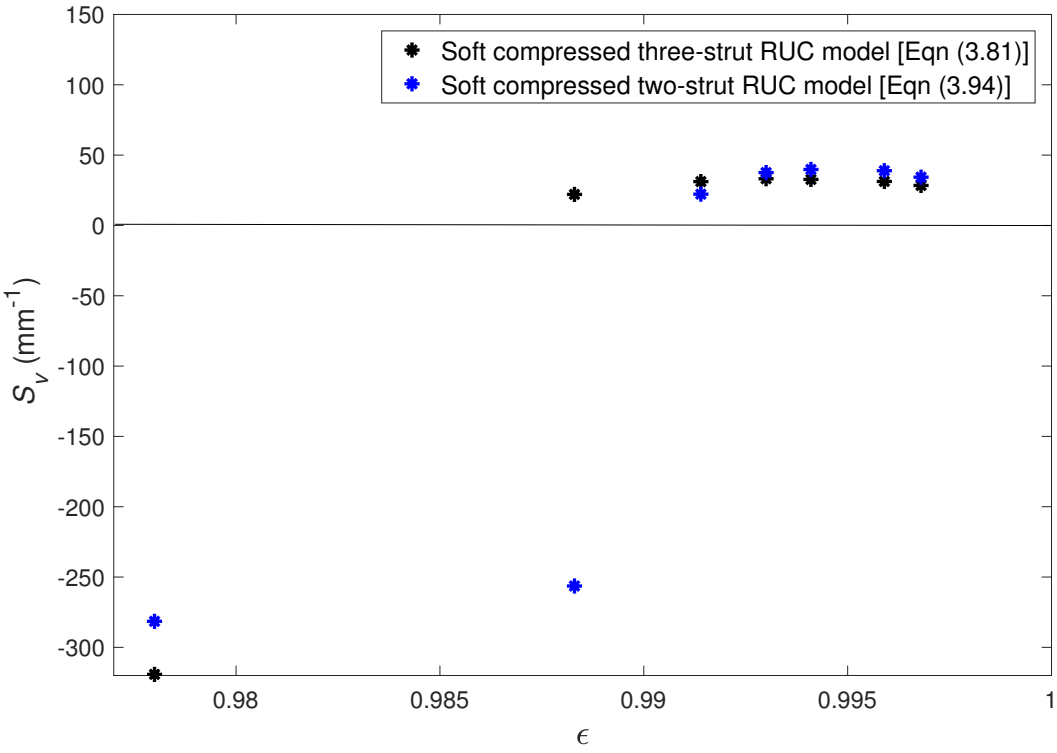

FIGURE 3.16: *Specific surface area versus porosity based on the kinetic approach for the soft compressed three- and two-strut RUC models using the experimental data of Akaydin et al. [11]*

Similarly to the rigid compressed three-strut model, the kinetic approach gives a negative specific surface area value, which is not viable. This approach for determining the specific surface area is once again not preferred for the compressed RUC models.

Combined approach

In the combined kinetic-geometric approach the specific surface area is determined by first rearranging equation (3.79) to obtain $d_{\parallel}$ in terms of S_v, i.e.

$$d_{\parallel} = \frac{4d_s\left[\sqrt{g_c}(e+1) - ed_s\right]}{d_{\perp}^2 S_v - 4d_s}\,, \tag{3.82}$$

where $g_c = (d_{\perp} - d_s)^2$.

Equation (3.82) is then substituted into equation (3.77) and rearranged to produce the specific surface area polynomial

$$\begin{aligned}&\left[24e^2Kd_s^3d_{\perp}^8(e+1) + 24Kd_sd_{\perp}^8g_c\right]S_v^3 + \left[-96e^2Kd_s^4d_{\perp}^6(e+1) - 288Kd_s^2d_{\perp}^6g_c\right.\\&-192eKd_s^3d_{\perp}^6\sqrt{g_c}(e+1)^2 - 4e^2d_s^3d_{\perp}^4g_c^2\sqrt{g_c}(e+1) + 4e^3d_s^4d_{\perp}^4g_c^2\left]S_v^2 + \right[1152Kd_s^3d_{\perp}^4g_c\right.\\&+768eKd_s^4d_{\perp}^4\sqrt{g_c}(e+1)^2 - 32e^2d_s^4d_{\perp}^2g_c^2\sqrt{g_c}(e+1) + 384Kd_s^3d_{\perp}^4g_c(e+1)^3\\&\left.+32ed_s^3d_{\perp}^2g_c^3(e+1)^2\right]S_v - 1536Kd_s^4d_{\perp}^2g_c - 1536Kd_s^4d_{\perp}^2g_c(e+1)^3 - 64d_s^3g_c^3\sqrt{g_c}(e+1)^3\\&+64ed_s^4g_c^3(e+1)^2 = 0\,.\end{aligned} \tag{3.83}$$

Expressing the polynomial in the following reduced form

$$a''S_v^3 + b''S_v^2 + c''S_v + d'' = 0\,,$$

yields the coefficients

$$\begin{aligned}a'' &= 24e^2Kd_s^3d_{\perp}^8(e+1) + 24Kd_sd_{\perp}^8g_c\,,\\b'' &= -96e^2Kd_s^4d_{\perp}^6(e+1) - 288Kd_s^2d_{\perp}^6g_c - 192eKd_s^3d_{\perp}^6\sqrt{g_c}(e+1)^2 - 4e^2d_s^3d_{\perp}^4g_c^2\sqrt{g_c}(e+1)\\&\quad + 4e^3d_s^4d_{\perp}^4g_c^2\,,\\c'' &= 1152Kd_s^3d_{\perp}^4g_c + 768eKd_s^4d_{\perp}^4\sqrt{g_c}(e+1)^2 - 32e^2d_s^4d_{\perp}^2g_c^2\sqrt{g_c}(e+1) + 384Kd_s^3d_{\perp}^4g_c(e+1)^3\\&\quad + 32ed_s^3d_{\perp}^2g_c^3(e+1)^2\,,\\\text{and}\quad d'' &= -1536Kd_s^4d_{\perp}^2g_c - 1536Kd_s^4d_{\perp}^2g_c(e+1)^3 - 64d_s^3g_c^3\sqrt{g_c}(e+1)^3 + 64ed_s^4g_c^3(e+1)^2\,.\end{aligned}$$

The specific surface area values are determined from the roots of the polynomial where the real root is again chosen in each case. The results are shown in Figure 3.17.

Comparing Figures 3.15 and 3.17 it is evident that the specific surface area values predicted by the soft compressed three-strut RUC model using a combined approach are slightly lower than the values obtained using the geometric approach. Figure 3.17 also shows that the specific surface area decreases as the $d_{\parallel_o}$-value decreases.

3.4.2 Two-strut RUC model

In Figure 3.4 the soft compressed two-strut RUC model is illustrated. Similarly as in the case of the soft compressed three-strut RUC model, the strut diameter d_s is divided into two components, $d_{s_{\parallel}} = ed_s$ and $d_{s_{\perp}} = d_s$. Equations (3.60) and (3.61) are furthermore also used to determine $d_{\parallel_o}$ since no D_h-values have been provided by Akaydin et al. [11] and isotropy in the uncompressed state has to be assumed. The pore diameter parallel to the streamwise direction $d_{\parallel}$ can then be solved using equation (3.1). The same variations in the values of $d_{\parallel_o}$ as in the case of the three-strut model will be considered for the two-strut model.

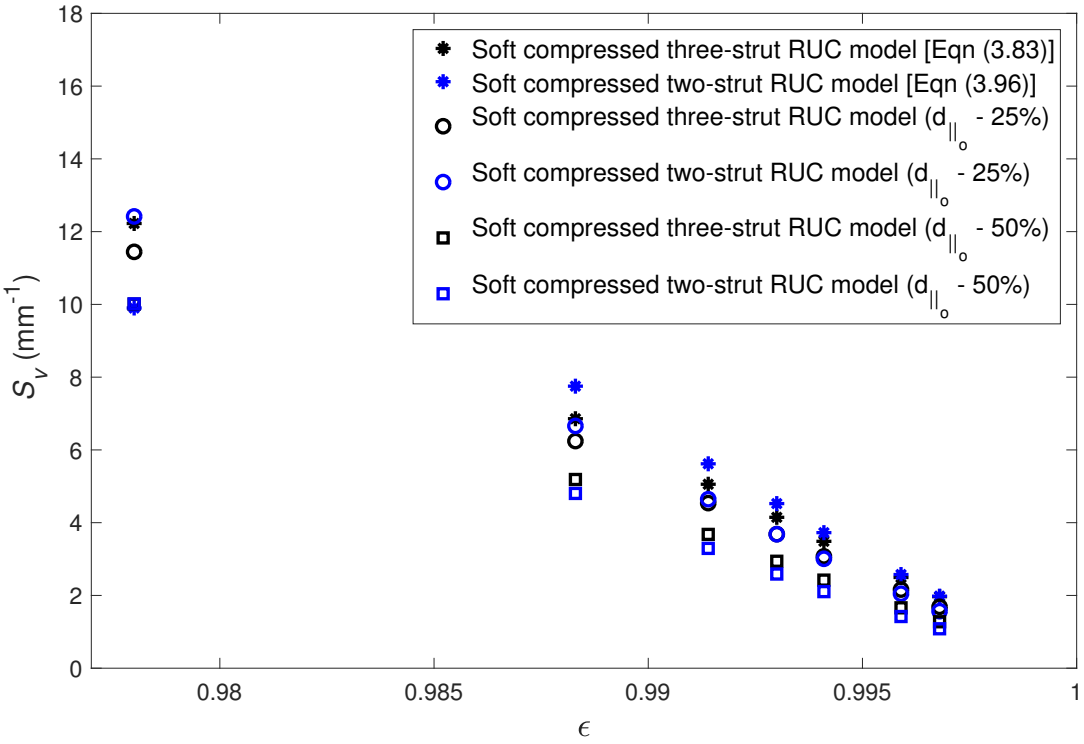

FIGURE 3.17: *Specific surface area versus porosity based on the combined kinetic-geometric approach for the soft compressed three- and two-strut RUC models using the experimental data of Akaydin et al. [11]*

The fluid volume can be determined from Figure 3.4(b) in a similar manner as in the cases of the other compressed RUC models. The porosity can therefore be deduced and is given by

$$\epsilon = \frac{d_\perp^2 d_\parallel - 2ed_s^2 d_\perp + ed_s^3}{d_\perp^2 d_\parallel}\,, \tag{3.84}$$

and consequently

$$d_\perp = \frac{d_s\left(ed_s + \sqrt{e^2 d_s^2 + ed_s d_\parallel(\epsilon - 1)}\right)}{d_\parallel(1-\epsilon)}\,. \tag{3.85}$$

Using equation (2.131) to determine the wall shear stresses, it can be deduced that $\tau_{w_\parallel}$ is then the same as equation (3.49), and that $\tau_{w_\perp}$ becomes

$$\tau_{w_\perp} = \frac{6\mu w_\perp}{(d_\parallel - ed_s)}\,, \tag{3.86}$$

for the soft compressed two-strut model. The magnitude of the streamwise average duct velocity is the same as in equation (3.51), and $w_\perp$, is determined by first finding the relationships between the cross-sectional flow areas. The streamwise and transverse cross-sectional flow areas can be determined from Figure 3.4(b), where $A_{p_\parallel}$ is once again given by equation (3.21), and $A_{p_\perp}$ is given by

$$A_{p_\perp} = d_\perp(d_\parallel - ed_s)\,. \tag{3.87}$$

Using equation (3.23) then leads to

$$w_\perp = \frac{qd_\perp}{(d_\parallel - ed_s)}\,. \tag{3.88}$$

The total solid surface area parallel to the streamwise direction is given by

$$S_{\parallel} = 4ed_s(d_{\perp} - d_s)\,, \tag{3.89}$$

and the total solid surface area perpendicular to the streamwise direction, $S_{\perp}$, is the same as in equation (3.55). Substituting equations (3.21), (3.49), (3.55), (3.86) and (3.89) into equation (2.130), leads to

$$\Delta p = \frac{24d_s d_{\perp}^2 \mu q}{(d_{\perp} - d_s)^2}\left[\frac{e}{(d_{\perp} - d_s)^2} + \frac{2d_{\perp} - d_s}{2d_{\perp}(d_{\parallel} - ed_s)^2}\right], \tag{3.90}$$

and the permeability is given by

$$K = \frac{d_{\parallel}(d_{\perp} - d_s)^2}{24d_s d_{\perp}^2}\left[\frac{e}{(d_{\perp} - d_s)^2} + \frac{2d_{\perp} - d_s}{2d_{\perp}(d_{\parallel} - ed_s)^2}\right]^{-1}. \tag{3.91}$$

The permeability predictions resulting from equation (3.91) are shown in Figure 3.14. The permeability predicted by the two-strut model is lower than that of the three-strut model for each $d_{\parallel_o}$-value considered.

The geometric, kinetic and combined kinetic-geometric approaches will also be applied to determine the specific surface area for the soft compressed two-strut RUC model.

Geometric approach

The specific surface area for the soft compressed two-strut RUC model determined using the geometric approach is obtained similarly as in the cases of the other compressed RUC models and yields

$$S_v = \frac{4d_s(d_{\perp} - d_s)(e+1) + 2d_s^2}{d_{\perp}^2 d_{\parallel}}\,. \tag{3.92}$$

The predictions provided by equation (3.92) are also shown in Figure 3.15. It can be observed that the specific surface area predictions of the soft compressed two-strut RUC model are higher than that of the soft compressed three-strut RUC model predictions. Other than in the case of three-strut model the different $d_{\parallel_o}$-values do not give significant differences in the results for the two-strut model.

Kinetic approach

The specific surface area determined using the kinetic approach commences once more with expressing the permeability of the soft compressed two-strut RUC model, given by equation (3.91) in terms of the hydraulic diameter, i.e.

$$K = \frac{d_{\parallel} D_h^2}{24d_s(D_h + d_s)^2}\left[\frac{e}{D_h^2} + \frac{2D_h + d_s}{2(D_h + d_s)(d_{\parallel} - ed_s)^2}\right]^{-1}. \tag{3.93}$$

Setting $g_k = (d_{\parallel} - ed_s)^2$, the following fourth order polynomial for D_h can then be determined from equation (3.93):

$$\begin{aligned}&(24Kd_s - d_{\parallel}g_k)D_h^5 + \left(60Kd_s^2 - d_s d_{\parallel} g_k\right)D_h^4 + 24Kd_s\left(eg_k + 2d_s^2\right)D_h^3 \\ &+ 12Kd_s^2\left(6eg_k + d_s^2\right)D_h^2 + 72eKd_s^3 g_k D_h + 24Ked_s^4 g_k = 0\,.\end{aligned} \tag{3.94}$$

The coefficients of the polynomial in D_h, given by

$$a'D_h^5 + b'D_h^4 + c'D_h^3 + d'D_h^2 + e'D_h + f' = 0\,,$$

are therefore

$$a' = 24Kd_s - d_\parallel g_k\,,\quad b' = 60Kd_s^2 - d_s d_\parallel g_k\,,\quad c' = 24Kd_s\left(eg_k + 2d_s^2\right)\,,$$
$$d' = 12Kd_s^2\left(6eg_k + d_s^2\right)\,,\quad e' = 72eKd_s^3 g_k \text{ and } f' = 24Ked_s^4 g_k\,.$$

Some of the roots obtained by solving equation (3.94) only gave negative values for the specific surface area when equation (1.6) was used, as indicated in Figure 3.16. Since the predicted specific surface area values do not decrease with an increase in porosity as is the case with the geometric and combined approaches, the kinetic approach is once again found not to be adequate in predicting the specific surface area.

Combined approach

The combined kinetic-geometric approach for determining the specific surface area commences with determining $d_\parallel$ in terms of S_v by rearranging equation (3.92), yielding

$$d_\parallel = \frac{4d_s\sqrt{g_c}(e+1) + 2d_s^2}{d_\perp^2 S_v}\,, \tag{3.95}$$

where $g_c = (d_\perp - d_s)^2$. Substituting equation (3.95) into equation (3.91), and rearranging terms leads to the following specific surface area polynomial:

$$\begin{aligned}&\left[24e^3Kd_s^3d_\perp^8 + 24Kd_sd_\perp^7 g_c\sqrt{g_c} + 12Kd_s^2d_\perp^7 g_c\right]S_v^3 + \left[-192e^2Kd_s^3d_\perp^6\sqrt{g_c}(e+1) - 4e^2d_s^3d_\perp^4 g_c^2\sqrt{g_c}(e+1)\right.\\ &\left.-96e^2Kd_s^4d_\perp^6 - 2e^2d_s^4d_\perp^4 g_c^2\right]S_v^2 + \left[384eKd_s^3d_\perp^4 g_c(e+1)^2 + 32ed_s^3d_\perp^2 g_c^3(e+1)^2\right.\\ &\left.+384eKd_s^4d_\perp^4\sqrt{g_c}(e+1) + 32ed_s^4d_\perp^2 g_c^2\sqrt{g_c}(e+1) + 96eKd_s^5d_\perp^4 + 8ed_s^5d_\perp^2 g_c^2\right]S_v\\ &- 64d_s^3g_c^3\sqrt{g_c}(e+1)^3 - 96d_s^4g_c^3(e+1)^2 - 48d_s^5g_c^2\sqrt{g_c}(e+1) - 8d_s^6g_c^2 = 0\,,\end{aligned} \tag{3.96}$$

or else,

$$a''S_v^3 + b''S_v^2 + c''S_v + d'' = 0\,,$$

for which

$$\begin{aligned}a'' &= 24e^3Kd_s^3d_\perp^8 + 24Kd_sd_\perp^7 g_c\sqrt{g_c} + 12Kd_s^2d_\perp^7 g_c\,,\\ b'' &= -192e^2Kd_s^3d_\perp^6\sqrt{g_c}(e+1) - 4e^2d_s^3d_\perp^4 g_c^2\sqrt{g_c}(e+1) - 96e^2Kd_s^4d_\perp^6 - 2e^2d_s^4d_\perp^4 g_c^2\,,\\ c'' &= 384eKd_s^3d_\perp^4 g_c(e+1)^2 + 32ed_s^3d_\perp^2 g_c^3(e+1)^2 + 384eKd_s^4d_\perp^4\sqrt{g_c}(e+1) + 32ed_s^4d_\perp^2 g_c^2\sqrt{g_c}(e+1)\\ &\quad + 96eKd_s^5d_\perp^4 + 8ed_s^5d_\perp^2 g_c^2\\ \text{and }\ d'' &= -64d_s^3g_c^3\sqrt{g_c}(e+1)^3 - 96d_s^4g_c^3(e+1)^2 - 48d_s^5g_c^2\sqrt{g_c}(e+1) - 8d_s^6g_c^2\,.\end{aligned}$$

The resulting predictions are shown in Figure 3.17 for which similar results are obtained as in the case of the three-strut model.

3.5 Chapter summary

Adaptations of the two- and three-strut RUC models as a result of streamwise compression were investigated in which two compression cases were considered. For the one case, the strut

diameter in the streamwise direction was assumed to remain constant and in the other case the strut diameter changed along with the compression, which was included for model application to soft polyester fibrous media. Three compression-porosity relationships were also presented and analysed. The three relationships were named the regression, general non-linear and specific non-linear relationships and, due to its performance, the specific non-linear relationship was chosen to represent the compression-porosity relationship where possible. The specific non-linear relationship however requires compression data, which is not always provided in data sets dealing with compressed fibrous media. The general non-linear relationship gives predictions that are close to those given by the specific non-linear relationship and only require porosity data and was therefore used in such cases where the compression data was not provided.

Equations predicting the permeability and specific surface area based on both the two-strut and three-strut RUC models were determined for both comparison cases. Specific surface area equations were obtained using the geometric, kinetic and combined kinetic-geometric approaches. The permeability predictions derived from the rigid compressed RUC model, i.e. the models without the compressed strut diameter adjustments, were compared to data sets involving fibres as porous medium. The predicting equations deduced to obtain specific surface area values from porosity and permeability data were analysed and furthermore compared to the predictions obtained from data involving the hydraulic diameter, along with equation (1.6).

The predicting equations of the compressed RUC models representing the soft fibrous media, were analysed by making use of experimental data of soft polyester material. No specific surface area data was provided by, but the permeability predictions of the models were compared with the experimental permeability data. The initial state of compression of the samples had to be assumed because compression ratio-porosity data has not been provided. Therefore three initial values of the streamwise pore diameter were considered: calculating the pore diameter by assuming that the model is initially isotropic, taking the pore diameter as 75% of the isotropic pore diameter and taking the pore diameter as 50% of the isotropic pore diameter.

A summary of all the equations for the prediction of the permeability are given in Table 3.5. Similarly, a summary of all the specific surface area equations obtained using the geometric approach are provided in Table 3.6 for easier reference.

TABLE 3.5: *Summary of permeability equations provided by the compressed RUC models*

Model	**Eqn no.**	$K[\mathrm{m}^2]$
Compressed three-strut RUC model	(3.33)	$\frac{d_{\parallel}(d_{\perp}-d_s)^2}{24d_s d_{\perp}^2}\left[\frac{2}{(d_{\perp}-d_s)^2}+\frac{1}{(d_{\parallel}-d_s)^2}\right]^{-1}$
Compressed two-strut RUC model	(3.58)	$\frac{d_{\parallel}(d_{\perp}-d_s)^2}{24d_s d_{\perp}^2}\left[\frac{1}{(d_{\perp}-d_s)^2}+\frac{2d_{\perp}-d_s}{2d_{\perp}(d_{\parallel}-d_s)^2}\right]^{-1}$
Soft compressed three-strut RUC model	(3.77)	$\frac{d_{\parallel}(d_{\perp}-d_s)^2}{24d_s d_{\perp}^2}\left[\frac{(e+1)}{(d_{\perp}-d_s)^2}+\frac{1}{(d_{\parallel}-ed_s)^2}\right]^{-1}$
Soft compressed two-strut RUC model	(3.91)	$\frac{d_{\parallel}(d_{\perp}-d_s)^2}{24d_s d_{\perp}^2}\left[\frac{e}{(d_{\perp}-d_s)^2}+\frac{2d_{\perp}-d_s}{2d_{\perp}(d_{\parallel}-ed_s)^2}\right]^{-1}$

TABLE 3.6: *Summary of the specific surface area equations provided by the compressed RUC models using a geometric approach*

Model	**Eqn no.**	$S_v[\mathrm{m}^{-1}]$
Compressed three-strut RUC model	(3.40)	$\frac{8d_s(d_\perp - d_s) + 4d_s(d_\parallel - d_s)}{d_\perp^2 d_\parallel}$
Compressed two-strut RUC model	(3.64)	$\frac{8d_s d_\perp - 6d_s^2}{d_\perp^2 d_\parallel}$
Soft compressed three-strut RUC model	(3.79)	$\frac{4d_s(d_\perp - d_s)(e+1) + 4d_s(d_\parallel - ed_s)}{d_\perp^2 d_\parallel}$
Soft compressed two-strut RUC model	(3.92)	$\frac{4d_s(d_\perp - d_s)(e+1) + 2d_s^2}{d_\perp^2 d_\parallel}$

In the following chapter an effect that differentiates between the permeability obtained using gas versus liquid flow, called the Klinkenberg effect, will be incorporated into the RUC models.

CHAPTER 4

Klinkenberg effect

The permeability of a gas versus that of a liquid has been known, from experimental studies, to differ. This phenomenon could be explained by the fact that a liquid is much less compressible than a gas and that adsorption occurs in porous media with low porosities. Another explanation is that it could be due to the Klinkenberg effect. The Klinkenberg effect is an effect caused by the slip condition of the flow at the walls of the pores (Woudberg and Du Plessis [60]). In this chapter the Klinkenberg effect will specifically be taken into consideration and the effect thereof on the permeability and specific surface area investigated.

The consequence of the Klinkenberg effect is that the flow deviates from Darcy's law. This leads to a slip-boundary condition that needs to be implemented and therefore an adjustment to the Navier-Stokes equation, as stated by Woudberg and Du Plessis [60]. In order to determine its effect it should first be known under which conditions the Klinkenberg effect causes a significant deviation from the no-slip results. This occurs when the permeabilities are low, that is, at near atmospheric (or low) pressure and in cases where the molecular mean free path and the dimensions of the pores are comparable (Woudberg and Du Plessis [60]). The latter occurrence can be quantified by a ratio known as the Knudsen number, Kn, given by

$$Kn = \frac{\lambda}{D_h}\,, \tag{4.1}$$

where λ is defined in Chapter 1. The Knudsen number has been used to classify different flow regimes. For which Knudsen numbers these flow regimes are generally applicable are given in both Hosseini and Vahedi Tafreshi [39] and Barber and Emerson [61]. The following three regimes of relevance to this study are as follows:

The continuum assumption of the Navier-Stokes equation is still valid when $Kn \leq 10^{-3}$ and the Klinkenberg effect is negligible, therefore the no slip-boundary condition can still be implemented. This is known as the continuum regime. A continuum approach is still valid when $10^{-3} < Kn < 10^{-1}$, but a slip-boundary condition at the pore walls has to be incorporated into the Navier-Stokes equation. This is known as the slip-flow regime. When $Kn \geq 10^{-1}$ however, non-continuum effects are present and consequently the Navier-Stokes equation cannot be used. This regime is known as the transition flow regime followed by the state of free molecular flow as the Knudsen number increases further. The required interval for the Knudsen number in which the Klinkenberg effect should be taken into account is therefore the interval where $10^{-3} < Kn < 10^{-1}$. It should be noted that this classification is rather empirical since it depends on the characteristic length used in the Knudsen number which makes the calculated Knudsen values geometry specific.

The relationship between the liquid permeability K_l and gas permeability K_g as a result of the

Klinkenberg effect is known as the Klinkenberg equation and was derived by Klinkenberg [62], to be

$$K_g = K_l \left(1 + \frac{b}{p_{\text{avg}}}\right) , \tag{4.2}$$

where b is the Klinkenberg factor and p_{avg} is the average of the inlet and outlet pressures.

4.1 Incorporation of the Klinkenberg effect

In Chapters 2 and 3 the permeability coefficients represented the liquid permeability. The objective is to obtain a relationship between the gas and liquid permeabilities for the RUC models in order to incorporate the Klinkenberg effect into the previously determined model predictions for the permeability and specific surface area. In order to obtain a relationship between the gas and liquid permeabilities for the three-strut and two-strut RUC models an expression for the gas permeability will be derived in which a slip flow boundary condition is included. As shown in Woudberg and Du Plessis [60], this can be accomplished by starting with the streamwise pressure gradient, given by equation (2.129).

In order to determine the wall shear stress along the streamwise ducts, that is $\tau_{w_\parallel}$, the magnitude of the average duct velocity, denoted by $w_\parallel$, needs to be determined. The onset of determining the magnitude of this velocity in which the Klinkenberg equation needs to be incorporated, is the Navier-Stokes equation for steady incompressible flow. For fully developed flow between parallel plates in which the effect of gravity is ignored, the Navier-Stokes equation simplifies to

$$\frac{\mathrm{d}p}{\mathrm{d}x} = \mu \frac{\mathrm{d}^2 u}{\mathrm{d}y^2} , \tag{4.3}$$

where the flow is in the x-direction and u represents the magnitude of the fluid velocity in the x-direction. Integrating equation (4.3) with respect to y where $\frac{\mathrm{d}u}{\mathrm{d}y} = 0$ at $y = \frac{d-d_s}{2}$, since the maximum velocity occurs halfway between the parallel plates a distance $d - d_s$ apart, leads to

$$\frac{\mathrm{d}p}{\mathrm{d}x} = \mu \frac{\mathrm{d}u}{\mathrm{d}y} \cdot \frac{1}{y - \frac{d-d_s}{2}} . \tag{4.4}$$

With rearrangement of equation (4.4), the following equation can be obtained:

$$\frac{\mathrm{d}u}{\mathrm{d}y} = \frac{1}{\mu} \frac{\mathrm{d}p}{\mathrm{d}x} \left(y - \frac{d-d_s}{2}\right) , \tag{4.5}$$

and thereafter equation (4.5) is integrated with respect to y once more. The boundary condition implemented for no-slip flow is $u = 0$ at the pore walls, i.e. where $y = 0$ and where $y = d - d_s$. Due to the Klinkenberg equation, however, a slip flow boundary condition needs to be implemented, i.e. (Woudeberg and Du Plessis [60])

$$\tau_{w_\parallel} = \beta \, w_\parallel , \tag{4.6}$$

where β is the slip coefficient. The slip coefficient can be expressed in terms of the molecular mean free path in the following manner:

$$\beta = \frac{\mu}{\left(\frac{2-\sigma}{\sigma}\right) \lambda} , \tag{4.7}$$

As mentioned in Chapter 1, the tangential momentum accommodation coefficient σ depends on the properties of the pore walls of the material and tends towards 0 if the surface is smooth and

towards 1 if the surface is rough. The wall shear stress for flow between parallel plates a distance $d - d_s$ apart can be expressed as follows:

$$\tau_w = \frac{d - d_s}{2}\left(-\frac{\mathrm{d}p}{\mathrm{d}x}\right) . \tag{4.8}$$

Substituting equation (4.4) into equation (4.8) and consequently substituting equation (4.8) into equation (4.6), leads to the boundary condition for slip flow, i.e.

$$\beta\, u_b = \pm\mu \left(\frac{\mathrm{d}u}{\mathrm{d}y}\right)_b , \tag{4.9}$$

where u_b and $\left(\frac{\mathrm{d}u}{\mathrm{d}y}\right)_b$ are the magnitudes of the velocity and velocity gradient, respectively, at the boundaries of the pore. The $y = 0$ boundary gives the '+' sign and the $y = d - d_s$ boundary gives the '−' sign in equation (4.9).

Finally integrating equation (4.5) with either the boundary conditions represented by equation (4.9) leads to

$$u(y) = \frac{1}{2}\frac{\mathrm{d}p}{\mathrm{d}x}\left[\frac{y}{\mu}(y - d + d_s) - \frac{d - d_s}{\beta}\right] . \tag{4.10}$$

The magnitude of the average velocity can then be determined from equation (4.10) as follows:

$$w_{\parallel} = \frac{1}{d - d_s}\int_o^{d-d_s} u(y)\,\mathrm{d}y = \frac{d - d_s}{2}\left(-\frac{\mathrm{d}p}{\mathrm{d}x}\right)\left[\frac{d - d_s}{6\mu} + \frac{1}{\beta}\right] . \tag{4.11}$$

Woudberg and Du Plessis [60] determined the hydraulic diameter to be $D_h = 2(d - d_s)$ since they chose the hydraulic diameter that resembled the hydraulic diameter of parallel plates. In this study, specifically in Chapter 3, the hydraulic diameter was however chosen to resemble the hydraulic diameter of a square duct. For the sake of consistency, the same choice will be maintained in this chapter. The hydraulic diameter will therefore be given by $D_h = d - d_s$ and thus the Knudsen number becomes

$$Kn = \frac{\lambda}{d - d_s} , \tag{4.12}$$

for the RUC model. Consequently λ resulting from equation (4.12) can be substituted into equation (4.7), leading to

$$\beta = \frac{\mu}{(d - d_s)\left(\frac{2-\sigma}{\sigma}\right)Kn} , \tag{4.13}$$

which is the slip coefficient in terms of the Knudsen number. Substituting equation (4.13) into equation (4.11) then leads to

$$w_{\parallel} = -\frac{(d - d_s)^2}{2\mu}\frac{\mathrm{d}p}{\mathrm{d}x}\frac{1}{6}\left(1 + 6\frac{(2-\sigma)}{\sigma}Kn\right) . \tag{4.14}$$

Equation (4.14) can be rearranged to an expression for the pressure gradient, i.e.

$$-\frac{\mathrm{d}p}{\mathrm{d}x} = \frac{12\mu w_{\parallel}}{(d - d_s)^2}\frac{1}{\left(1 + 6\frac{(2-\sigma)}{\sigma}Kn\right)} , \tag{4.15}$$

and substituting equation (4.15) into equation (4.8) for the wall shear stress results in

$$\tau_{w_{\parallel}} = \frac{6\mu w_{\parallel}}{d - d_s}\frac{1}{\left(1 + 6\frac{(2-\sigma)}{\sigma}Kn\right)} . \tag{4.16}$$

For the isotropic three-strut RUC model $w_{\parallel} = w_{\perp}$, so that

$$w_{\parallel} = w_{\perp} = \frac{qd^2}{(d-d_s)^2} = \frac{q\psi}{\epsilon}\,. \tag{4.17}$$

Substituting equation (4.17) into equation (4.16) finally leads to

$$\tau_{w_{\parallel}} = \frac{6\mu q\psi}{\epsilon(d-d_s)} \frac{1}{\left(1+6\frac{(2-\sigma)}{\sigma}Kn\right)}\,. \tag{4.18}$$

The streamwise pressure gradient for the isotropic three-strut model can therefore be determined by substituting U_o, A_s and $\tau_{w_{\parallel}}$ given by equations (2.76), (2.89) and (4.18), respectively, into equation (2.129), leading to

$$-\nabla\langle p\rangle = \frac{72\psi^2 d_s}{\epsilon d^3} \frac{1}{\left(1+6\frac{(2-\sigma)}{\sigma}Kn\right)}\mu\underline{q}\,. \tag{4.19}$$

The streamwise pressure gradient in terms of d_s can furthermore be obtained by making use of equation (2.93), which relates the parameter d to d_s, yielding (Woudberg and Du Plessis [60])

$$-\nabla\langle p\rangle = -\epsilon\nabla p_f = \frac{9\psi^2(\psi-1)^3}{\epsilon d_s^2} \frac{1}{\left(1+6\frac{(2-\sigma)}{\sigma}Kn\right)}\mu\underline{q}\,. \tag{4.20}$$

Since

$$-\nabla p_f = \frac{1}{K}\mu\underline{q}\,, \tag{4.21}$$

it follows that the gas permeability is given by

$$K_g = \frac{\epsilon^2 d_s^2}{9\psi^2(\psi-1)^3}\left[1+6\frac{(2-\sigma)}{\sigma}Kn\right]\,. \tag{4.22}$$

The permeability can be expressed in terms of d_p by using equation (2.206), yielding

$$K_g = \frac{\epsilon^2 d_p^2}{9\psi^2(\psi-1)(3-\psi)^2}\left[1+6\frac{(2-\sigma)}{\sigma}Kn\right]\,. \tag{4.23}$$

Comparing the gas permeability in equation (4.23) to the liquid permeability in equation (2.155) leads to the deduction that

$$K_g = K_l\left[1+6\frac{(2-\sigma)}{\sigma}Kn\right]\,, \tag{4.24}$$

which is the Klinkenberg equation for the RUC model. Rearranging equation (4.24) leads to an expression for K_l in terms of K_g, i.e.

$$K_l = \frac{K_g}{1+6\frac{(2-\sigma)}{\sigma}Kn}\,. \tag{4.25}$$

The Klinkenberg equation for the two-strut RUC model can also be derived similarly to that of the three-strut RUC model, but yields the same results, given by equations (4.24) and (4.25).

The Klinkenberg effect will be incorporated into the uncompressed RUC models, that is the isotropic three-strut RUC model and the uncompressed two-strut RUC model, as well as into the compressed three- and two-strut RUC models. Only the rigid compressed RUC models will

be considered. The Klinkenberg equations can also, similarly to the uncompressed models, be determined for the compressed models. Equation (2.130) is used instead of equation (2.129) and the Klinkenberg equations finally obtained are also equal to equations (4.24) and (4.25).

The Klinkenberg equation given by Woudberg and Du Plessis [60] is similar to equation (4.24), but instead of the coefficient of 6, they obtained a coefficient of 12. This is due to the different hydraulic diameter definitions used, as previously mentioned. Equation (4.24) is also of a similar form as the Klinkenberg type equation proposed by the theoretical model of Hooman et al. [32] for polygonal ducts. Instead of the coefficient of 6 in equation (4.24) resulting from the geometry of a rectangular duct, they used a value of 7.9 representative of a range of polygonal ducts. Panerai et al. [63] have also proposed a similar type of Klinkenberg equation as equation (4.24), given by

$$K_g = K_l \left[1 + 8\, c_{\text{Pan}} \frac{\lambda}{d_p}\right] = K_l \left(1 + \frac{b}{p_{\text{avg}}}\right) , \tag{4.26}$$

were c_{Pan} is a proportionality constant. Equation (4.26) is, however, an empirical equation since K_l and b are obtained from a least-squares fit of the resistance force versus the average pressure. The value of K_l is obtained from the slope and the b-value from the abscissa at zero ordinate divided by K_l. The value of c_{Pan} is calculated from an estimated equation for the average pore diameter.

4.2 Uncompressed RUC models for slip flow

The implementation of the Klinkenberg effect on the three- and two-strut RUC models involves changing the expressions in terms of the liquid permeability to expressions in terms of the gas permeability by utilizing equations (4.24) and (4.25). Therefore, all the model predictions containing the permeability coefficient need to be adjusted accordingly when gas flow, in the slip flow regime, is considered. Due to the permeability and specific surface area parameters being the focus of this study, the adaptations made to these parameters for the three- and two-strut RUC models will be discussed and evaluated. The specific surface area predictions based on the kinetic and combined kinetic-geometric approaches also need to be adapted since these approaches include the permeability coefficient.

The adaptation of the permeability coefficient will be considered first.

4.2.1 Permeability

The liquid permeability predictions are adapted by substituting the permeability coefficient into equation (4.24) to determine the equation for the gas permeability. The adapted permeability equations for the three- and two-strut RUC models are therefore determined as follows:

Three-strut RUC model

The liquid permeability equations for the three-strut RUC model are given by equations (2.155) and (2.207), in terms of d_p and d_s, respectively. The gas permeability in terms of d_p and d_s can then be determined for the three-strut RUC model by substituting the liquid permeabilities into equation (4.24). The gas permeability in terms of d_p is given by

$$K_g = \frac{\epsilon^2 d_p^2}{9\psi^2(\psi - 1)(3 - \psi)^2} \left[1 + 6\frac{(2 - \sigma)}{\sigma} Kn\right] , \tag{4.27}$$

and

$$K_g = \frac{\epsilon^2 d_s^2}{9\psi^2(\psi-1)^3}\left[1+6\frac{(2-\sigma)}{\sigma}Kn\right], \tag{4.28}$$

is the equation for the gas permeability in terms of d_s.

Two-strut RUC model

The liquid permeability equations for the two-strut RUC model are given by equations (2.176) and (2.209), in terms of d_p and d_s, respectively. The gas permeability in terms of d_p and d_s can then be determined for the two-strut RUC model by substituting the liquid permeability equations into equation (4.24). The gas permeability in terms of d_p is therefore given by

$$K_g = \frac{\epsilon^2 d_p^2}{12(\psi-\epsilon)(3\psi+\epsilon)}\left[1+6\frac{(2-\sigma)}{\sigma}Kn\right], \tag{4.29}$$

and the gas permeability in terms of d_s is given by

$$K_g = \frac{\epsilon^4 d_s^2}{12(\psi-\epsilon)^3(3\psi+\epsilon)}\left[1+6\frac{(2-\sigma)}{\sigma}Kn\right]. \tag{4.30}$$

The adaptations to incorporate the Klinkenberg effect in the specific surface area predictions of the RUC models using the kinetic approach will be considered next.

4.2.2 Specific surface area: Kinetic approach

In order to incorporate the Klinkenberg effect into the specific surface area equations obtained using the kinetic approach, the liquid permeability can be substituted with equation (4.25) in terms of the gas permeability. The equations for the specific surface area of the RUC models adapted in this manner are determined as follows:

Three-strut RUC model

For the three-strut RUC model the substitution of equation (4.25) into the equation for the specific surface area based on the kinetic approach, given by equation (2.157), leads to:

$$S_v = \frac{4\epsilon^2}{3\psi(3-\psi)}\sqrt{\frac{1+6\frac{(2-\sigma)}{\sigma}Kn}{K_g(\psi-1)}}. \tag{4.31}$$

Equation (2.157) is the version of the specific surface area in which equation (1.6) was used to determine S_v. Substituting equation (4.25) into the equation for the specific surface area based on the kinetic approach, given by equation (2.159), which is the specific surface area version in which equation (1.9) was used to determine S_v, leads to:

$$S_v = \frac{2\epsilon(1-\epsilon)}{\psi(3-\psi)}\sqrt{\frac{1+6\frac{(2-\sigma)}{\sigma}Kn}{K_g(\psi-1)}}. \tag{4.32}$$

In both equations (4.31) and (4.32), ψ is given by equation (2.88).

Two-strut RUC model

In order to determine the specific surface area based on the kinetic approach for the two-strut RUC model with the Klinkenberg effect incorporated, equation (4.25) is substituted into equation (2.178), which was determined from equation (1.6). The specific surface area equation is then given by

$$S_v = 2\epsilon^2 \sqrt{\frac{1 + 6\frac{(2-\sigma)}{\sigma} Kn}{3(\psi - \epsilon)(3\psi + \epsilon) K_g}} \,. \tag{4.33}$$

Equation (4.25) can be substituted into equation (2.180) based on the kinetic approach, which was determined using equation (1.9), and leads to

$$S_v = 3\epsilon(1-\epsilon) \sqrt{\frac{1 + 6\frac{(2-\sigma)}{\sigma} Kn}{3(\psi - \epsilon)(3\psi + \epsilon) K_g}} \,. \tag{4.34}$$

In both equations (4.33) and (4.34), ψ is given by equation (2.108).

4.2.3 Specific surface area: Combined approach

Similarly to the specific surface area equations obtained using a kinetic approach, incorporating the Klinkenberg effect into the specific surface area equations based on the combined approach is done by using equation (4.25). The adapted equations for the three- and two-strut RUC models are given next.

Three-strut RUC model

The substitution of equation (4.25) into the specific surface area based on the combined approach, given by equation (2.201), yields:

$$S_v = \frac{\epsilon(3-\psi)}{2\psi} \sqrt{\frac{(\psi - 1)\left[1 + 6\frac{(2-\sigma)}{\sigma} Kn\right]}{K_g}} \,, \tag{4.35}$$

where ψ is given by equation (2.88).

Two-strut RUC model

Similarly as in the case of the three-strut RUC model based on the combined approach, substituting equation (4.25) into the specific surface area for the two-strut model based on the combined approach, given by equation (2.204), leads to:

$$S_v = \frac{\epsilon^2(\psi - \epsilon)(3\epsilon + \psi)}{\psi^3} \sqrt{\frac{1 + 6\frac{(2-\sigma)}{\sigma} Kn}{3(\psi - \epsilon)(3\psi + \epsilon) K_g}} \,, \tag{4.36}$$

where ψ is given by equation (2.108).

The evaluation of the Klinkenberg adapted permeability and specific surface area equations will be addressed in the next section.

4.2.4 Model validation

In order to evaluate the RUC models involving the Klinkenberg effect, experimental data of foams or fibres containing gas permeability values and Knudsen numbers are needed within the slip flow regime. The data is therefore required to have Knudsen numbers, as defined by equation (4.1), no lower than 10^{-3} and no higher than 10^{-1}. If a value for the mean free path is not provided, it can alternatively be determined using equation (1.12) if the necessary gas variables are provided or can be attained.

Corresponding porosity and pore diameter or porosity and strut diameter data are needed when using equations (4.27) or (4.28) for the three-strut model and equations (4.29) or (4.30) for the two-strut model, respectively, in order to determine the permeability predictions of the three-strut and two-strut RUC models with the incorporated Klinkenberg effect. The specific surface area predictions obtained using a kinetic approach, with the Klinkenberg effect taken into account, requires corresponding porosity and gas permeability data. Equations (4.31) and (4.32) can then be used to obtain the predictions for the three-strut RUC model and equations (4.33) and (4.34) can be used to determine the predictions of the two-strut RUC model. To determine the specific surface area using the combined kinetic-geometric approach, corresponding porosity and gas permeability data are needed. Substituting the required values into equations (4.35) and (4.36), respectively, lead to specific surface area predictions for the three-strut and two-strut RUC models accounting for the Klinkenberg effect.

To summarize, evaluation of the uncompressed RUC models in which the Klinkenberg effect is incorporated requires corresponding porosity and permeability data, as well as Knudsen numbers and pore or strut diameter values within the slip flow regime. Such data could however not be found in the literature. Model validation involving experimental data could therefore not be provided.

Implementation of the Klinkenberg effect on the compressed RUC models will be discussed next.

4.3 Compressed RUC models for slip flow

In this section the Klinkenberg effect will be incorporated into the compressed RUC models introduced in Chapter 3. This will be achieved by utilizing equations (4.24) and (4.25) and involves determining expressions for the model predictions of the compressed RUC models in terms of the gas permeability instead of the liquid permeability. Only the rigid compressed RUC models will be investigated for incorporation of the Klinkenberg effect. Once again the focus will be on the permeability and specific surface area expressions. Both the kinetic and combined kinetic-geometric approaches used to obtain the specific surface area include the liquid permeability parameter, but in this section only the combined kinetic-geometric approach will be adapted. This is due to the fact that the kinetic approach did not predict viable results for the compressed RUC models, so there is no purpose in developing the approach and its expressions any further for the compressed models.

Furthermore, an expression for the Knudsen number that can be used for the compressed RUC models has to be determined. The hydraulic diameter present in the Knudsen number can be expressed in terms of $d_\perp$ and d_s, as in equation (3.34), for the compressed RUC models. Substituting the latter equation into equation (4.1) therefore yields the following expression for the Knudsen number for the compressed RUC models:

$$Kn = \frac{\lambda}{d_\perp - d_s}\,. \tag{4.37}$$

Equation (4.37) will be substituted into the adapted permeability predictions for the compressed RUC models in order to attain a continuous function for the permeability.

The permeability equations for the compressed RUC models will be adapted to incorporate the Klinkenberg effect in the following section.

4.3.1 Permeability

The permeability equations for the compressed RUC models with the Klinkenberg effect incorporated are determined by comparing the permeability equations determined in Sections 3.2 and 3.3 for the three- and the two-strut models respectively, with equation (4.24).

Three-strut RUC model

The gas permeability can be determined by substituting the liquid permeability given by equation (3.33) into equation (4.24). The gas permeability is then given by

$$K_g = \frac{d_{\parallel}(d_{\perp}-d_s)^2}{24d_s d_{\perp}^2}\left[\frac{2}{(d_{\perp}-d_s)^2}+\frac{1}{(d_{\parallel}-d_s)^2}\right]^{-1}\left[1+6\frac{(2-\sigma)}{\sigma}Kn\right], \tag{4.38}$$

where $d_{\parallel}$ and $d_{\perp}$ can be obtained from equations (3.1) and (3.15), respectively.

The gas permeability can also be given by

$$K_g = \frac{d_{\parallel}(d_{\perp}-d_s)^2}{24d_s d_{\perp}^2}\left[\frac{2}{(d_{\perp}-d_s)^2}+\frac{1}{(d_{\parallel}-d_s)^2}\right]^{-1}\left[1+6\frac{(2-\sigma)}{\sigma}\cdot\frac{\lambda}{d_{\perp}-d_s}\right], \tag{4.39}$$

which is the gas permeability of the compressed three-strut model in terms of the mean free path.

Two-strut RUC model

Substituting the liquid permeability given by equation (3.58) into equation (4.24), leads to the gas permeability for the compressed two-strut model, i.e.

$$K_g = \frac{d_{\parallel}(d_{\perp}-d_s)^2}{24d_s d_{\perp}^2}\left[\frac{1}{(d_{\perp}-d_s)^2}+\frac{2d_{\perp}-d_s}{2d_{\perp}(d_{\parallel}-d_s)^2}\right]^{-1}\left[1+6\frac{(2-\sigma)}{\sigma}Kn\right]. \tag{4.40}$$

In equation (4.40), $d_{\parallel}$ and $d_{\perp}$ can be obtained from equations (3.1) and (3.48), respectively.

The gas permeability in terms of the mean free path is given by

$$K_g = \frac{d_{\parallel}(d_{\perp}-d_s)^2}{24d_s d_{\perp}^2}\left[\frac{1}{(d_{\perp}-d_s)^2}+\frac{2d_{\perp}-d_s}{2d_{\perp}(d_{\parallel}-d_s)^2}\right]^{-1}\left[1+6\frac{(2-\sigma)}{\sigma}\cdot\frac{\lambda}{d_{\perp}-d_s}\right]. \tag{4.41}$$

The adapted expressions for the specific surface area obtained using the combined approach will be given next.

4.3.2 Specific surface area: Combined approach

In order to obtain the specific surface area equations for the compressed RUC models with the Klinkenberg effect incorporated and based on the combined approach, the liquid permeability needs to be expressed in terms of the gas permeability.

Three-strut RUC model

In Chapter 3 the specific surface area for the compressed three-strut RUC model was solved by first deriving a polynomial, given by equation (3.45), as a function of the liquid permeability. Consequently equation (4.25) can be substituted into equation (3.45) to obtain a specific surface area polynomial in terms of the gas permeability, i.e.

$$\begin{aligned}
&\left[48K_g d_s^3 d_\perp^8 + 24K_g d_s d_\perp^8 g_c\right] S_v^3 \\
&+ \left[-768K_g d_s^3 d_\perp^7 + 576K_g d_s^4 d_\perp^6 - 8d_s^3 d_\perp^5 g_c^2 n + 12d_s^4 d_\perp^4 g_c^2 n - 288K_g d_s^2 d_\perp^6 g_c\right] S_v^2 \\
&+ \left[3072K_g d_s^3 d_\perp^6 - 3072K_g d_s^4 d_\perp^5 + 128d_s^3 d_\perp^4 g_c^2 n - 320d_s^4 d_\perp^3 g_c^2 n + 192d_s^5 d_\perp^2 g_c^2 n + \right. \\
&\left. + 1152K_g d_s^3 d_\perp^4 g_c\right] S_v - 512d_s^3 d_\perp^3 g_c^2 n + 1792d_s^4 d_\perp^2 g_c^2 n - 2048d_s^5 d_\perp g_c^2 n + 768d_s^6 g_c^2 n \\
&- 12288K_g d_s^4 d_\perp^4 + 24576K_g d_s^5 d_\perp^3 - 12288K_g d_s^6 d_\perp^2 - 1536K_g d_s^4 d_\perp^2 g_c = 0\,,
\end{aligned} \tag{4.42}$$

where $n = 1 + 6(2-\sigma)/\sigma Kn$ and $g_c = (d_\perp - d_s)^2$.

The Knudsen number can be calculated using equation (4.37) and $d_\perp$ can be determined from equation (3.15). The coefficients for the polynomial given by the reduced form of the polynomial,

$$a'' S_v^3 + b'' S_v^2 + c'' S_v + d'' = 0\,,$$

are thus given by

$$\begin{aligned}
a'' &= 48K_g d_s^3 d_\perp^8 + 24K_g d_s d_\perp^8 g_c\,, \\
b'' &= -768K_g d_s^3 d_\perp^7 + 576K_g d_s^4 d_\perp^6 - 8d_s^3 d_\perp^5 g_c^2 n + 12d_s^4 d_\perp^4 g_c^2 n - 288K_g d_s^2 d_\perp^6 g_c\,, \\
c'' &= 3072K_g d_s^3 d_\perp^6 - 3072K_g d_s^4 d_\perp^5 + 128d_s^3 d_\perp^4 g_c^2 n - 320d_s^4 d_\perp^3 g_c^2 n + 192d_s^5 d_\perp^2 g_c^2 n + 1152K_g d_s^3 d_\perp^4 g_c\,,
\end{aligned}$$

and

$$\begin{aligned}
d'' = &-512d_s^3 d_\perp^3 g_c^2 n + 1792d_s^4 d_\perp^2 g_c^2 n - 2048d_s^5 d_\perp g_c^2 n + 768d_s^6 g_c^2 n - 12288K_g d_s^4 d_\perp^4 + 24576K_g d_s^5 d_\perp^3 \\
&- 12288K_g d_s^6 d_\perp^2 - 1536K_g d_s^4 d_\perp^2 g_c\,.
\end{aligned}$$

The specific surface area is then determined from the roots of the polynomial and the real root is retained in each case.

Two-strut RUC model

The specific surface area of the compressed two-strut RUC model including the Klinkenberg effect and based on the combined approach can be determined similarly as in the case of the compressed three-strut RUC model. The polynomial derived by substituting equation (4.25) into the liquid permeability in the specific surface area polynomial, given by equation (3.68), is therefore given by

$$\begin{aligned}
&\left[24K_g d_s^3 d_\perp^8 + 12K_g d_s d_\perp^7 (2d_\perp - d_s)(d_\perp - d_s)^2\right] S_v^3 \\
&+ \left[-48K_g d_s^2 d_\perp^6 (8d_\perp d_s - 6d_s^2) - d_s^2 d_\perp^4 (d_\perp - d_s)^4 (8d_\perp d_s - 6d_s^2) n\right] S_v^2 \\
&+ \left[24K_g d_s d_\perp^4 (8d_\perp d_s - 6d_s^2)^2 + 2d_s d_\perp^2 (d_\perp - d_s)^4 (8d_\perp d_s - 6d_s^2)^2 n\right] S_v \\
&- (d_\perp - d_s)^4 (8d_\perp d_s - 6d_s^2)^3 n = 0\,,
\end{aligned} \tag{4.43}$$

where n is once more given by $n = 1 + 6(2-\sigma)/\sigma Kn$, $d_\perp$ is as defined in equation (3.48) and Kn can be determined, where needed, from equation (4.37). Setting $g_c = (d_\perp - d_s)^2$ and $f = 8d_\perp d_s - 6d_s^2$, the coefficients of the reduced form of the polynomial

$$a'' S_v^3 + b'' S_v^2 + c'' S_v + d'' = 0$$

are given by

$$a'' = 24K_g d_s^3 d_\perp^8 + 12K_g d_s d_\perp^7 (2d_\perp - d_s) g_c\,, \quad b'' = -48K_g d_s^2 d_\perp^6 f - d_s^2 d_\perp^4 g_c^2 fn\,,$$
$$c'' = 24K_g d_s d_\perp^4 f^2 + 2d_s d_\perp^2 g_c^2 f^2 n \text{ and } d'' = -g_c^2 f^3 n\,.$$

The specific surface area is then determined from the roots of the polynomial and the real root is retained in each case.

The evaluation of the expressions for the permeability and the specific surface area of the Klinkenberg effect incorporated compressed RUC models will now be done using data found in the literature.

4.3.3 Model validation

In order to evaluate the permeability and specific surface area equations for the compressed RUC models in which the Klinkenberg effect is incorporated, data obtained from Le Coq [8] for the porosity, hydraulic diameter and air permeability are used. The Marmoret et al. [12] value for the mean free path of air, as given in Chapter 1, will be used, i.e. $\lambda_{\text{air}} = 0.0634\,\mu$m. In Table 4.1 the same information is as given in Table 3.2 but standard deviations for the measured hydraulic diameter values, denoted by s_{D_h}, are added. These values were obtained through personal communication with Le Coq. Knudsen numbers determined using equation (4.1) were also added.

TABLE 4.1: *Experimental data of Le Coq [8] for fibrous media (with $d_s = 2.7\,\mu$m) used to validate the predictions for K and S_v obtained from combined approach*

Experimental procedure	ϵ	e	D_h [μm]	s_{D_h} [μm]	K [μm^2]	Kn
mercury porosimetry	0.94	1	28	2.4	8.2	2.5×10^{-3}
	0.92	0.85	17	3.5	2.0	4.1×10^{-3}
	0.89	0.75	16.5	3.4	1.4	4.2×10^{-3}
	0.86	0.55	16.0	3.6	0.17	4.4×10^{-3}
permeametry	0.94	1	28	2.4	10	2.5×10^{-3}
	0.92	0.85	17	3.5	2.1	4.1×10^{-3}

From Table 4.1 it can be seen that the Knudsen numbers fall within the required interval for the Klinkenberg effect to be taken into account, i.e. $10^{-3} < Kn < 10^{-1}$. The tangential momentum accommodation coefficient, σ, was set equal to 0.2, due to Le Coq [8] having acquired the data using glass fibres which is assumed to have a smooth surface.

In order to utilize the Le Coq [8] data to determine $d_\parallel$ that appears (implicitly or explicitly) in the three- and two-strut RUC model permeability and specific surface area equations, the values as obtained in Sections 3.2 and 3.3 for the three- and two-strut models for $d_{\parallel_o}$, given by $10.1\,\mu$m and $8.91\,\mu$m, respectively, will be used. $d_\parallel$ is furthermore determined by substituting these values, along with the values obtained for e from the specific non-linear relationship given by equation (3.9), with $C = 0.0719$, into equation (3.1).

In order to obtain the permeability predictions for the compressed RUC models, with and without the Klinkenberg effect, the porosity and strut diameter values can be substituted into equations (3.33) and (4.39) for the three-strut RUC model, respectively, and into equations (3.58) and (4.41) for the two-strut RUC models, respectively. The results of these predictions, as well as the experimentally determined permeability values given by Le Coq [8], are shown in Figure 4.1.

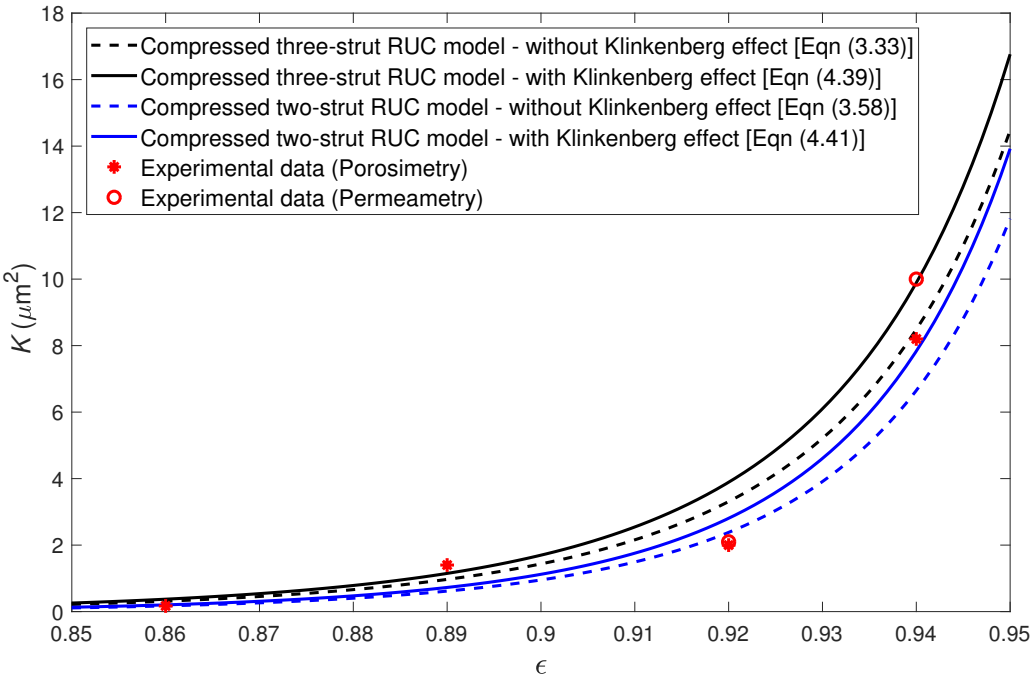

FIGURE 4.1: *Permeability predictions of the compressed three- and two-strut RUC models with and without the Klinkenberg effect versus porosity compared to the experimental data of Le Coq [8]*

It is evident that the models with the Klinkenberg effect predict higher permeabilities than the corresponding models without the Klinkenberg effect. It can also be noticed that the permeability predicted by the compressed two-strut RUC models are lower than the corresponding compressed three-strut RUC models. The permeability predictions of the compressed two-strut RUC model including the Klinkenberg effect give, on average, the most accurate prediction in comparison to the experimental permeability data. When the geometry of the glass fibres is considered, the two-strut RUC model provides a physically more realistic representation of the stacking of fibre layers forming parallel sheets of fibres and therefore agrees with this observation. The permeability predictions obtained by taking the standard deviation of the measured hydraulic diameter values into consideration are also shown in Figure 4.2. This is done by adding and subtracting the standard deviations from the corresponding hydraulic diameter values used to obtain the two-strut RUC model predictions in which the Klinkenberg effect is incorporated.

All the experimental values for the permeability is within the limits defined by the standard deviation included in the model prediction of the compressed two-strut RUC model with incorporated Klinkenberg effect, which is satisfactory.

The specific surface area values determined using the combined approach for the compressed RUC models with the Klinkenberg effect incorporated are obtained by substituting the values for the porosity, permeability and Knudsen number into the polynomials given by equations (4.42) and (4.43) for the three- and two-strut models, respectively. The compression ratio and hydraulic diameter values are furthermore used to obtain values for $d_{\parallel}$ and $d_{\perp}$, as mentioned previously. The values obtained by solving the polynomials, where the real positive roots were chosen in each case, given by equations (3.45) and (4.42) for the three-strut compressed RUC models without and with the Klinkenberg effect, respectively, as well as the polynomials given by equations (3.68) and (4.43) for the two-strut compressed RUC models without and with the Klinkenberg effect, respectively, are shown in Figure 4.3.

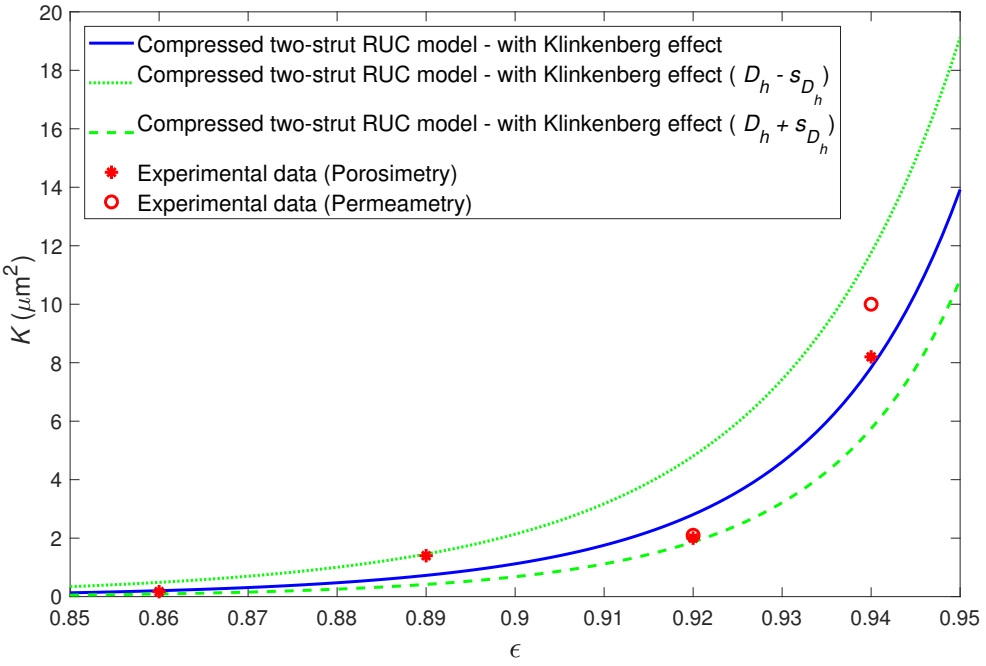

FIGURE 4.2: *Permeability predictions of the compressed two-strut model with incorporated Klinkenberg effect versus porosity with and without standard deviations in hydraulic diameters compared to the experimental data of Le Coq [8]*

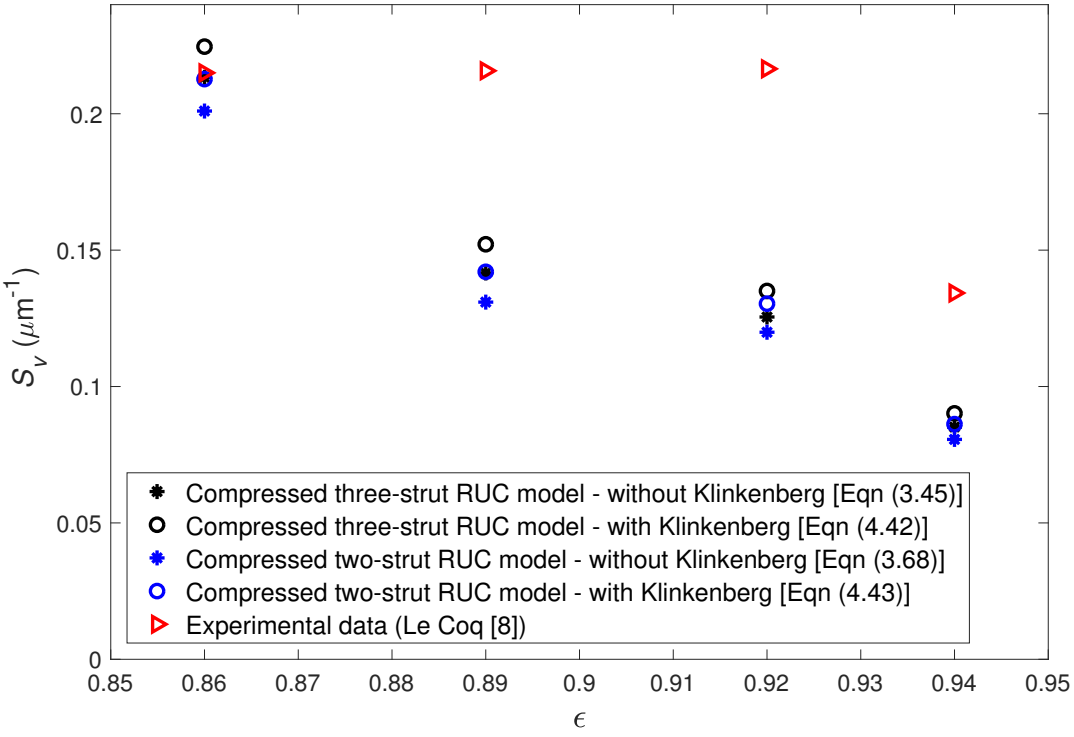

FIGURE 4.3: *Specific surface area with and without the Klinkenberg effect versus porosity compared to the experimental data of Le Coq [8]*

Similarly as in Chapter 3, values for the specific surface area to compare the model predictions with are determined using the experimental data given by Le Coq for ϵ and D_h, and equation (1.6). The resulting specific surface area values pose as experimental data and are also shown in Figure 4.3. Furthermore, only the mercury porosimetry data for the permeability was utilized once again in the model predictions for the specific surface area due to the permeametry data yielding almost indistinguishable results. It can be observed in Figure 4.3 that the values for the specific surface area predictions in which the Klinkenberg effect is included are higher than the corresponding model predictions without the Klinkenberg effect. The two-strut RUC models predict lower values than the three-strut RUC models for the models with and without the Klinkenberg effect. It can also be seen that the experimental data points generally predict values that are higher than what any of the models predict, except for the first data point. This could be due to the use of equation (1.6) to determine these experimental values which have been added to simply give an indication of the order of magnitude of the specific surface area values.

The compressed two-strut RUC model with the Klinkenberg effect incorporated will be discussed further due to it being a physically more realistic representation of the stacking of glass fibre layers and it yielding the most accurate permeability prediction. In Figure 4.4 the predictions given by the aforementioned model are shown, with the standard deviation included by adding or subtracting it from the measured hydraulic diameter values used in the model. The adjustments made to the experimental data points with the inclusion of the standard deviation are also shown, due to the use of equation (1.6) involving hydraulic diameter values to determine the specific surface areas. Figure 4.4 shows that the discrepancies between the predicted and experimental values are less when the standard deviation in the measured hydraulic diameter values are taken into consideration.

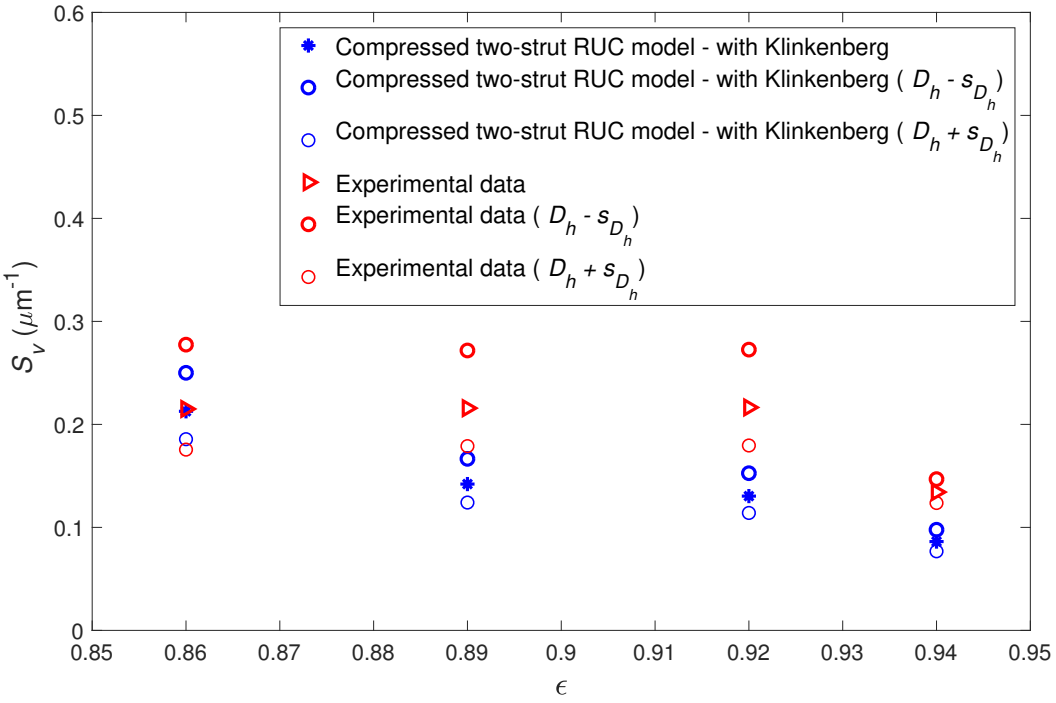

FIGURE 4.4: *Specific surface area predictions of the compressed two-strut RUC model with the Klinkenberg effect versus porosity and the standard deviation incorporated compared to the experimental data of Le Coq [8]*

Two ways of determining the average percentage differences were considered between the predicted and experimental values observed in Figure 4.4. In the first case the percentage difference was determined for each point where values predicted by the two-strut model without the incorporated standard deviation are compared to the experimental data values for which the standard deviations were also excluded. The average of these percentage differences were then determined. The percentage difference was similarly determined for each point between the two-strut model values and experimental data values in which the standard deviation is subtracted from the hydraulic diameter. The average percentage difference of these points were then also determined. In the case where the standard deviation was added to the hydraulic diameter, the average percentage difference was once again determined using the same method. The average of these three average percentage differences was then calculated yielding 29%. In the second case, all the two-strut model values excluding the standard deviations, the two-strut model values in which the standard deviation was subtracted from the hydraulic diameter and the two-strut model values in which the standard deviation was added to the hydraulic diameter were compared to the experimental data without any standard deviation adjustments and the average percentage difference was calculated and yielded the same percentage value of 29%.

The specific surface area predictions made by the RUC model are therefore fairly accurate compared to the experimental values.

4.4 Sensitivity analysis

The effect of a variation in the values of the mean free path λ and the tangential momentum accommodation coefficient σ on the permeability prediction of the two-strut model including the Klinkenberg effect is shown in Figures 4.5 and 4.6, respectively.

For the mean free path, values of $\lambda = 50\,\text{nm}$ and $\lambda = 100\,\text{nm}$ were chosen in order to cover a wide range of values beyond the actual value of 63.4 nm used for airflow in the experiment. The latter values for λ correspond to Kn-values in the range defined by $2.00 \times 10^{-3} \leq Kn \leq 1.25 \times 10^{-2}$.

Besides the value of $\sigma = 0.2$ used for a smooth surface, the effect of $\sigma = 1$, i.e. the value associated with a rough surface, representing the upper limit of σ, is also indicated in Figure 4.6.

Although the effect on the permeability prediction of the variation in the two parameters cannot be directly compared due to the different percentage ranges that they cover, the model predictions still provide relatively accurate predictions compared to the experimental data for the parameter variations considered. Thus small changes in the values of λ and σ do not have significantly large effects on the permeability predictions attained.

4.5 Chapter summary

The effect of gas versus liquid flow on the parameter predictions of fibrous media were investigated in this chapter by taking the Klinkenberg effect into consideration. A Klinkenberg equation for the RUC models, which gives the relationship between the liquid permeability and gas permeability, was derived and incorporated into the permeability and specific surface area predictions of the uncompressed and compressed RUC models. For the uncompressed RUC models this included the adaptation of the permeability equations and the specific surface area equations obtained using kinetic and combined approaches. The adapted equations for the compressed RUC models comprised of the permeability equations and the specific surface area equations obtained using only the combined approach, due to the kinetic approach not giving viable results.

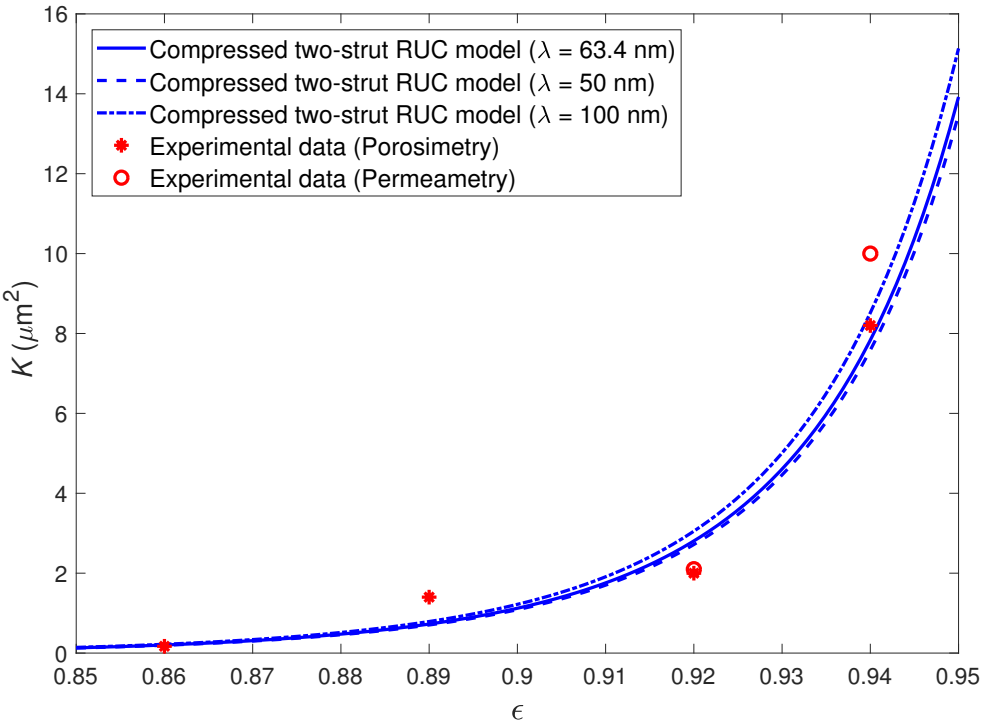

FIGURE 4.5: *Permeability predictions of the compressed two-strut RUC model for different λ values versus porosity compared to the experimental data of Le Coq [8]*

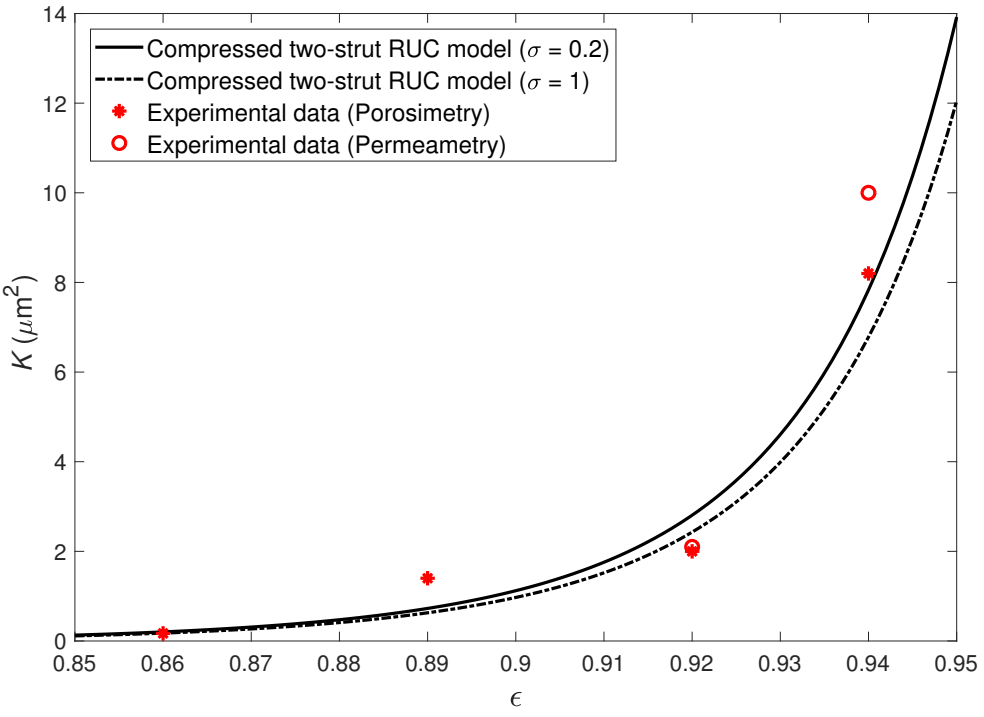

FIGURE 4.6: *Permeability predictions of the compressed two-strut RUC model for different σ values versus porosity compared to the experimental data of Le Coq [8]*

Permeability data for gas flow through fibrous media that fall within the slip flow regime are scarce and only one set of data was found, which was applicable to evaluate the model predictions obtained by the compressed RUC models including the Klinkenberg effect. For the uncompressed RUC models including the Klinkenberg effect, however, no data was found for evaluation or comparison.

A sensitivity analysis was also performed on the mean free path and tangential momentum accommodation coefficient present within the Klinkenberg equation incorporated into the compressed RUC models.

CHAPTER 5

Summary of modelling steps, conclusions and future work

In this chapter modelling steps will be given in order to calculate the permeability and specific surface area for the uncompressed and compressed three- and two-strut RUC models, along with the conclusions made and possible future work that can be considered resulting from this study.

Figure 5.1 shows an outline of the models used in this study to predict values for the permeability and specific surface area of fibrous porous media. It furthermore shows the adaptations implemented on the RUC models and the approaches used to obtain the specific surface area results.

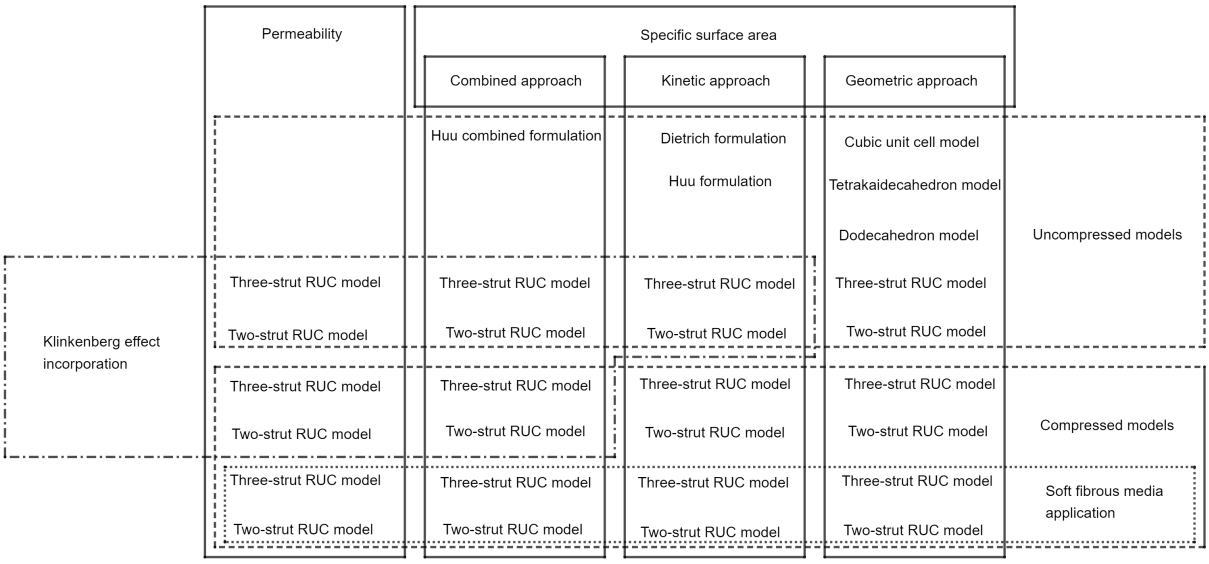

FIGURE 5.1: *Overview of models, model adaptations and approaches used in this study to predict permeability and specific surface area values of fibrous porous media*

The modelling steps will be given first.

5.1 Modelling steps

The modelling steps for utilizing the RUC models presented in this study will be divided into five categories: isotropic/uncompressed with liquid flow, anisotropic/compressed with liquid flow, soft compressed, isotropic/uncompressed with gas flow and anisotropic/compressed with gas flow. If the fibrous medium is a foamlike medium (e.g. metal foam), then the three-strut RUC model should be used and if the medium consists of fibre layers that are stacked on top of each other, then the two-strut RUC model should be used. In the modelling steps presented below the equations outside brackets refer to those obtained by the three-strut RUC models and the equations within the brackets will refer to those obtained by the two-strut RUC models.

5.1.1 Isotropic/uncompressed with liquid flow

1. Use equation (2.155) (equation (2.176)), if corresponding measured porosity and pore diameter values of media are known, to determine the **permeability**. Alternatively, use equation (2.207) (equation (2.209)) if porosity values and the mean strut diameter are known.

2. Use equation (2.96) (equation (2.116)), if corresponding measured porosity and pore diameter values of media are known, to determine the **specific surface area** using a *geometric* approach. Alternatively, use equations (2.94) (equation (2.114)) if porosity values and the mean strut diameter are known.

3. Use equation (2.159) (equation (2.180)), if corresponding measured porosity and liquid permeability values of media are known, to determine the **specific surface area** using a *kinetic* approach.

4. Use equation (2.201) (equation (2.204)), if corresponding measured porosity and liquid permeability values of media are known, to determine the **specific surface area** using a *combined* approach.

5.1.2 Anisotropic/compressed with liquid flow

1. Use equation (3.35) (equation (3.59)) to determine $d_{\parallel}$. Corresponding measured hydraulic diameter and porosity values should be known, as well as the mean strut diameter value.

2. Knowing $d_{\parallel}$, use $d_{\parallel_o} = d_{\parallel}/e$ to determine the values of $d_{\parallel_o}$. The experimentally measured compression ratios e need to be known (i.e. the sample thickness relative to its uncompressed state). Values for $d_{\parallel_o}$ are then obtained for the different stages of compression of which the average value should be calculated.

   Alternatively, if no hydraulic diameter or compression ratio values are available, use equation (3.36) (equation (3.60)) where only the initial porosity value along with the mean strut diameter need to be utilized to determine $d_{\parallel_o}$.

3. Knowing $d_{\parallel_o}$, calculate the streamwise dimension of the RUC by using equation (3.1) where e can be determined from equation (3.9). The value of C in equation (3.9) is obtained by dividing the experimentally measured compression ratios for each stage of compression by $1 - \epsilon$, where ϵ represents the corresponding measured porosity values, and taking the average. Should the compression ratios not be provided, e can be determined from equation (3.8).

4. Knowing $d_{\parallel}$, along with the mean strut diameter and porosity values, calculate the transverse dimension of the RUC by using equation (3.15) (equation (3.48)).

5. Knowing $d_{\parallel}$ and $d_{\perp}$, along with d_s, the **permeability** can be determined by using equation (3.33) (equation (3.58)).

6. Knowing $d_{\parallel}$ and $d_{\perp}$, along with d_s, the **specific surface area** using a *geometric* approach can be determined by using equation (3.40) (equation (3.64)).

7. Knowing $d_{\perp}$, along with d_s and experimental liquid permeability values, the **specific surface area** using a *combined* approach can be determined by solving the polynomial given by equation (3.45) (equation (3.68)).

5.1.3 Soft compressed

1. Follow steps 1 - 3 of Section 5.1.2 for the anisotropic/compressed media, to determine $d_{\parallel}$.

2. Knowing $d_{\parallel}$, along with the mean strut diameter value and corresponding experimental porosity and compression ratio values, determine $d_{\perp}$ by using equation (3.70) (equation (3.85)). The compression ratios are therefore required.

3. Knowing $d_{\parallel}$ and $d_{\perp}$, along with d_s and the e-values, the **permeability** can be determined by using equation (3.77) (equation (3.91)).

4. Knowing $d_{\parallel}$ and $d_{\perp}$, along with d_s and e-values, the **specific surface area** using a *geometric* approach can be determined by using equation (3.79) (equation (3.92)).

5. Knowing $d_{\perp}$, along with d_s, e-values and experimental permeability values, the **specific surface area** using a *combined* approach can be determined by solving the polynomial given by equation (3.83) (equation (3.96)).

5.1.4 Isotropic/uncompressed with gas flow

1. Use equation (4.1) to determine Kn, along with the λ-value of the gas used to acquire the experimental permeability and the hydraulic diameter values of the medium (or alternatively the pore diameter values). For flow in the non-slip regime, the Klinkenberg coefficient term can be neglected and the modelling steps outlined in Section 5.1.1 can be followed.

2. Use equation (4.27) (equation (4.29)), if the corresponding measured porosity and pore diameter values of media are known, to determine the **permeability**. Alternatively, use equation (4.28) (equation (4.30)) if the measured porosity values and the mean strut diameter are known. Furthermore, use the determined Kn-values and experimental, or estimated, σ-value to determine the Klinkenberg coefficient.

3. Knowing Kn, along with the corresponding experimental porosity, gas permeability values and σ, the **specific surface area** using a *kinetic* approach can be determined by using equation (4.32) (equation (4.34)).

4. Knowing Kn, along with the corresponding experimental porosity and permeability values and σ, the **specific surface area** using a *combined* approach can be determined by solving the polynomial given by equation (4.35) (equation (4.36)).

5.1.5 Anisotropic/compressed with gas flow

1. Follow steps 1 - 4 of Section 5.1.2 for the anisotropic/compressed media, to determine $d_{\parallel}$ and $d_{\perp}$.

2. Knowing $d_{\parallel}$ and $d_{\perp}$, along with the mean strut diameter, σ and λ, the **permeability** can be determined by using equation (4.39) (equation (4.41)). For flow in the non-slip flow regime, the Klinkenberg coefficient can be neglected and the modelling steps outlined in Section 5.1.2 can be followed.

3. Knowing $d_{\perp}$, along with d_s, σ, Kn and the experimental gas permeability, the **specific surface area** using a *combined* approach can be determined by solving the polynomial given by equation (4.42) (equation (4.43)). The Knudsen number used in the Klinkenberg coefficient can be determined by using equation (4.37) and the gas λ-value.

Some concluding remarks will be given in the next section resulting from the investigations conducted in this study.

5.2 Conclusions

The predictions obtained using the equations acquired from the different isotropic geometric models for the specific surface area showed that the tetrakaidecahedron, dodecahedron and three-strut RUC models give similar results and furthermore compared well to the experimental data considered. All the geometric models did, however, in general over-predict the experimental data. The tetrakaidecahedron model performed the best when compared to experimental data, followed by the three-strut RUC model and the dodecahedron model. The models that revealed the closest correspondence to the specific surface area predicted by the three-strut RUC model were the cubic unit cell model, the tetrakaidecahedron model as given by Buciuman and Kraushaar-Czarnetzki and the "slim" dodedcahedron models. The simplicity of the rectangular RUC geometry, as opposed to the complex geometry of the tetrakaidecahedron and dodecahedron models, allows for geometric adaptations which adds to the attractive qualities of this model. The balance between simplicity and accuracy of the three-strut RUC model is thus a useful model characteristic. This advantage is shared by the two-strut RUC model, although this model was not included in the comparisons to the experimental data for the specific surface area due to its geometry resembling fibres more closely than foams and the data considered was only applicable to foams. Another advantage of the RUC models are that they are the only geometric models that provide a geometric, kinetic and combined approach to determine the dimensionless specific surface area.

Two new versions of the tetrakaidecahedron model was proposed for predicting the specific surface area based on the geometric approach that separately incorporates the strut lengths of Buciuman and Kraushaar-Czarnetzki [25] and Richardson et al. [4]. The two newly proposed equations provided more accurate predictions for the dimensionless specific surface area in comparison to the experimental data considered than the model predictions provided by the cubic unit cell model of Giani et al. [14] and dodecahedron model of Huu et al. [20] with cylindrical "fat" struts.

In order to, however, address the question of whether the more complex geometries of the tetrakaidecahedron and dodecahedron models provide more accurate predictions than the simpler cubic unit cell and three-strut RUC models, depends on how the models are categorized with respect to complexity: If the tetrakaidecahedron and dodecahedron models are considered

together as the more complex models, the complex models provide more accurate predictions than the simpler three-strut RUC and cubic unit cell models. If the four models are considered individually and the complexity of the model with respect to geometry and modelling procedures in decreasing order are regarded to be the tetrakaidecahedron, dodecahedron, three-strut RUC and the cubic unit cell model, then the more complex models do not necessarily provide more accurate predictions due to the three-strut RUC model providing slightly more accurate predictions in some cases than the dodecahedron model.

In the kinetic approach it was determined that the specific surface area equations in terms of K_F yields more accurate predictions than those in terms of K. This may be due to the fact that the square root of K is calculated in the equations for the specific surface area and K appears in the denominator where-as this is not the case for the equations in terms of K_F. Although possible experimental errors are made smaller through the square root, it appearing in the denominator of the specific surface area equation enlarges the error. Furthermore, the formulation that performed best when compared to the given experimental data sets was the three-strut RUC formulation with d_p defined as in equation (1.9).

With regards to the evaluation of the models predicting the specific surface area of foams, the combined approach formulation that compared the best overall to the experimental data considered, was the three-strut RUC formulation. The "fat" dodecahedron model approach mostly over-predicted both data sets.

Comparison of the two- and three-strut RUC models with experimental permeability data obtained from glass fibres re-enforced the reasoning that the two-strut RUC model represents porous materials with a stacked fibre layer morphology more accurately than the three-strut RUC model since the predictions of the two-strut model provided better correspondence with the fibre data than the three-strut model.

For the compressed RUC models the specific non-linear relationship proved to be the most feasible method to use when compression factors are provided, otherwise the general non-linear relationship can be applied.

The rigid compressed RUC models, where the strut diameter remained constant under compression, performed well in predicting the permeability. In comparison to the experimental data considered the compressed three-strut RUC model performed better than the compressed two-strut model. The specific surface area predictions obtained using a geometric approach differed from the predictions obtained using a combined approach in that the geometric approach predicted higher values for the two-strut model and the combined approach predicted higher values for the three-strut model. Furthermore, when compared to the predictions based on the hydraulic diameter data, the specific surface area values determined using the combined approach corresponded slightly better to these predictions than the values obtained using the geometric approach. It has been determined, however, that the relationship between the hydraulic diameter and the specific surface area given by equation (1.6) do not give the expected correlation of these parameters in fibrous media. The predictions obtained from the hydraulic diameter data are therefore merely an indication of the order of magnitude and range within which the values of the specific surface area are expected to lie rather than an indication of the precise expected values, due to the predictions being obtained from equation (1.6).

The permeability predictions of the soft compressed RUC models, representing the soft polyester fibrous media subjected to compression, compared well with the experimental permeability data. The majority of the experimental data points were enclosed between the soft compressed three-strut RUC model permeability predictions based on the isotropic $d_{\|_o}$ and $d_{\|_o} - 50\%$ values. For each $d_{\|_o}$-value considered, the permeability predicted by the two-strut model was lower than

that of the three-strut model . The specific surface area predictions of the soft compressed RUC models showed that the geometric approach in general predicted higher values than the combined approach. The soft compressed two-strut RUC model furthermore gave higher predictions for the specific surface area than the soft compressed three-strut RUC model when the geometric approach was used. The different $d_{\|_o}$-values did not give significant differences in the specific surface area predictions of the two-strut model based on the geometric approach, whereas the differences in the predictions of the three-strut model attributed to the $d_{\|_o}$-values were not negligible.

For most of the cases where the kinetic approach was applied to the compressed RUC models in order to obtain specific surface area predictions, negative hydraulic diameter values and consequently negative specific surface area values were attained. The kinetic approach, in combination with the compressed RUC models, is therefore not a recommended approach to determine the specific surface area for compressed fibrous media based on the data used in the analysis.

The model predictions for the permeability and specific surface area in which the Klinkenberg effect was incorporated gave higher values than the model predictions where the Klinkenberg effect was not incorporated. The compressed two-strut RUC models furthermore gave lower predictions for the specific surface area than the corresponding compressed three-strut RUC models. The experimental permeability data and model comparisons, in which the standard deviation data provided for the hydraulic diameter was included, showed that the model that approximated the data most accurately was the compressed two-strut RUC model including the Klinkenberg effect, as apposed to the results where the Klinkenberg effect was not included. When the geometry of the glass fibres is considered, the two-strut RUC model provides a physically more realistic representation of the stacking of fibre layers forming parallel sheets of fibres and therefore agrees with this observation. The compressed two-strut RUC model with the Klinkenberg effect is therefore the preferred model for the permeability prediction of the compressed sheets of glass fibres.

The specific surface area predictions in which the Klinkenberg effect is included, of which only the combined approach was presented for the compressed RUC models, were higher than the corresponding model predictions without the Klinkenberg effect. The two-strut RUC models predicted lower values than the three-strut RUC models for the models with and without the Klinkenberg effect. With the exception of the lowest porosity data point, the predicted values for the specific surface area obtained from the experimental hydraulic diameter data generally gave higher predictions that the compressed RUC model predictions. The discrepancies between the model predictions and predictions based on the hydraulic diameter data were however less when the standard deviation in the measured hydraulic diameter values were taken into account. The models with the Klinkenberg effect incorporated overall gave satisfactory results for the compressed RUC models.

A sensitivity analysis of the mean free path and tangential momentum accommodation coefficient, present in the Klinkenberg equation incorporated into the RUC models, revealed that small changes in these parameters do not have significantly large effects on the permeability predictions of the models.

5.3 Contributions of author

The following adaptations made to the "foam" RUC models have not been done before by other authors: (i) the combined kinetic-geometric approach proposed for the uncompressed and compressed RUC models (ii) the incorporation of the Klinkenberg effect into the uncompressed and

compressed three-strut and two-strut RUC models and (iii) the incorporation of the compression ratio into the streamwise and transverse solid dimensions of the soft compressed three-strut and two-strut RUC models. The proposed permeability and specific surface area equations accounting for the combined effects of compression and slip flow contributes to the field of flow through fibrous media since similar equations could not be found in the literature.

In the following section some recommendations for possible future work will be given.

5.4 Future work

The performance of some of the adapted models could, for future study, be analysed more thoroughly by acquiring and utilizing additional data applicable to the models. Only the rigid compressed RUC model, where the strut diameter remained unchanged with compression, was adapted to account for the Klinkenberg effect and not the compressed RUC model representing soft polyester fibrous media. Consequently the latter model could also be adapted to take the Klinkenberg effect into account. The compression-porosity relationship could also further be investigated to take more physically representative responses of the porous materials to compression into account.

The RUC models could furthermore be adapted by introducing additional solid material to represent the solid lumps at the intersection of struts in actual foams, similarly to the case of the "fat" dodecahedron models. The effects of changing the square strut geometry of the isotropic RUC models representing fibrous porous media to rectangular strut geometry on the permeability and specific surface area predictions could also be investigated.

Another adaptation that could be introduced to further extend the range of applicability of the RUC models could be to replace the current use of the average pore diameter by a pore size distribution into the model predictions for the permeability and specific surface area. This adaptation would also allow for the use of the RUC models to predict the geometric parameters of fibrous porous media on the nanometer scale.

References

[1] S Woudberg and J P Du Plessis. An analytical Ergun-type equation for porous foams. *Chemical Engineering Science*, 148:44–54, 2016.

[2] B Dietrich, W Schabel, M Kind, and H Martin. Pressure drop measurements of ceramic sponges - Determining the hydraulic diameter. *Chemical Engineering Science*, 64:3633–3640, 2009.

[3] G I Garrido, F C Patcas, S Lang, and B Kraushaar-Czarnetzki. Mass transfer and pressure drop in ceramic foams: A description for different pore sizes and porosities. *Chemical Engineering Science*, 63:5202–5217, 2008.

[4] J T Richardson, Y Peng, and D Remue. Properties of ceramic foam catalyst supports: Pressure drop. *Applied Catalysis A: General*, 204:19–32, 2000.

[5] J F Liu, W T Wu, W C Chiu, and W H Hsieh. Measurement and correlation of friction characteristic of flow through foam matrixes. *Experimental Thermal and Fluid Science*, 30:329–336, 2006.

[6] S Woudberg, M C van Heyningen, L Le Coq, J Legrand, and J P Du Plessis. Analytical determination of the effect of compression on the permeability of fibrous porous media. *Chemical Engineering Science*, 112:108–115, 2014.

[7] M C van Heyningen. Investigating the effect of compression on the permeability of fibrous porous media. Master's thesis, Stellenbosch University, South Africa, 2014.

[8] L Le Coq. Influence on permeability of the structural parameters of heterogeneous porous media. *Environmental Technology*, 29:141–149, 2008.

[9] S Jaganathan, H V Tafreshi, E Shim, and B Pourdeyhimi. A study on compression-induced morphological changes of nonwoven fibrous materials. *Colloids and Surfaces A: Physicochemical and Engineering Aspects*, 337:173–179, 2009.

[10] G W Jackson and D F James. The permeability of fibrous porous media. *The Canadian Journal of Chemical Engineering*, 64:364–374, 1986.

[11] H D Akaydin, A Pierides, S Weinbaum, and Y Andreopoulos. Permeability of soft porous media under one-dimensional compaction. *Chemical Engineering Science*, 66:1–14, 2011.

[12] L Marmoret, M Lewandowski, and A Perwuelz. An air permeability study of anisotropic glass wool fibrous products. *Transport in Porous Media*, 93:79–97, 2012.

[13] J Higdon and G Ford. Permeability of three-dimensional models of fibrous porous media. *Journal of Fluid Mechanics*, 308:341–361, 1996.

[14] L Giani, G Groppi, and E Tronconi. Mass-transfer characterization of metallic foams as supports for structured catalysts. *Industrial and Engineering Chemistry Research*, 44:4993–5002, 2005.

[15] D Edouard, M Lacroix, C P Huu, and F Luck. Pressure drop modeling on SOLID foam: State-of-the art correlation. *Chemical Engineering Journal*, 144:299–311, 2008.

[16] S Mancin, C Zilio, A Cavallini, and L Rossetto. Pressure drop during air flow in aluminum foams. *International Journal of Heat and Mass Transfer*, 53:3121–3130, 2010.

[17] A Bhattacharya, V V Calmidi, and R L Mahajan. Thermophysical properties of high porosity metal foams. *International Journal of Heat and Mass Transfer*, 45:1017–1031, 2002.

[18] A Inayat, H Freund, T Zeiser, and W Schwieger. Determining the specific surface area of ceramic foams: The tetrakaidecahedra model revisited. *Chemical Engineering Science*, 66:1179–1188, 2011.

[19] G Manzo, Y Wu, G Chase, and A Goux. Comparison of nonwoven glass and stainless steel microfiber media in aerosol coalescence filtration. *Separation and Purification Technology*, 162:14–19, 2016.

[20] T J Lu, H A Stone, and M F Ashby. Heat transfer in open-cell metal foams. *Acta Materialia*, 46(10):3619–3635, 1998.

[21] T T Huu, M Lacroix, C P Huu, D Schweich, and D Edouard. Towards a more realistic modeling of solid foam: Use of the pentagonal dodecahedron geometry. *Chemical Engineering Science*, 64:5131–5142, 2009.

[22] J P Du Plessis, A Montillet, J Comiti, and J Legrand. Pressure drop prediction for flow through high porosity metallic foams. *Chemical Engineering Science*, 49(21):3545–3553, 1994.

[23] M Lacroix, P Nguyen, D Schweich, C P Huu, S Savin-Poncet, and D Edouard. Pressure drop measurements and modeling on SiC foams. *Chemical Engineering Science*, 62:3259–3267, 2007.

[24] L L Gibson and M F Ashby. *Cellular solids*. Pergamon Press, Oxford, 1988.

[25] F C Buciuman and B Kraushaar-Czarnetzki. Ceramic foam monoliths as catalyst carriers. 1. Adjustment and description of the morphology. *Industrial and Engineering Chemistry Research*, 42:1863–1869, 2003.

[26] J P Du Plessis and J H Masliyah. Mathematical modelling of flow through consolidated isotropic porous media. *Transport in Porous Media*, 3:145–161, 1988.

[27] J Grosse, B Dietrich, G I Garrido, P Habisreuther, N Zarzalis, H Martin, M Kind, and B Kraushaar-Czarnetzki. Morphological characterization of ceramic sponges for applications in chemical engineering. *Industrial and Engineering Chemistry Research*, 48:10395–10401, 2009.

[28] E A Moreira and J R Coury. The influence of structural parameters on the permeability of ceramic foams. *Brazilian Journal of Chemical Engineering*, 21(01):23–33, 2004.

[29] N Dukhan, R Picón-Feliciano, and Á R Álvarez Hernández. Air flow through compressed and uncompressed aluminum foam: Measurements and correlations. *Journal of Fluids Engineering*, 128:1004–1012, 2006.

[30] B V Antohe, J L Lage, D C Price, and R M Weber. Experimental determination of permeability and inertia coefficients of mechanically compressed aluminum porous matrices. *Journal of Fluids Engineering*, 119:404–412, 1997.

[31] K Boomsma and D Poulikakos. The effects of compression and pore size variations on the liquid flow characteristics in metal foams. *Journal of Fluids Engineering*, 124:263–272, 2002.

[32] K Hooman, A Tamayol, M Dahari, M R Safaei, H Togun, and R Sadri. A theoretical model to predict gas permeability for slip flow through a porous medium. *Applied Thermal Engineering*, 70:71–76, 2014.

[33] M D M Innocentini and V C Pandofelli. Permeability of porous ceramics considering the Klinkenberg and inertial effects. *Journal of the American Ceramic Society*, 84:941–944, 2001.

[34] F Civan. Effective correlation of apparent gas permeability in tight porous media. *Transport in Porous Media*, 82:375–384, 2010.

[35] C Li, P Xu, S Qiu, and Y Zhou. The gas effective permeability of porous media with Klinkenberg effect. *Journal of Natural Gas Science and Engineering*, 34:534–540, 2016.

[36] W Tanikawa and T Shimamoto. Klinkenberg effect for gas permeability and its comparison to water permeability for porous sedimentary rocks. *Hydrology and Earth System Sciences Discussion*, 3:1315–1338, 2006.

[37] Q Zheng, B Yu, Y Duan, and Q Fang. A fractal model for gas slippage factor in porous media in the slip flow regime. *Chemical Engineering Science*, 87:209–2150, 2013.

[38] J Marschall and F S Milos. Gas permeability of rigid fibrous refractory insulations. *Journal of Thermophysics and Heat Transfer*, 12(4):528–535, 1998.

[39] S A Hosseini and H V Tafreshi. Modeling permeability of 3-D nanofiber media in slip flow regime. *Chemical Engineering Science*, 65:2249–2254, 2010.

[40] F Aldakheel, M S Ismail, K J Hughes, D B Ingham, L Ma, M Pourkashanian, D Cumming, and R Smith. Gas permeability, wettability and morphology of gas diffusion layers before and after performing a realistic ex-situ compression test. *Renewable Energy*, 151:1082–1091, 2020.

[41] P Turtoi, T Cicone, and A Fatu. Experimental and theoretical analysis of (water) permeability variation of nonwoven textiles subjected to compression. *Mechanics and Industry*, 18:307, 2017.

[42] D Ehrlich and J A Schwille. Permeability of space vehicle fibrous thermal protection blankets in viscous and slip flow regimes. *International Journal of Aerospace Engineering*, 28(3):04014085, 2015.

[43] Y Awin and N Dukhan. Experimental performance assessment of metal-foam flow fields for proton exchange membrane fuel cells. *Applied Energy*, 252:113458, 2019.

[44] W C Tan, L H Saw, F Yusof, H A Thiam, and J Xuan. Investigation of functionally graded metal foam thermal management system for solar cell. *International Journal of Energy Research*, pages 1–17, 2019.

[45] A R A Hernandez. Combined flow and heat transfer characterization of open cell aluminum foams. Master's thesis, University of Puerto Rico, Puerto Rico, 2005.

[46] M S Hossain and B Shabani. Air flow through confined metal foam passage. *Experimental Thermal and Fluid Science*, 99:13–25, 2018.

[47] J G Fourie and J P Du Plessis. Pressure drop modelling in cellular metallic foams. *Chemical Engineering Science*, 57:2781–2789, 2002.

[48] R Bird, W Stewart, and E Lightfoot. *Transport Phenomena*. John Wiley & Sons, New York (NY), 2nd edition, 2007.

[49] C Schaschke. *Dictionary of Chemical Engineering*. Oxford University Press, 2014.

[50] J G Speight. *Rules of Thumb for Petroleum Engineers*. John Wiley & Sons, 2017.

[51] M L Hunt and C L Tien. Effects of thermal dispersion on forced convection in fibrous media. *International Journal of Heat and Mass Transfer*, 31(2):301–309, 1988.

[52] J Chastanet, P Royer, and J L Auriault. Does Klinkenberg's law survive upscaling? *Transport in Porous Media*, 56:171–198, 2004.

[53] A F Miguel and A Serrenho. On the experimental evaluation of permeability in porous media using a gas flow method. *Journal of Physics D: Applied Physics*, 40:6824–6828, 2007.

[54] R W Barber and D R Emerson. The influence of Knudsen number on the parallel plate micro-channels hydrodynamic development length within. In *Advances in Fluid Mechanics IV*, volume 2, pages 207–216, Southampton, UK, 2002. WITS Press.

[55] T Acharya and M J Martin. Variation of momentum accommodation coefficients with molecular mass and structure. *Journal of Thermophysics and Heat Transfer*, 33:773–778, 2019.

[56] S Woudberg. *Comparative analysis of predictive equations for transfer process in different porous structures*. PhD thesis, Stellenbosch University, Stellenbosch, 2012.

[57] F Achchaq, K Djellab, and H Beji. Hydric, morphological and thermo-physical characterization of glass wools: From macroscopic to microscopic approach. *Construction and Building Materials*, 23:3214–3219, 2009.

[58] S Zhu, R H Pelton, and K Collver. Mechanistic modelling of fluid permeation through compressible fiber beds. *Chemical Engineering Science*, 50:3557–3572, 1995.

[59] S Woudberg. Permeability prediction of an analytical pore-scale model for layered and isotropic fibrous porous media. *Chemical Engineering Science*, 164:232–245, 2017.

[60] S Woudberg and J P Du Plessis. Predicting the permeability of very low porosity sandstones. *Transport in Porous Media*, 73:39–55, 2008.

[61] R W Barber and D R Emerson. Challenges in modeling gas-phase flow in microchannels: From slip to transition. *Heat Transfer Engineering*, 27(4):3–12, 2006.

[62] L J Klinkenberg. The permeability of porous media to liquids and gases. *American Petroleum Institute*, 1941.

[63] F Panerai, J D White, T J Cochell, O M Schroeder, N N Mansour, M J Wright, and A Martin. Experimental measurements of the permeability of fibrous carbon at high-temperature. *International Journal of Heat and Mass Transfer*, 101:267–273, 2016.

[64] J M Wilms. On the hydrodynamic permeability of foamlike media. Master's thesis, Stellenbosch University, South Africa, 2006.

APPENDIX A

Volume of tetrakaidecahedron cell

The tetrakaidecahedron cell, as illustrated in Figure A.1(a), can be partitioned into three parts to calculate the volume of a cell, as shown in Figure A.1(b), A.1(c) and A.1(d). Four triangular prisms are fitted in the middle of the tetrakaidecahedron cell which forms two square prisms that connect the opposite square windows of the cell. Above and below these square prisms two incomplete pyramids are fitted. In Figure A.1(c) the small pyramid represents the pyramid removed from the top of the larger pyramid to form an incomplete one to fill the space at the top and at the bottom of the cell. Finally, to fill the gaps on the sides of the square prisms, eight incomplete tetrahedra are used. These incomplete tetrahedra are, similarly to the incomplete pyramids, represented in Figure A.1(d) where the small tetrahedral represents the tetrahedral removed from the bottom of the larger tetrahedral to form an incomplete one.

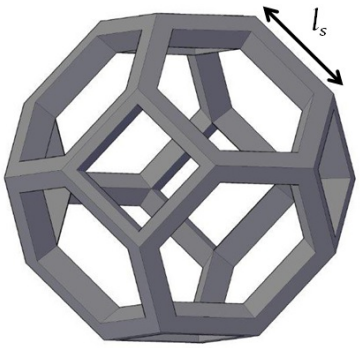

(a) *Tetrakaidecahedron cell*

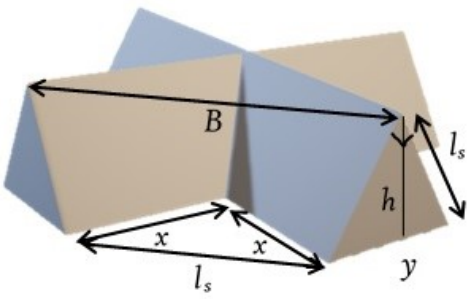

(b) *Triangular prisms*

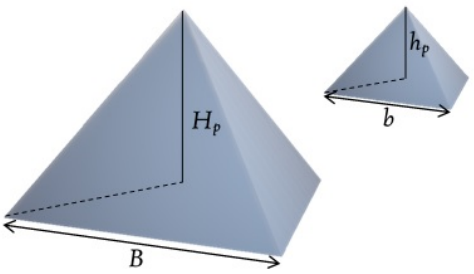

(c) *Incomplete pyramid*

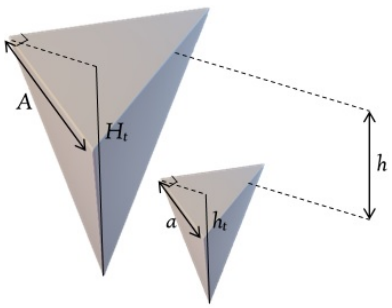

(d) *Incomplete tetrahedral*

FIGURE A.1: *Partitioning of the volume of a tetrakaidecahedron cell*

The volume of two intersecting triangular prisms, as shown in Figure A.1(b), can be determined by expressing the dimensions y, h and x in terms of l_s, i.e.

$$y = \sqrt{l_s^2 + l_s^2} = \sqrt{2}\, l_s \,,$$
$$h = \sqrt{l_s^2 - \left(\frac{y}{2}\right)^2} = \frac{1}{\sqrt{2}}\, l_s \,,$$

and

$$x = \sqrt{\frac{1}{2} l_s^2} = \frac{1}{\sqrt{2}}\, l_s \,.$$

Adding the volume of the two prisms while subtracting the volume of the center pyramid, leads to

$$\begin{aligned} &2 \times (\text{volume of triangular prism}) - (\text{volume of pyramid in center}) \\ &= 2\left[\frac{1}{2} y \times h \times (2x + y)\right] - \left[\frac{1}{3} y^2 \times h\right] \\ &= \frac{5\sqrt{2}}{3}\, l_s^3 \,. \end{aligned}$$

The volume of an incomplete pyramid, using the pyramids shown in Figure A.1(c), can be obtained by expressing the base level dimensions in terms of l_s using the dimensions shown in Figure A.1(b), i.e.

$$B = \sqrt{\left(x + \frac{1}{2} y\right)^2 + \left(x + \frac{1}{2} y\right)^2} = \sqrt{(\sqrt{2} l_s)^2 + (\sqrt{2} l_s)^2} = 2 l_s$$

and

$$b = l_s \,.$$

Furthermore the heights of both the larger and smaller pyramids can be determined by making use of the base level dimensions obtained, ratio similarity between the two pyramids and the Pythagoras theorem, which yields

$$H_p = \sqrt{2}\, l_s$$

and

$$h_p = \frac{1}{\sqrt{2}}\, l_s \,.$$

Using the latter expressions, the volumes of the big and small pyramids can be determined and subtracted from one another as follows:

$$\begin{aligned} &\text{volume of larger pyramid} - \text{volume of smaller pyramid} \\ &= \frac{\text{base area of larger pyramid} \times H_p}{3} - \frac{\text{base area of smaller pyramid} \times h_p}{3} \\ &= \frac{B^2 \times H_p}{3} - \frac{b^2 \times h_p}{3} \\ &= \frac{4\, l_s^2\, (\sqrt{2}\, l_s) - l_s^2 \left(\frac{1}{\sqrt{2}}\, l_s\right)}{3} \\ &= \frac{7\sqrt{2}}{6}\, l_s^3 \,. \end{aligned}$$

The volume of an incomplete tetrahedral, using the tetrahedra in Figure A.1(d), can be obtained by subtracting the larger tetrahedral from the smaller one, which in this case is the same as subtracting half of a larger pyramid from half of a smaller pyramid. Expressions for the base levels A and a and the heights H_t and h_t in terms of l_s can be obtained as follows:

$$A = x + \frac{1}{2}y = \sqrt{2}\,l_s \;\; ; \;\; a = x = \frac{1}{\sqrt{2}}\,l_s \;\; ; \;\; H_t = \sqrt{2}\,l_s$$

and

$$h_t = \frac{1}{\sqrt{2}}\,l_s\,,$$

where the heights were calculated by making use of the similarity ratio between the two tetrahedra and h (the difference in height of the two tetrahedra).

The volume of the incomplete tetrahedral can thus be obtained in the following manner:

$$\begin{aligned}
&\text{volume of larger tetrahedral} - \text{volume of smaller tetrahedral} \\
&= \frac{1}{2}(\text{volume of incomplete pyramid}) \\
&= \frac{1}{2}\left(\frac{A^2 \times H_t}{3} - \frac{a^2 \times h_t}{3}\right) \\
&= \frac{2\,l_s^2\,(\sqrt{2}\,l_s) - \frac{1}{2}\,l_s^2\,\left(\frac{1}{\sqrt{2}}\,l_s\right)}{6} \\
&= \frac{7\sqrt{2}}{24}\,l_s^3\,.
\end{aligned}$$

The total volume of the tetrakaidecahedron, as shown in Figure A.1(a), can then be obtained by adding the appropriate amount of individual parts to fill up the total volume, i.e. 2 of the intersecting triangular prisms, 2 of the incomplete pyramids and 8 of the incomplete tetrahedrals, yielding

$$\begin{aligned}
&2 \times (\text{volume of two intersecting triangular prisms}) + 2 \times (\text{volume of incomplete pyramid}) \\
&\qquad + 8 \times (\text{volume of incomplete tetrahedral}) \\
=&\frac{10\sqrt{2}}{3}\,l_s^3 + \frac{7\sqrt{2}}{3}\,l_s^3 + \frac{7\sqrt{2}}{3}\,l_s^3 \\
=&8\sqrt{2}\,l_s^3\,,
\end{aligned} \tag{A.1}$$

which is the volume of a tetrakaidecahedron cell with side length l_s.

APPENDIX B

Volume of triangular struts and tetrahedral nodes

The volume of the struts can be calculated using triangular strut geometry for the tetrakaidecahedron cell or the dodecahedron cell by determining the volume of a triangular prism, as shown in Figure B.1(a), which represents the struts, and the volume of a tetrahedral, as shown in Figure B.1(b), which represents the nodes between the struts. The volume of the triangular prism is then multiplied by the number of struts in each cell and then divided by the number of cells that shares each strut. The tetrahedral volume is multiplied by the number of nodes in each cell and then divided by the number of cells that shares each node.

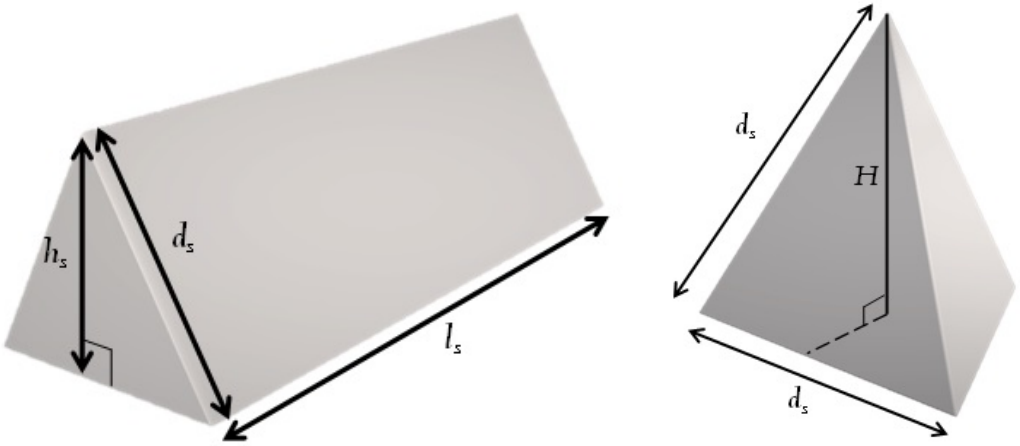

(a) *Triangular prism strut*

(b) *Tetrahedral node*

FIGURE B.1: *Triangular strut and node geometry*

The volume of the triangular prism can be calculated by first determining the perpendicular height h_s of the equilateral triangle of side length d_s, i.e.

$$h_s = \sqrt{d_s^2 - \left(\frac{1}{2}d_s^2\right)^2} = \frac{\sqrt{3}}{2}\,d_s\,.$$

The volume can then be calculated as follows:

$$\begin{aligned}\text{volume of triangular prism} &= \text{area of triangle} \times \text{length of prism} \\ &= \frac{1}{2}\, d_s\, h_s\, l_s = \frac{1}{2}\, d_s \left(\frac{\sqrt{3}}{2}\, d_s\right) l_s = \frac{\sqrt{3}}{4}\, d_s^2\, l_s\,. \end{aligned} \tag{B.1}$$

The volume of the tetrahedral with side lengths d_s, as shown in Figure B.1(b), can be calculated by first determining the perpendicular height H of the tetrahedral, i.e.

$$H = \sqrt{d_s^2 - \left(\frac{1}{\sqrt{3}}\, d_s\right)^2} = \sqrt{d_s^2 - \frac{1}{3}\, d_s^2} = \sqrt{\frac{2}{3}}\, d_s\,.$$

The volume can then be calculated as follows:

$$\begin{aligned}\text{volume of tetrahedral} &= \frac{\text{volume of pyramid}}{2} \\ &= \frac{\frac{1}{3}\, d_s \cdot h_s \cdot H}{2} = \frac{d_s \left(\frac{\sqrt{3}}{2}\, d_s\right) \left(\sqrt{\frac{2}{3}}\, d_s\right)}{6} = \frac{\sqrt{2}}{12}\, d_s^3\,. \end{aligned} \tag{B.2}$$

B.1. Using equations (B.1) and (B.2), the volume of the struts of the tetrakaidecahedron cell can thus be determined as follows:

$$\begin{aligned}&\frac{\text{number of struts per cell}}{\text{number of cells that shares each strut}} \times \text{volume of triangular prism} \\ &\qquad + \frac{\text{number of nodes}}{\text{number of cells that shares each node}} \times \text{volume of tetrahedral} \\ &= \frac{36}{3} \cdot \frac{\sqrt{3}}{4}\, d_s^2\, l_s + \frac{24}{4} \cdot \frac{\sqrt{2}}{12} d_s^3 \\ &= 3\sqrt{3}\, d_s^2\, l_s + \frac{1}{\sqrt{2}}\, d_s^3\,. \end{aligned} \tag{B.3}$$

B.2. Using equations (B.1) and (B.2), the volume of the struts of the dodecahedron cell with triangular struts can thus be determined as follows:

$$\begin{aligned}&\frac{\text{number of struts per cell}}{\text{number of cells that shares each strut}} \times \text{volume of triangular prism} \\ &\qquad + \frac{\text{number of nodes}}{\text{number of cells that shares each node}} \times \text{volume of tetrahedral} \\ &= \frac{30}{3} \cdot \frac{\sqrt{3}}{4}\, d_s^2\, l_s + \frac{20}{4} \cdot \frac{\sqrt{2}}{12}\, d_s^3 \\ &= \frac{5\sqrt{3}}{2}\, d_s^2\, l_s + \frac{5\sqrt{2}}{12}\, d_s^3\,. \end{aligned} \tag{B.4}$$

B.3. The volume of the struts of the dodecahedron cell with cylindrical struts is determined by first finding an expression for the volume of a cylinder with parameters as shown in Figure (2.8), i.e.

$$\text{volume of cylinder} = \pi \times \text{radius}^2 \times \text{length of cylinder} = \pi \left(\frac{d_s}{2}\right)^2 l_s = \frac{\pi\, l_s\, d_s^2}{4}\,.$$

The nodes are tetrahedral, therefore equation (B.2) can be used and the volume of the struts of the dodecahedron cell with cylindrical struts can thus be determined as follows:

$$\begin{aligned}
&\frac{\text{number of struts per cell}}{\text{number of cells that shares each strut}} \times \text{volume of cylinder} \\
&\qquad + \frac{\text{number of nodes}}{\text{number of cells that shares each node}} \times \text{volume of tetrahedral} \\
&= \frac{30}{3} \cdot \frac{\pi\, l_s\, d_s^2}{4} + \frac{20}{4} \cdot \frac{\sqrt{2}}{12}\, d_s^3 \\
&= \frac{5\pi\, l_s\, d_s^2}{2} + \frac{5\sqrt{2} d_s^3}{12}\,. \qquad \text{(B.5)}
\end{aligned}$$

APPENDIX C

Volume and surface area added to "fat" dodecahedron model

The "fat" dodecahedron model of a foam cell is illustrated in Figure C.1(a). In Figure C.1(b) the "fat" dodecahedron model minus the "slim" dodecahedron model is shown, i.e. the volume that was added to the "slim" model to attain the "fat" model.

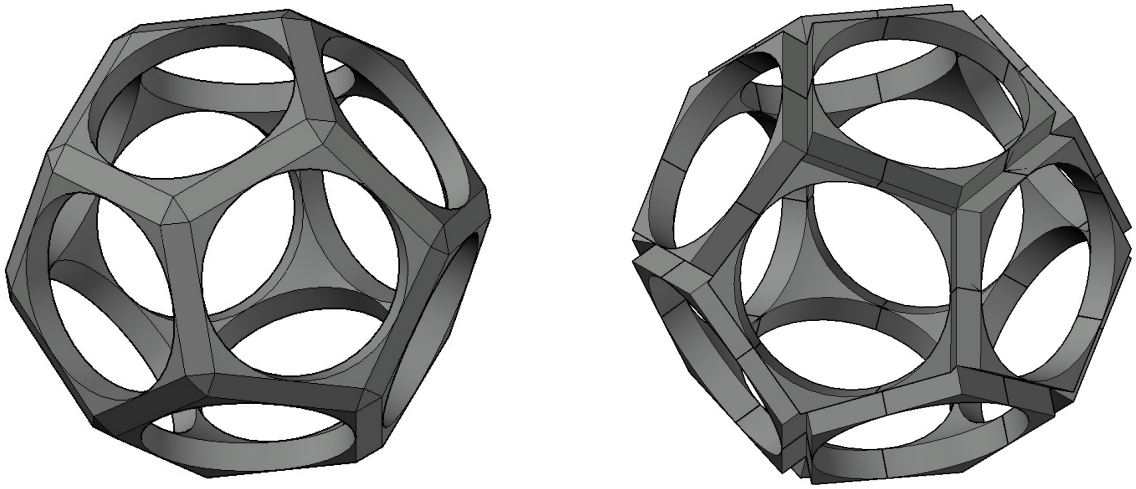

(a) *"Fat" dodecahedron model* (b) *Volume added to "fat" dodecahedron model*

FIGURE C.1: *Volume added to the nodes of a "fat" dodecahedron cell*

In order to calculate the strut volume of this model, a certain volume is added to the strut volume of the "slim" dodecahedron model with triangular strut geometry and cylindrical strut geometry and this added volume can be determined by first taking the faces of the cell into consideration.

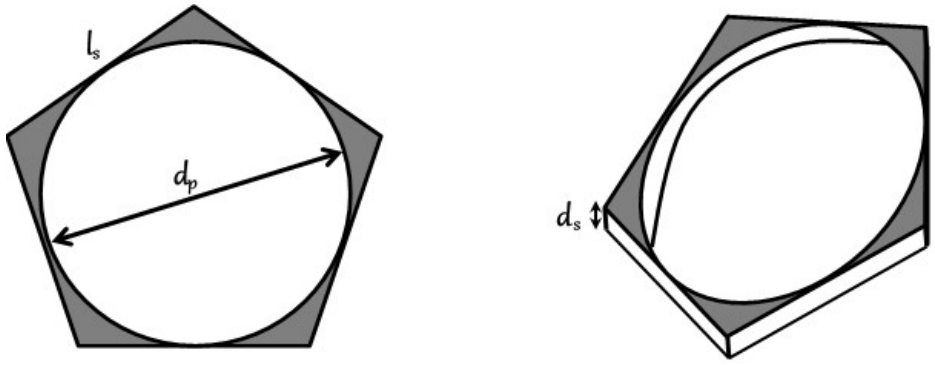

FIGURE C.2: *Volume added to the face of a "fat" dodecahedron cell*

Figure C.2 shows the volume added to each face of the cell, which can be calculated by making use of the indicated parameters as follows:

$$\begin{aligned}
\text{Volume}_{\text{face}} &= \text{width} \times \text{area} \\
&= d_s \text{ (area of pentagon} - \text{area of circle)} \\
&= d_s \left[\frac{5\,\phi}{4\sqrt{3-\phi}}\, l_s^2 - \pi \left(\frac{d_p}{2} \right)^2 \right] \\
&= d_s \left[\frac{5\,\phi}{4\sqrt{3-\phi}} - \frac{\pi\,\phi^2}{4\,(3-\phi)} \right] \left(c - \frac{1}{2}\sqrt{\frac{2}{3}}\, d_s \right)^2 ,
\end{aligned}$$

where equations (2.46) and (2.54) were used to express the volume in terms of c and d_s.

In order to find the total volume added to the faces of the cells, the volume added per face is multiplied by the number of faces and divided by the number of cells that share each face. Therefore, since there are 12 faces per cell and 2 cells that share each face, the total volume added to the faces of the cell can be expressed as:

$$\begin{aligned}
\text{Volume}_{\text{faces}} &= \frac{12}{2}\, d_s \left[\frac{5\,\phi}{4\sqrt{3-\phi}} - \frac{\pi\,\phi^2}{4\,(3-\phi)} \right] \left(c - \frac{1}{2}\sqrt{\frac{2}{3}}\, d_s \right)^2 \\
&= 6\, d_s \left[\frac{5\,\phi}{4\sqrt{3-\phi}} - \frac{\pi\,\phi^2}{4\,(3-\phi)} \right] \left(c - \frac{1}{2}\sqrt{\frac{2}{3}}\, d_s \right)^2 . \qquad \text{(C.1)}
\end{aligned}$$

Completing the calculation of the total volume added to each cell requires that the volume added to the nodes also be taken into consideration. Figure C.3(a) shows a type of tetrahedral volume fitted into the node space, as approximated by Huu et al. [21]. In Figure C.3(b) a tetrahedral with the node dimensions are shown in order to further visualize part of this volume calculation.

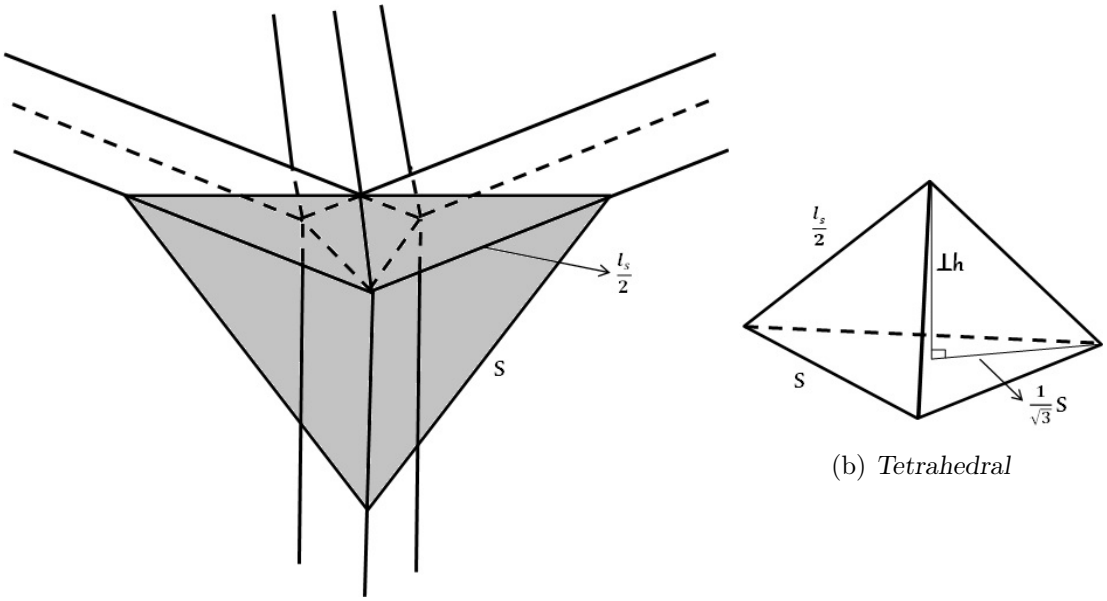

(a) *Volume added to node positioning in cell corner*

(b) *Tetrahedral*

FIGURE C.3: *Volume added to the node of a "fat" dodecahedron cell*

The volume of the adjusted tetrahedral can be expressed as

$$\begin{aligned} \text{Volume}_{\text{node}} &= \frac{1}{8} \cdot \frac{\text{base area} \times \perp h}{3} \\ &= \frac{\frac{1}{2} S^2 \sin\left(\frac{\pi}{3}\right) \times \sqrt{\frac{l_s^2}{4} - \frac{S^2}{3}}}{24} \\ &= \frac{S^2}{32\sqrt{3}} \sqrt{\frac{l_s^2}{4} - \frac{S^2}{3}} \,. \end{aligned} \tag{C.2}$$

Using the cell dimensions indicated in Figure C.4, S can be expressed in terms of d_p, i.e.

$$S = d_p \sin\left(\frac{\pi}{5}\right) \,. \tag{C.3}$$

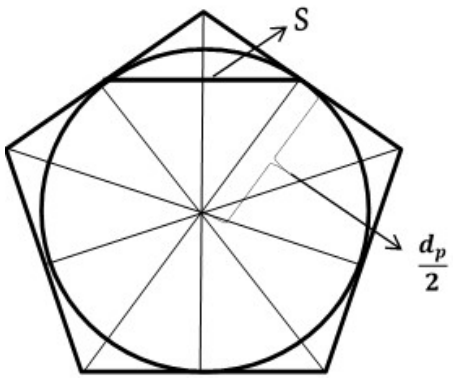

FIGURE C.4: *Dodecahedron cell parameters*

Equation (C.2) in terms of c and d_s can therefore be determined by incorporating equation (C.3),

as well as equations (2.46) and (2.54), which leads to

$$\text{Volume}_{\text{node}} = \frac{\sin^2\left(\frac{\pi}{5}\right)\,\phi^2\,\left(c-\frac{1}{2}\sqrt{\frac{2}{3}}\,d_s\right)^3}{32\,\sqrt{3}\,(3-\phi)}\sqrt{\frac{1}{4}-\frac{\sin^2\left(\frac{\pi}{5}\right)\,\phi^2}{9-3\,\phi}}\,. \tag{C.4}$$

The total volume added to the nodes will therefore be equal to the volume of a single adjusted tetrahedral multiplied by 20 due to the amount of nodes in each cell. Therefore the total volume added to the nodes is

$$\begin{aligned}\text{Volume}_{\text{nodes}} &= 20\cdot\frac{\sin^2\left(\frac{\pi}{5}\right)\,\phi^2\,\left(c-\frac{1}{2}\sqrt{\frac{2}{3}}\,d_s\right)^3}{32\,\sqrt{3}\,(3-\phi)}\sqrt{\frac{1}{4}-\frac{\sin^2\left(\frac{\pi}{5}\right)\,\phi^2}{9-3\,\phi}}\\ &= \frac{5\,\sin^2\left(\frac{\pi}{5}\right)\,\phi^2\,\left(c-\frac{1}{2}\sqrt{\frac{2}{3}}\,d_s\right)^3}{8\,\sqrt{3}\,(3-\phi)}\sqrt{\frac{1}{4}-\frac{\sin^2\left(\frac{\pi}{5}\right)\,\phi^2}{9-3\,\phi}}.\end{aligned} \tag{C.5}$$

Consequently the sum of equations (C.1) and (C.5) leads the total volume added for the "fat" dodecahedron cell model, i.e.

$$\begin{aligned}V_{\text{add}} =& 6\,d_s\left[\frac{5\,\phi}{4\,\sqrt{3-\phi}}-\frac{\pi\,\phi^2}{4\,(3-\phi)}\right]\left(c-\frac{1}{2}\sqrt{\frac{2}{3}}\,d_s\right)^2\\ &+\frac{5\,\sin^2\left(\frac{\pi}{5}\right)\,\phi^2\,\left(c-\frac{1}{2}\sqrt{\frac{2}{3}}\,d_s\right)^3}{8\,\sqrt{3}\,(3-\phi)}\sqrt{\frac{1}{4}-\frac{\sin^2\left(\frac{\pi}{5}\right)\,\phi^2}{9-3\,\phi}}\,.\end{aligned} \tag{C.6}$$

In order to determine the specific surface area of the "fat" dodecahedron model, the total surface area for each cell first needs to be calculated. This added surface area applies to both the triangular and cylindrical strut geometry. Figure C.5 shows the section that is the surface area of a face of the cell.

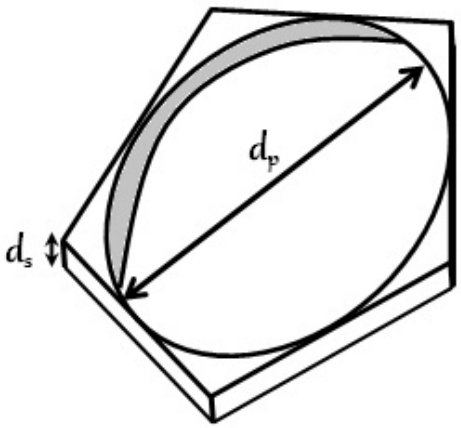

FIGURE C.5: *Surface area of the face of a "fat" dodecahedron cell*

The shaded section can be determined using the parameters indicated in the figure as follows:

$$2\,\pi\left(\frac{d_p}{2}\right)\times d_s = \pi\,d_p\,d_s\,.$$

Due to the 12 faces and each face being shared by 2 cells, the total surface area for this section per dodecahedron cell is

$$\frac{12}{2}\,\pi\,d_p\,d_s\,. \tag{C.7}$$

The base area of the tetrahedral in Figure C.3(b), i.e. an equilateral triangle of side length S, is used to calculate the added surface area around the nodes. This is, once again, an approximation made by Huu et al. [21] By using equation (C.3) this base area is given by

$$\frac{1}{4} \cdot \frac{1}{2} S^2 \sin\left(\frac{\pi}{3}\right) = \frac{\sqrt{3}}{16} S^2 = \frac{\sqrt{3}}{16} d_p^2 \sin^2\left(\frac{\pi}{5}\right) .$$

There are a total of 20 nodes and consequently the surface area surrounding the nodes per cell is

$$20\frac{\sqrt{3}}{16} d_p^2 \sin^2\left(\frac{\pi}{5}\right) . \tag{C.8}$$

Finally, the total surface area is equal to the sum of equations (C.7) and (C.8), i.e.

$$A_{\text{add}} = \frac{12}{2} \pi \, d_p \, d_s + \frac{20}{16}\sqrt{3} \, d_p^2 \sin^2\left(\frac{\pi}{5}\right) . \tag{C.9}$$

APPENDIX D

Cardanic method of solving a cubic polynomial

The Cardanic method (Wilms [64]) can be used to solve a cubic polynomial, such as

$$x^3 + a_1\,x^2 + a_2\,x + a_3 = 0\,, \tag{D.1}$$

where a_1, a_2 and a_3 are constants. The solutions to the cubic polynomial are

$$x_1 = 2\,\sqrt{-Q}\,\cos\left(\frac{1}{3}\,\Theta\right) - \frac{1}{3}\,a_1\,,$$
$$x_2 = 2\,\sqrt{-Q}\,\cos\left(\frac{1}{3}\,\Theta + \frac{2}{3}\,\pi\right) - \frac{1}{3}\,a_1$$

and

$$x_3 = 2\,\sqrt{-Q}\,\cos\left(\frac{1}{3}\,\Theta + \frac{4}{3}\,\pi\right) - \frac{1}{3}\,a_1\,,$$

where

$$Q = \frac{3\,a_2 - a_1^2}{9}\;;\; R = \frac{9\,a_1\,a_2 - 27\,a_3 - 2\,a_1^3}{54}\;;\; \cos\Theta = \frac{R}{\sqrt{-Q^3}} \text{ and } D = Q^3 + R^2\,,$$

if $D < 0$ and a_1, a_2 and a_3 are real. Then the roots of equation (D.1) are real and unequal.

Geometric factor of the three-strut RUC model

In order to solve for the geometric factor ψ of the three-strut RUC model in terms of ϵ, equation (2.87) is used, given by the polynomial

$$\psi^3 - 6\,\psi^2 + 9\,\psi - 4\,\epsilon = 0\,. \tag{D.2}$$

From the comparison of equation (D.2) to the cubic polynomial in equation (D.1), it can be deduced that

$$a_1 = -6 \;\;;\;\; a_2 = 9 \;\text{ and }\; a_3 = -4\,\epsilon\,,$$

from which it follows that

$$Q = \frac{3\,(9) - (-6)^2}{9} = -1\,,$$
$$R = \frac{9\,(-6)\,(9) - 27\,(-4\epsilon) - 2\,(-6)^3}{54} = 2\,\epsilon - 1\,,$$

and

$$D = (-1)^3 + (2\,\epsilon - 1)^2 = 4\,(\epsilon^2 - \epsilon)\,.$$

Since $0 < \epsilon < 1$, it follows that $\epsilon^2 < \epsilon$ which implies that $D < 0$. This condition being satisfied, leads to

$$\cos\Theta = \frac{2\,\epsilon - 1}{\sqrt{-(-1)^3}} = 2\,\epsilon - 1\,.$$

The solutions of equation (D.2) can therefore be expressed as

$$x_1 = 2\,\sqrt{-(-1)}\,\cos\left(\frac{1}{3}\,\Theta\right) - \frac{1}{3}\,(-6) = 2\,\cos\left[\frac{1}{3}\,\cos^{-1}(2\,\epsilon - 1)\right] + 2\,,$$
$$x_2 = 2\,\sqrt{-(-1)}\,\cos\left(\frac{1}{3}\,\Theta + \frac{2}{3}\,\pi\right) - \frac{1}{3}\,(-6) = 2\,\cos\left[\frac{1}{3}\,\cos^{-1}(2\,\epsilon - 1) + \frac{2}{3}\,\pi\right] + 2$$

and

$$x_3 = 2\,\sqrt{-(-1)}\,\cos\left(\frac{1}{3}\,\Theta + \frac{4}{3}\,\pi\right) - \frac{1}{3}\,(-6) = 2\,\cos\left[\frac{1}{3}\,\cos^{-1}(2\,\epsilon - 1) + \frac{4}{3}\,\pi\right] + 2\,.$$

If there are no stagnant zones, the geometric factor is equal to the tortuosity which would usually range between values of 1 and 2.

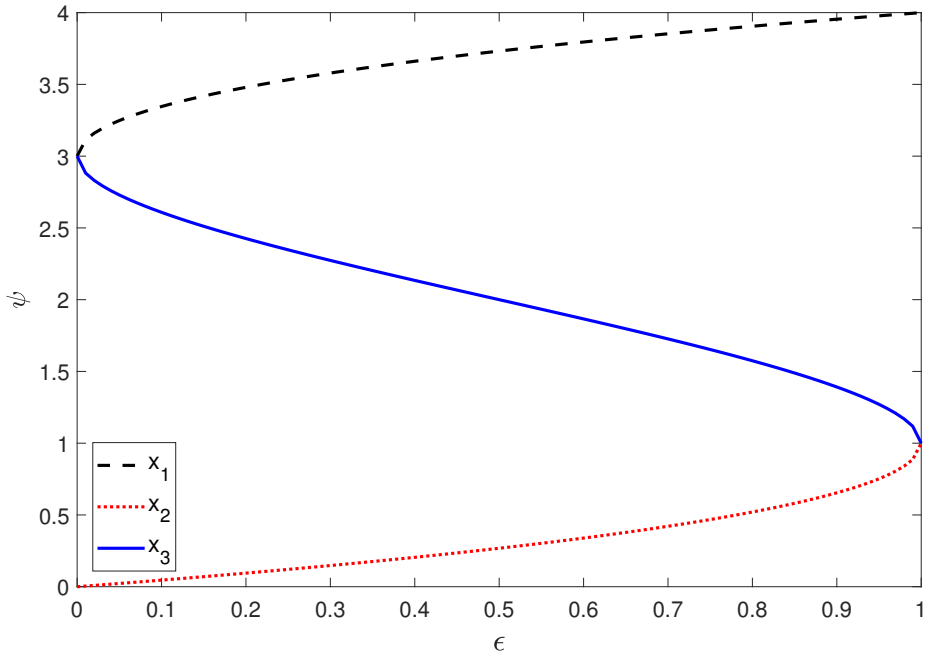

FIGURE D.1: *Solutions for the geometric factor versus porosity for the three-strut model*

It can therefore be concluded from Figure D.1 that the solution of equation (D.2) that is physically relevant, is the solution x_3, i.e.

$$\psi = 2 + 2\,\cos\left[\frac{4\,\pi}{3} + \frac{1}{3}\,\cos^{-1}(2\,\epsilon - 1)\right]\,, \tag{D.3}$$

which is the desired geometric factor in terms of porosity, for the three-strut model.

Geometric factor of the two-strut RUC model

In order to solve for the geometric factor ψ of the two-strut RUC model in terms of ϵ, equation (2.107) is used, that is the polynomial

$$\psi^3 - \psi^2 - \epsilon\,\psi + \epsilon^2 = 0\,. \tag{D.4}$$

Comparing equation (D.4) to the general cubic polynomial equation (D.1), it can be deduced that

$$a_1 = -1 \;\;;\;\; a_2 = -\epsilon \;\text{ and }\; a_3 = \epsilon^2\,,$$

and thus

$$\begin{aligned} Q &= \frac{3\,(-\epsilon) - (-1)^2}{9} = -\frac{3\epsilon + 1}{9}\,, \\ R &= \frac{9\,(-1)\,(-\epsilon) - 27\,(\epsilon^2) - 2\,(-1)^3}{54} = \frac{9\epsilon - 27\epsilon^2 + 2}{54}\,, \end{aligned}$$

and

$$D = \left(-\frac{3\epsilon + 1}{9}\right)^3 + \left(\frac{9\epsilon - 27\epsilon^2 + 2}{54}\right)^2 = \frac{1}{4}\epsilon^4 - \frac{11}{54}\epsilon^3 - \frac{5}{108}\epsilon^2\,.$$

Since $0 < \epsilon < 1$, it follows that $\epsilon^4 < \epsilon^3 < \epsilon^2$. Also, $\frac{1}{4} < \frac{11}{15} + \frac{5}{108}$ and therefore it implies that $D < 0$. This condition being satisfied, it further follows that

$$\cos\Theta = \frac{(9\epsilon - 27\epsilon^2 + 2)/54}{\sqrt{-\left(-\frac{3\epsilon+1}{9}\right)^3}} = \frac{9\epsilon - 27\epsilon^2 + 2}{2\sqrt{27\epsilon^3 + 27\epsilon^2 + 9\epsilon + 1}}\,.$$

The solutions of equation (D.4) can therefore be expressed as

$$\begin{aligned} x_1 &= \frac{2}{3}\sqrt{3\epsilon + 1}\cos\left[\frac{1}{3}\cos^{-1}\left(\frac{9\epsilon - 27\epsilon^2 + 2}{2\sqrt{27\epsilon^3 + 27\epsilon^2 + 9\epsilon + 1}}\right)\right] + \frac{1}{3}\,, \\ x_2 &= \frac{2}{3}\sqrt{3\epsilon + 1}\cos\left[\frac{1}{3}\cos^{-1}\left(\frac{9\epsilon - 27\epsilon^2 + 2}{2\sqrt{27\epsilon^3 + 27\epsilon^2 + 9\epsilon + 1}}\right) + \frac{2}{3}\pi\right] + \frac{1}{3}\,, \end{aligned}$$

and

$$x_3 = \frac{2}{3}\sqrt{3\epsilon + 1}\cos\left[\frac{1}{3}\cos^{-1}\left(\frac{9\epsilon - 27\epsilon^2 + 2}{2\sqrt{27\epsilon^3 + 27\epsilon^2 + 9\epsilon + 1}}\right) + \frac{4}{3}\pi\right] + \frac{1}{3}\,.$$

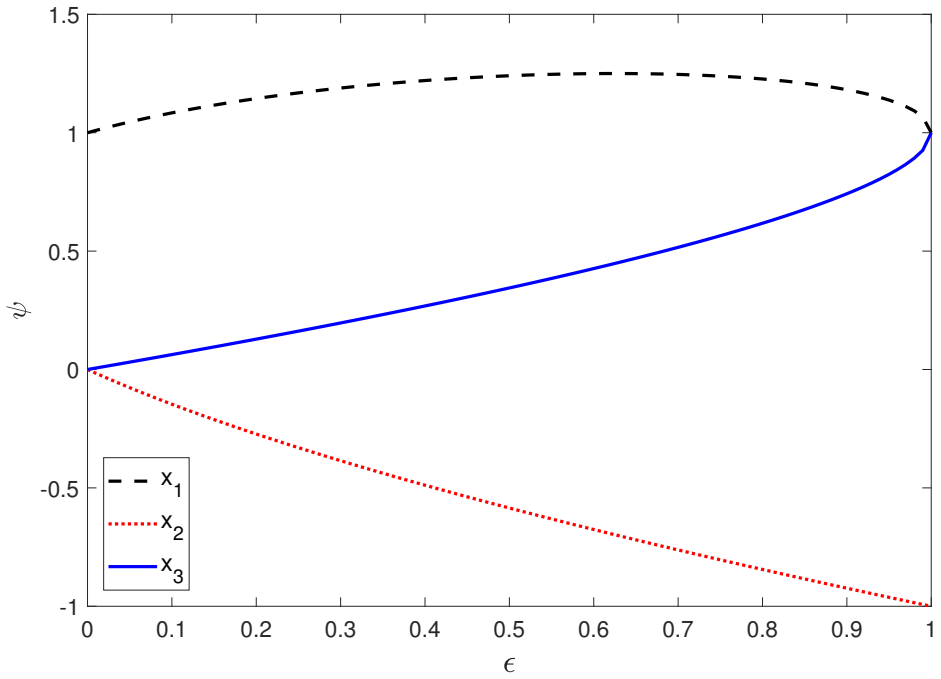

FIGURE D.2: *Solutions for the geometric factor versus porosity for the two-strut model*

The geometric factor would once again range between values of 1 and 2 and it can therefore be concluded from Figure D.2 that the solution for equation (D.4) that is physically relevant is the solution x_1, i.e.

$$\psi = \frac{2}{3}\sqrt{3\epsilon+1}\cos\left[\frac{1}{3}\cos^{-1}\left(\frac{9\epsilon-27\epsilon^2+2}{2\sqrt{27\epsilon^3+27\epsilon^2+9\epsilon+1}}\right)\right]+\frac{1}{3}\,, \tag{D.5}$$

which is the desired geometric factor in terms of the porosity for the two-strut model.